

Investigations of Magnetosphere-Ionosphere-Thermosphere System Under Varying Space Weather Conditions

A THESIS

submitted for the Award of Ph.D. degree of

MOHANLAL SUKHADIA UNIVERSITY

in the

Faculty of Science

by

Diptiranjan Rout



Under the Supervision of

Dr. D. Chakrabarty

Associate Professor

Space and Atmospheric Sciences Division

Physical Research Laboratory, Ahmedabad

Department of Physics

MOHANLAL SUKHADIA UNIVERSITY

UDAIPUR

Year of submission:2017

DECLARATION

I, **Mr. Diptiranjana Rout**, S/o Mr. Ananta Charan Rout, resident of RN-014, PRL student hostel campus, Thaltej, Ahmedabad 380059, hereby declare that the research work incorporated in the present thesis entitled, “**Investigations of Magnetosphere-Ionosphere-Thermosphere System Under Varying Space Weather Conditions**” is my own work and is original. This work (in part or in full) has not been submitted to any University for the award of a Degree or a Diploma. I have properly acknowledged the material collected from secondary sources wherever required and I have run my entire thesis on the antiplagiarism software namely, “iThenticate”. I solely own the responsibility for the originality of the entire content.

Date:

Diptiranjana Rout
(Author)

CERTIFICATE

I feel great pleasure in certifying that the thesis entitled, “**Investigations of Magnetosphere-Ionosphere-Thermosphere System Under Varying Space Weather Conditions**” by Mr. Diptiranjana Rout under my guidance. He has completed the following requirements as per Ph.D regulations of the University.

- (a) Course work as per the university rules.
- (b) Residential requirements of the university.
- (c) Regularly submitted six monthly progress reports.
- (d) Presented his work in the departmental committee.
- (e) Published minimum of one research papers in a referred research journal.

I recommend the submission of thesis.

Date:

Dr. Dibyendu Chakrabarty

Associate Professor

Space and Atmospheric Sciences Division,

Physical Research Laboratory,

Ahmedabad - 380009.

Countersigned by

Head of the Department

Dedicated to

My parents

for their unconditional love and sacrifices

Contents

List of Tables	xv
List of Figures	xvii
Acknowledgment	xxi
Abstract	xxv
List of publications	xxvii
1 Introduction	1
1.1 The Solar Wind	3
1.1.1 Magnetohydrodynamics (MHD) Description of Solar Wind Plasma: The Induction Equation	4
1.2 Coronal Mass Ejections (CMEs)	6
1.3 Corotating Interaction Regions (CIRs)	8
1.4 Solar Wind-Magnetosphere Interaction	9
1.5 Magnetosphere	11
1.6 Ionosphere	14
1.7 Thermosphere	18

1.8	Geomagnetic Storm	19
1.9	Magnetospheric Substorm	21
1.10	Magnetosphere-Ionosphere Coupling	26
1.10.1	Shielding: Undershielding (Prompt Penetration) and Over- shielding	28
1.10.2	Disturbance Dynamo Electric Field	32
1.11	The Bigger Picture and the Motivation of the Thesis	33
1.12	Organization of thesis	35
1.12.1	Chapter 1 – Introduction	35
1.12.2	Chapter 2 – Data and Techniques	35
1.12.3	Chapter 3 – Different Types of Prompt Electric Field Per- turbations and Their Equatorial Impacts	35
1.12.4	Chapter 4 – Prompt Penetration Electric Fields as Indi- cators of Geoeffectiveness of ICME	35
1.12.5	Chapter 5 – Prompt Penetration Electric Field and Geo- effectiveness of CIR Events	35
1.12.6	Chapter 6 – A New Type of Prompt Electric Field Dis- turbance Driven Solely by Solar Wind Density Variation	35
1.12.7	Chapter 7 – Scope of the Thesis	35
2	Data and Techniques	37
2.1	Introduction	37
2.2	OI630.0 nm Airglow Emission	38
2.2.1	Narrow band and narrow field of view 630.0 nm airglow photometer:	39

2.3	Digisonde	42
2.4	Incoherent and Coherent Radar Measurements	44
2.5	Geosynchronous Particle Injection Measurements (LANL and GOES)	46
2.6	Ground-based Magnetometer Observations	46
2.7	Other Data Sets	48
2.7.1	Solar Wind Observation	48
2.7.2	Geomagnetic Indices	48
2.7.3	Neutral Wind Velocity Measurements	50
2.8	Data Analysis Technique	50
2.8.1	Fast Fourier Transform	51
2.8.2	Lomb Scargle Fourier Transform (LSFT)	52
2.8.3	Cross Spectrum Analysis	53
3	Different Types of Prompt Electric Field Perturbations and Their Equatorial Impacts	55
3.1	Introduction	56
3.2	Measurements and Supporting Datasets	59
3.3	Results	61
3.4	Discussion	73
3.5	The effects of this space weather event in the day sector	81
3.6	Summary:	85
4	Prompt Penetration Electric Fields as Indicators of Geoeffectiveness of ICME	87

4.1	Introduction	88
4.2	Datasets	89
4.3	Results	91
4.4	Discussion	98
4.5	Summary	105
5	Prompt Penetration Electric Field and Geoeffectiveness of CIR Events	107
5.1	Introduction	108
5.2	Data Analysis and Result	110
5.3	Causal connection between IMF Bz and EEJ strength during CIR events	113
5.4	Causal connection and solar wind azimuthal flow angle	118
5.5	Discussion	118
5.6	Summary	124
6	A new type of prompt electric field disturbance driven solely by solar wind density variation	125
6.1	Introduction	126
6.2	Dataset:	129
6.3	Results	130
6.4	Discussion	137
6.5	Summary:	146
7	Scope of the Thesis	149

References	151
Attached Paper-1	181
Attached Paper-2	189

List of Tables

1.1	Properties of the solar wind at 1 AU	4
5.1	Table showing the relationship between azimuthal flow angle ($ \Phi $) and ionospheric effects of IMF Bz during CIR events . . .	119

List of Figures

1.1	Overview of the impacts of space weather	2
1.2	Archimedean spiral of IMF	5
1.3	A 3-D structure of ICME	7
1.4	A 2-D structure of CIR	9
1.5	Schematic of the Earth's magnetosphere	12
1.6	Altitude profiles of temperature and plasma of Earth's atmosphere	15
1.7	Quiet time vertical drift variation	17
1.8	Magnetic reconnection sites for southward and northward IMF .	19
1.9	Different phases of geomagnetic storm	20
1.10	Different phases of a magnetospheric substorm	23
1.11	Dipolarization and particle injection during substorm	24
1.12	Magnetic reconnection at the front-side of the magnetosphere .	27
1.13	Convection and corotation electric field	28
1.14	DP2 convection cells	29
1.15	Shielding and overshielding of electric field	31
2.1	Narrow band and narrow FOV 630.0 nm airglow photometers .	40
2.2	Schematic of narrow band and narrow FOV photometers.	40

3.1	Variations in IMF Bz and SYM-H during 22-23 January 2012. . .	60
3.2	Variation of h'F, vertical drift and 630.0 nm airglow	62
3.3	Solar wind, magnetospheric and ionospheric condition	65
3.4	ΔH variations over the Indian and Japanese sectors	68
3.5	Normalized periodograms and cross-spectral analyses in the night sector	70
3.6	Particle injection at geosynchronous orbit	72
3.7	Ionograms showing ESF over Thumba	78
3.8	Solar wind and ionospheric signatures on day sector	82
3.9	Normalized periodograms and Cross-spectral analyses in the day sector	84
4.1	The sheath and magnetic cloud signatures of an ICME	90
4.2	Global ionospheric electric field variations during the passage of sheath region	93
4.3	Spectral analyses of IEFy, EEJ, and vertical drift	95
4.4	Electron injection at geosynchronous orbit during onset of a pseudo-breakup event	97
4.5	ΔX variations of auroral electrojet stations	102
5.1	Solar wind and magnetospheric signatures during CIR events . .	111
5.2	Superposed epoch analyses for V, Tp, Np and Φ	113
5.3	Histograms of periodicities of IMF Bz and EEJ.	114
5.4	Spectral analyses of IMF Bz and EEJ during CIR events show- ing the presence of causal relationship	116

5.5	Spectral analyses of IMF Bz and EEJ during CIR events showing the absence of causal relationship	117
5.6	Schematic for explaining the mechanism of solar wind flow angle and its ionospheric effects	121
5.7	Location of magnetopause	122
6.1	Variations in IMF Bz, V, Np, P and vertical drift during solar wind ram pressure change	127
6.2	A global map with the magnetometer stations	129
6.3	The interplanetary and magnetospheric conditions during solar wind density change	131
6.4	Particle injection signatures at geosynchronous orbit during solar wind density change	133
6.5	ΔX variations over the globe	134
6.6	Latitudinal variation in the amplitude of ΔX during the density change	136
6.7	Variations in $\Delta H_{TIR} - \Delta H_{ABG}$ and $h_m F2$	137
6.8	High latitude ionospheric convection map	141
6.9	High latitude ionospheric convection map	141
6.10	High latitude ionospheric convection map	142
6.11	Average line of sight velocity from the HF radars over Stokkseyri, Iceland	142

Acknowledgments

The acknowledgments page never does justice to all the people who have contributed towards the work. Whatever little knowledge that I have gained in this life is because of my teachers. They have come in different forms in my life. It is they, who have influenced my thought processes and inspired me to learn. The journey of a doctoral thesis is a long one and without the help and support of many people, completion of a thesis is not possible.

When I started my Ph.D. program, I had very little knowledge on the subject and did not know how to go about it. Now, at the end of five years, I feel more confident to approach any problem. This would not have been possible without Prof. D. Chakrabarty, my thesis advisor. I would like to express my sincere gratitude to him for his patience, motivation, enthusiasm and constant guidance through all these years. He has been a guide, friend, critic, inspiration throughout. His belief in me during the critical junctures of my research works helped me to emerge out with more patient and confident. I will be forever indebted to him.

This thesis work has also been carried out under the close supervision of Prof. R. Sekar. I immensely gained from the intense discussion sessions on the subject and scientific practices with him. He taught me the essence of critical thinking while addressing a problem. He has been a great teacher and mentor for this work and throughout. I thank him for serving as one of my DSC committee members and his constructive suggestions that helped improving this thesis.

I am grateful to Prof. D. Pallamraju for serving in my DSC committee and for his valuable discussions about my research from time to time. His friendly nature and encouragements helped me discuss a wide range of subjects without any inhibitions. This helped me grow both in personal and profession life. Thank you Sir.

I am grateful to Prof. R. Sridharan for his guidance, encouraging words and valuable scientific discussions during this thesis work. I thank him for his kind support. I would also like to extend my thanks to Prof. A. C. Das for his constructive suggestions during the seminars.

I steal this opportunity to express my thanks to some of my international and national collaborators for providing me with data and allowing me to use the global space weather models. Special thanks goes to Prof. G. D. Reeves from Los Alamos National Laboratory, Los Alamos, New Mexico, USA; Prof. K. Shiokawa, STEL, Nagoya University, Japan; Prof. J. M. Ruohoniemi, Virginia Polytechnic Institute and State University, Blacksburg, USA; Prof. B. G. Fejer, Utah State University, Logan, USA; Dr. Nestor Aponte and Dr. Mike Sulzer, Arecibo Observatory, USA; Dr. John D. Mathews, Pennsylvania State University, USA; Dr. Robert B. Kerr and Dr. John Noto, Computational Physics Inc., USA; Dr. Swadesh Patra, Department of Physics, University of Oslo, Norway; Dr. T. K. Pant, Space Physics Laboratory, VSSC, India; Dr. B. Veenadhari and Mr. Atul S. Kulkarni, Indian Institute of Geomagnetism, Navi Mumbai, India; Dr. S. Sarkhel, Indian Institute of Technology Roorkee, Uttarakhand, India; and Prof. P. Janardhan, Dr. Debrup Hui and Kuldeep Pandey, Physical Research Laboratory, India for many wonderful collaborations. I am really grateful to them for their enthusiasm and constant support towards my research work. I must mention all the help and support I received from the company of Dr. Tarun Kumar Pant and Narayan during my field campaigns. I am grateful to Prof. S. P. Gupta for his scientific discussions and keeping the environment lively. I must thank Dr. Smitha V. Thampi, Space Physics Laboratory, VSSC, for her scientific discussions. I am obliged to Prof. Pawan Kumar, NIT, Rourkela, India for his encouragement and guidance during my masters, which greatly motivated me to do research in physics.

I am obliged to Department Of Space, Govt. of India for the research grant offered to me during my tenure at PRL. I extend my thanks to Prof.

Anil Bhardwaj, the Director, Prof. P. Janardhan, the Dean, Dr. Bhushit Vaishnav, Head, Academic Services and Prof. J. S. Ray, the Registrar, Physical Research Laboratory for providing me with timely administrative helps and the necessary facilities to carry out my thesis work. My special thanks goes to Prof. S. Ramachandran, Chairman of Academic Committee and SPASC division who always guided me in matters of academic and administrative matters. I am also thankful to the members of academic committee for their critical evaluation. I am also thankful to the Dean and Head of Physics Dept. at MLSU, Udaipur, and Hemant ji for their extended co-operations. I would also like to acknowledge the all the staff members from various departments. My special thanks to Mr. Pradeep Kumar Sharma and Mr. Senthil Babu for their ever-willingly help.

I express my sincere thanks to all the faculty members and colleagues of Space and Atmospheric Sciences Division for divisional work. I am especially thankful to Atul for helping me out in computational work and Sneha(N) for all the administrative help from division. I would like to thank some of the faculties from PRL for their academic and non-academic help. My special thanks goes to Dr. Aweek Sarkar, Dr. Sachindra Naik, Dr. R. P. Singh, Dr. R. D. Deshpande, Dr. Vijayan, Dr. Arvind Singh, Dr. G. K. Samanta, Dr. R. Bhushan.

Spending all these years at PRL would have never been easy without friends. Although I couldn't name all, each one made my life enjoyable at Thaltej. I am extremely thankful and grateful to my batch mates: Deepak, Bivin, Lalit, Venky, Chandana, Sukanya, Apurv, Pankaj, Rahul, and Newton for all those happiness they brought to me. I specially thank Deepak for being such a nice friend, cooking special dishes for me, and I still remember the day we came here together. I spent many memorable moments with some of the former students at PRL. I am really obliged to all those friends who made my graduation life memorable. I am grateful to their wonderful company at PRL:

Tiku, Kedar, Priyanka, Sweta, Sneha(Y), Wageesh, Arko, Naveen, Monojit, Avdhesh, Gaurav (T), Gaurav (J), Vrunda, Sagarika, Rajesh, Ritushree, Subir, Deepika, Prahalad, Priyank, Chandan, Aarthy, Archita, Shivangi, Nidhi, Shefali, Navpreet, Rupa, Rukmani, Avik, Arun, Sampurnanand, Aditya, Richa, Abhaya, Girish, Manu, Aman, Anil, Sandeep, Sushree, and Alok.

I am privileged to have such good friends like Amitava dada, Debrup and Kuldeep who have been an indispensable part of this journey. I will surely miss the party, we had in Debrup's room. Thank you all for being so supportive and kind to me. It has always been very amusing to listen jokes and poems from Anil. I would also like to my school friends (Pintu and Biswaranjan) and my college friends (Mohan, Narayan, Ali, Susnata, Gyana) for their constant encouragement and support. I would like to thank Susant Bhai, Satyapriya bhabi, and Nigam Bhai for their unconditional support even during bad times. It gives me immense pleasure to mention the name of Amrita ma'am for her care and affection. Thank you so much ma'am for the wonderful foods and specially the tea during long discussions with sir.

I express my deepest thanks and gratitude to my parents (Sri. Ananta Charan Rout and Late Smt. Surekha Rout) for their never ending love and support. Thank you for letting me chase my dreams. Without your selfless sacrifices from my childhood, this thesis would never have been transpired to its present entity. I miss my mother, who is not with me today to see and share this day; but, her inspirations and sacrifices for me will keep motivating me throughout my life. Undoubtedly, she would have been the happiest person to see this day. I am thankful to my grandmother and relatives who have always been supportive of my work. Last but not the least, I express my gratefulness towards my entire family members (Dei, Baba, Mummy, Gadidada, Badadada, Chuadada, Sanabau, Badabau, Pintu, Gudli, Chintu, Beta, Sili, Jhili, Gehli, Bhima and Pandu) who always supported my cause in all weathers.

Diptiranjana Rout

ABSTRACT

The interaction between the solar wind and the Earth's magnetosphere decides the energy input into the terrestrial plasma environment and this, in turn, controls the magnetosphere-ionosphere (MI) coupling processes. The solar wind-magnetosphere interaction drives the magnetospheric plasma convection from the high to low latitude ionosphere through the prompt penetration (PP) electric field. This PP electric field modifies the ionospheric dynamo electric field, driven by tidal winds over low latitudes. Therefore, the origin, strength and efficiency of the PP electric field depend on the solar wind (interplanetary), magnetospheric and ionospheric conditions. The present thesis work comprises of various aspects of the effects of PP electric field on the global ionosphere, in general, and low latitude ionosphere, in particular.

Chapter 1 of this thesis work introduces the background physics that is required to understand the results discussed in chapters 3-6. In order to address the impacts of different types of prompt penetration electric fields on the global ionosphere, data from various measurement techniques are adopted. Further, the analyses techniques used in the investigations are also discussed in **Chapter 2**.

Chapter 3 brings out different types of prompt electric field perturbations on equatorial ionosphere during a geomagnetic storm based on coordinated digisonde and OI 630.0 nm airglow observations from Thumba (TVM). It is shown that although, traditionally, these prompt electric field perturbations are classified under one category (Disturbance-Polar current Type 2 or DP2) during long duration events, these might constitute phenomenologically different processes that include the electric field perturbations due to substorm and pseudo-breakup. In fact, for the first time, signatures of substorm and pseudo-breakup induced electric field perturbations in 630.0 nm nightglow emission intensities over equatorial region are also brought out in this chapter.

In **Chapter 4**, the responses of the global ionospheric electric field associated with the passage of the ICME sheath region have been investigated using Incoherent scatter radar measurements of Jicamarca and Arecibo along with the variations of EEJ strength over India. This investigation shows that ICME can be geoeffective in terms of PP electric field perturbations even if variation in ring current indices suggest absence of a typical geomagnetic storm.

In **Chapter 5**, a total of 43 CIR-induced geomagnetic storms during the deep solar minimum of solar cycle 23 (2006-2010) are studied. The daytime ionospheric effects are investigated by using the EEJ strength over Jicamarca as the signature of geoeffectiveness during these CIR events. It is found that PP electric field perturbations affect equatorial ionosphere when the average solar wind azimuthal angle is below 6 degree at the first Lagrangian point (L1) of the Sun-Earth system. Therefore, this result, for the first time, provides a method to forecast the geoeffectiveness of CIR events based on the observations from the L1 point.

Chapter 6 brings out a new type of PP electric field disturbance which is driven by changes in solar wind density alone. The density-driven electric field has not only enhanced the high-latitude ionospheric convection pattern but also enhanced the EEJ strength and the peak height of the F layer (hmF2) over the Indian dip equatorial sector. It is suggested that this type of electric field originates in the magnetosphere and is phenomenologically different from conventional PP electric fields.

Chapter 7 brings out the scope of the thesis.

Keywords: CME, CIR, Geomagnetic storm, Magnetospheric substorm, Pseudo-breakup, Magnetosphere-Ionosphere coupling, Prompt penetration electric field, Space weather, 630.0 nm airglow, Geoeffectiveness

LIST OF PUBLICATIONS

1. **Three different types of electric field disturbances affecting equatorial ionosphere during a long-duration prompt penetration event.**

Chakrabarty, D., **Diptiranjan Rout**, R. Sekar, R. Narayanan, G. D. Reeves, T. K. Pant, B. Veenadhari, and K. Shiokawa (2015), **J. Geophys. Res. Space Physics**, 120, 4993-5008. doi: 10.1002/2014JA020759.

2. **An evidence for prompt electric field disturbance driven by changes in the solar wind density under northward IMF Bz condition.**

Diptiranjan Rout, D. Chakrabarty, R. Sekar, G. D. Reeves, J. M. Ruohoniemi, T. K. Pant, B. Veenadhari, and K. Shiokawa (2016), **J. Geophys. Res. Space Physics**, 121, 4800-4810, doi:10.1002/2016JA022475.

3. **Solar wind flow angle and geoeffectiveness of corotating interaction regions: First results.**

Diptiranjan Rout, D. Chakrabarty, P. Janardhan, R. Sekar, V. Maniya, and K. Pandey (2017), **Geophys. Res. Lett.**, 44, doi:10.1002/2017GL073038.

4. **The ionospheric impact of a CME driven sheath region over Indian and American sectors in the absence of a typical geomagnetic storm.**

Diptiranjan Rout D. Chakrabarty, S. Sarkhel, R. Sekar, B. G. Fejer, G. D. Reeves, Atul S. Kulkarni, Nestor Aponte, Mike Sulzer, John D. Mathews, Robert B. Kerr, and John Noto, (2017), **To be communicated shortly.**

PUBLICATIONS NOT INCLUDED IN THIS THESIS

1. **Role of IMF B_y in the prompt electric field disturbances over equatorial ionosphere during a space weather event.**

Chakrabarty, D., D. Hui, **Diptiranjan Rout**, R. Sekar, A. Bhattacharyya, G. D. Reeves, and J. M. Ruohoniemi (2017), **J. Geophys. Res. Space Physics**, 122, 2574-2588, doi:10.1002/2016JA022781.

2. **The changing shape of the terrestrial bow shock and magnetopause response to the long term decline in solar magnetic field.**

Ingale M., Janardhan P., Fujiki, K., Bisoi S., **Diptiranjan Rout**, (2017), **Astrophysical Journal (Under review)**.

Chapter 1

Introduction

The Sun which contains more than 99.8% of the total mass of the solar system, is the prime source of energy for the planets including the Earth. It constantly emits its energy in various forms into the solar system. This energy is being transmitted into the interplanetary medium in the form of electromagnetic and corpuscular radiation. The pressure gradient between the surface of the Sun and the interplanetary medium causes a steady flow of plasma called the solar wind. Sometimes, sudden explosions in the solar corona facilitated by the Sun's magnetic field causes an enormous release of mass and energy, known as coronal mass ejection (CME). CMEs and solar flares are main drivers of space weather and can have huge impact on terrestrial environment. To quote *Bothmer and Daglis (2007)*, "Space weather, a field of research that will provide new insights into the complex influences and effects of the Sun and other cosmic sources on interplanetary space, the Earth's magnetosphere, ionosphere, and thermosphere, on space- and ground-based technological systems, and beyond that, on their endangering affects to life and health". Figure 1.1 depicts a schematic of Earth's space environment affected by space weather. The technologies available in the human society have been significantly advanced in the last few decades and we live in the era of satellites, space travel, air travel and long distance electrical power transmission. All these man-made

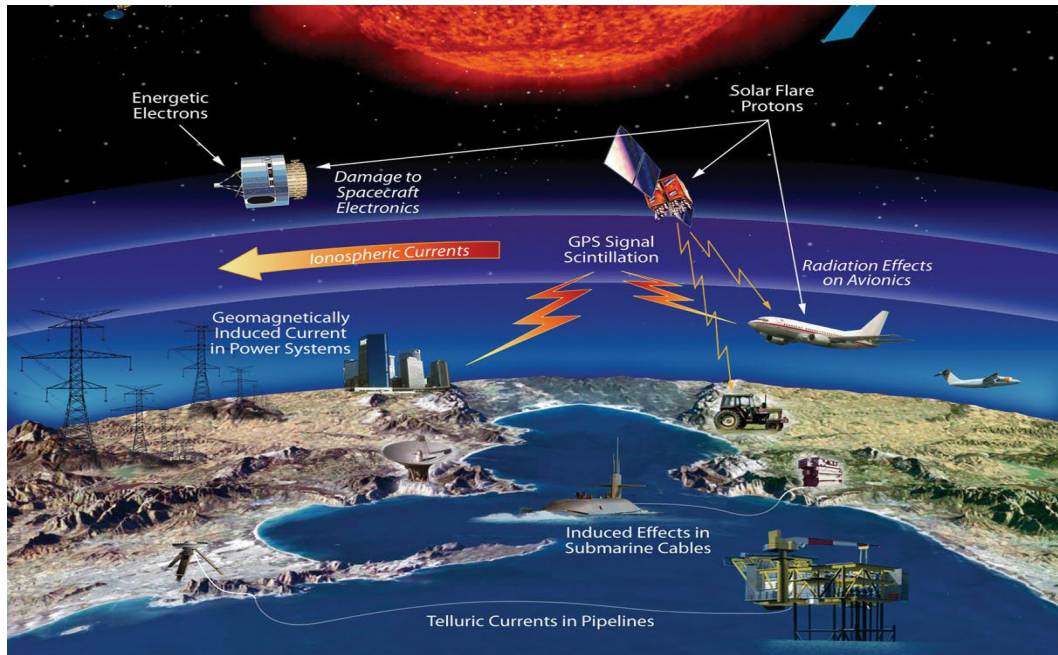


Figure 1.1: A schematic overview of the possible impacts of space weather on the terrestrial technological systems (Credit: <https://www.nasa.gov/sites/default/files/thumbnails/image/faq13.jpg>).

technology can be affected by extreme space weather events. These effects include disruptions in GPS and communication systems, charging of satellites, high-frequency communication blackouts, large scale power outages and damage of pipelines due to large scale geomagnetically induced current (GIC). GIC mainly enhances during strong geomagnetic storms, and can impact many earth-based technologies including power transmission, railroads and pipelines. Low-Earth-Orbiting (LEO) satellites are also affected by increased atmospheric drag during high solar activity period which finally leads to the decay of the spacecraft's orbit. The high energy solar protons and radiation belt particles can cause huge damage to the solar cells and electronic systems of spacecraft. Further, the radiations can be very hazardous to astronauts during space walks and while traveling into the deep space missions. The effects of space weather can also create spectacular displays of aurora, which can be seen through naked eyes over high latitudes. There was a time when ancient people used to at-

tribute aurora as the god of winter and death and particularly, the red aurora was considered a sign of ill omen from heavens. Our scientific skills and technologies have tremendously evolved over time and it is known that aurora is a visual manifestation of the changes in upper atmosphere of the Earth caused by disturbances in the near-earth space. Increased dependence on space-borne intelligence systems makes space weather a very challenging and exciting topic for research. Therefore, a comprehensive knowledge on extreme space weather events is of great importance for the modern human society and the present thesis work on the coupling of solar wind-magnetosphere-ionosphere system is expected to add values to the on current space weather research.

1.1 The Solar Wind

The Sun is the most important source of plasma in our solar system. The supersonic outflow of electrically charged particles, mainly protons, electrons and alpha particles from outer atmosphere of the solar corona, is called the solar wind. The solar wind was first theoretically predicted by E N Parker, in 1958. Later on, Parker's theory of solar wind was experimentally verified by in situ measurements from the spacecraft Mariner 2 (*Neugebauer and Snyder, 1962*). The solar corona has a temperature of more than a million kelvin. The huge pressure difference between the outer corona and the local interstellar medium drives the plasma outward, despite the restoring influence of solar gravity. The typical observed properties of solar wind plasma at 1 AU are listed in Table-1.1 (*Kivelson and Russell, 1995*).

The solar wind is turbulent and flowing radially outward. The plasma beta (β) is defined as the ratio of thermal to magnetic pressure. It is given by

$$\beta = \frac{P}{(B^2/2\mu_0)} \quad (1.1)$$

where $P = n_p k T_p + n_e k T_e$ (T_e and T_p are the electron and proton temperatures and n_e and n_p are the electron and proton number density respectively), B is

the magnetic field strength, k is the Boltzmann constant and μ_o is the magnetic permeability of vacuum. For all solar wind conditions, β is greater than unity i.e. the magnetic field is relatively weak and the solar magnetic field is carried by the solar wind flow into the interplanetary medium. This is known as the interplanetary magnetic field (IMF). The typical value of the IMF at 1 AU is ~ 5 nT during geomagnetically quiet conditions.

Table 1.1: Properties of the solar wind at 1 AU (from *Kivelson and Russell, 1995*)

Proton density	6.6 cm^{-3}
Electron density	7.1 cm^{-3}
He ²⁺	0.25 cm^{-3}
Flow Speed	450 km s^{-1}
Proton temperature	$1.2 \times 10^5 \text{ K}$
Electron temperature	$1.4 \times 10^5 \text{ K}$
Magnetic field	5 nT

1.1.1 Magnetohydrodynamics (MHD) Description of Solar Wind Plasma: The Induction Equation

The induction equation is one of the most important magnetohydrodynamic (MHD) equations in plasma physics. It is useful in understanding dynamics of magnetic fields in the solar wind plasma.

$$\frac{\partial \mathbf{B}}{\partial t} = \nabla \times (\mathbf{v} \times \mathbf{B} + \eta \nabla \times \mathbf{B}), \quad (1.2)$$

where \mathbf{B} is the magnetic field, \mathbf{v} is the (plasma) velocity field, $\eta = 1/\sigma$ is the magnetic diffusivity of the system and σ is the electric conductivity of the fluid. If magnetic diffusivity is constant in space, this induction equation reduces to

$$\frac{\partial \mathbf{B}}{\partial t} = \nabla \times (\mathbf{v} \times \mathbf{B}) + \eta \nabla^2 \mathbf{B} \quad (1.3)$$

The first term on the right-hand side in the above equation shows that the magnetic field at a point in a plasma can be changed by a motion of the

plasma and the second term shows that the magnetic field can also be changed by the diffusion process. The ratio of the first to the second term on the R.H.S. of the above equation is commonly known as magnetic Reynolds number i.e. $R_m = \frac{LU}{\eta}$, where U is the average plasma velocity perpendicular to the magnetic field and L is the characteristic length over which the field varies. This number is very important as it decides whether a medium is diffusion or flow dominated. For a perfectly conductive plasma, electrical conductivity, $\eta \rightarrow 0$. For example, the magnetic Reynolds number for the solar wind, R_m is $\sim 10^{16}$ (i.e. $R_m \gg 1$). In this case the flow dominates and the magnetic field simply moves with the flow. The magnetic field is frozen-in and therefore, the second term $\nabla^2 \mathbf{B}$ can be neglected. The induction equation reduces to

$$\frac{\partial \mathbf{B}}{\partial t} = \nabla \times (\mathbf{v} \times \mathbf{B}) \quad (1.4)$$

This equation implies the frozen-in condition of plasma flow, and this was

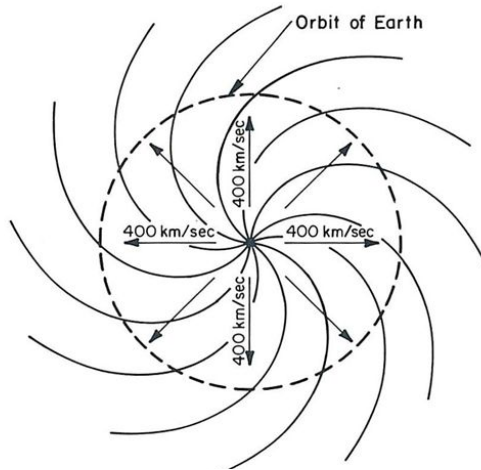


Figure 1.2: Archimedean spiral of IMF associated with solar rotation and plasma flow (from [Parker, 1965](#)).

first proposed by [Alfvén \(1943\)](#) which is known as “Alfvén’s theorem of flux freezing”. The solar wind is mostly radial and it rotates with the Sun. The combined effects of the solar rotation and plasma flow lead to a spiral configuration of the IMF in the solar equatorial or ecliptic plane (see Figure 1.2).

This is very similar to a spraying of water by a garden hose as viewed from above. In the solar wind, this configuration of IMF is referred to as the Parker spiral and the value of Parker angle at 1 AU $\sim 45^\circ$ for a solar velocity of 450 km s⁻¹.

1.2 Coronal Mass Ejections (CMEs)

Coronal mass ejections (CMEs) are explosive ejections of high energy plasma into interplanetary space from the outer atmosphere of solar corona. It releases an average of 10^{31} ergs of kinetic energy into the interplanetary medium ([Webb and Howard, 1994](#)). Most of the CMEs originate from an area of solar corona having many sunspots and its frequency of occurrence is highly dependent upon the solar cycle. CMEs occur most often during solar maximum. A typical CME can eject $\sim 10^{23}$ Maxwell of magnetic flux and 10^{16} gm of plasma into the interplanetary medium ([Gosling, 1990](#); [Forbes, 2000](#)). CMEs are often associated with solar flares. Solar flare is a phenomenon in which the Sun explosively releases enormous energy in a wide range of electromagnetic spectra, encompassing from radio waves to gamma rays. The total power of a typical solar flare is about $10^{20} - 10^{22}$ W and the amount of energy release may reach $\sim 10^{25}$ J in 10 min. However, the relationship of solar flare and CME is not very clearly understood. The stored magnetic energy is transferred to the plasma particles during CME ([Temmer et al., 2010](#)). When a CME is directed towards the Earth it is called a “halo” CME.

When a CME travels in the interplanetary medium, it is called Interplanetary CME or ICME. An ICME is known to have three distinctly different regions: the shock, the sheath, and the magnetic cloud (MC) (e.g. [Rouillard, 2011](#)) although this may change from one ICME to other. When the CME is moving faster than the surrounding solar wind magnetosonic speed, a shock is formed at the leading edge of the ICME. A sheath is a turbulent and heated

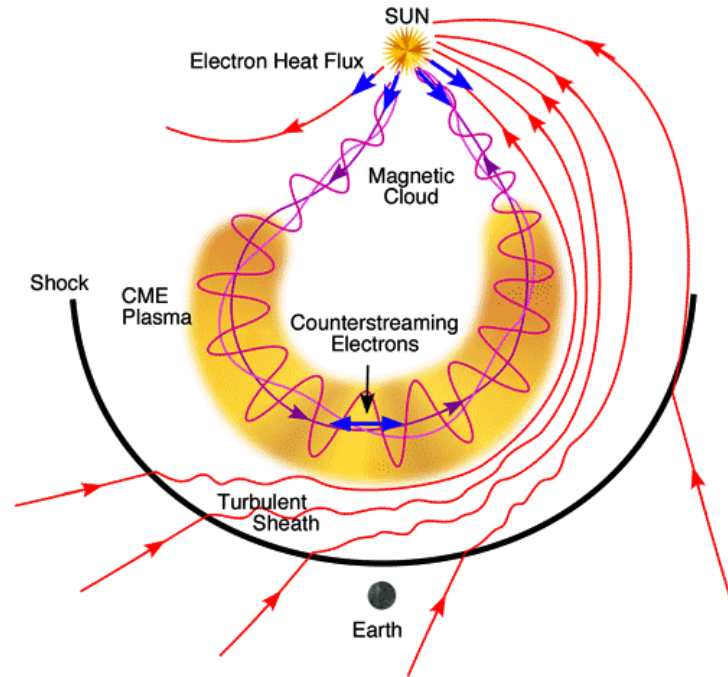


Figure 1.3: Schematic of an ICME revealing the shock, sheath and the magnetic cloud regions. (from [Zurbuchen and Richardson, 2006](#)).

region of the ICME structure located just behind an interplanetary shock. It is a highly compressed and turbulent region. The ICME sheath is generally characterized by enhanced and fluctuating magnetic fields, solar wind proton density, velocity, dynamic pressure and temperature. The magnetic field is usually draped around the ejecta and it deviates from the local Parker spiral orientation ([Gosling and McComas, 1987](#)). The MC part of an ICME follows the sheath part and it is generally associated with the following signatures: changes in magnetic field that rotates slowly through a large angle, low proton temperature, low proton density, monotonic decrease in solar wind speed, low plasma beta, enhanced alpha to proton ratio, elevated oxygen charged states, enhanced Fe charged states, bidirectional electron streaming etc. (e.g. [Zurbuchen and Richardson, 2006](#); [Rouillard, 2011](#)). A schematic of the three-dimensional structure of an ICME showing different regions (shock, sheath and magnetic cloud) along with the magnetic field lines, plasma, and particle signatures are given in Figure 1.3 ([Zurbuchen and Richardson, 2006](#)).

1.3 Corotating Interaction Regions (CIRs)

In contrast to solar maxima, the coronal holes become most frequent and prominent solar features during the declining phase of solar cycle (solar minima). Coronal holes are regions of the Sun with extremely low temperature and density compared to the surrounding medium. During the declining phase of the solar cycle the coronal holes originate over high latitudes and gradually extend towards the lower latitudes and reach closer to the ecliptic equator (*Tsurutani et al., 2006*). The magnetic field lines coming from the coronal holes are either inward or outward (*Alves et al., 2006*). These apparently open field lines penetrate deep into the interplanetary space. Coronal holes are the primary source for the high speed solar wind of 700-800 km s⁻¹ (*Pizzo, 1978; Forsyth and Marsch, 1999; Jian et al., 2006*). The fast stream (600-800 km s⁻¹) of solar wind continuously coming from coronal holes catches up the slow stream (300-400 km s⁻¹) of solar wind and interact near the ecliptic plane. The kinetic energy of the fast solar wind is thus converted into thermal energy. As a result, the plasma heating takes place and density decreases (rarefaction). This region between slow and fast solar wind is called the stream interface (SI) (*Alves et al., 2006*). An intense magnetic field is produced at the interface region between fast and slow stream in the solar wind. The regions where the fast solar wind originates from Sun, are long lived and try to “corotate” with the Sun with a period of 27 days and subsequently, a periodic perturbation in the near earth-space environment is observed. These interaction regions in interplanetary medium are called as “Corotating Interaction Regions” or CIRs (*Kamide et al., 1998; Tsurutani et al., 2006*). In a CIR, the stream interface is defined by rise in solar wind velocity, sharp drop in proton density, rise in proton temperature, and shear in solar wind flow and it is believed that it acts as a boundary or a transition region where the slow solar wind interacts with the fast solar wind (*Tsurutani et al., 1995; Forsyth and Marsch, 1999*). A typical

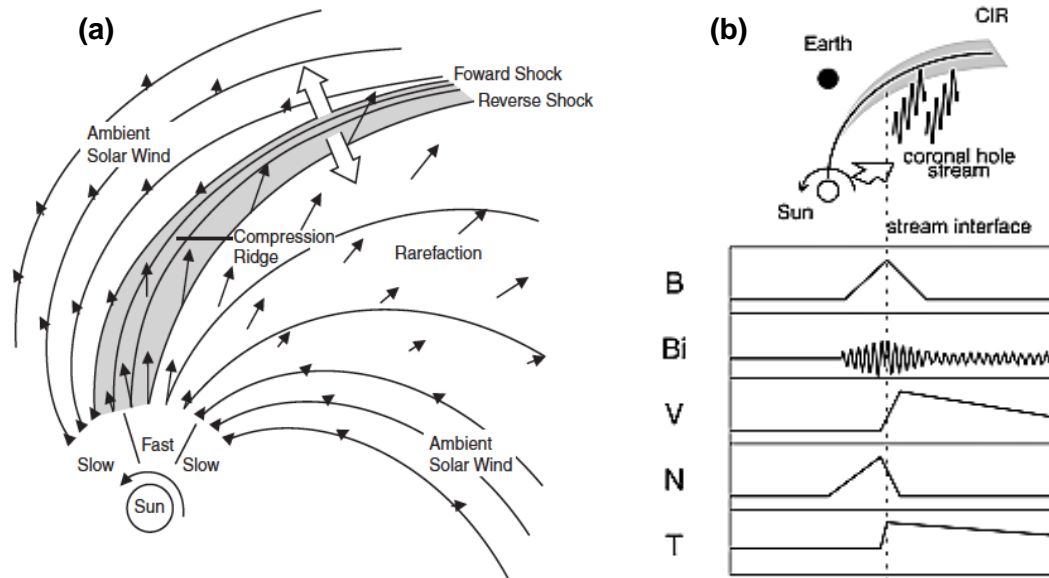


Figure 1.4: (a) Schematic illustrating 2-D corotating stream structure in the solar equatorial plane in the inner heliosphere (from [Pizzo, 1978](#)) and (b) the signatures in solar wind parameters at stream interface (SI) (from [Kataoka and Miyoshi, 2006](#)). Figure 1.4 (b) depicts (from top to bottom) variations in magnetic field strength (B), different components of magnetic field (Bi), solar wind velocity (V), solar wind density (N) and temperature (T). The stream interface is marked by dashed line.

solar wind interaction during CIR is displayed in Figure 1.4(a) ([Pizzo, 1978](#)). The Sun is situated at the bottom of the figure. The fast solar wind bends lesser than the slow solar wind and catches up with the slow wind creating an interaction region (IR). Figure 1.4(b) depicts (from top to bottom) variations in magnetic field strength (B), different components of magnetic field (Bi), solar wind velocity (V), solar wind density (N), and temperature (T). The stream interface is marked by dashed line ([Kataoka and Miyoshi, 2006](#)).

1.4 Solar Wind-Magnetosphere Interaction

In order to know the solar wind-magnetosphere interaction, it is important to measure the solar wind properties and the evolutions of its characteristic

features in the interplanetary medium. There are a few satellites that take measurements of solar wind parameters round-the-clock in the interplanetary medium. For round-the-clock solar wind measurements, it is important that these satellites are positioned suitably between the Sun and the Earth. For the present thesis work, the data from the Advanced Composition Explorer (ACE) and WIND satellites have been extensively used. These satellites are located in halo orbits around the 1st Lagrangian point of the Sun-Earth system. A Lagrange point is a position in space where the gravitational forces of two celestial bodies equals the centripetal force required for a small object to move with them. The interaction of the forces creates a point of equilibrium where a spacecraft is placed to make observations. There are five Lagrangian positions in Sun-Earth system. Among these, the first point, L1, is situated in between the Earth and the Sun at a distance of ~ 1.5 million km from the Earth.

In order to deal with the propagation of solar wind in the interplanetary medium and its impact on the Earth's magnetosphere, two Geocentric coordinate systems are generally adopted. These are Geocentric Solar Ecliptic (GSE) and Geocentric Solar Magnetospheric (GSM) coordinate systems. In GSE system, the positive X-direction points from the Earth towards the Sun, positive Y-direction is in the ecliptic plane pointing towards dusk and the positive Z-direction is parallel to the ecliptic north pole. In GSM system, the positive X-direction points towards the Sun, the positive Z-direction points to northern geomagnetic pole, and the Y-direction completes the orthogonal system according to the right-hand rule. Positive Y direction points to the dusk side. Therefore, the GSE and the GSM coordinate systems are related through a rotation around the X-axis which is common for both the coordinate systems. Although these coordinate systems are used interchangeably, GSE coordinate system is more useful for studying the solar wind propagation in the interplanetary medium and the GSM system is more frequently used for the evaluation of the impact of solar wind on terrestrial magnetosphere.

The solar wind is collisionless and highly conducting. For an observer on the Earth, the solar wind electric field is given by the following equation,

$$\mathbf{E}_{\text{sw}} = -\mathbf{V}_{\text{sw}} \times \mathbf{B}_{\text{sw}} \quad (1.5)$$

where \mathbf{V}_{sw} and \mathbf{B}_{sw} are the solar wind radial velocity and magnetic field, respectively. It is well known that the southward component of IMF is more geoeffective as it favors magnetic reconnection with the Earth's dipolar magnetic field which points towards north. If in a coordinate system (GSE or GSM), the direction of solar wind velocity is in negative X-direction (as solar wind is earthward) and the IMF is in the negative Z-axis (southward), an electric field is observed in the Y-direction with respect to the Earth's reference frame. The Y-component of interplanetary electric field (IEF_y) is very important for the solar wind-magnetosphere interaction. Before this interaction is introduced in Section 1.10, a discussion on magnetosphere is presented below.

1.5 Magnetosphere

The Earth is shielded from the influence of the solar wind because of the geomagnetic field. The geomagnetic field deflects the solar energetic wind from reaching the Earth. The Earth's geomagnetic field is approximately dipolar in nature. The interaction between Earth's magnetic field and the solar wind plasma results in a cavity like structure called the magnetosphere, which has a long comet-like tail in nightside and a compressed dayside facing the Sun. The Earth's magnetosphere is shown in Figure 1.5 which represents various plasma domains in magnetosphere. The magnetopause is the outer layer of the magnetosphere, separating it from the shocked region. In front of the magnetopause, a bow shock is formed due to the supersonic nature of the solar wind. The region between the bow shock and the magnetopause is known as the magnetosheath, where supersonic solar wind flow slows down to subsonic level and the plasma is hotter and more turbulent than the ambient solar wind.

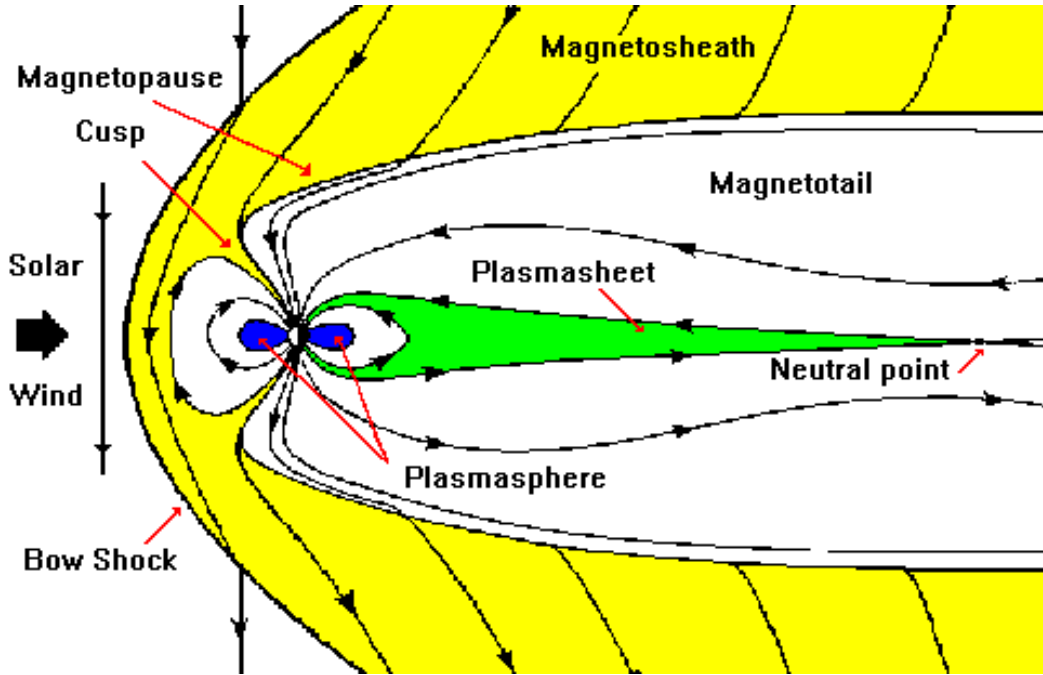


Figure 1.5: Shows a schematic of the Earth's magnetosphere. (Credit:<https://helios.gsfc.nasa.gov/magneto.html>)

The magnetopause is situated at the location where the plasma pressure of the solar wind and the magnetic pressure of the Earth's magnetosphere are balanced. The solar wind's dynamic pressure is defined as $P_{dyn} = (1/2)\rho v^2$, where ρ and v are the proton density and flow speed, respectively. The location of dayside boundary of the magnetosphere can be estimated by balancing the solar wind dynamic pressure with the magnetic pressure exerted by the geomagnetic field (*Kivelson and Russell, 1995*). i.e.

$$L_{mp}(R_E) = 107.4(\rho v^2)^{-1/6} \quad (1.6)$$

where the magnetopause distance (L_{mp}) is in R_E (R_E is the Earth's radius). The Earth's magnetosphere extends from the top of the ionosphere (the partially ionized layer of the Earth upper atmosphere), all the way to hundreds of Earth radii in the night side (tail region), but only up to $\sim 14 R_E$ in the day side.

The region inside magnetopause is generally divided into two subregions:

the outer magnetosphere and inner magnetosphere. The outer magnetosphere mainly contains some of the large-scale magnetospheric current systems like: cross-tail current and magnetopause current. The plasma/current sheath typically contains hot plasma (keV) with densities varying between $0.1\text{-}1\text{ cc}^{-1}$ (*Kivelson and Russell, 1995*). Compared to the plasma sheet, the tail lobes have much lower plasma densities (0.1 cc^{-1}) with energies in the range of 5-50 keV. The plasma can easily escape as the tail lobe magnetic field is “open” to the solar wind. The inner magnetosphere includes the ring current, plasmasphere, and the inner and outer Van Allen radiation belts. The radiation belts generally contain the energetic particles (keV to MeV) trapped by the Earth’s magnetic field and drifting across the magnetic field lines. The inner radiation belt mostly consists of high energy protons (0.1 MeV-40 MeV) and also substantial amount of energetic electrons (hundreds of keV) at a distance of 0.2 to $2 R_E$. The outer belt is mostly populated by energetic electrons (keV to MeV) at a distance of 4 to $5 R_E$. The outer radiation belt is very dynamic and strongly depends on the geomagnetic conditions while the inner belt is relatively more stable. Recent mission of Van Allen Probes spacecraft reveal the existence of a transient third radiation belt region (*Baker et al., 2013*). Further, the inner magnetosphere also contains the ring current which flows at distance of $2\text{-}6 R_E$ due to differential motion of electrons and ions. The plasmasphere is the region of the inner magnetosphere consisting of dense ($\sim 10^3\text{ cc}^{-1}$) low energy ($\sim 1\text{ keV}$) plasma and corotates with the Earth. Plasmasphere starts just above the Earth’s upper atmosphere and the outer boundary is known as plasmopause (at a distance of $4\text{-}5 R_E$) where the plasma density sharply drops by orders of magnitude. To the first approximation, corotation and convection electric fields cancel at plasmopause.

1.6 Ionosphere

The ionosphere is the partially ionized region of the Earth's upper atmosphere which has sufficient plasma density to influence the radio wave propagation. There are two main sources to ionize the neutral atmosphere i.e. the photo-ionization caused by EUV and UV radiation from the Sun and energetic particle precipitation (*Kivelson and Russell, 1995*). Photo-ionization is the primary source for ionization over low latitudes while energetic particle precipitation is a significant process over high latitude (auroral) ionosphere in addition to Photo-ionization. The partially ionized region in the Earth's atmosphere is extended from 60km to 1000 km in altitude and is divided into three layers i.e. the D, E and F-region (shown in Figure 1.6). Further, the F-layer, on many occasions, splits into F1 and F2 layers around noontime. The F region is mainly dominated by transport processes and the lifetimes of the atomic ions in this region are of the order of a few hours. Therefore, F layer sustains at nighttime even in the absence of ionizing radiation. On the other hand, photochemical equilibrium exists at the height of the E layer and therefore, nearly an order of magnitude less ionization densities exist in E-region during nighttime due to the lack of solar radiation and presence of recombination (loss process). The extent of D, E and F-regions are 60-90 km, 90-150 km and >150 km respectively. The D-region is primarily caused by the ionization of nitric oxide (NO) due to the solar hard X-ray (0.1-0.8 nm). The molecular ions (e.g. NO^+ and O_2^+) are dominant the E and lower F regions whereas atomic ions (e.g. O^+) are dominant in the upper F region. The ionization mainly caused by solar X-rays (0.8-14 nm) and UV radiation (79.6-102.7 nm) in the E region whereas F region mostly gets ionised by solar extreme ultraviolet radiation (roughly in the range of 14.0-79.6 nm). It is important to note that the three layers are also classified according to the ratio of collision and gyro frequencies at these heights. The plasma in the D-region is collisionally

dominated i.e. the magnetic field (Collision frequency, $\nu_{i,e} \gg$ Gyro frequency, $\omega_{i,e}$, at 80 km where $\nu_{i,e}$ essentially means collisions of ions and electrons with neutrals, i.e., ν_{in} and ν_{en} ; in D-region, $(\frac{\nu}{\omega})_i \gg 1$, $(\frac{\nu}{\omega})_e \approx 2$). In the E region, the motion of electrons are governed by the geomagnetic field while the motion of ions are still dominated by collision processes ($\nu_i > \omega_i$ but $\nu_e < \omega_e$ at 120 km; $(\frac{\nu}{\omega})_i \approx 2$, $(\frac{\nu}{\omega})_e \ll 1$). In the F-region, both electron and ion movements are controlled by magnetic field ($\nu_{i,e} \ll \omega_{i,e}$ at 300 km; $(\frac{\nu}{\omega})_i \approx \frac{1}{300}$, $(\frac{\nu}{\omega})_e \ll 1$).

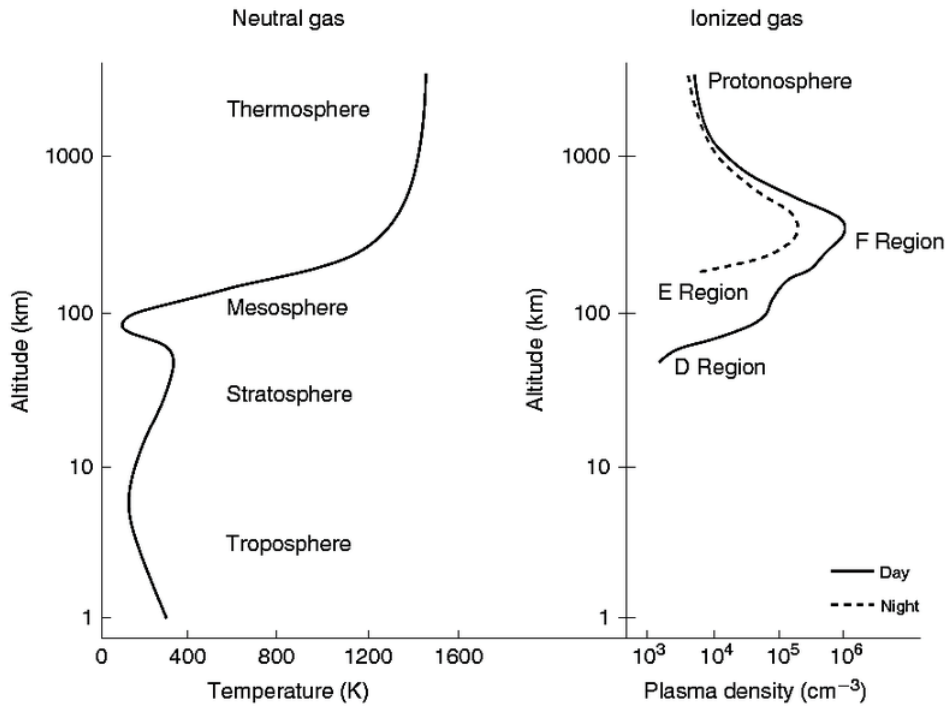


Figure 1.6: Altitude profiles of temperature in the atmosphere (left) and ionospheric layers (right) during day (solid line) and nighttime (dashed line) (from [Kelley, 1989](#)).

Sun and moon produce tidal forces in the atmosphere with periods of the solar and lunar day and its subharmonics. These forces result in primarily horizontal air motions. The motion of air, carrying ions with it in the E region, cuts across the geomagnetic field lines and induces electromotive force. This e.m.f. drives the solar quiet time (Sq) ionospheric currents. Because of the anisotropic nature of conductivities in the presence of Earth's magnetic

field, currents cannot flow freely in all directions and polarization charges are set up. It modifies the flow of current and generates the quiet time electric field. This electric field is thus generated in the E region, mapped to the F region through equipotential geomagnetic field lines and causes F region plasma drifts. F region plasma drifts have strong day to day variabilities. The zonal and vertical plasma drifts are caused by vertical and zonal electric fields respectively. The F region zonal and vertical plasma drifts over dip equatorial ionosphere are extensively studied (e.g. [Fejer et al., 1991, 2005](#)) by using incoherent scatter radar observations from Jicamarca. The vertical drifts are upward during daytime and downward in nighttime (see Figure 1.7). It is also to be noted that the vertical drift shows a strong enhancement during the post-sunset hours by a strong influence of eastward electric field due to the F region dynamo and its coupling with E region ([Rishbeth, 1981](#)). This is known as prereversal enhancement of the vertical drift. There is also a seasonal and solar cycle dependence on the variations of vertical drifts. In addition to these effects, the vertical and zonal drifts are significantly influenced by disturbance electric field perturbations associated with various geophysical conditions over low latitude (e.g. [Fejer, 1991](#); [Fejer and Scherliess, 1997](#); [Scherliess and Fejer, 1998, 1999](#); [Sastri et al., 2002](#)).

The ionospheric conductivities (Pedersen and Hall conductivities) maximize at a narrow altitude region in the E-layer. Any current flow in vertical direction is inhibited to a great extent above and below the E-region height. Therefore, a thin slab geometry is fairly good approximation with condition of zero net current in vertical direction. Under the influence of eastward electric field, electrons drift upward whereas the ions are dragged by the neutrals. As a result, a vertical polarization electric field gets developed. The strength of the vertical electric field is about 30 times at ~ 105 km altitude ([Anandarao, 1976](#); [Pandey et al., 2016](#)) of the zonal electric field. This polarization electric field drifts the electrons towards west causing the intense jet of current.

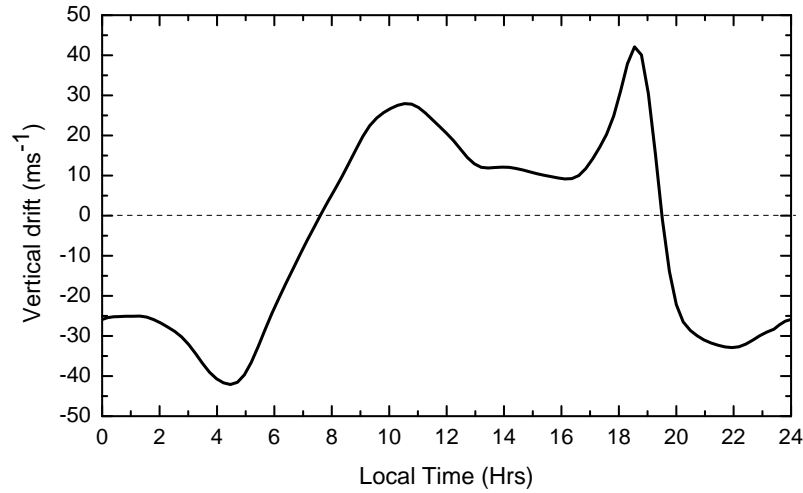


Figure 1.7: A typical quiet time vertical drift variation over Indian sector. (from [Fejer et al., 2008](#)).

This current flows in a narrow latitudinal band ($\pm 3^\circ$) over the dip equatorial E-region (~ 105 km) and is known as the equatorial electrojet (EEJ). However, on certain occasions, the zonal electric field changes its direction from eastward to westward and drives a westward current during daytime, which is known as the Counter Electrojet (CEJ). As the zonal electric field gets affected during geomagnetically disturbed conditions which eventually affects the EEJ strength. The variations in EEJ strength can be taken as a proxy to infer the zonal electric field over equatorial ionosphere if the change in ionospheric conductivity is insignificant during the time under consideration.

The ionogram traces during nighttime, on occasions, show a spread in range and/or in frequency due to presence of equatorial F region plasma irregularities after local sunset. This is traditionally known as Equatorial Spread F (ESF). After the local sunset, the plasma density in the E-layer decreases rapidly due to the absence of photoionization and presence of recombination processes. On the other hand, the ionization in the F region is maintained by the dynamical processes. Thus, a steep vertical electron density gradient is generated at the bottomside F region. This situation is an unstable configuration as a

heavier fluid is supported by lighter fluid against gravity. The direction of electron density gradient is just anti-parallel to that of gravity. This type of plasma density configuration gives rise to Rayleigh-Taylor (RT) instability. It grows non-linearly and generates plasma irregularities. The scale sizes of these plasma irregularities range from several hundreds of kilometers to a few centimeters. Several nonlinear simulation studies have been invoked to understand the nonlinear evolution of plasma instability (*Sekar and Raghavarao, 1987; Sekar et al., 1994, 1995; Sekar and Kelley, 1998; Sekar, 2003*). The large scale size (a few hundreds of kilometers) plasma irregularities are generally originated due to the generalized Rayleigh-Taylor instability process which is triggered/driven by zonal electric field, zonal winds in presence of tilted ionosphere and vertical winds (e.g. *Sekar and Kelley, 1998*, and references therein). It is also shown (*Martinis et al., 2005; Sekar and Chakrabarty, 2008*) that the penetration electric fields during geomagnetic disturbed conditions can significantly influence the development of ESF.

1.7 Thermosphere

The Earth's upper atmosphere consists of both neutral and plasma species. The temperature of the neutral species sharply increases from $\sim 150\text{K}$ to $\sim 1500\text{K}$ as the altitude is increased from $\sim 90\text{km}$ to $\sim 500\text{km}$ (Figure 1.6) and eventually remains almost constant. This portion of the terrestrial atmosphere is known as thermosphere. This is the hottest part of the atmosphere. In the thermosphere, a diffusive equilibrium is maintained by the neutral species just above the turbopause region ($\sim 100\text{ km}$). Therefore, the vertical distribution of the neutrals depends upon the respective masses of the species. For example, at $\sim 300\text{km}$ the O_2 concentration is $\sim 10^7\text{ cc}^{-1}$ whereas the O concentration is $\sim 10^9\text{ cc}^{-1}$. The thermospheric temperature increases upward as the heat conduction takes place in the downward direction. However, the temperature does not keep on increasing beyond a certain altitude as the heat conductiv-

ity becomes very high in the upper thermosphere making nearly an isothermal condition. Many airglow emissions (like OI630 nm) emanate from the thermospheric altitude that can be used as “tracer” to probe the ionosphere-thermosphere system (ITS).

1.8 Geomagnetic Storm

A geomagnetic storm is a disturbance in the terrestrial geomagnetic environment that happens primarily when the Z-component of interplanetary magnetic field (IMF B_z) turns southward and remains that way. It is generally known that the magnetospheric dynamics are primarily controlled by two external drivers: the solar wind plasma and the interplanetary magnetic field (IMF). The magnetic reconnection is a very important process which decides

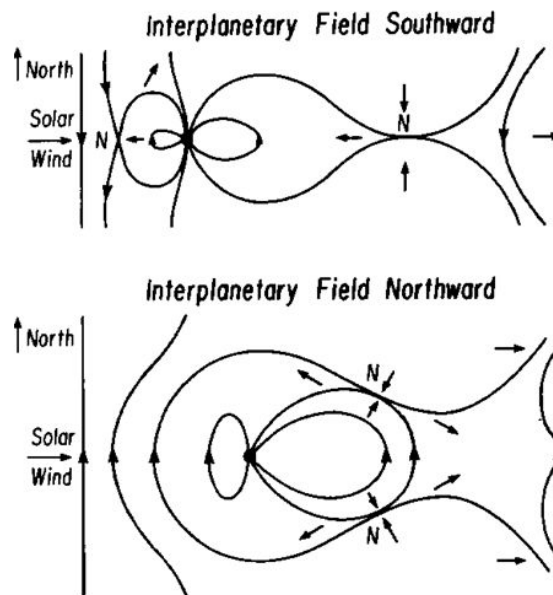


Figure 1.8: Magnetic reconnection for southward IMF (top) and northward IMF (bottom) conditions. (Taken from [Russell, 2000](#)).

transfer of energy from solar wind to the magnetosphere and eventually to ionosphere. The concept of reconnection was first introduced by [Dungey \(1961\)](#)

and he first proposed that the solar wind energy input into the Earth's magnetosphere is controlled by the solar wind plasma and the IMF. The schematic of Figure 1.8 shows the plasma flow through the magnetosphere driven by magnetic reconnection along with the location of reconnection sites during south and northward IMF B_z conditions. The location of the reconnection site is very crucial factor in determining the geoeffectiveness of the event and how the mass and energy transport takes place. The magnetic reconnection first occurs on the dayside. Then, the open field lines are dragged by solar wind towards the night side and further reconnection takes place in the magnetotail. Large-scale reconnection process in the magnetotail region can quickly release energy stored in the magnetosphere, accelerating plasma in earthward direction. These accelerating earthward particles are trapped by the Earth's magnetic field. When these particles encounter closed field lines, electrons start drifting towards east and protons towards west that results in westward ring current at a distance of $4-6 R_E$. This current produces an induced magnetic field in the southward direction over the Earth's surface. This indicates the occurrence of geomagnetic storm. The corresponding decrease in the horizontal component of Earth's magnetic field strength is used to know the severity of the magnetic storm via an index known as the storm-time disturbance index (Dst).

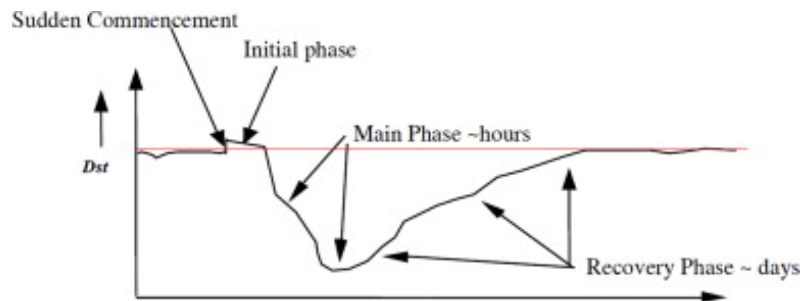


Figure 1.9: Different phases of a geomagnetic storm as seen in the Dst index. The red horizontal line indicates the zero level of the index. Image adapted from [Andriyas and Andriyas \(2015\)](#)

There are four different phases of storm i.e. (i) storm sudden commencement (SSC), (ii) initial phase, (iii) main phase, and (iv) recovery phase. Some geomagnetic storms begin with a sudden impulse. The different phases of a geomagnetic storm is presented in Figure 1.9. The red horizontal line indicates the zero level of Dst index. During storm sudden commencement (SSC), the solar wind ram pressure ($P_{dyn} = \frac{1}{2}\rho v^2$ where ρ is solar wind mass density and v is velocity) increases that causes a sudden compression of the magnetosphere. As a result, the Dst index (horizontal component of Earth's geomagnetic field) shows an enhancement like a step-function and the SSC is followed by an initial phase. The initial phase mostly develops during the northward IMF Bz conditions. During initial phase, the Dst index remains elevated. During southward IMF Bz, the ring current enhances, known as the main phase and is characterized by a reduction in Dst. When IMF Bz changes the direction from southward to northward direction, the recovery phase starts and during this phase, loss of ring current ions takes place due to charge exchange processes with the neutral species and pitch angle scattering ([Gonzalez et al., 1994](#)). The life time of a typical geomagnetic storm can range from a few hours to few days. It is to be noted that the geomagnetic storms can be driven by both ICMEs and CIRs. The CIR-induced geomagnetic storms are generally less intense as compared to ICME driven storm due to fluctuating IMF Bz.

1.9 Magnetospheric Substorm

Magnetospheric substorm is a process in which huge amount of stored magnetic energy from the nightside magnetotail is released. The concept of a geomagnetic substorm was first introduced by [Akasofu and Chapman \(1961\)](#) to describe magnetic perturbations in the polar region during magnetic storms. It was initially believed that storms are summation of multiple substorms. However, substorms can also occur in the absence of any geomagnetic storm. Unlike storm, it can be triggered by reversal in the polarity of IMF Bz (or

IEFy), enhancements in solar wind ram pressure, etc. Substorms can also occur without any apparent triggering mechanism also these are generally referred as “spontaneously triggered substorms” (*Henderson et al., 1996*). It is believed that magnetospheric plasma instability processes play critical role in causing the so-called “spontaneously triggered substorms” (*Liu et al., 2011; Henderson et al., 1996*). The exact processes which trigger substorms are still under debate (*Johnson and Wing, 2014*). The life time of a substorm lasts for about 2-3 hours. During substorms, highly structured and explosive auroras are seen over auroral ionosphere. The occurrence of substorm is random in nature but some times, periodic substorms are also seen. Similar to storm, there are three phases of a substorm. These are known as growth, expansion, and recovery phases (see Figure 1.10). In growth phase, the energy is stored in magnetotail. In expansion phase, the energy gets released explosively and dipolarisation (i.e. the stretched magnetic field configuration returning to a more dipole-like configuration) occurs and in the recovery phase, magnetosphere comes back to its pre-storm condition. During the growth phase of substorm, smaller localized activations may occur which are commonly known as pseudo-breakups (e.g. *Pulkkinen et al., 1998*). They may not lead to a full-fledged substorm expansion though they show very similar characteristics of substorms. It is also defined as short lived auroral activation whose spatial scale sizes are limited to a few hundred kilometers. The factors that decide whether a substorm grows fully or ends as a pseudo-breakup are not understood till date (*Pulkkinen, 1996*).

The magnetic reconnection in magnetotail region during substorm causes diversion of cross-tail current through the auroral ionosphere, heating of the plasma sheet, particle precipitation over auroral region and also causes a strong convection of these hot particle towards the Earth’s geosynchronous orbit (Figure 1.11) (*Reeves, 1998*). Substorm injections can be observed when the particles fluxes for multiple energy channels increase at the same time at geosyn-

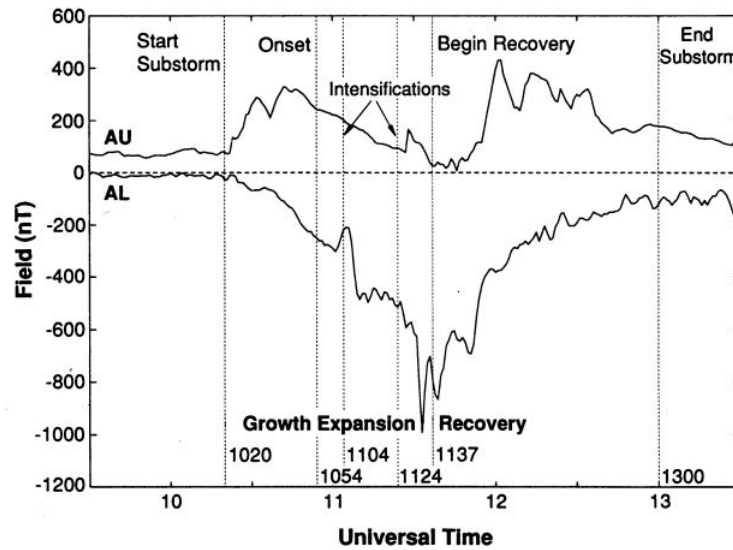


Figure 1.10: Different phases of a magnetospheric substorm as seen from AU and AL indices. (from [Kivelson and Russell, 1995](#))

chronous orbit. This is generally referred as “dispersionless injections” ([Reeves et al., 2003](#)). The electrons from the geosynchronous orbit get deposited over auroral region through field lines which results in the enhancement of auroral electrojet (AE), a strong current system that flows in the auroral E-region. AL (westward auroral electrojet), AU (eastward electrojet), AE (AU-AL), ASY-H (partial ring current), PC (polar cap) indices, Pi2 pulsations and most importantly, dispersionless particle injection at the geosynchronous orbit are used as proxies to know the occurrence of substorms. So to say, the dispersionless particle injection at geosynchronous orbit is the most convincing signature of the occurrence of substorms. The understanding of magnetospheric substorms has greatly improved by simultaneous measurements from space and ground along with the global numerical models. Many phenomenological substorm models, such as the near-Earth neutral line model (NENL), substorm current wedge (SCW) model, and the near-Earth current disruption model (NECD) have been developed to understand the substorm process. However, none of these models could explain all the characteristic features of substorms. It is apparent that the relationship between storm and substorm is highly complex.

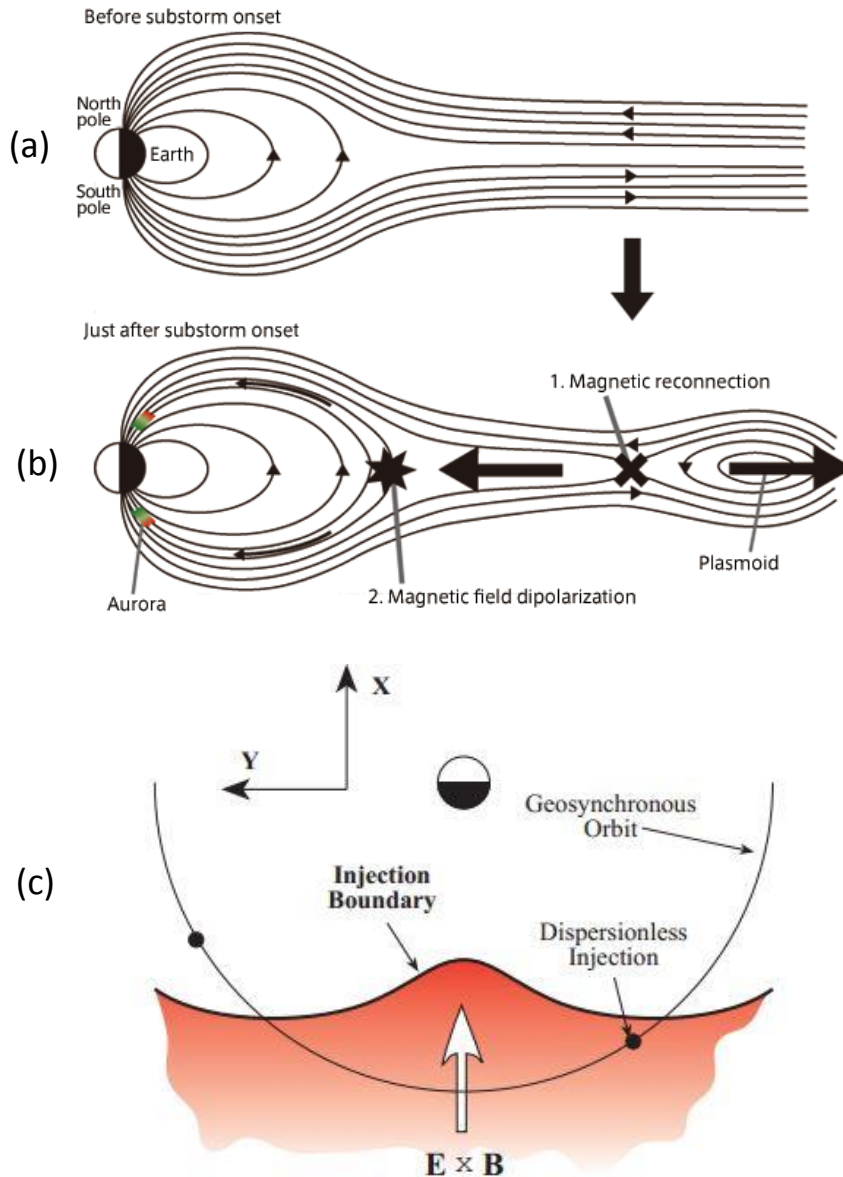


Figure 1.11: Schematic represents (a) antiparallel magnetic field lines before the substorm onset, (b) the magnetic reconnection region and dipolarization of magnetic field lines after onset of substorm (c) dispersionless particle injection at the geosynchronous orbit at the onset of the expansion phase of substorm (from [Reeves, 1998](#)). (Credit: <http://www.isas.jaxa.jp/e/forefront/2010/miyashita/02.shtml>)

The fast varying magnetic field induces an electric field ($\nabla \times \mathbf{E} = -\partial \mathbf{B} / \partial t$) in the magnetosphere during the substorm dipolarisation ([Reeves, 1998](#)). On

many occasions, these induced electric fields can be much larger than the large-scale convection electric field imposed by the solar wind. This substorm-induced transient electric fields are highly localized in space, which makes their characterization difficult (*Pulkkinen, 2007*). Further, *Li et al. (1998)* and *Sarris et al. (2002)* showed that substorm-related localized electric field pulses produce a strong $\mathbf{E} \times \mathbf{B}$ drift which are very effective to transport plasma towards Earthward direction. This electric field can penetrate into the high latitude ionosphere and strengthen the auroral electrojet. Such type of electric disturbances are generally known as DP1 (Polar Disturbance type 1) type electric field perturbation which occurs during the expansion phase of the auroral substorm (*Obayashi and Nishida, 1968*). During the substorm expansion, tail field collapses and forms “substorm current wedge (SCW)” that connects through the polar ionosphere (*Kepko et al., 2015*). The positive and negative bay signatures (*Sastri et al., 2003*) are observed due to SCW formation over the ground. It is to be noted that the low latitude ionosphere is also simultaneously affected by this inductive electric field. The impact on the low latitude ionospheric electric field during substorms are extensively studied by several researchers (*Kikuchi et al., 2003; Sastri et al., 2003; Huang et al., 2004; Huang, 2009, 2012, 2013; Hui et al., 2017*). Recently, it is shown (*Hui et al., 2017*) that the substorm-induced electric fields can be significant and can, at times, compete with the IEFy in terms of their equatorial impacts. The polarity of the substorm-induced electric fields on the equatorial ionosphere is one topic that still remains to be comprehensively understood. Storm time substorm and its impact on low latitude ionosphere-thermosphere system can provide important clues that are important to understand many aspects of magnetosphere-ionosphere coupling.

1.10 Magnetosphere-Ionosphere Coupling

As already discussed in section 1.4, during the southward IMF B_z condition, the solar wind can impose an electric field in the dawn-dusk direction. As this electric field can generate earthward plasma convection in the plasma sheet, this is also known as convection electric field. In the plasma sheet, the direction of the convective flow is sunward i.e. perpendicular to the Earth's magnetic field (Figure 1.12). After the magnetic reconnection on the dayside, the movements of the footprints of open field lines on high latitude ionosphere follow the other end of magnetic field lines in magnetotail region. The dawn-dusk component of convection electric field maps down to high latitude ionosphere through the highly conducting geomagnetic field lines and forms a two-cell convection pattern. This is also known as DP2 (Disturbance-Polar current Type 2) cells. Eventually, this convection electric field promptly penetrates from high latitude to low latitude ionosphere. This is generally known as “**prompt penetration electric field**”. The convection or prompt penetration (PP) electric field plays an important role in magnetosphere-ionosphere coupling process. The convection electric potential (*Volland, 1973*) can be expressed as

$$\mathbf{E}_c = -\nabla\Phi_{\text{conv}} \quad (1.7)$$

Where \mathbf{E}_c is the convection electric field. This potential can rise up to hundreds of volt during geomagnetically disturbed conditions. The PP electric field has been studied by several researchers by various techniques (*Nishida, 1968; Wolf, 1970; Vasyliunas, 1970; Volland, 1973; Senior and Blanc, 1984; Sastri et al., 2000; Kelley and Makela, 2002; Kelley et al., 2003; Huang et al., 2005; Fejer et al., 2007; Chakrabarty et al., 2017*).

In order to obtain the full picture of magnetospheric plasma motion, one must take into account the co-rotation electric field in addition to the convection field (Figure 1.13) (*Wolf et al., 2007*). The Earth with its plasma environment co-rotates in a fixed frame of reference which extends up to the

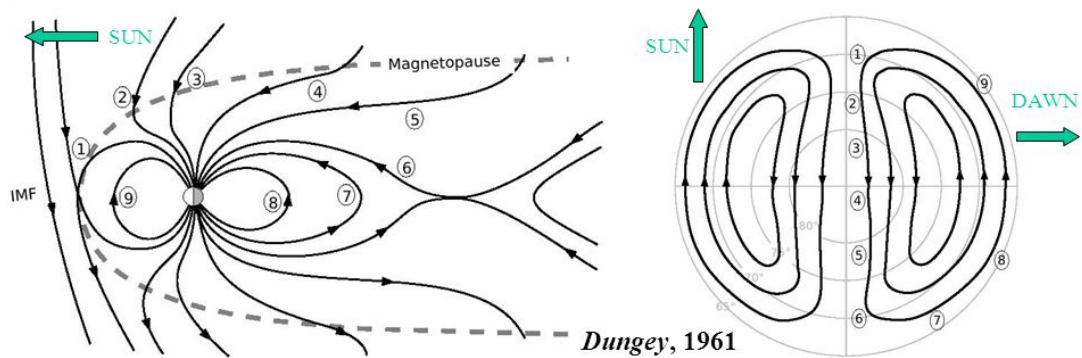


Figure 1.12: The schematic represents the reconnection process at the front-side of the magnetosphere as proposed by ([Dungey, 1961](#)). The numbers 1-9 at various magnetic field lines indicate the evolution of the field lines (left side) and the movement of footprints in the high-latitude polar ionosphere (right side). After reconnection between solar wind magnetic field lines with magnetospheric field lines at the frontside of the magnetosphere, the magnetic field line is dragged toward the night side. The field lines eventually reconnect once again in the tailside of magnetosphere. Image adapted from ([Kivelson and Russell, 1995](#))

plasmopause in the equatorial plane. As a consequence, the plasma drift is caused by the co-rotational electric field around the Earth once every 24 hours. In this case, the plasma remains bounded at the same geographic location and time and the drift trajectories are concentric circles about the geographic pole ([Schunk and Nagy, 2009](#)). All the particles move with a constant velocity will experience an $\mathbf{E} \times \mathbf{B}$ drift. The co-rotation electric potential turns out to be -92 kV. However, the rate of change of co-rotation electric field is slower than the corresponding changes in convection electric field. Therefore, on many occasions, the fast changes in ionospheric plasma dynamics are caused by changes in convection electric field. In order to know the impact of the convection or PP electric field on ionosphere, it is important to understand the shielding and overshielding mechanism of this PP electric field.

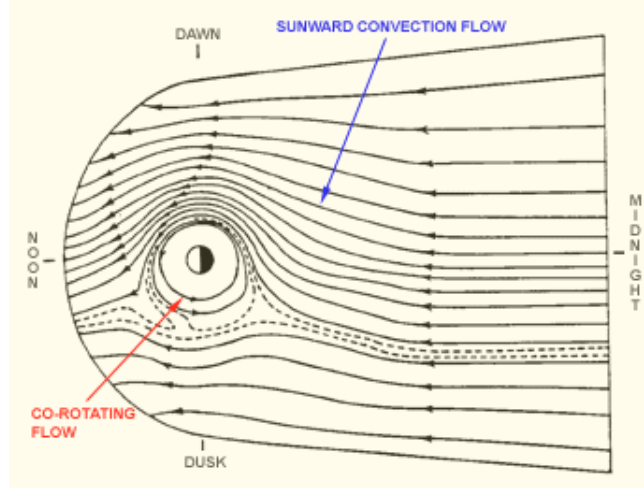


Figure 1.13: Schematic showing the flow of charged particles in the equatorial plane of the magnetosphere. The arrow indicating $\mathbf{E} \times \mathbf{B}$ drift in an Equipotential plane for the case of a uniform convection and corotation electric field. (Credit: <http://pluto.space.swri.edu/image/glossary/convection.html>).

1.10.1 Shielding: Undershielding (Prompt Penetration) and Overshielding

When the plasma (electrons and ions) in the outer magnetosphere, driven by convection electric field, reaches to the closed field lines near the Earth, it undergoes two important drift motions. These are follows:

$$\text{Grad-B drift: } \mathbf{v}_{\mathbf{B}} = \frac{1}{2} v_{\perp} r_L \frac{\mathbf{B} \times \nabla \mathbf{B}}{B^2} \quad (1.8)$$

$$\text{Curvature drift: } \mathbf{v}_{\mathbf{R}} = \frac{m v_{\parallel}^2}{q} \frac{\mathbf{R}_{\mathbf{c}} \times \mathbf{B}}{R_c^2 B^2} \quad (1.9)$$

Where v_{\perp} and r_L are the perpendicular velocity and Larmour radius of the plasma and R_c is the radius of curvature. Since $\mathbf{R}_{\mathbf{c}}$ and $\nabla \mathbf{B}$ are in opposite directions, $\mathbf{v}_{\mathbf{B}}$ and $\mathbf{v}_{\mathbf{R}}$ are in the same direction for a given charge. Therefore, the energetic ions and electrons from the tail tend to drift toward the dusk and dawn side of the inner magnetosphere, respectively due to the gradient and curvature drifts. The different drift paths along with differences in the ions

and electrons pressure lead to a charge separation wherein positive charges accumulate on the dusk side and negative charges accumulate on the dawn side. Therefore, a polarization electric field is built in the inner edge of ring current, directed from dusk to dawn and it shields the inner magnetosphere from further penetration of convection electric field.

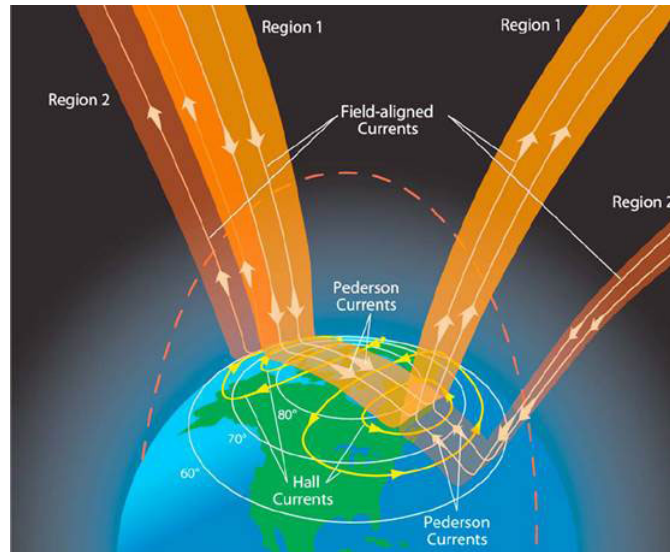


Figure 1.14: A schematic showing region 1 and region 2 FACs over auroral ionosphere. DP2 convection cells are also shown. (Courtesy: [Le et al., 2010](#)).

In order to satisfy the divergence of the current density, the field-aligned currents are generated that connects auroral ionosphere with the inner and outer magnetosphere. These are known as Region 1 (R1 FAC) and Region 2 (R2 FAC) field-aligned currents (Figure 1.14). R1 FACs are located in regions of higher latitudes (between $\sim 67^\circ$ and $\sim 75^\circ$), while R2 FACs are found in regions of lower latitudes (between $\sim 63^\circ$ and $\sim 68^\circ$). The R1 FAC flows out from the ionosphere at the dusk side and into the ionosphere at the dawn side. The R1 FAC plays a very important role in magnetosphere-ionosphere coupling as it connects outer magnetosphere with auroral the ionosphere. The R1 FAC enhances during the magnetospheric convection driven by solar wind/IMF ([Volland, 1978](#); [Heelis et al., 1982](#); [Kamide et al., 1981](#); [Ridley and Liemohn, 2002](#)). Further, the R2 FAC closes through the highly conducting auroral

ionosphere and shields the effects due to R1 FAC. The dusk-dawn electric field cancels the driving magnetospheric convection electric field under a steady magnetospheric convection. It is the competition between convection electric (dawn-dusk) and shielding electric field (dusk-dawn) which eventually decides the effects in MI-system. There are many theoretical models which address the generation mechanism of large scale electric fields and current systems in MI-system (*Jaggi and Wolf, 1973; Volland, 1978; Fejer and Scherliess, 1997; Toffoletto et al., 2003*). The MHD model by *Vasyliunas (1970)* showed that the plasma pressure gradient can contribute in magnetospheric convection and the pressure gradient drives the field aligned currents which connect to magnetosphere and ionosphere. The ion pressure is normally more than the electron pressure at the inner edge of the ring current during convection. The pressure difference is more prominent in the dawn-dusk terminator and this dawn-dusk asymmetry drives a current known as partial ring current (PRC) (*Li et al., 2011*). The R2 FAC currents which play an important role in shielding mechanism gets closed through the PRC via the auroral ionosphere (*Fukushima and Kamide, 1973; Iijima and Potemra, 1976; Ridley and Liemohn, 2002*). Further, the model studies suggest that magnetospheric convection is also controlled by the auroral conductivity, temperature and number density of plasma sheath in addition to plasma pressure in the inner edge of the ring current (*Vasyliunas, 1970; Jaggi and Wolf, 1973; Southwood, 1977; Senior and Blanc, 1984; Spiro et al., 1988*).

In addition, shielding electric field has larger time constant compared to convection time constant and hence it takes relatively more time than PP electric field to build up. During this time, the convection or PP electric field, which can change very fast, is experienced inside the inner magnetosphere and ionosphere. When IMF B_z suddenly changes the direction from south to north after being stably southward for some time, the convection electric field becomes zero. As the shielding electric field takes some time to decay, this

residual electric field can be experienced in the inner magnetosphere which is called as the overshielding electric field (Figure 1.15b). The PP and overshielding electric fields play a significant role in changing the electrodynamical environment of over low-equatorial latitude ionosphere. The polarity of prompt penetration electric field is generally eastward in the day sector and westward in the night sector (*Fejer and Scherliess, 1997; Kelley et al., 2003*). Further, the work of *Nopper and Carovillano (1978)* showed the local time dependence of PP electric field and suggested that the polarity of PP electric field can be eastward up to 2200 LT. On the other hand, local time dependence of the polarity of overshielding electric field is just opposite compared to that of PP electric field in general. It is to be noted that the PP of interplanetary electric field (IEF) generally occurs during the main phase of the storm whereas the overshielding occurs during the onset of the recovery phase.

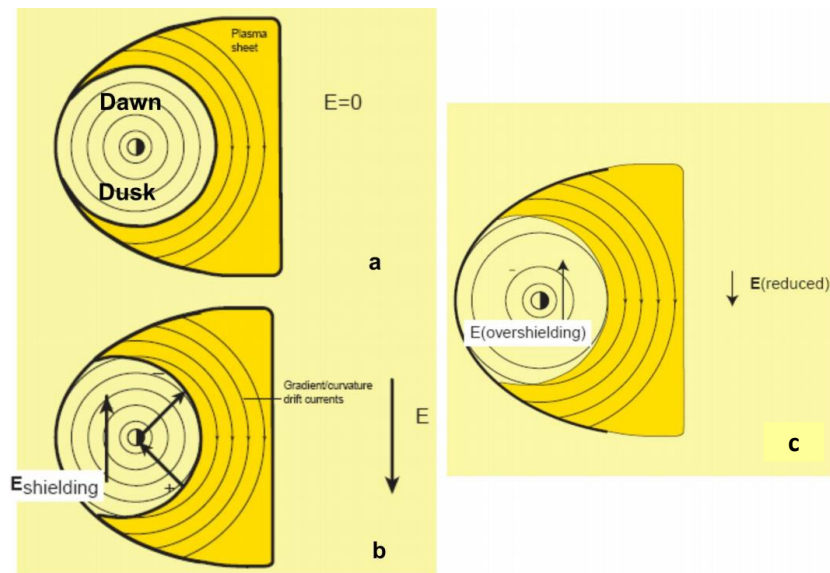


Figure 1.15: Schematic demonstrating (a) a perfect shielding condition where no convection, with plasma-sheet edge aligned with contours of constant potential, (b) rapid increase of convection electric field and the associated shielding electric field, (c) sudden decrease of convection electric field and the associated overshielding electric field. (Courtesy: *Wolf et al., 2007*)

Another important aspect of PP electric field is the efficiency with which the penetration electric field reaches over low latitudes. The efficiency of penetration is defined as the ratio of the magnitude of the PP electric field over low latitude to that of IEFy. It is to be noted that the potential across the magnetosphere, which gets mapped into the ionosphere, is not fully imposed across the polar cap. The efficiency of penetration of IEFy is found to be 6.6% by Jicamarca ISR measurements (e.g. *Kelley et al., 2003*) and it is further suggested by *Huang et al. (2007)* that the efficiency is 9.6% by taking a statistically large data sets. The magnitude and duration of penetration electric field depends on the strength of the magnetospheric convection which can be driven by the solar wind condition or the IMF as well as on the MI-coupling. The duration of penetration is decided by shielding time constant which is of ~ 20 -30 minutes (*Senior and Blanc, 1984; Somayajulu et al., 1987; Spiro et al., 1988; Kikuchi et al., 2000; Peymirat et al., 2000*). However, long duration penetration events are also observed (e.g. *Huang et al., 2005; Chakrabarty et al., 2005, 2008*). It is believed that during time-varying disturbances, the distribution of magnetospheric plasma and the shielding currents do not get sufficient time to develop the appropriate shielding electric field and in this situation, the penetration may last for several hours. Further, *Kikuchi et al. (2000)* showed that the coherence of fluctuations at magnetic stations over varying latitudes during DP2 event are broken during substorm. In fact, presence of substorm during storm makes the MI-coupling even more complex.

1.10.2 Disturbance Dynamo Electric Field

In addition to DP2 type electric field perturbations during geomagnetic storm, the particle precipitation over high latitude ionosphere leads to Joule heating in the auroral zone and drives a global thermospheric circulation that generates the Disturbance Dynamo Electric Field (DDEF). The energy input from the magnetosphere into the high latitude ionosphere drives an equatorward wind system at midlatitude. The equatorward wind turns westward due

to Coriolis force. The westward winds, in turn, drives the positive and negative charges at the dusk and dawn terminators, respectively. As a result, polarization electric fields get generated in dusk-dawn (westward) direction on dayside and in the dawn-dusk direction (eastward) on the nightside which are opposite to the normal quiet-time fields. This physical process is known “ionospheric disturbance dynamo” (*Blanc and Richmond, 1980; Yamazaki and Maute, 2017*). Therefore, the disturbance dynamo produces an “anti-Sq” type current system on the dayside ionosphere. The disturbance dynamo effects are mainly observed during the recovery phase of a storm (e.g *Le Huy and Amory-Mazaudier, 2005; Yamazaki and Kosch, 2015*). The DDEF can persist for many hours which can significantly influence low latitude ionospheric electrodynamics (*Huang, 2013*). The DDEF effects are delayed due to its association with thermospheric wind circulation. It is very important to note here that it is always very difficult task to delineate the relative contribution of PP and DD electric field effects over low latitude ionosphere as both effects can modulate ITS over low-equatorial latitudes during storm-time (*Maruyama et al., 2005; Klimenko and Klimenko, 2012*).

1.11 The Bigger Picture and the Motivation of the Thesis

The energy that releases from Sun in the form of solar wind, CME, solar flare and magnetic field etc., cause ICME, CIR and shocks in the interplanetary medium. The geomagnetic storms and substorms are the manifestations of the CMEs and CIRs and it is important to understand the consequences of these space weather events in today’s technologically driven society. However, to understand and predict the geoeffectiveness of these events need systematic and global observations as well as modeling efforts. During the geomagnetic storm, the prompt penetration (PP) electric field is one of the important mediators for

the magnetosphere-ionosphere (MI) coupling. Unlike geomagnetic storm, the magnetospheric substorms can sometimes be triggered by changes in solar wind parameters and can sometimes be spontaneously triggered by internal plasma processes in the magnetosphere. The induction electric field plays an important role in MI-coupling during substorms. The origin, polarity, duration, local time dependence of the PP and induction electric fields associated with storms and substorms and their impact over low latitudes remain poorly understood till date. The broad objective of this thesis work is to address some of these issues in order to improve our understanding on various aspects of MI-coupling during space weather events and their low latitude impact.

1.12 Organization of thesis

The work carried out in the thesis is focused on prompt penetration electric field and their equatorial impacts. The thesis is organized as follows:

1.12.1 Chapter 1 – Introduction

1.12.2 Chapter 2 – Data and Techniques

1.12.3 Chapter 3 – Different Types of Prompt Electric Field Perturbations and Their Equatorial Impacts

1.12.4 Chapter 4 – Prompt Penetration Electric Fields as Indicators of Geoeffectiveness of ICME

1.12.5 Chapter 5 – Prompt Penetration Electric Field and Geoeffectiveness of CIR Events

1.12.6 Chapter 6 – A New Type of Prompt Electric Field Disturbance Driven Solely by Solar Wind Density Variation

1.12.7 Chapter 7 – Scope of the Thesis

Chapter 2

Data and Techniques

2.1 Introduction

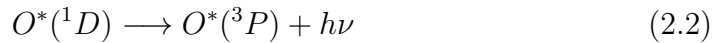
Study of the solar wind-magnetosphere-ionosphere coupling processes require simultaneous global observations. This is achieved by means of both space based and work of network of ground based measurements. There are highly advanced satellites in the interplanetary medium which make systematic measurements of solar wind and the interplanetary parameters. The high resolution measurements by instruments on board these satellites facilitate us to study changes in the solar wind and its impact on magnetosphere-ionosphere system. Some satellites are at L1 point (1st Lagrangian point) of the sun-earth system and also at other parts of interplanetary medium. In order to study the ionosphere from ground, observations from the airglow photometers developed in-house have been used in addition to the data obtained from various radars and chains of magnetometers throughout the globe. The airglow photometers used in this work have narrow spectral bandwidth and narrow field-of-view and these were operated in campaign modes from a number of field stations in India. However, appropriate lunar phase and inclement weather reduced the effective airglow observation periods. Before the instrumental and data analy-

ses techniques are introduced, a short note on the OI 630.0 nm thermospheric airglow emission is provided in the next section.

2.2 OI630.0 nm Airglow Emission

Earth's upper atmosphere is like an active laboratory where a wide range of photochemical, chemical and dynamical interactions occur between the plasma and the neutral species continuously. In this process, these species (atoms, molecules and ions) get excited. They emit photons while getting de-excited from higher energy states. These emissions are collectively termed as 'Airglow'. In the process of de-excitation, the transitions take place from higher energy channels to ground state through metastable states on many occasions. The lifetimes of these metastable states are much longer than the characteristic transitions rate (10^{-8} sec). Due to this reason, these transitions are often referred as "forbidden" as they violate the selection rules for the electric dipole transition. The present thesis work deals with the OI630.0 nm nightglow emission. Various electro-dynamical processes can be studied by using this airglow emission line during nighttime.

During nighttime, the dissociative recombination of molecular oxygen ion with the ambient electrons produces oxygen atom in excited metastable state. The life time of this metastable state (1D) has a long lifetime of 110 sec which subsequently decays to 3P state, giving off 630.0 nm photon emission.



The 630.0 nm emission rate depends on column integral of the product of $[O^+]$ and $[O_2]$. This factor decides the peak of the 630.0 nm airglow emission layer at an altitude of ~ 250 km with the semi-thickness of 20-30 km during nighttime. However, by the ground based measurements, a column integrated quantity of the airglow is obtained. The column emission intensity of 630.0 nm

is ~ 50 Rayleigh during nighttime. $1 \text{ Rayleigh} = 10^6 \text{ photons cm}^{-2} \text{ s}^{-1} \text{ ster}^{-1}$. The empirical relationship between the instantaneous intensity of OI 630.0 nightglow intensity ($Q_{630.0nm}$), ionospheric parameters like the peak height of the F2 layer ($h_p F_2$) and the peak frequency corresponding to the F2 layer ($f_o F_2$) is given by *Barbier (1961)*:

$$Q_{630.0nm} = A + B(f_o F_2)^2 \exp[-(h_p F_2 - 200)/40] \quad (2.3)$$

where, A and B are constants. $(f_o F_2)^2$ is related to electron density ($N_m F_2$) in the following way,

$$N_m F_2 = 1.24 \times 10^{10} (f_o F_2)^2 \quad (2.4)$$

where, $f_o F_2$ is expressed in MHz and $N_m F_2$ is expressed in m^{-3} . Equations 2.3 and 2.4 reveal that the intensity of OI 630.0 nm depends on F-layer height and density. F-layer height is dependent on the ionospheric electric field over the magnetic dip equator. Therefore, variations in the OI 630.0 nm airglow emission intensity can be used to capture the variations in the ionospheric electric field over the magnetic dip equator.

2.2.1 Narrow band and narrow field of view 630.0 nm airglow photometer:

It is already shown (*Chakrabarty et al., 2005*) that, in absence of systematic high temporal resolution electric field measurements over Indian sector, narrow band, narrow field of view (FOV) airglow photometry (*Chakrabarty, 2007*) of OI 630 nm airglow emission can be used to infer the space weather related electric field perturbations efficiently. Therefore, in order to capture the space weather related changes in the 630.0 nm airglow intensity, the narrow band (0.3 nm) and narrow field of view (3.0°) airglow photometers were operated in campaign modes from Trivandrum (Geog. Lat. 8.5°N , Geog. Lon. 77°E) and other places like Mt. Abu (Geog. Lat. 24.6°N , Geog. Lon. 72.7°E). These photometers were operated to measure the airglow intensity variations at the central wavelength of 630.0 nm with a temporal resolution of ~ 5 seconds.



Figure 2.1: A typical field set up of the two portable narrow band and narrow field of view 630.0 nm airglow photometers. The red and orange colored photometers are operated in zenith and east mode, respectively.

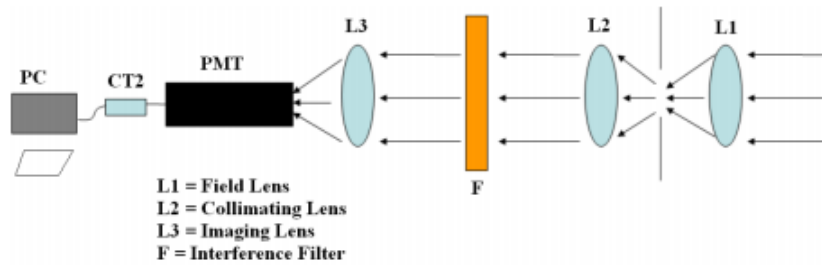


Figure 2.2: Optical schematic of the narrow band and narrow field of view portable photometers.

The photometers were operated in such a way that one of these was oriented towards the zenith and the other one was directed at an angle of 45° to east (shown in Figure 2.1) by means of a mirror assembly. The airglow photometers have three sections, viz. front-end optics, filter section and detector section (Figure 2.2). The photometers employ $f/2$ optics. The FOV (3.0°) of the photometers is decided by the field lens and the aperture in the front-end optics. The collimating lens converts incoming rays into parallel beam before they are incident on the interference filter.

The interference filters are multi-layer thin film devices and these basically work like low-order Fabry-Perot etalons. The interference filters are designed in such a way that these enable constructive interference for the desired wavelength. The central passband wavelength of an interference filter shifts towards lower wavelength if the angle of incident increases. In addition, the transmittance spectrum of interference filter also depends on the temperature. As the temperature increases, the refractive indices of the layers change. This causes shift of the central wavelength towards shorter wavelength side. Therefore, it is important to maintain the temperature of the filter chamber reasonably accurately for narrow bandwidth operations. The temperature controlled interference filter is tuned at 35°C in the present case. The temperature of the filter chamber is controlled using a heating-type temperature controller.

The filtered rays are focused on the cathode of the photomultiplier tube (PMT) by the imaging lens housed in the rear-end optics section. A PMT primarily consists, of a photocathode, a number of dynodes, and an anode that are vacuum-sealed into a glass tube. When light falls on the photocathode, the photoelectrons are emitted into the vacuum due to photoelectric effect. These photoelectrons are multiplied, accelerated and focused by a series of electrodes called dynodes and a given dynode is maintained at positive potential with respect to the previous dynode. The primary electrons are multiplied by means of secondary electron emission. The multiplied secondary electrons emit-

ted by the last dynode are finally collected by the anode. Quantum efficiency at a particular wavelength is defined as the number of photoelectrons emitted by photocathode divided by number of incident photons. It is expressed in percentage. In the present experimental setup, the PMTs (H7421-40 and H7421-50) comprise of photocathode made of GaAsP and GaAs, the quantum efficiency of the PMTs are 40% and 12%, respectively. The sensitivity of these PMTs range from 300 nm to 720 nm and 380 nm to 890 nm, respectively. As the airglow intensity is very low, the PMT is operated in counting mode. A laptop is attached to the counting unit to store the data in terms of the photon counts s^{-1} . In low light condition, the photon counting obeys Poisson statistics and the standard deviation is \sqrt{n} , where, n is number of photons measured.

2.3 Digisonde

In addition to airglow photometer, HF radar (digisonde) is also used to study the variations in the E and F layers of ionosphere. A digisonde works on the principle of reflection of radio waves by plasma. The digisonde sends HF radio signals at sweep frequency starting from 1 MHz to 30 MHz. When the frequency of the signal matches with the plasma frequency at a particular ionospheric height, it gets reflected back. Based on the echo obtained, the virtual height and electron density can be obtained.

In the presence of geomagnetic field, the ionospheric plasma behaves as a doubly refractive crystal. This theory, known as magneto-ionic theory, is derived by Appleton and Hartree (also known as Appleton-Hartree equation). If collisions and the magnetic field are neglected, a simplified expression of the refractive index can be written as follows.

$$n^2 = 1 - \frac{\omega_N^2}{\omega^2} \quad (2.5)$$

Where ω_N is the angular plasma frequency and is given by

$$\omega_N = (N_e e^2 / \epsilon_0 m)^{1/2} \quad (2.6)$$

It is clear from equation 2.6 that ω_N^2 is proportional to the electron density N_e . As a radio wave penetrates into the ionosphere, the electron density will start increasing till the F region peak and hence, the refractive index will decrease. If $\omega_N > \omega$, the refractive index (n) will be imaginary and the wave cannot propagate anymore in that case. hence, the radio wave signal will reflect back when $\omega_N = \omega$. Putting all values in equation 2.6, the peak electron concentration in the ionosphere is given by

$$f_N = (80.5N_e)^{1/2} \quad (2.7)$$

Where f_N and N_e are in Hz and m^{-3} , respectively. The height is found from the time delay of echo by assuming that the pulse signal travels at the speed of light. In the ionosphere, the radio wave travels more slowly than light because of group retardation. Therefore, the height information obtained from the time delay is not a “true height” and is called as the “virtual height”. The virtual height of E or F layers are termed as $h'E$ and $h'F$, respectively. The maximum plasma frequency of a given ionospheric layer is called the critical frequency for that layer. A digital ionosonde (DPS-4D) over Thumba (TVM, an Indian dip equatorial station) is used to measure the virtual height in order to know the ionospheric conditions during the time of airglow observations and also for the other event studies. The cadence of ionosonde observation in the present case is 7 minutes.

In the absence of incoherent scatter radar and direct systematic electric field measurements over Indian sector, the rate of change in $h'F$ ($dh'F/dt$) is used to derive the apparent F-region vertical plasma drift particularly during nighttime. The F-region vertical plasma drift, derived in this manner, is used as a proxy for zonal electric field (F-region) over the dip equator during nighttime after appropriately accounting for the chemical loss. It is known that at lower heights, particularly below 300 km, recombination effect (chemical loss) can produce significant upward drift (*Bittencourt and Abdu, 1981*). Hence, in order to obtain the true electrodynamic drift, one needs to subtract the

chemical loss contribution from $dh'F/dt$. This has been done following the methodology of *Subbarao and KrishnaMurthy (1994)* with the exception that the scale length is estimated from the measured electron density profiles. The apparent drift due to loss process (βH) is quantified by the product of the recombination coefficient (β) and scale length ($H = 1/(N^{-1}dN/dh)$) where N is electron density and h is height). The recombination coefficient β is given as $\beta = k_1[N_2] + k_2[O_2]$ where k_1 and k_2 are the reaction rates dependent on ambient temperature (*Anderson and Rusch, 1980*) and $[N_2]$, $[O_2]$ are the concentrations of N_2 and O_2 , respectively. The neutral temperatures and the concentrations are obtained from the MSISE-90 model (*Hedin, 1991*).

2.4 Incoherent and Coherent Radar Measurements

The Incoherent Scatter Radar (ISR) is a ground based technique which can provide ionospheric electric field accurately based on precise drift measurements. This technique is based on the principle of Thomson scattering by electrons in the ionosphere. The IS radar transmits a radio wave at a certain frequency. The typical operating frequencies used are from 50 MHz to 1.3 GHz. The electric field in the transmitted wave causes the electrons to oscillate. These oscillating electrons behave like a short dipole and re-radiate at almost the same frequency as that of the transmitted signal of the radar. The power in the returned signal is proportional to the electron concentration in the volume irradiated. The power of the incoherent signal from each electron is very weak. As a consequence, large power-aperture product is a characterization of ISR systems. The frequency spectrum received from the scattered signals gives the information of electron and ion density, temperature of electron and also the vertical drift velocity of plasma. There are several ISRs operating over the globe. In the present thesis work, the vertical drift

data from two IS Radars (Jicamarca and Arecibo) have been used. Jicamarca (JIC: 12°S, 77°W, Dip angle: 0.8°) is a dip equatorial station whereas Arecibo (18.3°N, 67°W, Dip angle: 45°) is a magnetically mid-latitude station. The Jicamarca radio observatory (JRO) operates at 50 MHz and an antenna array of 18,432 dipole elements, covering an area of approximately 85,000 m^2 . The operating frequency of Arecibo is 430 MHz and unlike JRO, it has a spherical reflector receiver of 305 m in diameter. The maximum power-aperture products of Jicamarca and Arecibo ISRs can go up to 337.5 GWm^2 and 137.5 GWm^2 , respectively. Jicamarca ISR has the largest power-aperture product in the world in the VHF band.

In addition to ISR measurements, the Super Dual Auroral Radar Network (SuperDARN) radar measurements have also been used to study the ionospheric convection during space weather events. SuperDARN comprises of 11 ground-based coherent-scatter radars over northern hemisphere and 7 over southern hemisphere. It is to be noted that the data from 11 northern hemisphere SuperDARN radars are used in this thesis. Each radar operates in the high-frequency (HF) range of 8-20 MHz. SuperDARN was designed to provide continuous measurements of high-latitude ionospheric plasma convection patterns and structures. The ionospheric plasma drifts ($\mathbf{E} \times \mathbf{B}$) are calculated at F region heights. The convection velocity \mathbf{v} is related to convection potential (Φ) through the relationships,

$$\mathbf{E} = -\nabla\Phi_{\text{conv}} \quad \text{and} \quad \mathbf{v} = \frac{\mathbf{E} \times \mathbf{B}}{|\mathbf{B}|^2} \quad (2.8)$$

The model takes the measurements of \mathbf{v} from the radars and constructs the convection pattern. In practice, there may be missing data points due to either the lack of radar coverage or propagation effects. Therefore, in order to construct overall flow patterns, an algorithm is used to fit the convection to an estimated harmonics model (*Chisham et al., 2007*).

2.5 Geosynchronous Particle Injection Measurements (LANL and GOES)

Energetic particles are injected into the geosynchronous orbit of Earth's magnetosphere during the time of substorm. Substorm can be identified when the particle fluxes for different energy channels increase at the same time. This is known as “dispersionless” injection ([Reeves et al., 1991](#)). If a satellite is inside an the injection region, it can capture the charecterstic changes in the particle fluxes. In the present thesis work, the data from Los Alamos National Laboratory (LANL) satellites and Geostationary Operational Environmental Satellites (GOES) are used. The Synchronous Orbit Particle Analyzer (SOPA) detectors on-board the LANL geosynchronous satellites measure the energetic particle fluxes counts s^{-1} in the near earth equatorial region at a nominal radial distance of $6.6 R_E$ (R_E , Earth's radius). These satellites measure both electron and proton counts per second from where the flux values are derived by multiplying a flux conversion factor (FCF) ([Cayton and Tuszewski, 2005](#)). The FCF depends on integration time, geometry of the detector and the energy range. Electron counts in four energy channels (E1: 48.15-69.85 keV; E2: 68.5-102.5 keV; E3: 99.95-149.45 keV; E4: 145.6-220.6 keV) and proton counts in three energy channels (P1:50-75 keV; P2: 75-113 keV; P3: 113-170 keV; P4: 170-250 keV), as measured by different satellites, are used in the present work. The Energetic Particle Sensor of GOES satellites measures electron fluxes in four energy channels (E1: 75 keV; E2: 150 keV; E3: 275 keV; E4: 475 keV).

2.6 Ground-based Magnetometer Observations

In order to know the of geomagnetic conditions, the global magnetometer data are used in the present study. It is to be noted that various geomagnetic indices like; AE, AL, AU, Dst, SYM-D, SYM-H, ASYM-D, ASYM-H

and PC are constructed based on ground-based magnetometer observations and are obtained from the WDC for Geomagnetism at University of Kyoto (<http://wdc.kugi.kyoto-u.ac.jp/wdc/Sec3.html>). All these data sets are also available in NASA GSFC CDAWeb (https://cdaweb.gsfc.nasa.gov/istp_public/) with the minimum time resolution of 1 minute. In addition to these, data from different chain of magnetometers across the globe have also been used for the present thesis work. These data were taken from SuperMAG (<http://supermag.jhuapl.edu>) and 210MM magnetometer networks (<http://stdb2.stelab.nagoya-u.ac.jp/mm210/>). SuperMAG is a worldwide collaboration of organizations and national agencies that currently operate more than 300 ground based magnetometers. SuperMAG provides easy access to validate ground magnetic field perturbations in the same coordinate system, identical time resolution and with a common baseline removal approach (*Gjerloev, 2012*). 210 Magnetic Meridian (210MM) magnetometer chain provides 3-dimensional vector geomagnetic field data even with 1 sec resolution obtained by fluxgate magnetometers.

In the absence of direct ionospheric electric field measurement over the Indian dip equatorial sector, magnetometers measurements are used to infer the electric field perturbations during daytime. It is known that $\Delta H_{TIR} - \Delta H_{ABG}$ represents the difference in the variation in the horizontal component of geomagnetic field over dip equatorial station Tirunelveli (TIR: 8.7°N, 77.8°E, and Dip angle 0.5°) and an off-equatorial station Alibag (ABG: 18.6°N, 72.9°E, and Dip angle 26.4°) in the Indian sector. Therefore, this difference cancels out the magnetospheric contribution and can be taken to represent as daytime equatorial electrojet (EEJ) current. It was shown (*Rastogi and Patil, 1986; Pandey et al., 2017*) that $\Delta H_{TIR} - \Delta H_{ABG}$ efficiently represents the E region electric field variations during daytime over the Indian dip equatorial region. The small variations in the EEJ strength can be captured with high precision (~ 0.1 nT) based magnetic measurements. Similarly, the EEJ strength

over the Jicamarca sector, given by $\Delta H_{JIC} - \Delta H_{PIU}$, is based on the difference between the horizontal component of geomagnetic field over Jicamarca (JIC:12°S, 76.8°W, 0.8° dip) and an off-equatorial station Piura (PIU: 5.2°S, 80.6°W, 6.8° dip). The EEJ strength over Jicamarca was shown to be the same with the variations deduced from JULIA radar observations for the ionospheric E-region electric field (*Anderson et al.*, 2002, 2006; *Alken and Maus*, 2010). The time resolution of all the EEJ data is 1 min.

2.7 Other Data Sets

2.7.1 Solar Wind Observation

The interplanetary data were taken from the OMNIweb database and the time shifted data are available in NASA GSFC CDAWeb (<http://cdaweb.gsfc.nasa.gov/istppublic/>). The data base is composed of multiple satellites data. This helps to compare solar wind measurements and geomagnetic observations. The data for the present study were obtained from the instruments on-board ACE and WIND satellites. Both the satellites are in halo orbits around the point L1. The maximum data resolution is of 1 mins. The satellites measure solar wind proton velocity, density, temperatures, and different components of interplanetary magnetic fields. Some are derived parameters (solar wind dynamic pressure, interplanetary electric field, plasma beta and Alfvén Mach number). These parameters are adjusted for the propagation-lag up to the nose of the terrestrial bow shock (*Weimer et al.*, 2003).

2.7.2 Geomagnetic Indices

The range indices K, Kp and Ap: The K index was first introduced by *Bartels et al.* (1939). K index is a range index for a field component at a given station that routinely measures the level of geomagnetic activity. It is a quasi-logarithmic 3 hrs value and ranges from 0 to 9. Kp is 3-hour-range

planetary K index. It is a mean standardized K-index from 13 geomagnetic observatories between 44 degrees and 60 degrees northern or southern geomagnetic latitude. The Ap index is a daily average of 3 hours ap index and derived from the 3-hourly Kp values. It mainly gives the idea about the geomagnetic activity for a day (*Kivelson and Russell, 1995*).

The storm indices Dst, SYM-H and ASY-H: The disturbance storm index Dst, is a measure of strength of ring current. The different phases of geomagnetic storm are mainly decided by this index. SYM-H is effectively the high resolution Dst index and is the symmetric component of ring current. The time resolutions of Dst and SYM-H are 1 hr and 1 minute, respectively. The SYM-H can more efficiently be used to study the effects of rapid variation of the solar wind parameters. The ASY-H is the asymmetric part of ring current which represents the strength of partial ring current. The asymmetric component (ASY-H) at each station is obtained by subtracting the symmetric component (SYM-H) from each magnetic station.

The substorm indices AU, AL, AE and AO: The auroral-electrojet indices were first introduced by *Davis and Sugiura (1966)* to measure the global auroral activity. The AE index is derived from the 13 geomagnetic stations over northern auroral region. AU and AL, respectively, represent the upper and lower envelopes of the superposed plots of all the data from these stations as functions of UT. AE is defined by the difference between AU and AL i.e. $AU - AL$, and the mean value of the AU and AL, i.e. $(AU + AL)/2$, defines the AO index. The AU and AL indices represent the strength of eastward and westward auroral electrojet current, respectively. The AE index represents the overall activity of the auroral region. These indices generally indicate the substorm activity over auroral region. The different phases of substorms can be inferred from AL and AU indices.

The polar cap index PC: The polar-cap index (PC: PCN: northern; PCS: southern) was introduced by *Troshichev et al. (1988)* to measure the

strength of the sheet current flowing sunward across the polar cap, closing the two auroral electrojets. The PCN and PCS are derived from the two magnetic observatories (Thule and Vostok) at a single near-pole station. It can be used as a proxy for polar ionospheric electric field and useful for high latitude-low latitude coupling studies.

2.7.3 Neutral Wind Velocity Measurements

Thermospheric neutral wind velocity and temperature can be measured by using a Fabry-Perot interferometer during nighttime. In this technique, both zonal and meridional components of wind velocity can be measured (*Burnside et al., 1981*). In upper atmosphere, the natural airglow emissions (like OI630.0 nm) are generally associated with forbidden electronic transitions. The life time of the metastable states associated with these transitions are larger than the life time of the spectroscopic transition time (10^{-8} s). Therefore, the excited species tend to attain thermal (statistical) equilibrium due to multiple collisions with the surrounding medium before emission. The width of the emission line profile gives the ambient temperature of the region from where the emission occurs if the inter-collisional period is much less than the lifetime of the excited state. In addition, it also gives the bulk motion of the neutral wind in that region in terms of Doppler shift. By observing the apparent wavelength of the 630.0 nm airglow emission line, the line of sight velocity can be determined at 250 km height. For a neutral wind of 50 ms^{-1} the Doppler shift of the 630 nm line corresponds to 10^{-4} nm (*Hargreaves, 1992*). In one of the works in this thesis, the thermospheric wind measured from Arecibo have been used.

2.8 Data Analysis Technique

The data sets used from various experiments are not always equally spaced in time domain. It is needed that the periodicities are derived from the time

series and coherency as well as phase spectra are obtained to establish causal connection between two processes. In the present work, in order to know the fast fluctuations present in the data sets, the residuals are extracted out (by detrending) using Savitzky-Golay (SG) smoothing algorithm (*Savitzky and Golay, 1964*). The advantage of SG algorithm is its ability to generate the residuals from a time series data with minimal distortion. In general, in order to know the dominant periodicities present in a given parameter, detailed spectral analyses are carried out. The data analysis involves spectrum analyses of the airglow, digisonde, magnetometers and other datasets. In order to compute the periodicities in time-series data, Fast Fourier Transfer (FFT) is adopted. A few salient features of FFT are discussed below before the necessity of a different algorithm is brought in.

2.8.1 Fast Fourier Transform

A physical process can be described either in the time domain $h(t)$ or in the frequency domain $H(f)$. The relation between $h(t)$ and $H(f)$ is defined by Fourier transform,

$$H(f) = \int_{-\infty}^{\infty} h(t)e^{2\pi ift} dt \quad (2.9)$$

$$h(t) = \int_{-\infty}^{\infty} H(f)e^{-2\pi ift} df \quad (2.10)$$

The total power of a signal is constant whether we calculate it in the time domain or in the frequency domain. This result is known as Parseval's theorem.

The total power of a signal is given by,

$$\int_{-\infty}^{\infty} |h(t)|^2 = \int_{-\infty}^{\infty} |H(f)|^2 \quad (2.11)$$

As in the most practical situations, the data series is not a continuous series, the **Discrete Fourier Transform (DFT)** is very useful. Let $h(t)$ is an evenly sampled time series function with a time interval of Δ . For any sampling interval Δ , the **Nyquist critical frequency** (f_c) is given by

$$f_c = \frac{1}{2\Delta} \quad (2.12)$$

Nyquist criterion demands that the frequency of a signal ranges from $-f_c$ to f_c . Any frequency which lies outside of this range $-f_c < f < f_c$ is not acceptable as this may cause **aliasing effect** making unambiguous determination of frequency (from a time series).

With N numbers of input and the equation (2.9) can be written in form of discrete Fourier transform,

$$H(f_n) = \sum_{k=0}^{N-1} h_k e^{2\pi i f_n t_k} \Delta = \Delta \sum_{k=0}^{N-1} h_k e^{2\pi i k n / N} \quad (2.13)$$

$$\text{where, } f_n = \frac{n}{N\Delta}, \quad \text{for } n = \frac{-N}{2}, \dots, \frac{+N}{2} \quad \text{and } k = \frac{t_k}{\Delta} \quad (2.14)$$

The equation (2.10) can be simplified as,

$$H_n \equiv \sum_{k=0}^{N-1} h_k e^{2\pi i k n / N} \quad (2.15)$$

It is possible to compute DFT more efficiently and very fast by using the FFT algorithm. This reduces the number of operations from N^2 times to $N \log_2 N$. However, FFT, although computationally efficient, is applicable for 2^N data points and evenly spaced time series. Sometimes, the measured data are not evenly spaced time series as bad data points are generally removed. As interpolation of the data gaps can introduce “red noise” (artificial spectral contaminations towards the low-frequency side) in the frequency domain, a suitable algorithm is needed which can handle the unevenly sampled dataset without interpolation. Lomb Scargle Fourier Transform (LSFT) is one such technique.

2.8.2 Lomb Scargle Fourier Transform (LSFT)

Lomb (1976) and *Scargle* (1982, 1989) developed an algorithm for DFT which can be applied to both evenly and unevenly spaced time series data. Let there are N number of data points $h_i = h(t_i)$, $i = 1, \dots, N$. Then the mean and variance of the data are given by the formula,

$$\bar{h} = \frac{1}{N} \sum_1^N h_i \quad \text{and} \quad \sigma \equiv \frac{1}{N-1} \sum_1^N (h_i - \bar{h})^2 \quad (2.16)$$

Now, the Lomb normalized periodogram (spectral power as a function of angular frequency, $\omega = 2\pi f$) is defined by

$$P_N(\omega) = \frac{1}{2\sigma^2} \left\{ \frac{\left[\sum_j (h_i - \bar{h}) \cos \omega(t_j - \tau) \right]^2}{\sum_j \cos^2 \omega(t_j - \tau)} + \frac{\left[\sum_j (h_i - \bar{h}) \sin \omega(t_j - \tau) \right]^2}{\sum_j \sin^2 \omega(t_j - \tau)} \right\} \quad (2.17)$$

where, τ is defined by the relation

$$\tan(2\omega\tau) = \frac{\sum_j \sin 2\omega t_j}{\sum_j \cos 2\omega t_j} \quad (2.18)$$

The constant τ is a kind of offset that ensures $P_N(\omega)$ completely independent of shifting all the t_i s by any constant. The particular choice of τ gives a best fit to the sine and cosine functions to the time series by means of least squares.

$$h(t) = A \cos \omega t + B \sin \omega t \quad (2.19)$$

In order to know significant level of a peak in the spectrum $P_N(\omega)$, it is very important to test the null hypothesis of the Lomb normalized periodogram. For a given α , the null hypothesis of a signal (signal with pure white noise) is rejected, and $(1 - \alpha)$ gives the confidence level of a periodic signal where $P_N(\omega)$ has its maximum value. The algorithm generates normalized periodograms wherein the power in each spectral element is normalized with respect to the total power. This procedure makes the relative distribution of the spectral power independent of the spectral windowing used in the algorithm. “Significant” periodic components in both the time series exceed the critical level determined by Siegel’s test ([Siegel, 1980](#)). In the present thesis work, these analyses are addressed by an established algorithm ([Schulz and Stattegger, 1997](#)).

2.8.3 Cross Spectrum Analysis

In order to establish the causal relationship between two time series, cross spectrum analysis is carried out. “**Coherency**” is a measure of the degree of relationship, between two time series as a function of frequency. The squared

coherence of two stochastic processes $x(t)$ and $y(t)$ is calculated as

$$C_{xy}^2(f) = \frac{|F_{xy}(f)|^2}{F_{xx}(f)F_{yy}(f)} \quad (2.20)$$

i.e. the spectral coherence between two time series, $x(t)$ and $y(t)$, is the modulus-squared of the cross-spectral density divided by the product of the auto-correlation of $x(t)$ and $y(t)$. The coherence is the spectral equivalent of the cross-correlation function. The spectral coherence lies between 0 (i.e. no cross correlation) and 1 (full coherence) at all frequencies i.e. $0 \leq C_{xy}^2(f) \leq 1$. If x and y are two independent processes, then the squared coherency is 0 at all frequencies. The phase synchronization of two time series, $x(t)$ and $y(t)$ is given by

$$\Phi_{xy}(f) = \tan^{-1} \left[\frac{\text{Im}(C_{xy}(f))}{\text{Re}(C_{xy}(f))} \right] \quad (2.21)$$

In order to establish a causal relationship between two time series, it is very important to have a high coherency and stable phase at same periodicities. In the present investigations, the above factors are evaluated by a standard algorithm ([Schulz and Stattegger, 1997](#)).

Chapter 3

Different Types of Prompt Electric Field Perturbations and Their Equatorial Impacts

Abstract: In recent times, long duration PP events have been reported. However, DP2 type electric field perturbations are generally believed to constitute the long duration PP events. In this chapter it is shown that long duration PP events can consist of phenomenologically different processes like substorm (DP1). As recent studies show that shielding can remain broken for a much longer time than theoretically expected, it is important to identify the processes that constitute long duration PP events. The present chapter is devoted to this objective. The chapter also brings out the efficacy of narrow spectral band, narrow field-of-view OI 630.0nm nightglow observations in capturing the PP electric field perturbations over equatorial ionosphere.

3.1 Introduction

The zonal component of equatorial F-region electric field is generally eastward during day time and westward during night time. Under quiescent geomagnetic conditions, this scenario does not change except during the June solstice of the solar minimum years over Indian region when the F-region zonal electric field, in a statistically significant manner, turns to the eastward direction for sometime during midnight hours (*Chakrabarty et al., 2014*). The neutral wave dynamics (*Pallamraju et al., 2010*), prompt electric field perturbations during geomagnetic storms (*Fejer and Scherliess, 1997*) and magnetospheric substorms (*Huang, 2012*) can affect the electric field over low latitudes. The altered zonal electric field can play an important role (*Chakrabarty et al., 2006; Sekar and Chakrabarty, 2008*) in the generation of plasma irregularities in the equatorial ionosphere during local nighttime which is commonly referred to as Equatorial Spread F (ESF) events. Although the storm-time disturbances are global in nature, the impact of these disturbances can have longitudinal and seasonal dependences (*Fejer et al., 2008*). On the other hand, substorms occur in the nightside magnetotail and are known to be longitudinally confined (*Belehaki et al., 1998*).

Since the work of *Nishida (1968)*, it has been acknowledged that the DP2 fluctuations due to the perturbations in the interplanetary magnetic field (IMF) can appear coherently all over the globe during geomagnetic storms. DP2 fluctuations are different from the fluctuations due to polar substorms (DP1) in the sense that they do not originate from the auroral electrojet similar to DP1. Subsequently, a number of investigators (e.g. *Fejer et al., 2007*, and references cited therein) have reported DP2-type penetration electric field fluctuations as well as substorm-induced electric field fluctuations (*Kikuchi et al., 2003*) in the equatorial ionosphere. Further, transient electric field disturbances due to storm sudden commencements have also been observed

(*Sastri, 2002*). In addition to these prompt electric field disturbances, delayed electric field perturbations owing to the disturbance dynamo effect (*Blanc and Richmond, 1980*) can also modify the equatorial ionospheric dynamics at the later phase of a geomagnetic storm. Therefore, depending on the phase of the storm and the substorm, the space weather related electro-dynamical effects on the equatorial ionosphere can be entwined in a complex manner. Although, these effects have been studied in isolation, decoupling of these effects will lead to comprehensive understanding of the critical aspects of the magnetosphere-ionosphere (MI) coupling on a global scale.

In order to address the prompt electric field disturbances on the equatorial ionosphere during space weather events, it is ideal to have direct electric field/vertical plasma drift measurements (e.g. *Kelley et al., 2003*) by incoherent scatter radar. In absence of incoherent scatter radar over the Indian sector, the temporal variations in the height of the equatorial F region during nighttime can be interpreted as representing vertical plasma drift and used as a proxy for the zonal electric field. However, the ionosonde derived drifts during nighttime can be significantly modulated by recombination effects especially when the base of the F-layer height is below 300 km (*Bittencourt and Abdu, 1981*). In addition, routine ionosonde observations may suffer from low temporal resolution. On the contrary, magnetometer observations can provide high temporal resolution and primarily be useful to study ionospheric effects during daytime. Low latitude ionospheric conductivity is not large enough to support substantial currents during nighttime and, therefore, significant variations in the horizontal magnetic field over low latitudes during nighttime are believed to be due to the magnetospheric current variations (e.g. *Chakrabarty et al., 2005*). Photometric measurements of thermospheric airglow emission like OI 630.0 nm airglow emission can provide high temporal resolution and reliable informations on ionospheric processes during nighttime in moon-less, cloud-less conditions.

In recent times, based on narrow band 630.0 nm nightglow photometry, it was shown (*Chakrabarty et al., 2005*) that the periodicities of ~ 0.5 hr and ~ 1.0 hr in the interplanetary electric field (IEF) promptly penetrated into the low latitude ionosphere. Further, transient electric field perturbations associated with the onset of the expansion phase of a magnetospheric substorm, captured by 630.0 nm dayglow measurements from low latitude, was also reported (*Chakrabarty et al., 2010*). These events brought out the effects of fast fluctuations in IEF and the the ephemeral (lasting ~ 0.5 hr) effects of induction electric field associated with the substorm dipolarization on the equatorial F-region plasma dynamics. Interestingly, more often than not, changes in the solar wind drivers like polarity reversals in the interplanetary magnetic field (IMF) (*Lyons, 1996*) and/or sharp changes in the solar wind ram pressure trigger the onset of the expansion phase of magnetospheric substorms (*Lyons et al., 2008*). As IMF Bz condition significantly controls convection in the nightside plasma sheet during storms and the cross-tail current in the plasma sheet is generally believed to get altered during substorms, interaction between storm and substorm processes can impose electric field disturbances on the equatorial ionosphere which can be entwined at times making it difficult to identify the root mechanism. This problem is particularly severe during long duration prompt penetration (PP) events (*Huang et al., 2005*) when the probability of substorm occurrence is also high. As long duration PP events are mainly characterized by DP2 type electric field perturbations, it is important to explore whether other types of prompt electric field penetrations (like due to substorms and pseudo-breakups) occur within a long duration PP event. It is very important to delineate other geophysical effects (which are mentioned above).

The present investigation has been initiated to explain the OI 630.0 nm airglow intensity undulations recorded over an Indian dip equatorial station during a magnetically disturbed night. While doing so, this study aims to iden-

tify various magnetosphere-ionosphere coupling processes that occurred during a long duration penetration event which otherwise would have been clubbed into a generic PP event associated with IMF Bz. The role of these PP electric fields in the generation of F-region plasma irregularities is also explored. It is important to be mentioned here that the OI 630.0 nm nightglow observations from Thumba (an Indian dip equatorial station) helped us to identify the different types of electric field perturbations over equatorial ionosphere during a long duration PP event.

3.2 Measurements and Supporting Datasets

A coordinated experimental campaign involving two portable 630.0 nm airglow photometers and a collocated digisonde (DPS-4D) was conducted from Thumba, Trivandrum (TVM: Geog. Lat. 8.5°N , Geog. Lon. 77°E , and Dip angle 0.5°) during 18-30 January, 2012. One of the photometers was directed towards the zenith and the other was designed (through mirror arrangement) to obtain emissions from eastern sky at a zenith angle of 45° . A photomultiplier tube (PMT) is used as a detector in the photometer that measures the emissions at the zenith direction (hereafter, zenith photometer). For the eastward viewing photometer (hereafter, east photometer), a different PMT (H7421-50) was used as a detector because an identical PMT was not available during this campaign. Intensity fluctuations (and not the absolute intensities) are addressed in this work. The temporal resolutions of airglow intensity and ionograms are 5 sec and 420 sec, respectively. It is noted here that many attempts during my thesis tenure were made to get the simultaneous observations of airglow and HF radar from Thumba and other places. Only a few observations are available. The limitation is due to inclement weather conditions over Thumba and unsuitable lunar phases. One of the interesting observation is discussed in this chapter.

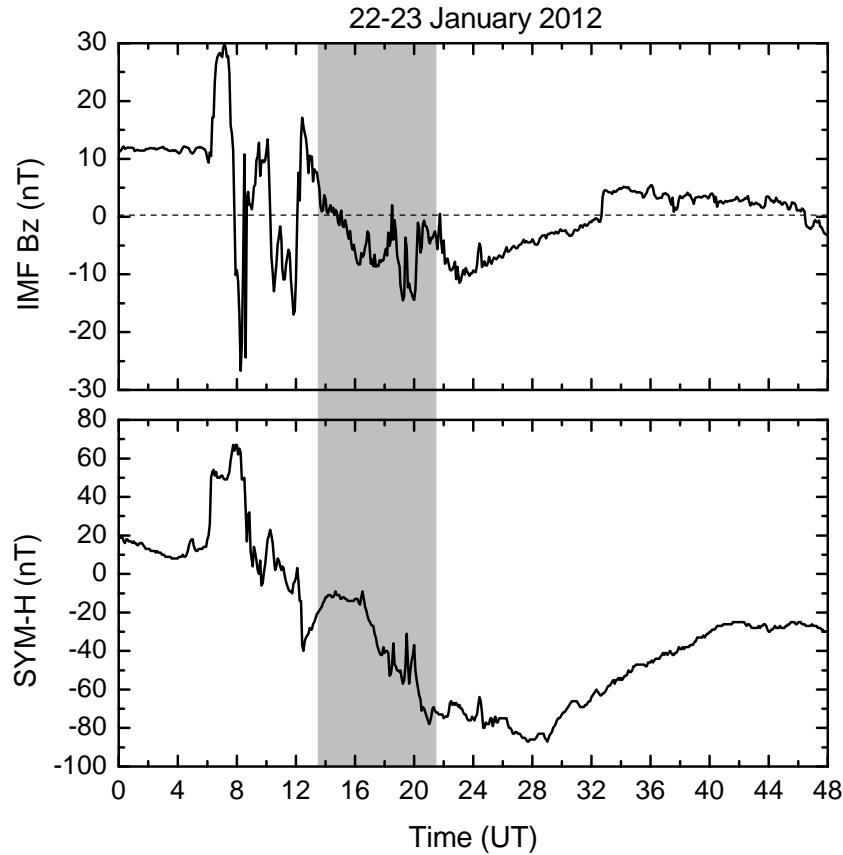


Figure 3.1: Variations in (a) IMF Bz in nT and (b) SYM-H in nT during 22-23 January 2012. The interval (1330-2130 UT) marked by gray shaded rectangular box shows the duration when the 630.0 nm airglow observations were made from Thumba.

In addition to the solar wind parameters (like solar wind velocity, density, magnetic field etc.), the horizontal magnetic field (H) variations over a few stations in the Indian, Japanese and American stations are used in the present study. The Indian stations include Tirunelveli (TIR: 8.7°N, 77.8°E, and Dip angle 0.5°), Alibag (ABG: 18.6°N, 72.9°E, and Dip angle 26.4°) and Jaipur (JPR: 16.9°N, 75.8°E, and Dip angle 41.9°). The equatorial electrojet strength over the Indian and south American sectors are utilized to study the effects on both the day and night sectors. The Japanese stations include Kagoshima (KAG: 31.5°N, 130.7°E, and Dip angle 45.4°) and Kototabang (KTB: 0.2°S, 100.3°E, and Dip angle 28.7°). The temporal resolution of the H data is 1 min.

For the substorm study, the energetic particle measurements at geosynchronous orbit by Los Alamos National Laboratory (LANL) satellites are provided for both electron and proton channels. Electron counts in four energy channels (E1: 48.15-69.85 keV; E2: 68.5-102.5 keV; E3: 99.95-149.45 keV; E4: 145.6-220.6 keV) and proton counts in three energy channels (P2: 75-11 keV; P3: 113-170 keV; P4: 170-250 keV), as measured by the LANL-02A and LANL-04A satellites, are used in this work. During the events discussed here, both these satellites were on the nightside.

3.3 Results

Figure 3.1a shows the variations of IMF Bz (in nT) and SYM-H (in nT) during 22-23 January 2012. It can be seen from the SYM-H variations that the SSC of geomagnetic storm started at ~ 0600 UT on 22 January 2012 which is followed by a long initial phase of 2.5 hrs. Further, the main phase started at ~ 0800 UT on 22 January 2012 and ended at ~ 0500 UT on 23 January 2012. SYM-H values reached a minimum of ~ -88 nT at the end of the main phase after which a long recovery phase ensued. The interval (1330-2130 UT) marked by gray shaded rectangular box shows the duration when the 630.0 nm airglow observations were made from Thumba (TVM). It is to be noted that the observation interval here falls under the main phase. The results from this campaign are discussed in the following sections.

Figure 3.2a shows the nocturnal variations of the base height of the F-layer ($h'F$, in km) over Thumba (TVM) during 1900-0300 IST on 22-23 January 2012 ($A_p = 24$). The average morphological variations in $h'F$ over Thumba during December solstice in solar minimum and maximum are reproduced from [Chakrabarty et al. \(2014\)](#) in Figures 3.2b and 3.2c. Figure 3.2d facilitates comparison between the F-region vertical plasma drift (derived from the $h'F$ variation and in blue) and OI 630.0 nm airglow intensity over zenith (in red)

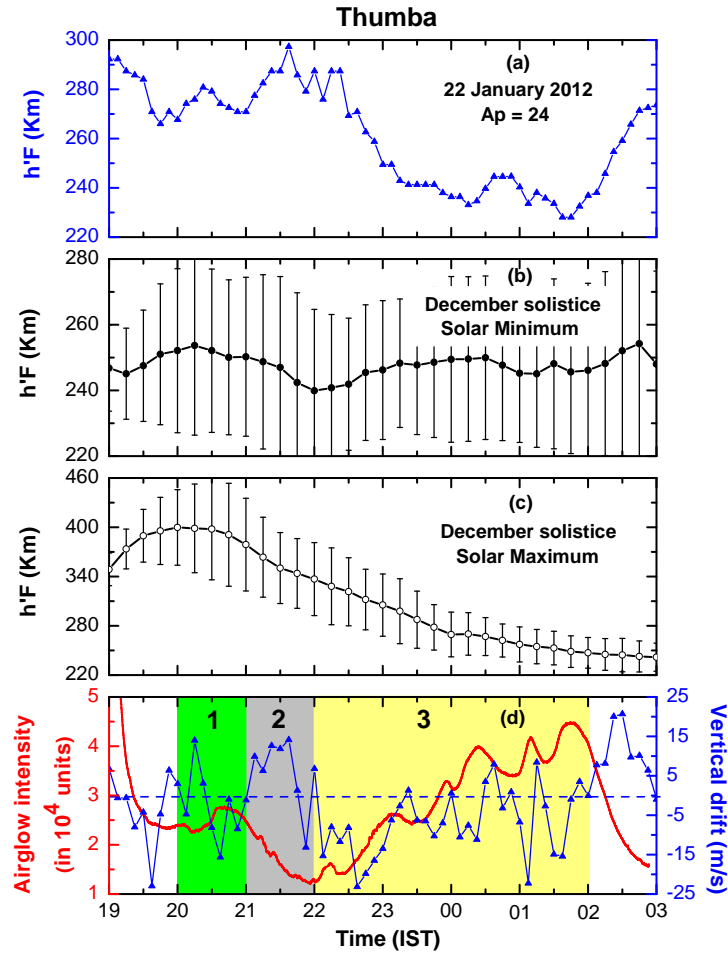


Figure 3.2: (a) Variation of $h'F$ (in km, in blue) during 1900-0300 IST (IST = UT + 5.5 hrs) on 22-23 January 2012 over Thumba, (b) and (c) morphological variations in $h'F$ over Thumba (taken from *Chakrabarty et al. (2014)* along with the standard deviations during the December solstice in the solar minimum and maximum epochs, respectively, and (d) F-region vertical plasma drift (recombination corrected, in blue) derived from the variations in $h'F$ on 22-23 January 2012 superimposed on the OI 630.0 nm airglow intensity variations (in red) recorded from Thumba. The three segments, wherein the $h'F$ variations on this night are visibly different from the morphological variations, are marked by green, gray and yellow colors and denoted by 1, 2 and 3, respectively. The segments 1, 2, 3 are characterized primarily by the westward electric field, eastward electric field and DP2 type fluctuating electric field perturbations, respectively.

recorded at Thumba on the same night. The X-axis is in Indian Standard Time (IST) which is 5.5 hours ahead of Universal Time (UT). Figure 3.2a reveals that there are conspicuous dips in $h'F$ at ~ 2000 and ~ 2100 IST and a peak at ~ 2115 IST reaching 300 km altitude. Thereafter, $h'F$ starts decreasing from ~ 2200 IST onwards. It is known that over the dip equator, vertical plasma drift is a good proxy for the zonal electric field (*Murthy and Hari, 1996; Fejer et al., 2008*). Therefore, to understand the role of space weather related electric field perturbations in the equatorial F-region ionosphere, it is important that true vertical plasma drifts are calculated from the variations in $h'F$. In order to determine the F-region vertical plasma drift over Thumba on 22-23 January 2012, the temporal rate of changes (in ms^{-1}) in $h'F$ ($dh'F/dt$) are first calculated. This provides vertical drift without chemical loss correction. The chemical loss contribution from ($dh'F/dt$) has also been subtracted out to get the true vertical plasma drift.

It can be noted that the $h'F$ variations observed on 22-23 January 2012, are substantially different from the average morphological variations described in Figure 3.2b and 3.2c. The monotonic rise in $h'F$ associated with the pre-reversal enhancement (PRE) of eastward zonal electric field at ~ 2015 IST, as evident in the average variations, seems to be absent on this night. Instead, fluctuations in $h'F$ are seen during 1930-2100 IST and even beyond this time. The F-region vertical plasma drifts, thus obtained, are overlaid on the OI 630.0 nm airglow intensity fluctuations (zenith) in Figure 3.2d. It can be noticed that the two peaks (interspersed by a trough) in the airglow intensity during 2000-2100 IST are concomitant with downward vertical drifts (westward electric fields). The airglow intensity variation over a low latitude station at this hour is generally marked by monotonic decrease (e.g *Sekar et al., 2004*) in the absence of plasma irregularity events and geomagnetic disturbances. Clearly, the airglow intensity variations at 2000 and 2033 IST stand out as intensity enhancements. Interestingly, the monotonic decrease in the airglow intensity

is observed during 2100-2200 IST which is associated with the upward drift (eastward electric field). Further, the undulations in the airglow intensity (6 intensity peaks during 4 hours) during 2200-0200 IST are just out-of-phase with the fluctuations in the vertical drift (fluctuations in the electric field). The drift fluctuations seem to precede the airglow fluctuations by ~ 5 minutes. However, this time delay issue will not be addressed further as this is difficult to resolve considering the temporal resolution of digisonde observation is 7 minutes. Based on the comparison of the F-region vertical drift and 630.0 nm airglow intensity (Figure 3.2d), three distinctly different segments can be identified. Segment-1 (marked by green rectangular box) spans roughly between 2000-2100 IST when westward electric field perturbations are observed for at least two times corresponding to which airglow intensity shows enhancements. Segment-2 (marked by gray rectangular box) spans from 2100-2200 IST when eastward electric field perturbation is present and airglow intensity reveals monotonic decrease. Segment-3 (marked by yellow rectangular box) is characterized by quasi-periodic fluctuations in drift and airglow intensity during 2200-0200 IST clearly under the influence of oscillating electric field.

Subsequent figures are presented to determine the cause of the fluctuations in the vertical drift and airglow intensity marked in segments 1-3 on 22-23 January 2012. Figure 3.3 (a-h) depicts the temporal variation (in IST and corresponding UTs) of the solar wind flow pressure (in nPa), Z-component (north-south) of the interplanetary magnetic field (IMF B_z) in nT, symmetric component of ring current as represented by SYM-H (in nT), asymmetric component of ring current as represented by ASY-H (in nT), Y-component (dawn-to-dusk) of interplanetary electric field (IEF_y) in mV/m, westward auroral electrojet indices (AL), vertical drift (in ms^{-1}) and normalized 630.0 nm airglow intensity variations over zenith (red) and eastern (green, 45° zenith angle) directions. As the two photometers consists of detectors with different quantum efficiencies and spectral sensitivity, the airglow intensity in each di-

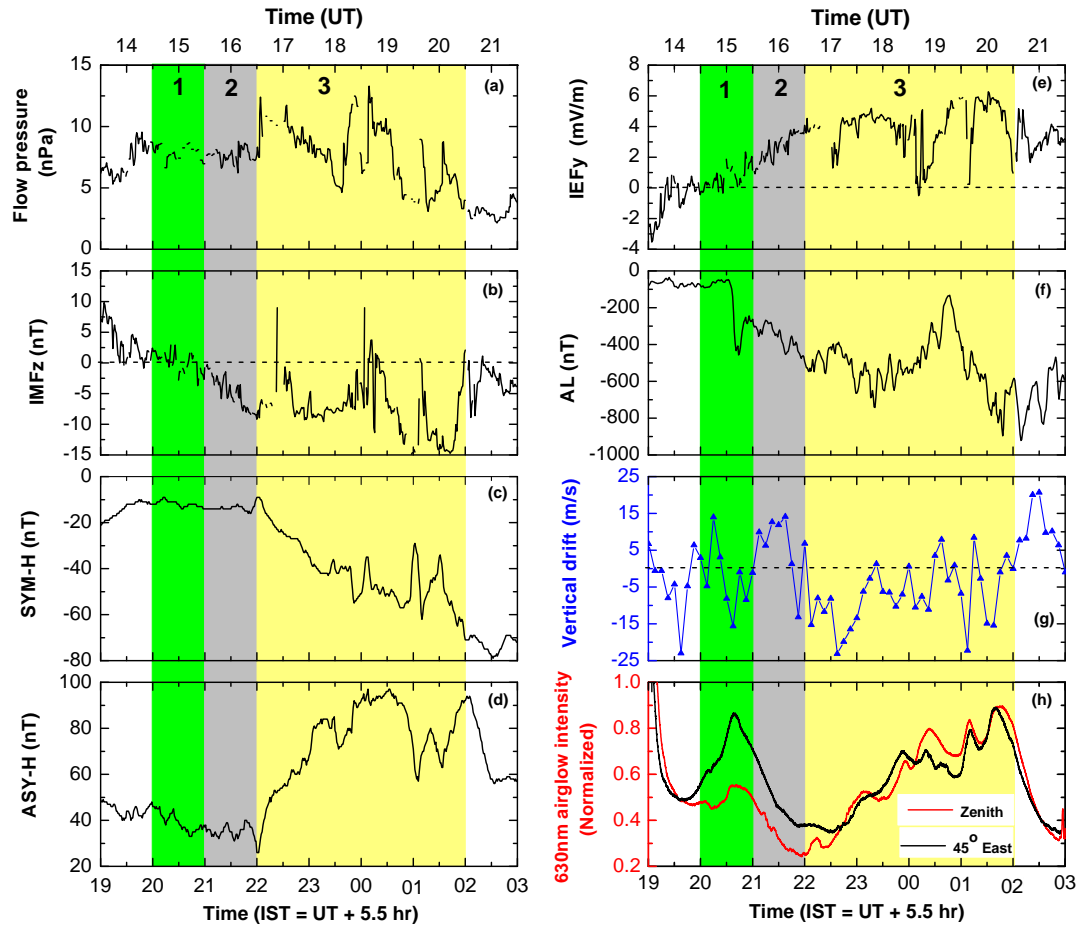


Figure 3.3: Variations in (a) solar wind flow pressure, (b) IMF Bz, (c) SYM-H, (d) ASY-H, (e) IEFy, (f) AL, (g) vertical drift (in blue), and (h) 630.0 nm airglow intensity from zenith (red) and 45° east (green) during 1900-0300 IST on 22-23 January, 2012. Time in UT is also shown on top of the two panels. The three segments are also marked. One can notice the fluctuations in IMF Bz (and IEFy) around the zero line in segment-1 before it fully turns to southward direction (IEFy turns to dawn-to-dusk direction) in segment-2. Fluctuations in IMF Bz (and IEFy) are noticed in segment 3. Intensification of AL starts at 2033 IST.

rection is normalized w.r.t. the maximum count in that direction for effective comparison of the temporal variabilities.

A number of interesting points can be noted from Figure 3.3. The solar wind flow pressure does not change significantly during segments 1 and 2.

SYM-H and ASY-H also do not change significantly during these intervals. At this juncture, it must be noted that AL variation does indicate the onset of intensification (goes below -400 nT) of westward auroral electrojet at ~ 2033 IST (segment 1) on 22 January, 2012. Two enhancements in airglow intensity are observed at ~ 2000 IST and ~ 2033 IST during segment 1. These enhancements are associated with downward drifts and the enhancement at ~ 2033 IST is also concomitant with intensification of AL. However, the airglow enhancement at ~ 2000 IST occurs when there are no substantial changes in the solar wind parameters and geomagnetic indices including AL. IMF Bz is found to be nominally northward at ~ 2000 IST and southward at ~ 2033 IST. During segment 2, IMF Bz does not show sharp fluctuations after turning southward. It is during this interval that vertical drift becomes predominantly upward in contrast to the downward drift expected (*Scherliess and Fejer, 1999*) during this time of the night. Airglow intensity variation over zenith reveals monotonic decrease during segment-2 which supports the upward drift during this interval. In segment 3, the quasi-periodic fluctuations are observed in the variations of IEF_y , vertical drift as well as in airglow intensity over zenith. The quasi-periodic fluctuations in airglow intensity cease to exist after 0200 IST. An interesting point must be noted here i.e. the airglow intensity fluctuations in both the directions during 2000-0200 IST are found to be nearly simultaneous. If one considers the centroid of airglow emission layer to be at 250 km, the zenith and 45° east in the sky are separated in the zonal direction by almost 250 km. Nevertheless, the undulations in the airglow intensity in both the directions have one to one correspondence without any appreciable time delay. On critical inspection, it can be noted that the relative amplitudes of the fluctuations differ in two directions particularly during 2000-2200 IST. The airglow enhancements at 2000 and 2300 IST are less conspicuous in the output of the photometer directed towards east as these enhancements are buried in larger emission volumes along the zonal slant path. The airglow variations in the east and zenith directions are also found to be slightly different during 0030-

0100 IST. Despite these deviations, the overall similarities are striking and this additionally confirms that the intensity fluctuations addressed in the present case are related to the space weather related prompt electric field disturbances (and not to any zonal transport of plasma structures) that are expected to affect of the two spatially separated regions in the sky nearly simultaneously.

Figure 3.4 depicts the variations in the horizontal component of magnetic field (ΔH) over the Indian and Japanese sectors during 1900-0300 IST (1330-2130 UT). Two vertical shaded boxes are overlaid on Figures 3.4(a-e) to highlight the variations in ΔH during 2000-2100 IST (1430-1530 UT) and \sim 0100 IST (1930 UT). It is observed that ΔH decreases steadily over the Indian sector (particularly over JPR which is almost a mid latitude station) and increases steadily over Japanese sector (particularly over KAG which is a mid latitude station) during 2000-2100 IST (1430-1530 UT). Smaller fluctuations in ΔH are also observed during this interval. These fluctuations are particularly prominent over Japanese sector and probably due to variations in the proton injection during 2000-2100 IST (1430-1530 UT) (see Figure 3.6). Interestingly, a pronounced positive bay is seen at 0100 hrs over all the stations in the Indian and Japanese sectors simultaneously. In addition to these variations, identical fluctuations in ΔH with no time delay are observed during 2200-0200 IST (1630-2030 UT) in all the stations that are widely separated in longitude as well as latitude. In order to find out the periodicity, the fast fluctuations in ΔH are extracted by using Savitzky-Golay (SG) smoothing algorithm (*Savitzky and Golay, 1964*). The smooth curves generated by the SG algorithm are marked by red line and overlaid on the ΔH variations during 2200-0200 IST (1630-2030 UT). The fast fluctuations in ΔH , separated from the original variations, are subjected to harmonic analyses using a standard algorithm (*Schulz and Stattegger, 1997*) (already explained in chapter 2). The results of the harmonic analyses are shown in Figures 3.4 (a1-e1). The “significant” spectral peaks stand over the “critical level” (marked by dashed

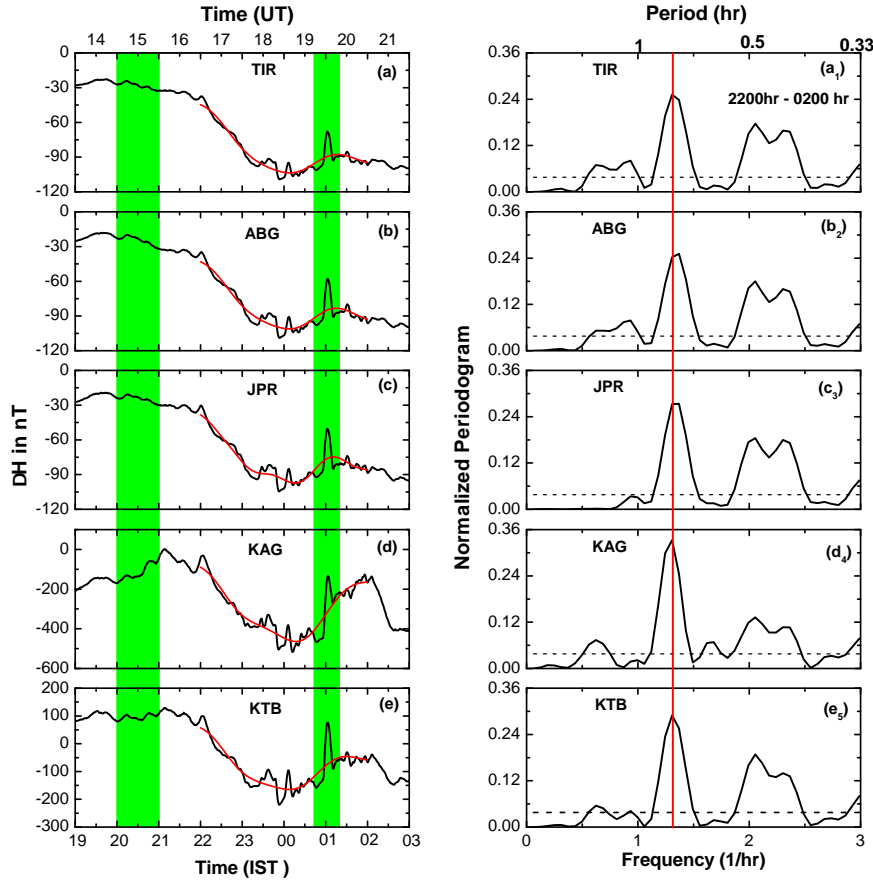


Figure 3.4: Variations in ΔH over the Indian and Japanese sectors during 1900-0300 IST on 22-23 January 2012. Indian stations are (a) Tirunelveli (b) Alibag (c) Jaipur and the Japanese stations include (d) Kagoshima and (e) Kototabang. The two vertical shaded boxes highlight the variations in ΔH during 2000-2100 IST (segment-1) and ~ 0100 IST. During segment-1, ΔH decreases over Indian stations and increases over Japanese stations. A sharp positive bay is seen at ~ 0100 IST over both Indian and Japanese stations. Note the identical fluctuations in ΔH during 2200-0200 IST (Segment-3) over both Indian and Japanese stations. The smoothed variations during 2200-0200 IST are marked by red lines and overlaid on the actual variations. The right panel (a₁-e₁) depicts the normalized periodograms of the fluctuations during the interval 2200-0200 IST. Periodicity of ~ 40 min is present over all stations.

horizontal line) determined by Siegel's test. Periodicity of ~ 40 min (marked by vertical red line) is found to be "significant" and present over all the stations.

Although other periods are also simultaneously present over all the stations, ~ 40 min periodicity is only discussed here for reasons that will be clear in the subsequent sections.

The results of similar harmonic analyses of drift, airglow intensity fluctuations and IEF_y data during segment 3 (2200-0200 IST) are depicted in Figure 3.5(a-c). It is found that ~ 40 min periodicity is present and “significant” in all the parameters. The black, blue and red colors in Figure 3.5(a-c) correspond to the spectra obtained from IEF_y, vertical drift and 630.0 nm airglow intensity, respectively. Further, the results of detailed cross-spectral analyses between IEF_y and drift as well as IEF_y and airglow intensity are depicted in Figure 3.5d and 3.5e, respectively. These analyses generate the squared coherency and phase spectra for the two time series under consideration. Coherency is considered “significant” if it is close or more than the 95% false alarm level depicted by dashed line in the plots. “Significant” coherency with a stable phase relationship (around the periodicity to be tested) is considered necessary to infer causal relationship. It is found that the ~ 40 min periodicities in drift as well as in airglow are highly coherent with the ~ 40 min periodicity in IEF_y and phase relationship is also nearly stable around this periodicity. This confirms that the 40 min periodicities in the equatorial drift and airglow intensity have its origin in IEF_y.

As stated earlier, two enhancements in airglow intensity are observed at ~ 2000 IST and 2033 IST (segment 1). These enhancements in airglow intensity at ~ 2000 IST and 2033 IST are concomitant with downward drifts and hence with westward electric field disturbances. Interestingly, although the airglow intensity enhancement at 2033 IST is concomitant with intensification of AL, similar variation in AL is not seen during the airglow enhancement at 2000 IST. One of the reasons could be that IMF B_z is northward at this time. In order to understand these aspects from a bigger perspective, the temporal variations (in UT as well as in IST which is UT + 5.5 hrs) in the

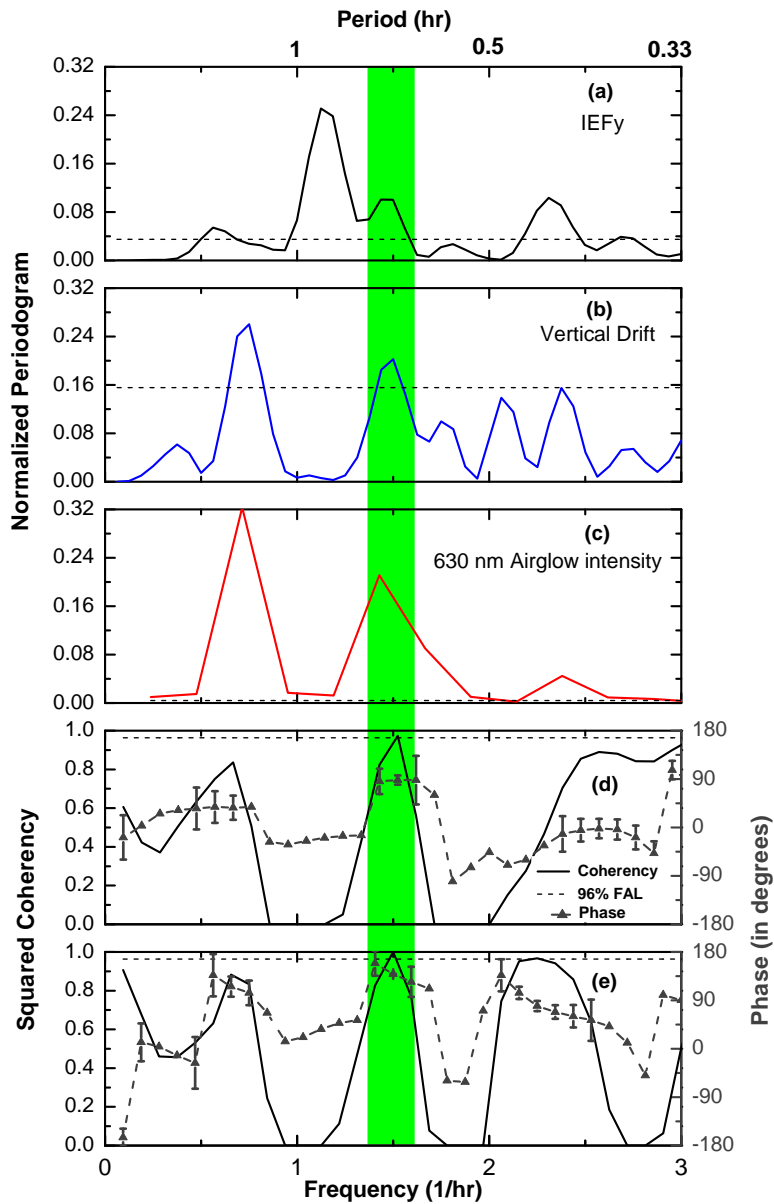


Figure 3.5: Normalized periodograms for the fast fluctuations in (a) IEFy (in black), (b) vertical drift (in blue), and (c) 630.0 nm airglow intensity from zenith (in red) for the interval 2200-0200 IST (segment-3). Periodicity of ~ 40 min is present in all the three parameters and is marked by the vertical shaded box. Cross-spectral analyses between (d) IEFy-drift and (e) IEFy-airglow intensity reveal high (above the critical level marked by the dashed horizontal lines) coherencies and stable phase relationships between these pairs corresponding to 40 min periodicity. This suggests the role of IEFy in causing the fluctuations in drift and airglow intensity.

electron counts s^{-1} at the geosynchronous altitudes by LANL-04A and LANL-02A satellites which were at $\sim 70^\circ E$ and $\sim 103^\circ E$, respectively at the nightside are presented in Figure 3.6(a-b). The LANL-02A satellite was closer to midnight. Dispersionless injections of energetic electrons at geosynchronous orbit were observed by LANL-04A at 0100 IST. Similar injections were observed by LANL-02A satellite at 2000 IST and 0100 IST. Clearly, the onset of the substorm at 2000 IST took place closer to midnight sector and hence, seen by LANL-02A but not picked up by LANL-04A. It is interesting to note that AL (Figure 3.6e) does not register any significant change at 2000 IST, although the airglow intensity over Indian dip equatorial region (Figure 3.6f) registers a small enhancement. Interestingly, when AL registers the onset of intensification at 2033 IST, there is no electron injection event observed by either LANL-04A or LANL-02A. However, downward plasma drift (Figure 3.3g) as well as enhancement in 630.0 nm airglow (Figure 3.3h) are observed over the dip equator at this time. In order to understand this aspect, proton injection events at the geosynchronous altitude, as measured by these satellites (Figure 3.6c-d), are investigated. It is found that onset of the substantial enhancement of proton injection starts at 2033 IST and detected by both LANL-04A and LANL-02A. Therefore, intensification of AL at 2033 IST seems to be concomitant with proton injection at the geosynchronous altitude and AL remains insensitive to “dispersionless” electron injection at 2000 IST detected by LANL-02A satellite. Interestingly, similar to the “dispersionless” electron injection event at 0100 IST, the proton injection event at 0100 IST is also found to be “dispersionless”. AL starts weakening from 2330 IST when both the electron and proton counts start decreasing and eventually go to a negligible value before the onset of “dispersionless” injection at 0100 IST. Further intensification of AL starts after this injection event. In addition, it can also be noticed that although SYM-H and ASY-H respond to the “dispersionless” electron and proton injection events at 0100 IST, both these indices seem to remain unaffected by the “dispersionless” electron injection event at 2000 IST

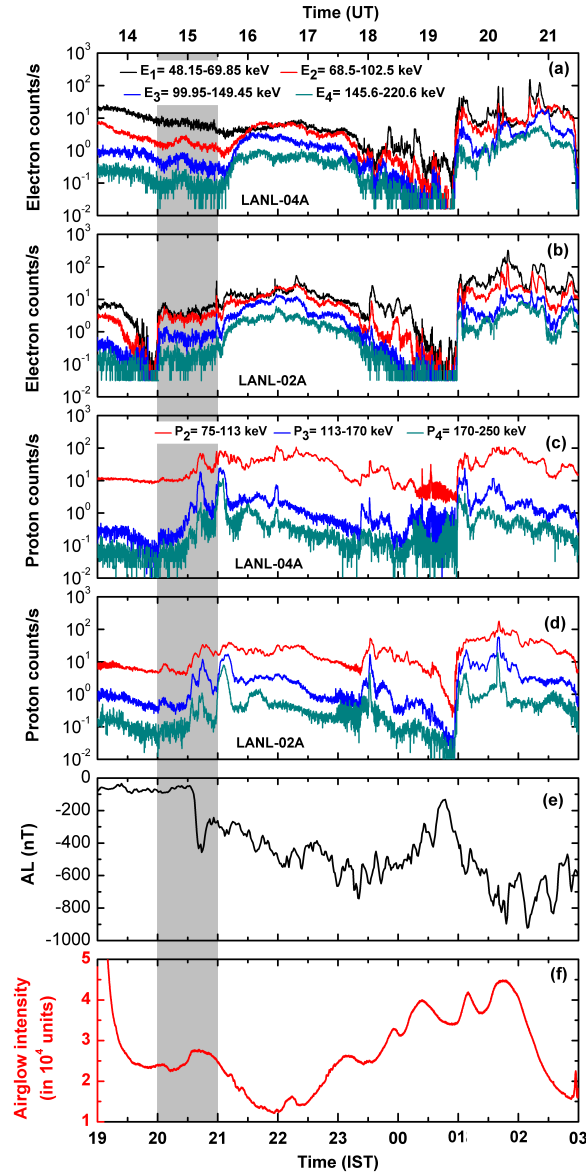


Figure 3.6: (a) and (b) Electron counts s^{-1} as measured on-board LANL-04A and LANL-02A, respectively. These satellites were on the Indian and Japanese sectors, respectively during 1900-0200 IST. (c) and (d) Proton counts s^{-1} , as measured by these satellites. Dispersionless electron and proton injections are seen over Indian and Japanese sectors at 0100 IST. However, “dispersionless” electron injection at 2000 IST is seen only over Japanese sector. Proton injections are seen over both Indian and Japanese sectors at 2033 IST. Note that the onset of AL intensification is concomitant with this proton injection event.

(Figure 3.3c and 3.3d, respectively). It is worth recalling at this juncture that ΔH decreases over the Indian sector and increases over Japanese sector during 2000-2100 IST (1430-1530 UT) and a pronounced positive bay is seen at 0100 hrs over all the stations in the Indian and Japanese sectors simultaneously. The implications of these results will be discussed in the ensuing section.

3.4 Discussion

The electric field disturbances during segment-1 brings out two enhancements (at 2000 IST and 2033 IST) in airglow intensity during 2000-2100 IST. This is clearly due to the downward plasma drifts over dip equatorial region as a consequence of the westward electric field disturbances associated with substorm activities during this interval. During this time, ΔH decreases over Indian longitudes and ΔH increases over Japanese longitudes. Further, LANL-02A satellite, which was longitudinally closer to Japanese longitude ($\sim 103^\circ\text{E}$), registers one “dispersionless” electron injection event at 2000 IST. However, there is no significant injection event at this time over Indian sector as suggested by the LANL-04A ($\sim 70^\circ\text{E}$) data. From these observations, it seems that the central meridian of the substorm current wedge (SCW) was over the Japanese sector during this event and Indian sector was outside the SCW. This explanation is offered for the following reasons.

The ground-based magnetic signatures associated with the onset of magnetospheric substorms are generally interpreted based on the substorm current wedge (SCW) model proposed by *McPherron (1991)*. Following this model, a positive bay in the ΔH -component variation is expected about the wedge central meridian and negative bay is expected outside the wedge. These predictions are consistent with observations also (*McPherron et al., 1973; Sastri et al., 2003*). In the present investigation, ΔH decreases over the Indian sector and increases over the Japanese sector during 2000-2100 IST which provides a

clue that the central meridian of the SCW might have been over Japanese sector (local midnight). Indian sector (local evening) happened to lie just outside the formed SCW. This scenario is also consistent with the LANL observations as “dispersionless” injection is seen by the LANL-02A satellite at $\sim 103^\circ\text{E}$ but not seen by LANL-04A satellite at $\sim 70^\circ\text{E}$.

Although these observations are consistent with the SCW model predictions, a few inconsistencies can also be noticed. If the event at 2000 IST is a substorm event, why there are no corresponding signatures in SYM-H and ASY-H? This casts doubt on the inference that the event at 2000 IST is a genuine substorm event or not. This doubt is further strengthened by the absence of corresponding enhancement of AL at this time. It is to be noted that LANL-02A observes “dispersionless” electron injection at this time. Therefore, this satellite seems to be inside the injection region. LANL-04A is further west at this time and the energy dispersion observed by this satellite indicates that this satellite was outside the injection region. It seems that there is a very narrow region where “dispersionless” events are seen for electrons but not for ions. Therefore, absence of enhancement in AL indicates the location of the injection region relative to the AL stations and also points towards the longitudinal confinement of this event. One of the possibilities could be that this event is a pseudo-breakup event and not a fully-grown substorm event. Pseudo-breakups are known (*Pulkkinen et al., 1998; Rostoker, 1998*) to be short-lived and localized substorm-like disturbances preceding the onset of the expansion phase of a full-fledged substorm. As the characteristic magnetospheric and ionospheric signatures corresponding to the pseudo-breakups do not differ significantly from those of substorms, it is difficult to differentiate between these two processes (*Pulkkinen et al., 1998; Rostoker, 1998; Sastri et al., 2003*). It is, however, argued (*Pulkkinen et al., 1998*) that pseudo-breakups, more often than not, occur during the interval when the solar wind energy input into the magnetosphere is still going on. *Rostoker (1998)* argued that the pseudo-breakups

have the normal characteristics of an expansive phase onset associated with a substorm but have amplitudes below some subjective limit. As a consequence, it is difficult to identify a pseudo-breakup event based on observations. *Rosotoker (1998)*, however, suggested, that pseudo-breakups, phenomenologically, occur during a period of increasing energy input into the magnetosphere and “true” auroral break-ups occur during the release of stored tail energy that is accompanied with the decline in the rate of energy input into the magnetotail. Interestingly, in the present case, one can notice that although IMF B_z is generally northward around 2000 IST (even after considering maximum uncertainty of ~ 5 min in the propagation lag calculation), there were at least two very small southward excursions in the run-up to this event. This indicates interruptions in the energy input into the magnetosphere that might hinder the onset of a fully-grown expansive phase. Therefore, the magnetospheric and ionospheric signatures at 2000 IST in the present case could very well be signatures of a pseudo-breakup event. Importantly, the westward electric field perturbations associated with this pseudo-breakup event gets registered in the 630.0 nm airglow intensity over dip equatorial station also. Further, “dispersionless” injections have also been observed in the past during pseudo-breakups (*Koskinen et al., 1993; Nakamura et al., 1994; Pulkkinen et al., 1998*) similar to the present case.

The geosynchronous particle injection signatures at 2033 IST, when downward (westward electric field) F-region plasma drift as well as airglow enhancement are observed over the Indian dip equatorial region, are also quite interesting. At this time, LANL-02A as well as LANL-04A satellite observations indicate absence of electron injections but presence of proton injections at the geosynchronous altitudes. It is at this time that AL shows sharp decrease below -400 nT (Figure 3.6). *Janzhura et al. (2007)* noted that in order to be classified as substorm, AL should exceed at least -400 nT during that event. This condition is satisfied in the present case. Further, *Reeves et al. (1991)*

showed that “dispersionless” injections of protons may be observed independently on many occasions during substorms. This result is also supported by the test particle simulations of *Birn et al. (1998)*. *Chi et al. (2006)* also showed that proton auroral intensification at the onset of substorm and proton injection at the geosynchronous altitude can occur at the same magnetic local time (longitude). *Weygand et al. (2008)* demonstrated that the intensification of the westward auroral electrojet and the “dispersionless” particle injection can occur at about (within the uncertainty of the averages) the same time. Despite the geosynchronous injections and AL intensification, the substorm at 2033 IST in the present case does not seem to be associated with any sudden change in the solar wind parameters. It is found that even the maximum uncertainty of 5 minutes in the solar wind propagation delay does not change IMF B_z polarity at 2033 IST. Therefore, the substorm event do not seem to be associated with clear northward turning of IMF B_z . It is also verified that IMF B_y (shown in Figure 3.7b) or solar wind dynamic pressure do not change significantly at and around this time. *Lyons (1996)* proposed that northward turnings of IMF B_z or reductions in IMF B_y or even enhancements in dynamic pressure (*Lyons et al., 2008*) trigger most of the substorms. However, *Lee et al. (2007)* showed that some solar wind changes do not trigger substorms and it was suggested that the nontriggering types do not reduce the convection strength in the plasma sheet. In the present case, the role of IMF B_z (or other solar wind parameters) in triggering the substorm at 2033 IST is not clear and this requires further investigation. Nevertheless, the present observations strongly suggest the onset of the expansion phase of a substorm at ~ 2033 IST causing westward electric field disturbance as well as enhancement in 630.0 nm airglow intensity. It needs to be mentioned here that several authors (e.g. *Hashimoto et al., 2011*, and references cited therein) invoked the important role of R2 FAC in determining the polarity of electric field disturbances on equatorial ionosphere at the substorm onset during both day and nighttime. The westward electric field disturbances on the nightside equatorial ionosphere

at the substorm onset presented here is consistent with the narrative of [Huang et al. \(2004\)](#).

It is clear from Figure 3.2 that an upward drift (eastward electric field disturbance) is registered at ~ 2130 IST during segment 2 (2100-2200 IST) which is opposite in polarity (at this local time) if one compares it with the outputs of the Scherliess-Fejer model of quiet time equatorial F-region vertical drift ([Scherliess and Fejer, 1999](#)). In general, when the IMF is southward, IEF_y is positive (pointing dawn to dusk). Therefore, PP electric field is generally eastward on the dayside and westward on the nightside both pointing from dawn to dusk. Nevertheless, modeling calculations (e.g. [Nopper and Carovillano, 1978](#); [Senior and Blanc, 1984](#); [Tsunomura and Araki, 1984](#)) have indicated the presence of eastward penetration electric field as late as 2200 LT. However, observational evidence in this regard is sparse. In addition, the polarity of overshielding electric field is generally westward during daytime and eastward during nighttime. As IMF B_z remains southward with increasing strength during 2100-2200 IST, the overshielding effect (associated with IMF B_z) is ruled out in the present case. Therefore, this is clearly a case of the effect of eastward PP electric field associated with IMF B_z turning steadily southward at this time. In this context, it is relevant to note that [Abdu et al. \(1998\)](#) and [Chakrabarty et al. \(2006\)](#) reported eastward PP electric field over Indian sector during dusk (1730-1900 LT) and 2030 IST, respectively. However, in the present case, this eastward PP electric field is observed as late as 2200 IST when quiet time ionospheric electric field polarity is expected to be westward. This is surely not a case of PRE getting enhanced as the electric field already turned to westward direction during post-sunset hours which can be seen from Figure 3.2d (~ 1930 IST). Therefore, the present case elicits that the polarity of the PP electric field can be eastward even during pre-midnight hours.

The consequences of the presence of westward and eastward electric field perturbations during segment 1 and 2 are also noticed from the critical in-

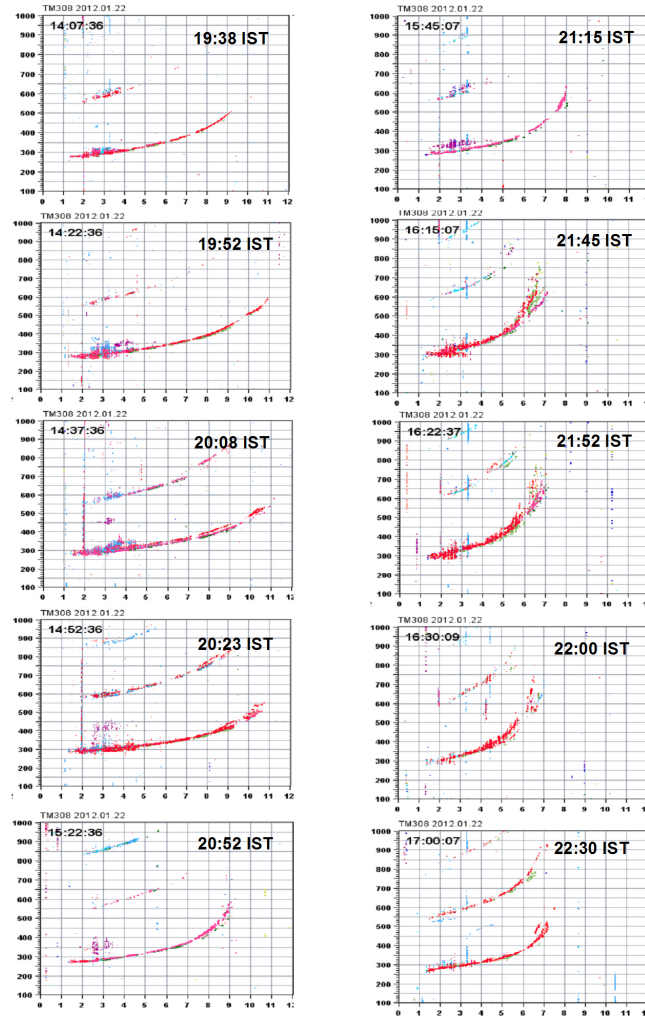


Figure 3.7: A series of ionograms obtained over Thumba during 1938-2052 IST (left column) and 2115-2230 IST (right column). The left column shows the presence of weak range spread-F at 1952 IST. The altitude extent of the spread decreases after the onset of the pseudo-breakup event at 2000 IST as seen from the ionogram at 2008 IST. The altitude extent of the spread increases after the pseudo-breakup event is over (see ionogram at 2023 IST). The altitude extent of the spread again decreases (see ionogram at 2052 IST) after the onset of the substorm at 2033 IST. The right column shows the presence of weak spread at 2115 IST which develops into an admixture of range and frequency spread-F after the imposition of eastward PP electric field during segment-2 (2100-2200 IST). Interestingly, after the equatorial electric field becomes fully westward at 2230 IST, the spread-F activity stops. No ESF activity is noticed during segment-3.

spection of the ionograms during these periods. Figure 3.7 is presented to highlight this aspect. The left column of Figure 3.7 shows a few representative ionograms obtained from Thumba during 1938-2052 IST. It can be noticed that a weak range spread-F event was present at 1952 IST which got subdued (reduction in the altitude extent of the spread) around 2008 IST indicating influence of westward electric field due to the onset of the pseudo-breakup event at 2000 IST. The echoes developed with larger altitudinal extent at 2023 IST that indicated reduction in the westward electric field influence. The altitude extent of spread-F echoes again got reduced at 2052 IST owing to the influence of substorm-induced westward electric field perturbation. In order to highlight the eastward electric field perturbation during segment 2, the right column of Figure 3.7 is presented wherein a few representative ionograms during 2115-2230 IST are shown. It can be noticed that eastward PP electric field makes the range spread-F event stronger and this is clear from the ionogram at 2115 IST. The weak range spread-F event at 2115 IST then turns into an admixture of range and frequency spread-F event (see the ionograms at 2145 and 2152 IST). Interestingly, once the influence of the eastward PP field ceases to exist after 2200 IST, the weak ESF event also comes to an end. This is amply evident from the ionogram at 2230 IST in which ESF is absent. Therefore, the westward and eastward electric field perturbations during segment 1 and 2 are also consistent with the evolution of weak ESF event on this night. It is verified that ESF was absent during 2200-0200 IST and was not responding to occasional eastward electric field probably due to lower F-layer base height. It is known that the eastward electric fields assist the generalized Rayleigh-Taylor (GRT) instability which is known to be prime causative mechanism of ESF. On the other hand, the westward electric fields inhibit the growth of GRT particularly at lower altitudes. The temporal pattern of the altitude extent of ESF echoes on ionograms in Figure 3.7 is consistent with the effects of electric fields on the development of ESF (e.g. *Sekar and Kelley, 1998*). As the spread in the ionogram echoes during 1952-2200 IST starts beyond 300

km altitude which is above the centroid of 630.0 nm emission, the airglow intensities are devoid of ESF signatures. This inference is strengthened by the absence of significant (a few tens of minutes) time delay between the points of mutual correspondence in the observed airglow intensities from zenith and eastern directions (see Figure 3.3h) indicating the origin to be due to space weather disturbances as mentioned earlier.

The last important aspect of this investigation is the PP of ~ 40 min periodicity in IEF_y into equatorial ionosphere (segment-3) that results in fluctuations in equatorial vertical drifts and corresponding 630.0 nm airglow intensity variations. As ~ 40 min periodicity is observed in the magnetic data simultaneously, the present observation probably provides a clear evidence of DP2 type fluctuations during midnight and post-midnight hours over equatorial region. The present case, similar to the case of *Sastri et al. (2000)* with the periodicity of 25-35 min, provides another evidence for DP2 type (occasionally eastward too) electric field perturbations affecting the dip equatorial ionosphere even during midnight hours. The eastward polarity (similar to daytime polarity) of the DP2 electric field during midnight hours is in contrast (e.g. *Sastri et al., 2000*) to the expectation (*Tsunomura, 1999*) and requires further investigation. It is interesting to note that during the interval (Segment-3) of DP2 type PP, a substorm onset also took place at 0100 hrs. This substorm onset conspicuously makes SYM-H less negative (see Figure 3.3c), causes enhancement in ASY-H (see Figure 3.3d) and generates clear positive bay in the ΔH variations over both Indian and Japanese sectors (see Figure 3.4). However, the influence of this substorm onset is difficult to delineate from the variations in the equatorial drift and 630.0 nm airglow intensity in the presence of the PP event. Therefore, it is not clear based on the present study how the substorm-induced electric field has modulated the PP (of IEF_y) electric field during segment 3. This is a topic which requires further attention. In the context of PP of ~ 40 min fluctuation in IEF_y , the optical observation by *Sakai et al. (2014)* is pertinent.

These author presented 630.0 nm airglow intensity variations over Svalbard associated with polar cap patches during 1800-2400 UT on 22 January, 2012. Although not reported by *Sakai et al.* (2014), ~ 40 min periodicity can be noticed in the observed 630.0 nm airglow intensity variation during 1800-2030 UT on this night. Therefore, it is clear that the ~ 40 min fluctuation in IEF_y has a global effect on this particular night and strengthens the argument for the DP2 origin of the fluctuations with similar periodicity observed over the equatorial region during midnight hours. Further, considering the theoretical shielding time constant to be ~ 20 min (*Senior and Blanc, 1984*), PP of 40 min fluctuations in IEF_y for 4 hours into low latitude ionosphere need further investigation on the magnetosphere-ionosphere coupling conditions that determine penetration events for longer duration.

3.5 The effects of this space weather event in the day sector

In order to study the effects of three different types of electric field perturbations on day-side ionosphere, the equatorial electrojet strength has been explored over Jicamarca sector. Figure 3.8 shows (a) IEF_y in mV/m (b) IMF B_y in nT (c) PC index (d) 630.0 nm night time airglow intensity (e) The vertical drift over Thumba in ms^{-1} , and (f) the equatorial electrojet (EEJ in nT) strength over Jicamarca. It has already been discussed that the electric field perturbations in segment 1 are due to pseudo-breakup and substorm, segment-2 for the southward turning for IMF B_z and the segment 3 is associated with DP2 type electric field perturbations. The three segments are distinctly marked by green, gray and yellow color, respectively. The respective local times are mentioned on the top of the X-axis of the Figure (d) and (f). It can be easily noticed that the EEJ strength does not show any significant variations during segment 1 and 2. However, EEJ shows a clear oscillating

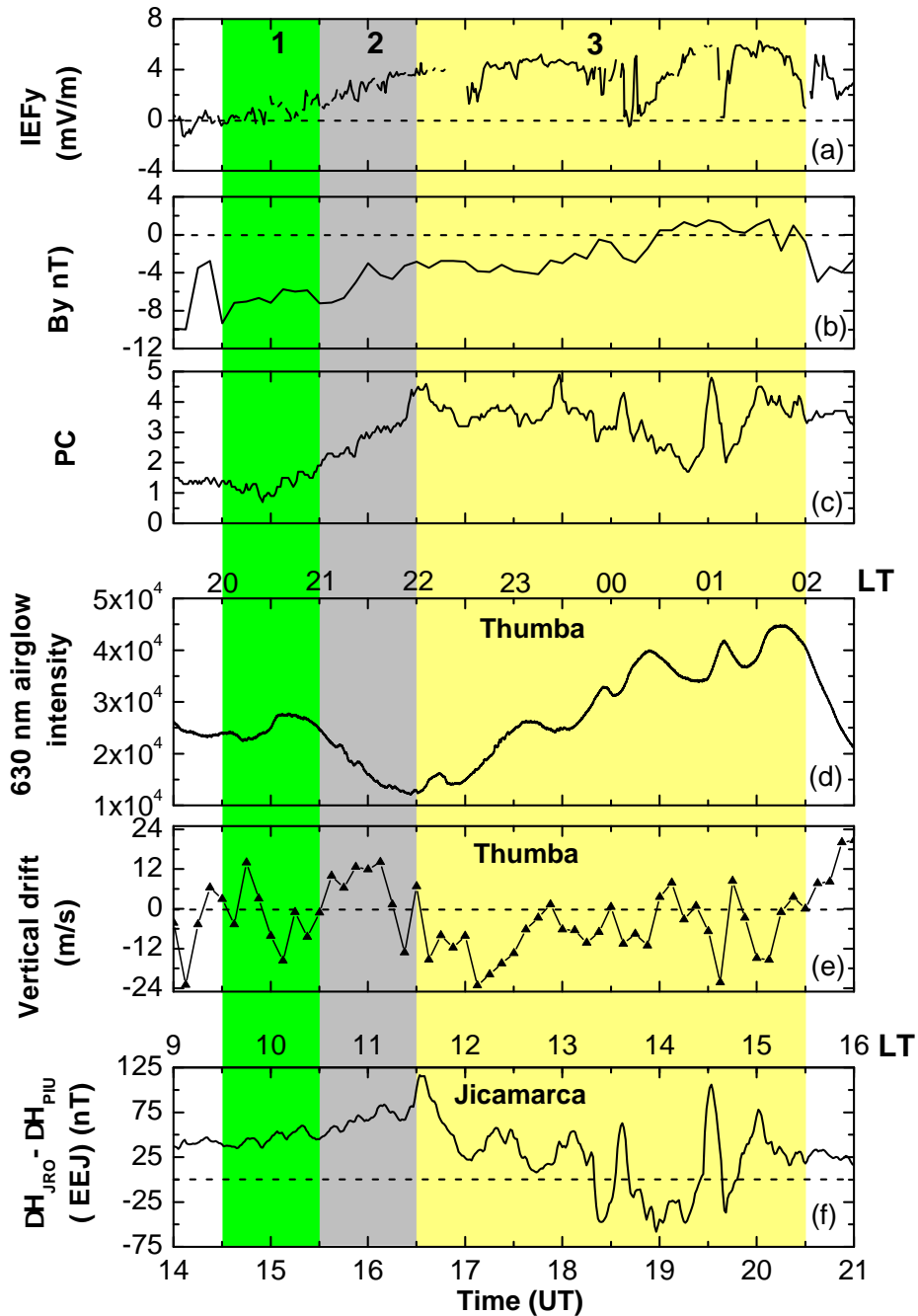


Figure 3.8: Variations in (a) IEFy in mV/m (b) PC index (c) 630.0 nm night time airglow intensity (d) The vertical drift over Thumba, and (e) the equatorial electrojet (EEJ) strength over Jicamarca are shown during 1400-2100 UT. The respective local times are mentioned on the top of the X-axes of the plot (d) and (f). The three segments (1, 2 and 3) are marked by green, gray and yellow colors, respectively.

behavior in segment 3 which is just opposite to vertical drift over Thumba. Further, the variations in EEJ strength also goes hand in hand with the 630.0 nm airglow intensity and PC index during this interval.

In order to know the frequency of oscillations and the causal relationship between the EEJ and IEFy, similar cross spectrum analyses (as shown in Figure 3.5) have been carried out. Figure 3.9 shows the normalized periodograms for (a) IEFy and (b) EEJ for the interval 1630-2030 UT (segment 3) and (c) the coherency and phase spectra between IEFy-EEJ. It reveals that 40 min periodicity is present in EEJ and IEFy. There is also a high coherency and stable phase relationship between the IEFy and EEJ at this periodicity. This suggests that the EEJ variations over Jicamarca are mainly due to change in IEFy in segment 3.

The above results bring out the effects of three types of electric field perturbations over Jicamarca during daytime. It is clearly evident that the electric field perturbations owing to pseudo-breakup, substorm (in segment 1) and southward turning of IMF Bz (in segment 2) are not well captured by EEJ variations during daytime. However, the DP2 type 40 min periodic perturbations are well captured by the EEJ variations. It is important to mention here that the ionosphere is considered to be electrostatic in nature and curl free. As a result, the opposite polarities of electric fields are expected in day and night sectors. So according to this condition, a westward electric field is expected during these magnetospheric events (substorm/pseudo-breakup). It is to be noted that the pseudo-breakups and substorms are highly longitudinal localized and nightside process. This may be the reason for which the substorm and pseudo-breakup induced electric fields are not propagated to dayside efficiently and these induced electric fields are possibly getting nullified by other longitude sectors. There are very few studies which show the impact of PP electric field in both the hemisphere by taking the simultaneous measurements (*Kelley et al., 2007; Chakrabarty et al., 2017*). It remains an outstanding prob-

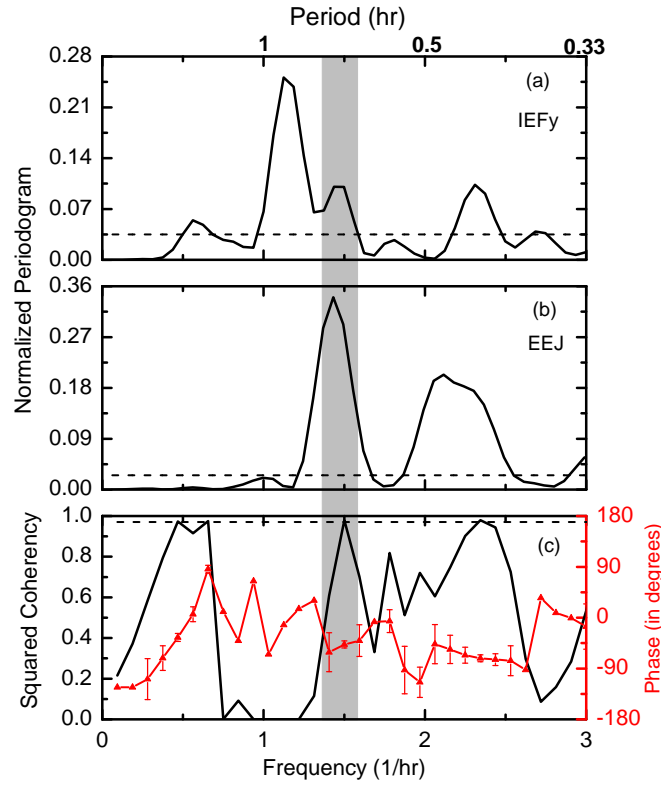


Figure 3.9: Normalized periodograms for (a) IEFy and (b) EEJ strength over Jicamarca for the interval 1630-2030 UT (segment-3). Periodicity of ~ 40 min is also seen to be present in the variations of EEJ strength over Jicamarca and is marked by the vertical shaded box. Cross-spectral analyses (c) between IEFy-EEJ strength reveal high (above the critical level marked by the dashed horizontal lines) coherency and stable phase relationship corresponding to 40 min periodicity. This suggests the role of IEFy in causing the fluctuations in EEJ over Jicamarca.

lem that how the ionospheric electric field gets satisfied the curl free condition over the globe during these magnetospheric (substorm/pseudo-breakup) processes. This is a less explored area in MI-coupling process and to address these issues, simultaneous observations are needed over the globe. Further, in the segment-2, the same polarity of PP electric field may be explained by the IMF By changes. It seems that there is a small increase in IMF By during this interval. Recently, it is suggested (*Chakrabarty et al., 2017*) that the sharp change in IMF By component under southward IMF Bz condition can skew

the DP2 cell patterns over the dip equator and it can also rotate the electro-dynamical boundary between the dawn and dusk cells. During this scenario, one can expect the same polarity over two equatorial antipodal points. In the present study, this is clearly seen in segment 3 for DP2 type PP. Further, this needs to be further investigated that how the global electric field gets adjusted during such processes.

3.6 Summary:

Based on observations by multiple techniques, it is shown that three primarily different types of PP electric fields, occurring in sequence, have affected the equatorial ionosphere-thermosphere system over an interval of 6 hours (2000-0200 IST) on a single night (22-23 January, 2012). The salient points that have emerged from this investigation are as follows:

1. Westward electric field perturbations over Indian sector owing to a pseudo-breakup and a substorm event (each lasting for about 30 min) are identified. The substorm event follows the pseudo-breakup event. The effects of these magnetospheric events on equatorial F-region zonal electric field are elicited and the evidences for the effects on nocturnal 630.0 nm air-glow intensity over equatorial region are presented for the first time. Further, geosynchronous electron and proton signatures are also found to be different for these longitudinally confined magnetospheric events.
2. Observational evidence for eastward electric field perturbation (lasting for about an hour) as late as 2200 IST over Indian sector owing to the southward polarity reversal of IMF Bz, is presented. The upward F-region vertical plasma drift (instead of the usual downward drift encountered during pre-midnight hours) and decrease in the 630.0 nm airglow intensity are consistent with eastward polarity of the penetration electric field. The eastward polarity of the electric field perturbation during pre-

midnight hours is consistent with a few model predictions (e.g. *Nopper and Carovillano, 1978; Senior and Blanc, 1984; Tsunomura and Araki, 1984*) but observations are sparse in this regard.

3. Quasi-periodic (period ~ 40 min) fluctuations in the vertical drift and 630.0 nm airglow intensity over Indian sector (sustaining for about 4 hours) are shown to have causal connection with the similar fluctuations in IEFy. This is a possible signature of DP2 type electric field perturbations affecting the dip equatorial ionosphere even during midnight hours. Further, the occasional eastward polarity (similar to daytime polarity) of the DP2 electric field during midnight hours is in contrast with what is expected of equatorial DP2.
4. The investigation also captures the suppression of weak spread-F under the effects of westward electric fields due to the pseudo-breakup/substorm events as well as the evolution of the range spread-F event into an admixture of range and frequency spread-F event due to the eastward PP electric field. It is also observed that occasional eastward polarity reversals during a DP2 type event do not trigger any plasma irregularity event during midnight hours probably due to low F-layer base height.
5. The pseudo-breakup and substorm imposed electric fields are not observed during daytime. In addition, the large eastward electric field perturbations due to the southward excursion of IMF Bz during night sector is also not reflected in EEJ over Jicamarca. However, the DP2 type of electric fluctuations are well captured by the EEJ strength during daytime.

Chapter 4

Prompt Penetration Electric Fields as Indicators of Geoeffectiveness of ICME

Abstract: It was shown in the previous chapter that the equatorial ionosphere can be perturbed by various types of prompt electric fields disturbances during a geomagnetic storm. Further, it is well known that the intense geomagnetic storms occur mostly due to the interaction of CME and the terrestrial magnetosphere. A CME in an interplanetary medium is known as ICME and it has three distinctly different parts on many occasions i.e. Magnetic cloud (MC), shock and sheath region. In the MC region, the magnetic field is enhanced and rotates slowly through a large angle whereas the sheath region is bounded by the shock front and the MC region. Plasma in an ICME sheath region is highly compressed and turbulent and other different properties of these structures are already explained in chapter-1 in detail. It is important to mention here that most of the intense geomagnetic storms are mainly driven by the MC region as this region is generally associated with strong and steady southward IMF B_z . In the present chapter, the ICME event on 11 April 2013 is investigated. This ICME event is special as the MC region in this ICME was not geoeffective

and did not drive and geomagnetic storm in contrast to the general scenario. However, the PP electric is found to affect the global ionosphere during the passage of the sheath region of this ICME. Therefore, it is shown in this chapter that the PP electric field perturbations (rather than the changes in the ring current indices or changes in SYM-H) can be considered as an indicator of geoeffectiveness of ICME.

4.1 Introduction

The sheath regions are the cause of strong auroral activity *Huttunen and Koskinen (2004)*. In addition, the CME-driven interplanetary (IP) shock during the sheath region can accelerate particles to energies of hundreds of MeV on many occasions and this acceleration process strongly depends on the geometry of the shock and the structure of the sheath region *Manchester et al. (2005)*. *Huttunen et al. (2006)* showed that the asymmetry in the ring current intensity develops during the passage of sheath and magnetic cloud domains of ICMEs. It was further suggested that the sheath region driven storms cause larger morning/afternoon asymmetry in the ring current than MC driven storms. This asymmetry for MC-driven storm arises mainly due to the ions drifting on open trajectories whereas in case of a sheath driven storm, the sudden intensifications of the substorm associated current systems add significantly to the asymmetry. The turbulent structures present in the sheath region of ICME are very promising candidates to trigger substorms during their passage in the magnetosphere (*Zuo et al., 2007; Despirak et al., 2009, 2011*). It is argued that the sheath-driven storms show stronger auroral activity whereas the cloud driven storms show strong enhancement in ring current (*Huttunen et al., 2002; Pulkkinen et al., 2007*).

During the passage of ICME sheath and MC regions at 1 AU, the Y-component (dawn-dusk) of interplanetary electric field (IEFy) can penetrate

instantaneously from magnetosphere to low latitude ionosphere ([Wei et al., 2011](#)). There exist very few studies on PP electric field over low latitude driven particularly by sheath region of an ICME. The work of [Guo et al. \(2011\)](#) showed that the effects of PP electric field over low latitude in daytime associated with magnetic cloud and sheath regions of ICME. In this case, an oscillatory ionospheric electric field was observed during the passage of a sheath region. It is also to be noted that the passage of sheath region caused the SYM-H to reach ~ -80 nT. In addition, [Wei et al. \(2011\)](#) found multiple electric field penetration over dip equatorial ionosphere during a passage of an ICME sheath in daytime and a strong geomagnetic storm followed due to the passage of MC region that reduce SYM-H to less than -200 nT. In contrast to these studies, the present investigation deals with a special event in which the low latitude PP electric field perturbations were purely due to the passage of an ICME sheath region and the MC was not geoeffective. As a consequence, PP electric field perturbations affected low latitude ionosphere in the absence of a typical geomagnetic storm as SYM-H did not go below -7 nT. Therefore, the geoeffectiveness of an ICME event should not be solely decided based on Dst (or SYM-H) index rather in terms of their ionospheric impact.

4.2 Datasets

In addition to solar wind data, the vertical plasma drift data over Jicamarca and Arecibo are used for this investigation. This event was on a world day when both the ISR radars were operated. The linear regularization technique applied in the Arecibo data introduces smoothing ([Sulzer et al., 2005](#)) of the drifts. Arecibo being a mid-latitude station, the meridional wind velocity measured by a collocated Fabry-Perot interferometer, is also taken into consideration to delineate the plasma drift arising due to electric field alone. The height integrated (256-404 km) perpendicular north velocity is used for Arecibo along with the meridional wind measurements to infer the plasma

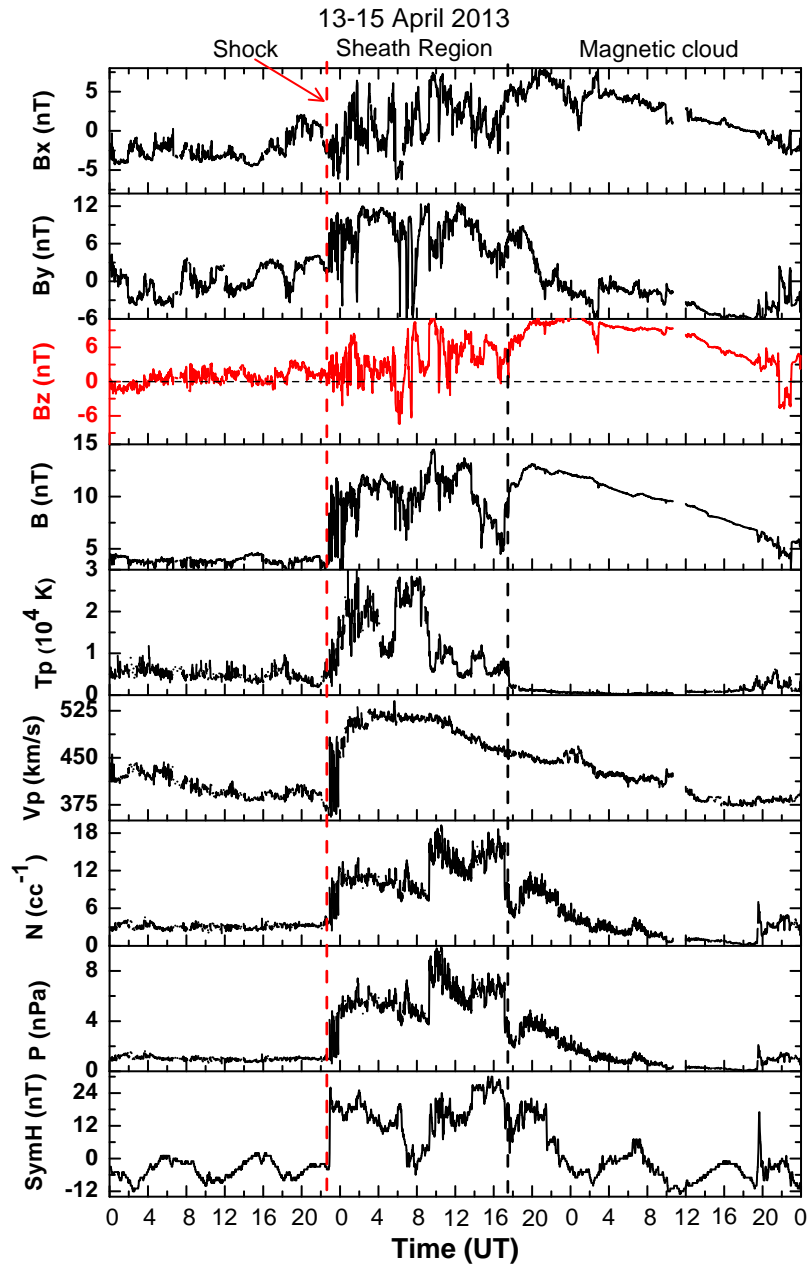


Figure 4.1: Variation in (a) the X-component interplanetary magnetic field (IMF B_x in nT) (b) IMF B_y in nT (c) IMF B_z in nT (d) the total magnetic field intensity ($|B|$ in nT) (e) solar wind proton temperature (T_p in K) (f) solar wind velocity (V in km s^{-1}) (g) solar wind proton density (N_p in cc^{-1}) (h) solar wind dynamic pressure (P , in nPa) and (i) symmetric component of ring current (SYM-H in nT) during 13-15 April 2013 in UT. The arrival time of the CME driven IP shock at 2250 UT on 13 April 2013 is marked by vertical red line. The sheath and magnetic cloud regions are also marked.

drift due to electric fields. The EEJ strength is also taken over Indian sector to infer the electric field perturbations during daytime. In order to identify the onset of substorm, if any, during this event, the energetic electron flux measurements at geosynchronous altitude by LANL and GOES-13 satellites are considered. The magnetometer data from eight individual AE stations are also utilized to further verify the occurrence of pseudo-breakup event. The data from the following magnetometer stations are used: Narssarssuaq (NAQ: 61.2°N, 45.8°W), Fort Churchill (FCC: 58.8°N, 94°W), Yellowknife (YKC: 62.4°N, 114.4°W), College (CMO: 64.9°N, 147.8°W), Barrow (BRW: 71.3°N, 156.8°W), Tixie (TIK: 71.6°N, 129°E), Dixon (DIK: 73.6°N, 80.6°E) and Abisko (ABK: 68.4°N, 18.8°E).

4.3 Results

Figure 4.1 shows the observations of interplanetary parameters at L1 point in GSM coordinate system and geomagnetic SYM-H index during 13-15 April, 2011. The variations of (a) the X-component interplanetary magnetic field (IMF B_x in nT) (b) IMF B_y in nT (c) IMF B_z in nT (d) the total magnetic field intensity ($|B|$ in nT) (e) solar wind proton temperature (T_p in K) (f) solar wind velocity (V_p in kms⁻¹) (g) solar wind proton density (N_p in cc⁻¹) (h) solar wind dynamic pressure (P, in nPa) and (i) symmetric component of ring current (SYM-H in nT) are shown in Figure 4.1 (from top to bottom) during 13-15 April 2013 in UT. The arrival time of the CME driven IP shock is marked by vertical red line at 2250 UT on 13 April 2013. It is followed by a prolonged sheath region which continues for more than 18 hours. When the IP shock arrived at 2250 UT on 13 April 2013, there were changes in solar wind speed from 350 to 540 kms⁻¹, density from 3 to 12 cc⁻¹, and the dynamic pressure from 1 to 6 nPa. The sheath region of ICME is present between the two vertical dashed lines after 2250 UT on 13 April 2013 till 1735 UT on 14 April 2013. The sheath region is followed by a MC region.

It can be clearly noticed that the solar wind magnetic field components were highly fluctuating in the sheath region. In contrast to the sheath region, the signatures of MC region can easily be observed from the decrease in solar wind density, dynamic pressure and the plasma temperature and increase in magnetic field strength (~ 14 nT) and smooth variations in the magnetic fields. Interestingly, observations of SYM-H did not reveal the usual signatures of a typical geomagnetic storm as IMF Bz was predominantly northward inside the MC except during 0545-0800 UT on 14 April 2013.

Figure 4.2 presents the variations in IEFy and its responses during 0545-0800 UT on 14 April 2013 over polar, mid and equatorial latitudes in addition to the meridional wind velocity over Arecibo. Figure 4.2 shows (a) propagation time lag corrected IEFy (in mV/m) (following the methodology adopted in [Chakrabarty et al. \(2015\)](#)) (b) variations in polar cap (PC) index over polar region (c) averaged perpendicular north plasma drift (V_{pn} in ms^{-1}) over Arecibo (black line) along with its seasonal quiet time variations (in blue line) from [Fejer \(1993\)](#) obtained using Fabry-perot interferometry (d) variations of meridional wind velocity (filled black triangles) over Arecibo (d) ISR measured vertical plasma drift over Jicamarca (V_d in ms^{-1}) in black along with quiet time vertical drift (in blue line) from [Scherliess and Fejer \(1999\)](#) (f) EEJ strength (in nT) over India in black on the top of which a quiet day (13 April 2013) EEJ variation in blue during 0000-1200 UT is overlaid. The X-axis (Figure 4.2f) is marked by universal time (UT) and the corresponding local times (LT) of different measurements are mentioned on the top of the X-axis in Figure 4.2c, 4.2e and 4.2f for Arecibo, Jicamarca and Tirunelveli respectively. The grey shaded mark shows the duration of penetration of IEFy during 0545-0800 UT. It is to be noticed from figures 4.2a and 4.2b that the variations in PC index over polar region goes hand in hand with the dawn-dusk component of IEFy during this interval. The PC index can be used as a proxy of the ionospheric electric field in the near-pole region ([Troshichev et al., 2000](#)). In

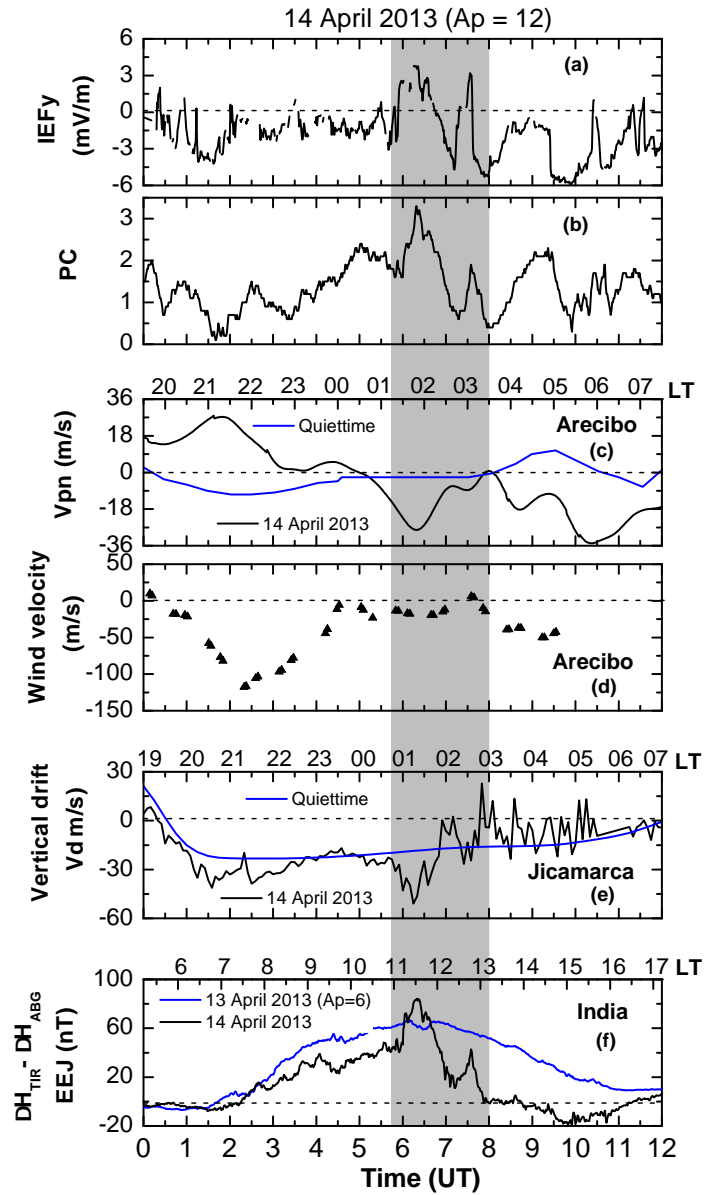


Figure 4.2: Variation in (a) propagation time lag corrected IEFy (in $mV m^{-1}$) (b) polar cap (PC) index (c) averaged perpendicular north plasma drift (V_{pn} in ms^{-1}) over Arcibo along with seasonal quiet time variations (in blue line) from [Fejer \(1993\)](#) (d) variations of meridional wind velocity over Arcibo (d) ISR measured vertical plasma drift over Jicamarca (V_d in ms^{-1}) in black along with quiet time vertical drift (in blue line) from [Scherliess and Fejer \(1999\)](#) (f) Equatorial electrojet strength (EEJ in nT) over India in black which is overlaid with a quiet day (14 April 2013) EEJ variation in blue during 0000-1200 UT. The grey shaded region (0545-0800 UT) marks the interval when PP electric field perturbation are seen over Arcibo/Jicamarca and Indian sector.

order to know the prompt electric field perturbation over geomagnetically mid-latitude region (geographically low-latitude), the ISR measured perpendicular plasma drift over Arecibo has been taken along with meridional wind velocity (Figure 4.2d). It is easily seen from Figure 4.2c that the perpendicular plasma drift is very different from the average quiet time plasma drift (marked with blue line).

The perpendicular plasma drift is more downward during 0545-0800 UT (0115-0330 LT) when the meridional wind velocity remains nearly constant ($\sim -20 \text{ ms}^{-1}$) and equatorward. The plasma drift has attained a minimum value of $\sim -29 \text{ ms}^{-1}$ at 0618 UT despite an equatorward wind suggesting a clear westward electric field perturbation. In the Figure 4.2e, the average quiet time drift over Jicamarca clearly suggests that the electric field is generally westward during nighttime. Thus, the sharp deviation from the nocturnal variations of vertical drift can be taken as the direct contribution from the PP electric field from high latitude to low latitude. A large downward plasma drift is observed during the interval 0545-0800 UT (0045-0300 LT) which is exactly opposite to the dawn-dusk component of IEF. The westward plasma drift changed from -22 ms^{-1} at 0545 UT to -52 ms^{-1} at 0618 UT. The maximum change in drift with respect to quiet time change is -30 ms^{-1} during 0545-0618 UT. It is to be noted that the drift velocity of -30 ms^{-1} corresponds to a westward electric field of 0.75 mV/m over Jicamarca. The EEJ strength (in Figure 4.2f) also shows a very good correlation with IEF_y. This is quite different from the quiet day variations on 13 April 2013 ($A_p = 6$). Further, it is to be noted that the EEJ strength sharply changed from 42 nT at 0545 to 84 nT at 0618 UT. So the change in EEJ strength is 42 nT during this time. It is very interesting to note that the variations in the PC index and EEJ closely resemble with each other. In addition, the variations in EEJ and vertical drifts over Jicamarca/Arecibo are out of phase with each other.

In order to bring out the periodic components in IEF_y, EEJ and vertical

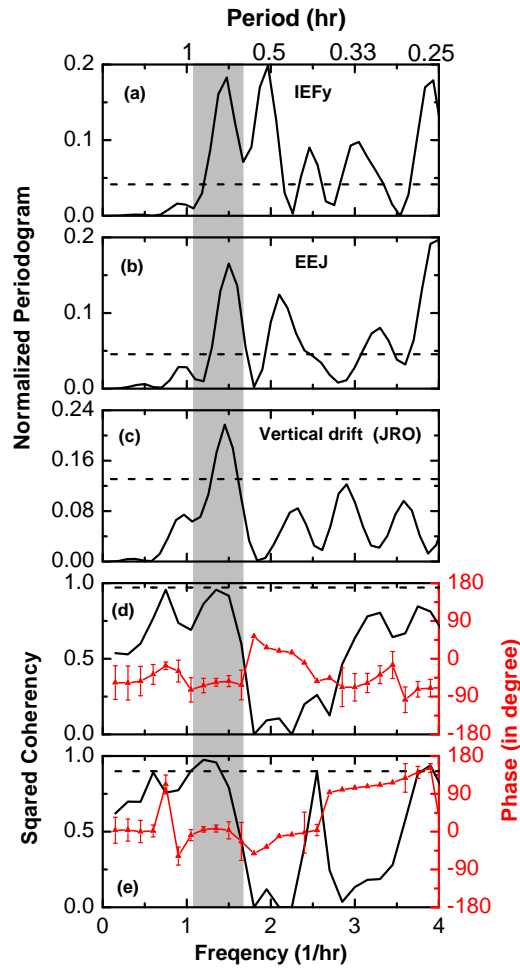


Figure 4.3: Harmonic analyses of (a) IEFy, (b) EEJ, and (c) vertical drift during the interval 0545-0800 UT. The dashed horizontal lines in Figure 4.3(a-c) are marked at 95% significance level determined by Siegel's test. The squared coherency (black) and phase spectra (red) between IEFy and EEJ strength, and IEFy and vertical drift are depicted in Figure 4.3d and 4.3e respectively. The horizontal dashed line in Figure 4.3d and 4.3e are marked at 90% false alarm level. 40 min periodicity in IEFy can be seen to affect EEJ over India and vertical drift over Jicamarca as coherency high and phase spectra is stable at this periodicity.

plasma drift during the passage of a sheath region, harmonic analyses are performed by using the standard algorithm (*Schulz and Stattegger, 1997*). Figure 4.3 depicts the periodic components of (a) IEFy, (b) EEJ, and (c) vertical drift during the interval 0545-0800 UT. The dashed horizontal lines in Figure

4.3(a-c) are marked at 95% of significance level by determined by Siegel's test. Periodicity of 40 min (marked by grey shaded box) is found to be significant and present in all the parameters. Further, to know the causal relationship between two time series at this given frequency, cross coherency analyses are performed. The squared coherency and phase spectra between IEFy and EEJ strength as well as IEFy and vertical drift are depicted in Figure 4.3d and 4.3e respectively. The horizontal dashed line in Figure 4.3d and 4.3e are marked at 90% false alarm level. It is found that the 40 min periodicities in EEJ and vertical drift are highly coherent with 40 min periodicity in IEFy and the phase is also stable around this period. This proves that the 40 min periodic component in EEJ and vertical drift is due to corresponding variations in IEFy during the passage of the ICME sheath region.

In order to delineate the possible effects due to other sources substorm/pseudo-breakup and its impact on equatorial ionosphere during the passage of the ICME sheath region, LANL data sets are looked into. Figure 4.4 shows the variations of electron injections (counts s^{-1}) measured at geosynchronous orbit by (a) LANL-01A, (b) LANL-08A (c) GOES satellites, along with (d) the eastward (AU index) and westward (AL index) auroral electrojet index, (e) PC index, and (f) EEJ strength during 0000-1200 UT (0512-1712 LT) on 14 April 2014. The energy channels of LANL and GOES-13 satellites are mentioned in the right side of the corresponding figures. The LANL-01A and LANL-08A were at the longitudes $146^{\circ}W$ and $165^{\circ}W$ respectively. It can be observed that the two satellites (LANL-01A and GOES-13) showed nearly dispersionless electron injection at 0810 UT (red dashed vertical line) although the LANL-08A measurements and auroral electrojet strengths did not show any significant change at this time. It must be noted that the two LANL satellites (LANL-01A and 08A) were just separated only by 19° in longitude. However, only one of the satellites (LANL-01A) captured the dispersionless like injections at 0810 UT. Further, the higher energy channels (e.g. 220-341 keV and 341-490

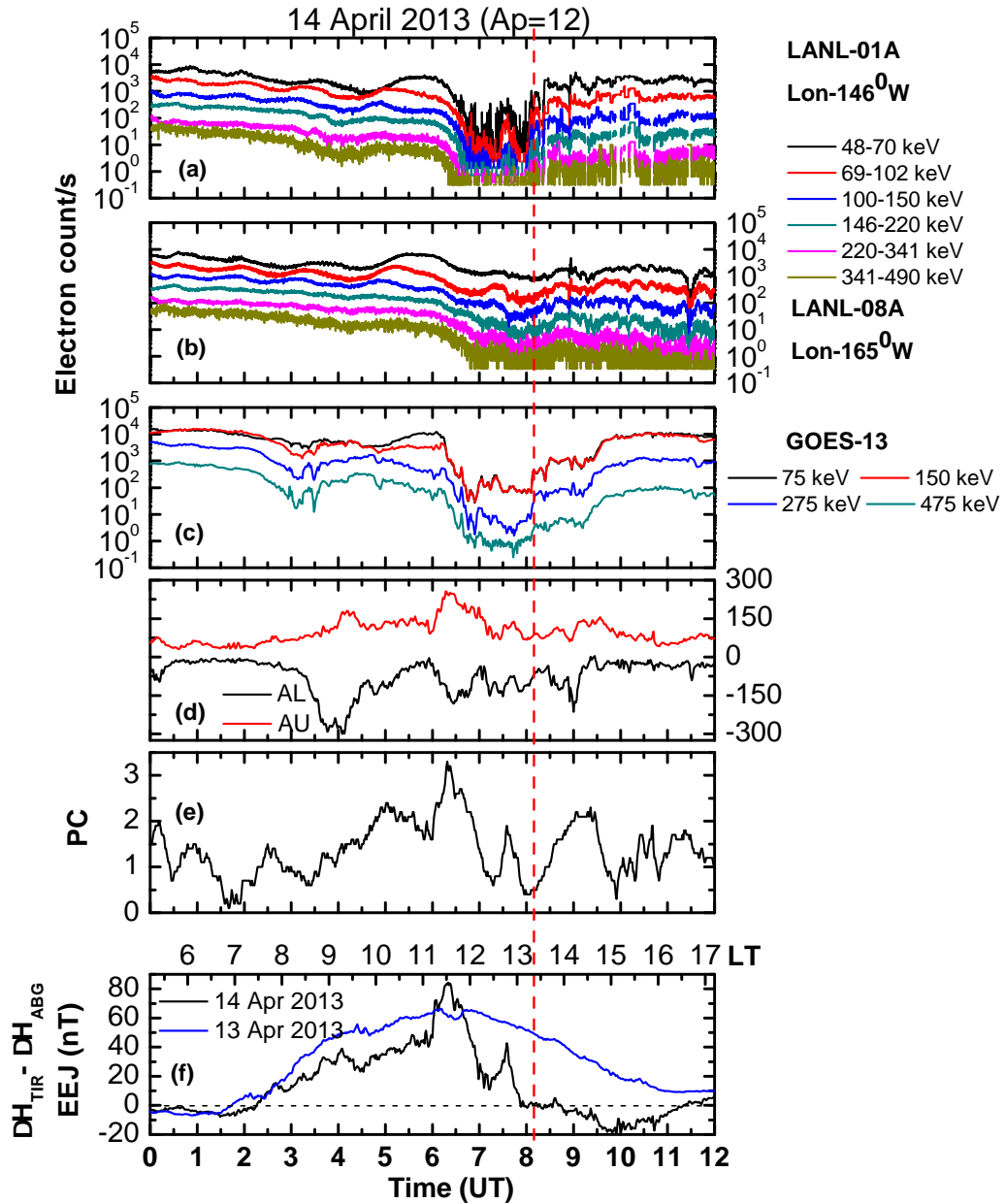


Figure 4.4: Electron injection data measured at geosynchronous orbit by (a) LANL-01A, (b) LANL-08A (c) GOES satellites, (d) the eastward (AU index) and westward (AL index) auroral electrojet strength, (e) PC index, and (f) EEJ strength during 00:00-12:00 UT (05:12-17:12 LT) on 14 April 2014. The energy channels of LANL and GOES satellites are mentioned in the right side of the corresponding figures. The red dashed vertical line indicates the onset of a pseudo-breakup event (see text) at 0810 UT.

keV of LANL-01A) do not seem to get affected much as the to lower energy channels. These observations along with absence of any significant variation in AL suggest that the particle injection is highly localised in longitude. The PC index also shows an enhancement at 08:10 UT. Interestingly, the counter electrojet (CEJ) (Figure 4.4g) started at 08:10 UT, just after the dispersion-less injection as seen in LANL-01A and GOES-13. Though the strength of CEJ was not very strong, the reduction in electrojet strength as compared to quiet day (13 April 2013) was conspicuous. The EEJ reached to a minimum value of -20 nT at ~ 1000 UT (1530 LT). Therefore, electron injection event seems to have caused a westward electric field perturbation during daytime which reduced the electrojet strength. This is similar to what was suggested by *Kikuchi et al. (2003)* during substorms. The plasma drifts over Jicamarca and Arecibo are found to be upward although the values are not significantly large after onset of the pseudo-breakup.

4.4 Discussion

A CME that erupted from the active region NOAA11719 on 11 April 2013 passed by Earth during 13-14 April 2013 (*Vemareddy and Mishra, 2015*). The present investigation brings out various aspects of ionospheric and magnetospheric effects during the passage of this sheath region. It is known that a geomagnetic storm can be induced by a sheath and MC (the leading and trailing part) region (*Wu and Lepping, 2002*). However, in this case, neither the sheath region nor the MC was able to cause significant depression in SYM-H so as to be attributed as a typical geomagnetic storm. It was further shown that the perpendicular shocks are more geoeffective than a parallel shock as the perpendicular shock front can compress the IMF more than the parallel one (*Kataoka et al., 2005; Yue and Zong, 2011*). In this case, the shock normal angle is found to be 60.50 (*Oliveira and Raeder, 2015*) i.e. the shock is more quasi-perpendicular. Though the IP shock is more perpendicular, the

absence of predominantly southward IMF Bz, led to a condition wherein, the ring current intensity did not increase in strength. The IMF Bz is predominantly northward during this event except for a small duration 0545-0645 UT on 14 April 2013. The enhancement in SYM-H at $\sim 22:50$ UT on 13 April 2013 is caused by an over-compression by quasi-perpendicular shock during the passage of ICME. It is to be noted that the energy transfer from solar wind to magnetosphere depends on the rate and duration of magnetic reconnection process between the Earth and interplanetary magnetic field (IMF Bz or the dawn-dusk component of IEFy) (*Dungey, 1961*). Therefore, not only a perpendicular shock, but also a southward IMF Bz inside the ICME is required to increase the ring current strength (*Yue and Zong, 2011*). As the sheath region is highly turbulent, the solar wind parameters fluctuate very fast. The fluctuating solar wind plasma and IMF can trigger geomagnetic substorms during the passage of sheath region of an ICME and hence can drive high-level auroral activity (e.g *Tsurutani and Gonzalez, 1987*; *Huttunen and Koskinen, 2004*). It was also suggested that a strong cross-tail and partial ring current develop in a sheath-driven storm due to substorm occurrence (*Pulkkinen et al., 2006*) and the partial ring current enhances the asymmetry in SYM-H. Due to strong stretching and fluctuating magnetic field in magnetotail region of a sheath region, the particle density decreases at geosynchronous orbit. This helps the energetic particles to drift very fast and the ions to follow an open drift paths at the magnetopause region. As a result, a relatively less number of ions get trapped which makes ring current more asymmetric and sheath storm do not grow beyond a limit (*Pulkkinen et al., 2007*). In addition to the sheath region of ICME, the MC region is also dominated by northward IMF Bz in the present case. Therefore, the ICME sheath region or the MC did not cause any geomagnetic storm and make SYM-H to restrict at -7nT . However, the global ionospheric electric field is found to be affected corresponding to the north-south oscillations of IMF Bz during 0545-0800 UT in the sheath region.

The present investigation shows a strong evidence of PP electric field from high to low latitude ionosphere both in day and night sectors during the passage of ICME sheath. In this case, the PP electric field is mainly associated to DP2 type periodic perturbation over the dip equator which is driven by an ICME sheath. The periodic perturbations of 40 min in IEFy are causally connected to EEJ and drift over low latitude (see Figure 4.3). During the DP2 type events, the magnetometers show a coherent and similar magnetic variations from high to low latitudes as the interplanetary electric field penetrates from high to low latitude nearly simultaneously (*Nishida, 1968; Yizengaw et al., 2016*). It is to be noted that the ionospheric electric field was found to oscillate east and westward corresponding to north and southward fluctuations in IMF Bz and the time scale of quasi-periodic fluctuations can range from half an hour to several hours (*Kikuchi et al., 2000; Chakrabarty et al., 2005*). A wide range of periodicities of 30-40 min (*Kikuchi et al., 1996*), 25-35 min (*Sastri et al., 2000*) and 40 min (*Chakrabarty et al., 2008, 2015*) have been reported by earlier investigations by various measurements. Further, a recent investigation of *Rout et al. (2017)* revealed that periodicities of 30 and 60 min in IMF Bz are found to affect the equatorial ionosphere during the corotating interaction region (CIR) driven storms. It is also shown that CIR events are geoeffective if the azimuthal flow angle does not exceed $\pm 6^\circ$. However, the penetration of 40 min periodic fluctuations in IEFy associated with sheath region of an ICME is brought out for the first time by the present investigation. In addition, it is also to be noticed that the polarity of PP electric field is westward (eastward) during night sector (day sector) when IMF Bz turns to southward during 0545-0800 UT.

Identical variations between PC index and EEJ strength (see the shaded interval in Figure 4.2b and 4.2f) during 0545-0800 UT on 14 April 2013, unambiguously suggest that the effects of PP electric fields at polar and equator are nearly simultaneous. It has been shown that the PC index (*Troshichev and*

Andrezen, 1985) and IEFy are well correlated and it can effectively be used as ionospheric polar electric field during geomagnetic disturbed time (*Nagatsuma et al., 2000; Troshichev et al., 2000*). The large change in EEJ strength (from ~ 40 nT to ~ 84 nT) at 0545 UT is caused by a strong eastward electric field perturbation in day sector. During this event (0545-0800 UT on 14 April 2013), Arecibo and Jicamarca stations were located in night sector whereas India was in day sector. The plasma-dynamics over Arecibo is more complex than Jicamarca and India as the plasma drift can be influenced by meridional wind at Arecibo due to finite dip angle (45°). Although the very small temporal scale fluctuations are absent in vertical drift over Arecibo due to reduced data cadence (smoothing), the downward drift due to westward electric field perturbation during 0545-0800 UT associated with the sheath region of ICME is very clear (see Figure 4.2c). It is to be noted that the meridional wind velocity over Arecibo was in equatorial direction although the magnitude was relatively less (~ 20 ms $^{-1}$). The equatorial wind would have moved the plasma upward, but the downward plasma drift at this time strongly indicates the clear influence of a westward electric field. In the present investigation, the polarities of PP electric field during day and night time are in agreement with earlier works by *Nopper and Carovillano (1978)* and *Fejer et al. (2008)*. The westward polarity of PP electric field has also been observed by earlier studies at this local time over Arecibo (*Buonsanto et al., 1999; Erickson et al., 2010*) and these events were mainly associated with strong geomagnetic storms. Opposite polarities of PP electric field over Indian and Jicamarca sectors are also in accordance with the earlier results (*Kelley et al., 2007*).

The sheath regions are highly turbulent due to plasma instabilities and can trigger substorms on many occasions (*Akasofu and Chao, 1980; Pulkkinen et al., 2007*). However, the observations suggest that the electron injection event in this case is not associated with a substorm but with a pseudo-breakup event. It must be noticed that the LANL-08A which is very close to LANL-

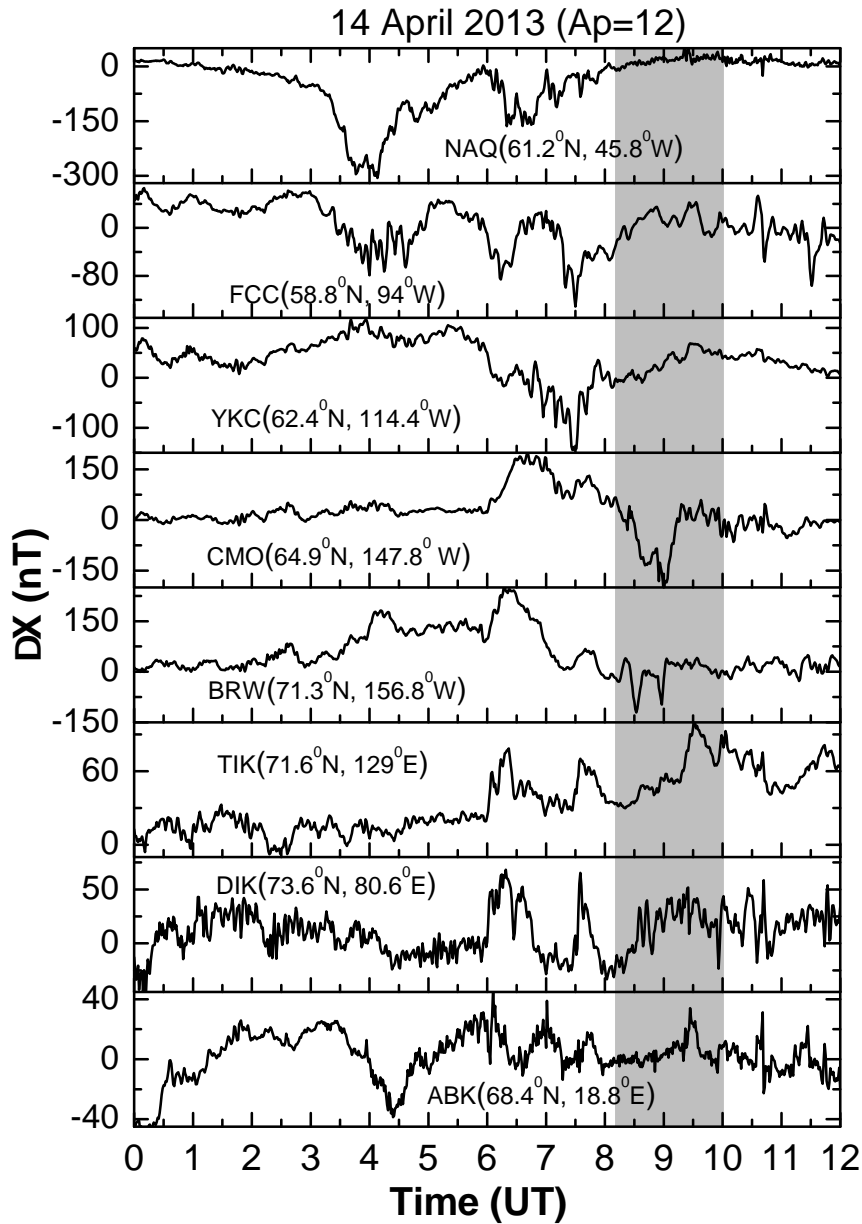


Figure 4.5: The ΔX variations of available eight individual auroral electrojet stations are shown during 0000-1200 UT on 14 April 2013. The geographic latitudes and longitudes are mentioned in the figure. The vertical grey shaded region (0810-1000 UT) shows the interval after the onset of the pseudo-breakup event at 0810 UT. The variations of ΔX particularly over CMO and partly over BRW are different during the shaded interval suggesting a pseudo-breakup event confined to these longitudes.

01A does not show any dispersionless injection like signatures. The particle injection at LANL-01A satellite is quite different from substorm time injection (*Reeves et al., 2003; Hui et al., 2017*) and not a very clear “dispersionless” injection. This has a much extended growth phase which continues for ~ 1.5 hrs. The satellite, LANL-08A seems to be outside the injection region whereas both the LANL satellites are just spatially separated by 19° in longitude. At the same time, it can be easily seen from Figure 4.4 that both the AL and/or AU indices do not show significant change during the particle injections measured by LANL and GOES satellites. *Janzhura et al. (2007)* suggested that a substorm seems to have occurred if the intensity of AL index exceeds 400 nT. On the other hand, pseudo-breakups are short-lived and highly localized substorm-like disturbances (*Pulkkinen et al., 1998*). *Nakamura et al. (1994)* did a comparison between major substorm onset and pseudo-breakup events and suggested that no significant westward electrojet activity was detected for pseudo-breakup cases in contrast to those in substorm and also observed “dispersionless” like particle injection at geosynchronous orbit associated with pseudo-breakup events. Further, the particle injections occur in relatively lower energies in case of pseudo-breakup events. This can be clearly observed from the Figures 4.4(a) and 4.4 (c) reveal no significant changes in higher energy channels at this time. The larger rate of change of magnetic field during major substorm onset in magnetotail region accelerates the high energy particles more towards Earth. Therefore, the higher energy particles are injected during substorm onset and this is relatively less in case of pseudo-breakup events. From these observations, it appears that the present event is a pseudo-breakup event. In order to further verify this, Figure 4.5 is presented. The ΔX components of magnetic field variations of available eight individual auroral electrojet stations are shown during 0000-1200 UT on 14 April 2013. The geographic latitudes and longitudes are denoted inside the subplots. It can be noticed that the ΔX variations during 0810-1000 UT over CMO and BRW are quite different from other stations. These two stations are just 9° longitu-

dinally apart from each other and are nearly at the same longitude where the LANL-01A satellite made observations. This indicates that the electron injection has taken place in a narrow and localized longitude region. In addition to this fact, the minimum values of magnetic field variations are -200 nT and -140 nT over CMO and BRW, respectively. These observations confirm that the present event is indeed a pseudo-breakup event. Further, this pseudo-breakup event has also been captured by PC index though the magnitude of increase in PC index is not very large. The PC index is not only used as a proxy for the polar ionospheric electric field but also can be used to measure the magnetospheric substorm activity (*Troshichev and Sormakov, 2015; Huang et al., 2005*). As this event is associated with a pseudo-breakup onset, the magnitude of PC index might be less. The CEJ event which is mainly driven by a westward electric field seems to have been caused by the pseudo-breakup event (see Figure 4.4g). Study related to the impact of pseudo-breakup events on low latitude ionospheric electrodynamics is very sparse. In one such case, the pseudo-breakup related westward electric field perturbation was first reported by *Chakrabarty et al. (2015)* over dip equatorial ionosphere using nighttime 630.0 nm airglow and digisonde measurements. It is generally suggested that the substorm-related equatorial CEJ is caused by the enhancement of region-2 field aligned current (R2FAC) during substorm (*Kikuchi et al., 2003*). The equatorial CEJ occurred in the recovery phase of the substorm, when the polar cap potential decreased due to the northward turning of the IMF Bz. It has also been argued by *Hashimoto et al. (2011)* that direction of electric field and currents are reversed compared to the normal DP2 currents at subauroral to equatorial latitudes during the expansion phase of substorm when the convection electric field reduces abruptly. This reversed current appears as a CEJ at the dayside dip equator and also causes a negative bay in the afternoon sector over equatorial ionosphere. The R2FAC connects to Pedersen current over high latitude and drives the CEJ. It is important to mention here that in the present study, although it is a pseudo-breakup event and not a full-grown

event, it could drive an equatorial CEJ. To the best of this author's knowledge, this is the first evidence of a CEJ caused by a pseudo-breakup event.

4.5 Summary

Based on the observations using multiple techniques, it is shown that the global ionosphere has been affected by the PP electric field perturbations associated with the passage of sheath region of ICME. The present investigation brings out the following salient points:

1. The sheath region of ICME during this event passes 1 AU for a long duration (~ 18 hr) which is followed by an MC. Neither the sheath nor the MC region is able to cause the geomagnetic storm in near-Earth space environment as the minimum depressions in SYM-H is restricted to -7 nT.
2. The DP2 type quasiperiodic fluctuations of 40 min in the vertical drift are observed over Jicamarca and EEJ over Indian sector. It is shown for the first time that the DP2 type electric field perturbation over equatorial ionosphere is driven by a sheath region of ICME.
3. The polarity of PP electric field, associated to sheath region of ICME is found to be westward over Jicamarca/Arecibo (night sector) and eastward over Indian sector (daytime) during 0545-0800 UT. The polarity of PP electric field corresponding to the local time observations are in agreement with the earlier works by *Nopper and Carovillano (1978)* and *Fejer et al. (2008)*.
4. A pseudo-breakup event is identified based on magnetometer and geosynchronous particle measurements during the passage of the ICME sheath. Further, for the first time a CEJ event is shown to be driven by a pseudo-breakup event.

Chapter 5

Prompt Penetration Electric Field and Geoeffectiveness of CIR Events

Abstract: It is known from the previous chapter that the low latitude electric field can be significantly influenced by ICME-driven storms where the IMF B_z is found to be steadily southward. It is also explained in chapter-1 that the steady southward IMF B_z condition supports strong magnetospheric and ionospheric plasma convections. In contrast to ICME driven storms, IMF B_z is found to be highly fluctuating during CIR driven storms that result in weak plasma convections. Thus, CIR driven storms, on most occasions, are weaker than ICME driven storms in terms of growth of ring current. Nevertheless, during low solar activity period, CIRs play a significant role in geomagnetic disturbances. Therefore, it is important to understand the factors that can influence the geoeffectiveness of CIR events. In this chapter, it is shown that the PP electric field perturbations have a connection with the azimuthal solar wind flow angle at the first Lagrangian point of the Sun-Earth system (L1 point) during the passage of CIR and this can be used to evaluate the geoeffectiveness of CIR driven storms.

5.1 Introduction

In the solar corona where the plasma beta ($\beta = \frac{2nkT}{B^2/2\mu_0}$) is low, coronal mass flows upward along open magnetic field to become the solar wind. As β increases this solar wind drags the magnetic field out into the well-known Parker spiral. It is well known that the fast solar wind (600–800 km s⁻¹) originates in high latitude coronal holes while the slow speed solar wind (300–400 km s⁻¹) is confined to the low latitude equatorial belt (*McComas et al., 2000*). The fast solar wind interacts with the slow stream solar wind near the ecliptic plane in the interplanetary medium (IPM) creating an interaction region generally known as a “Corotating Interaction Region” or CIR (*Tsurutani et al., 2006; Denton et al., 2006*). In a CIR, the stream interface is conventionally identified by increase in solar wind velocity and proton temperature, a sharp drop in proton density as well as shear in solar wind flow that can make the flow angle non-radial (*Forsyth and Marsch, 1999; Tsurutani et al., 1995*). The interaction regions are long-lived, have intense magnetic field and co-rotate with the Sun and is bounded by forward and reverse shock regions. It has been suggested by *Pizzo (1989)* that for a co-rotating solar wind structure, the interface acts like a wall or an obstacle thereby deflecting the impinging solar wind and making it non-radial. However, the deviation from the radial nature of the solar wind is in general not very significant, with azimuthal velocities being usually between 30–50 km s⁻¹ and non-radial flow angles rarely exceeding 10° (*Owens and Cargill, 2004*). Some extreme cases of long lasting non-radial solar wind outflows have however, been reported when azimuthal flow velocities exceeded 100 km s⁻¹ (*Janardhan et al., 2005, 2008*). Such events are small in number, and may not be a conventional CIR in terms of their generation mechanism (*Usmanov et al., 2005*). In present work, no attempt is made to address this aspect. The characteristic changes in solar wind parameters, as discussed above, are used to only identify the CIR or CIR-like events.

It is also known that the Alfvénic waves associated with the high-speed streams (*Burns et al., 2012*) cause fast fluctuations in the IMF Bz. In a CIR, such Alfvénic fluctuations can affect the equatorial ionosphere nearly instantaneously if the rate of change of the IMF Bz fluctuations (or in other words, fluctuations in IEFy) is faster than the shielding time constant (e.g. *Senior and Blanc, 1984*) at the inner edge of the ring current region. The electric field perturbations that arise from the fast fluctuations in IEFy are generically known as prompt penetration (PP) electric field (e.g. *Kelley et al., 2003*). As the solar wind speed remains relatively steady compared to the fast fluctuations in IMF Bz, the fluctuations in IEFy or convection electric field can be attributed to the fluctuations in IMF Bz.

A comprehensive knowledge about the PP electric field periodicities during CIR events can be used to gauge their geoeffectiveness. Though the impacts of the CIR events on ionosphere and thermosphere, with periodicities of the order of solar rotational period (27 day) and its sub-harmonics (e.g. 27 day 13.5, 9 days etc.) have been reported (e.g. *Lei et al., 2008; Crowley et al., 2008; Pedatella et al., 2010; Pallamraju et al., 2010; Qian et al., 2010; Liu et al., 2010; Deng et al., 2011; Tulasi Ram et al., 2010*), signatures of the same periodic components have not been found in EEJ (*Tulasi Ram et al., 2012*). Despite a few investigations (*Yeeram, 2017*) that showed the effects of PP on equatorial ionosphere in general, there has been no investigation that brought out specifically the effects of the short period (≤ 2.0 hrs) fluctuations in IMF Bz on the equatorial ionosphere. It is to be noted here that the fast fluctuations in IMF Bz are generically associated with PP events. Further, the existing results mentioned earlier have revealed inconsistent (observed sometimes and not observed on other occasions) impact of CIR events on the equatorial ionosphere. Given this context, the present investigation is important on two counts: First, the investigation explores the effects of PP electric field during CIR-driven storms on equatorial ionosphere (particularly in terms of periodic perturbations ≤ 2.0

hrs that were not addressed earlier) and second, the possible reason(s) for the apparently inconsistent impact of the CIR events is(are) also searched.

5.2 Data Analysis and Result

A total of 43 minor geomagnetic storm events during 2006-2010, the deep solar minimum of solar cycle 23, are selected for the present investigation. For these events, the stream interface (SI) is identified using the methodology described in *Forsyth and Marsch (1999)*.

A typical example is shown in Figure 5.1 which depicts the signatures that exist during the CIR events. It reveals the solar wind conditions at 1 AU as measured by the ACE satellite and also magnetospheric and auroral ionospheric responses of an event during 6-8 August 2006. The solar wind parameters have been corrected for propagation lag till the bow shock nose. The event started on 7 August, 2006 ($A_p = 32$) at 0500 UT. The stream interface is marked by the vertical dotted line at ~ 0510 UT. The characteristic increase in V and T_p , drop in N_p and the change in Φ downstream of the stream interface region can be clearly seen in a CIR where the discontinuity starts. The left panels (from top to bottom) of Figure 5.1 show the variations of solar wind flow speed (V in km s^{-1}), proton density (N_p in cc^{-1}), proton temperature (T_p in k) and flow direction (Φ in degree) respectively. The azimuthal flow angle, Φ is defined as $\Phi = \tan^{-1} \left(\frac{V_y}{V_x} \right)$ in degrees. The right panels (from top to bottom) of Figure 5.1 show the variations in IMF B_z in nT , strength of total magnetic field ($|B|$ in nT), magnitude of the ring current intensity (SYM-H in nT) and auroral electrojet strength (AE in nT), respectively and the X-axes show the time in UT during 6-8 August 2006. It is noticed that there is a sharp rise in solar wind flow speed, proton temperature, strength of magnetic field, solar wind flow angle and a sharp drop in proton density at ~ 0500 UT on 7 August 2006. The slow speed ($\sim 350 \text{ km s}^{-1}$) solar wind gradually started

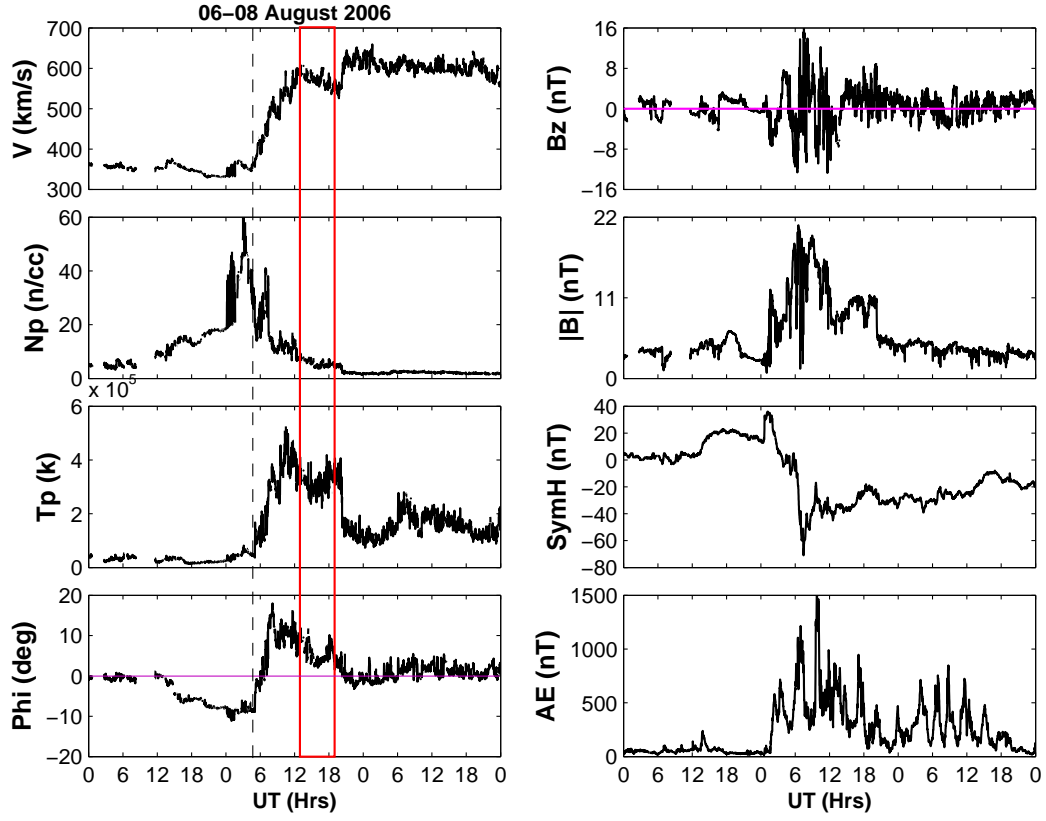


Figure 5.1: The left panels (from top to bottom) show the variations of solar wind flow speed (V in km s^{-1}), proton density (N_p in cc^{-1}), proton temperature (T_p in K) and flow direction ($\Phi = \tan^{-1}(\frac{V_y}{V_x})$ in degree) respectively. The right panels (from top to bottom) show the variations in IMF B_z in nT, strength of total magnetic field ($|B|$ in nT), SYM-H in nT and AE in nT respectively and the X-axes show time in UT from 6-8 August 2006. The stream interface is marked by the vertical dotted line at ~ 0510 UT. The red rectangular box is marked during 1300-1900 UT for a typical event when the EEJ data have been analyzed (explained in section 5.4)

to increase to a relatively high speed from 0500 UT and attained a maximum value of $\sim 660 \text{ km s}^{-1}$ at 2300 UT. The proton density falls from 60 cc^{-1} to 17 cc^{-1} , proton temperature raises up to $5 \times 10^5 \text{ k}$, flow angle changes from -10° to $+15^\circ$ and the magnitude of IMF increases to $\sim 22 \text{ nT}$ due to the interaction/collision between two streams. The above signatures in solar wind are the typical properties of “stream interface” in a CIR. At 0030 UT on 7 August, a sharp increase in plasma density and velocity cause increase in ram

pressure and this, in turn, causes positive increase in SYM-H during this time. It is then followed by the main phase which continued for ~ 6 Hours. The IMF Bz shows an oscillating behavior varying from 15 nT to -15 nT in north-south direction during 0002-2000 UT. SYM-H decreased from 36 nT to -70 nT at ~ 0730 UT on 7 August 2006. It can also be noticed from the SYM-H variation that the value is not less than -100 nT and does not decrease sharply like in CME-driven storm. It is a weak geomagnetic storm. The values of AE index are mostly more than 400 nT and the peak AE value is 1500 nT for this event. It is important to note here that these similar kinds of signatures are noticed in all 43 cases of CIR-driven geomagnetic storm. It is seen that in a CIR, the “stream interface” is the boundary of sharp discontinuities.

In order to extract the average trends of the solar wind parameters, a superposed epoch analysis was performed with the zero epoch corresponding to the time when the near-earth space is hit by the stream interface. Figure 5.2 (a-d) shows superposed epoch plots for V, T_p , N_p and Φ for the 43 events and reveals the important characteristics of the stream interface typically associated with CIR events. The dashed line and the green envelope show respectively, the zero epoch time and the standard deviation from the mean values. It can be seen from Figure 5.2 that the important characteristics and the magnetospheric signatures of SI at L1 point in CIR are (i) increase in flow speed, (ii) a sharp rise in proton temperature, (iii) a sharp reduction in proton density, and (iv) a sharp discontinuity in flow angle. The change (or change in slope) in flow speed is more gradual than other parameters. The gradual change in flow speed may be due to the proximity of the measurement point closer to the shocked region. It is known that the shock accelerates particles along the magnetic field lines. Therefore, it may be possible that if the spacecraft is closer to the CIR related shock region, the changes in velocity may be more gradual compared to the changes in other parameters that will change more sharply.

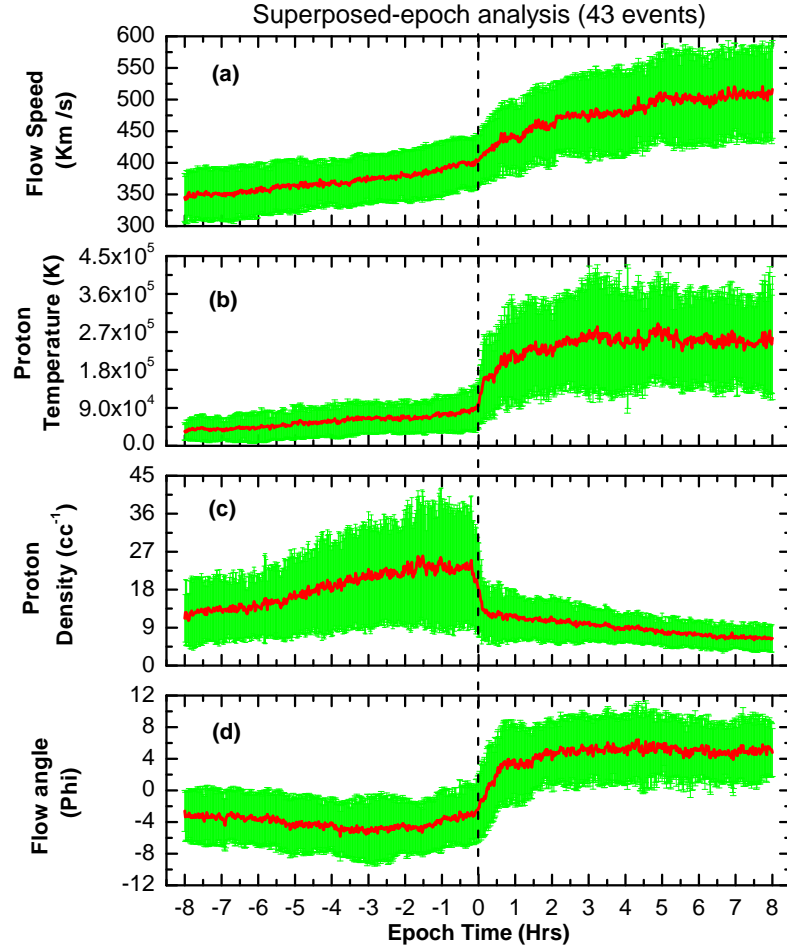


Figure 5.2: Superposed epoch analyses for (a) V , (b) T_p , (c) N_p and (d) Φ for all the 43 events are shown. The dashed line represents zero epoch time. The green envelop represents the standard deviations from the mean values.

5.3 Causal connection between IMF Bz and EEJ strength during CIR events

The EEJ strength over the Jicamarca sector, given by $\Delta H_{JIC} - \Delta H_{PIU}$, is based on the difference between the horizontal component of geomagnetic field over Jicamarca (JIC:12°S, 76.8°W, 6.8° dip) and an off-equatorial station Piura (PIU: 5.2°S, 80.6°W, 0.8° dip). For Jicamarca, the local time (LT) = Universal time (UT) - 5 hrs. The EEJ strength over Jicamarca was shown

to follow the vertical drift variations obtained from JULIA radar (*Alken and Maus, 2010*). EEJ data with 1 minute resolution during 1300-2100 UT (0800-1600 LT) were considered. As the EEJ data are available only during daytime, the investigation was restricted to 22 out of 43 events considered.

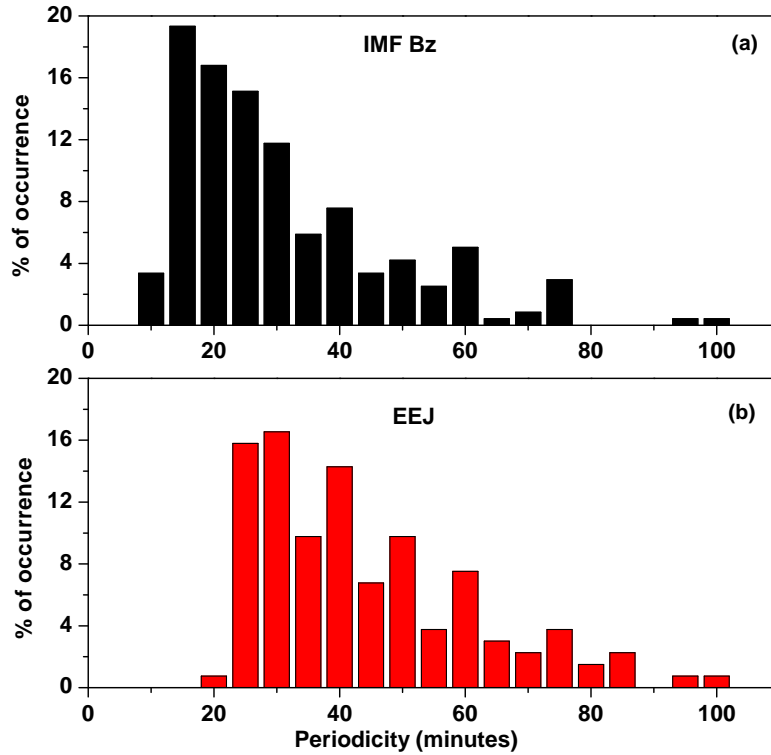


Figure 5.3: Histograms of periodicities of (a) IMF Bz and (b) EEJ.

The fast (≤ 2.0 hrs) fluctuations (residuals) in EEJ and IMF Bz during these events were extracted (by detrending) using Savitzky-Golay (SG) smoothing algorithm (*Savitzky and Golay, 1964*). In order to know the dominant periodicities present in IMF Bz and EEJ, a detailed spectral analysis was carried out by using the standard Lomb-Scargle method (*Schulz and Stattegger, 1997*). Only periodicities exceeding the 95% confidence limit were considered. Histograms with 5 minutes' bin size based on the periodicities obtained from IMF Bz and EEJ residual time series data for 22 events are shown in Figure 5.3(a) and (b) respectively. It is to be noted here that the lower cut off periodicity in this case is chosen to be 10 min as it is known that Alfvénic waves

in CIR with periods more than 8 minutes (e.g. *Korth et al., 2011*) can efficiently affect ionosphere. In addition, the Brunt-Vaisaala period at E-region height is ~ 5 min. As the EEJ data are available mostly for 6-8 Hours and one requires at least two cycles to unambiguously infer the maximum periodicity in a data set, periodicities ≤ 3.0 hrs can safely be addressed. It is noticed that periodicities of 20-100 min and 10-100 min are present in IMF Bz and EEJ strength respectively. It is clear from the histograms that the two most dominant periodic components in EEJ are 25 and 30 min, whereas in case of IMF Bz, the dominant periodic components are 15 and 20 min during the CIR events. In fact, some other common significant periodicities (30, 40, 50 and 60 min) are also present in both the parameters. It is also interesting to note that both the EEJ and IMF Bz periodic distributions are positively skewed.

As mere presence of common periodic components does not establish the causal relationship between IMF Bz and EEJ, cross spectral analyses with coherency and phase spectra calculations were carried out using the standard algorithm of *Schulz and Stattegger (1997)*. In Figure 5.4(a), the top left panel shows the temporal variations of EEJ (red) and IMF Bz (black) during 1300-1900 UT on 4 July 2006 ($A_p=12$). The middle two rows show the corresponding Lomb-Scargle normalized periodograms for EEJ and IMF Bz where the blue dashed horizontal line is marked at 95% confidence limit and the last row represents the squared coherency (red) with the phase spectra (black) for the two-time series. The false alarm level is marked at 80% and is shown by a red dashed line. Figures 5.4(b) and 5.4(c) show similar results for the other two events for i.e. 1 February 2008 ($A_p=18$) and 13 March 2009 ($A_p=17$) during 1300-2100 UT. The rectangular box is marked to show the common periodic components wherein the time series of EEJ and IMF Bz show significant coherency with stable phase relationship (essential to infer causal relationship). The periodicity of 60 min is found to be causally connected on 4 July 2006. Similarly, the periodicities of 70 min and 60 min in EEJ are found to be causally

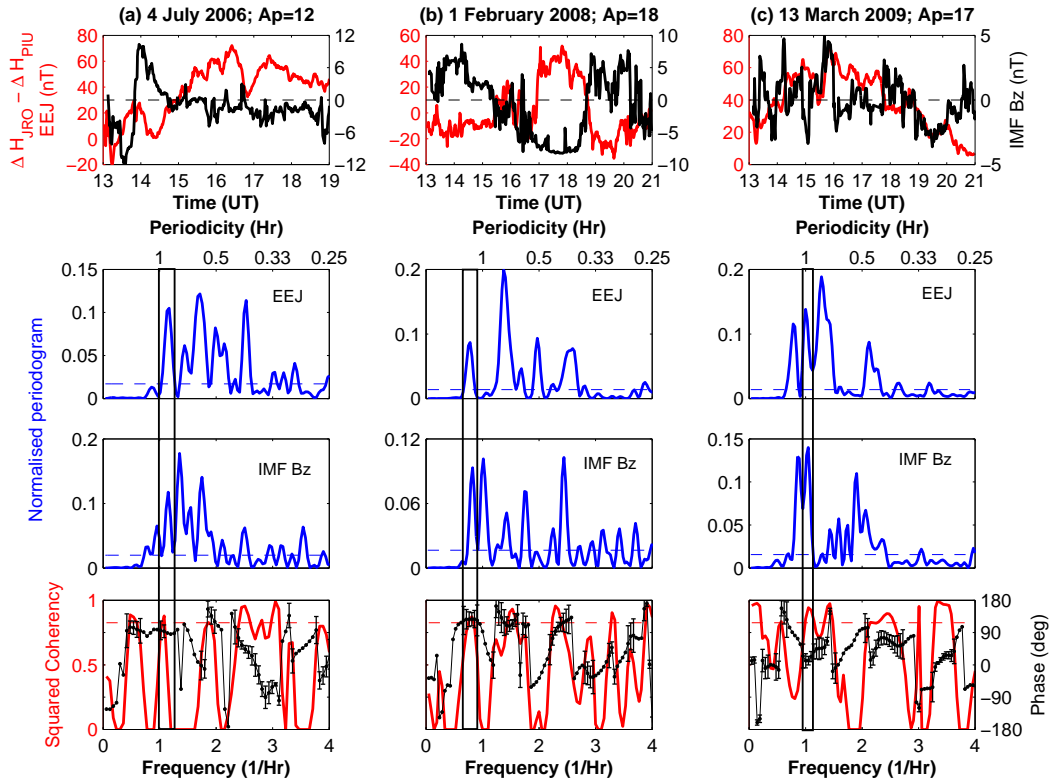


Figure 5.4: The top left panel (5.4a) shows the temporal variations of EEJ (red) and IMF Bz (black) during 1300-1900 UT on 4 July 2006. The middle two rows show the corresponding Lomb-Scargle normalized periodograms for EEJ and IMF Bz where, the blue horizontal line shows the 95% confidence limit and the last row represents the squared coherency (red) with the phase spectra (black) for the two-time series. The false alarm level is marked at 80% and is shown by a red dashed line. Figures 5.4(b) and 5.4(c) show the similar results for the other two events on 1 February, 2008 and 13 March, 2009 during 1300-2100 UT respectively. The rectangular box is marked to show the common periodic components where the time series of EEJ and IMF Bz show significant coherency with stable phase relationship (essential to infer causal relationship).

connected with IMF Bz on 01 February 2008 and 13 March 2009 respectively. Though there are multiple common periodicities present in both the parameters, only a few periodic components in EEJ are found to be responding to the corresponding fluctuations in IMF Bz. It is to be noted that, on many

occasions (Figure 5.4) periodicities adjacent to the causally connected ones do not show either high coherency and/or stable phase relationship. This probably indicates sharp frequency response as far as the M-I coupling is concerned. Figure 5.5 is the same as Figure 5.4, but for (a) 16 November 2006 ($A_p=8$) during 1300-1800 UT, (b) 10 February 2008 ($A_p=21$) during 1330-1900 UT and (c) 23 December 2008 ($A_p=11$) during 1300-2000 UT respectively. In all these cases, both EEJ and IMF Bz show fast fluctuations and they have common periodicities as well. However, they do not show any causal relationship with each other. As an example, one can take the case shown in Figure 5.5a wherein the 60 min periodicity is present in both IMF Bz and EEJ on 16 November 2006 but they are not causally related as neither the coherency is high nor the phase relationship is stable.

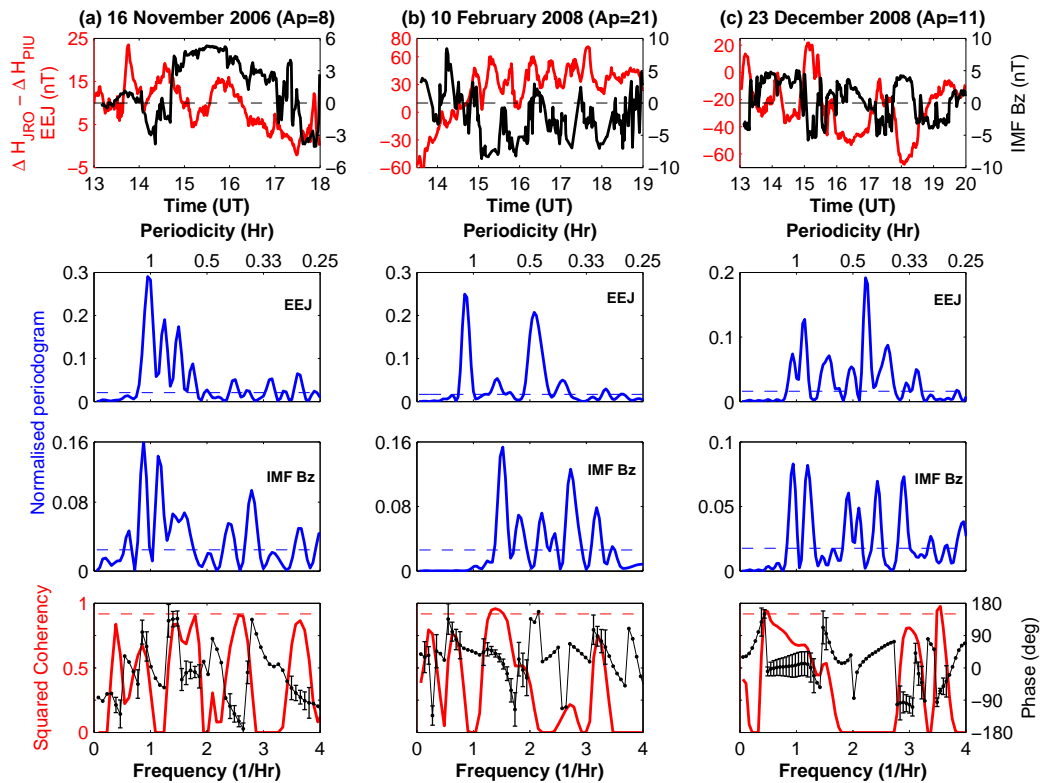


Figure 5.5: Same as Figure 5.4, but for (a) 16 November 2006 during 1300-1800 UT, (b) 10 February 2008 during 1330-1900 UT and (c) 23 December 2008 during 1300-2000 UT respectively. No causal relationship is noticed in these cases.

5.4 Causal connection and solar wind azimuthal flow angle

In Figure 5.1 (left panel), the red rectangular box is marked for a typical event where the EEJ data have been analyzed (1300-1900 UT on 7 August 2006). For all the events considered, the modulus of the average value of the solar wind azimuthal flow angle ($|\Phi|$ in degrees) during this interval was calculated. This choice of the same interval of Φ is based on the consideration that the Φ data are already time shifted till the nose of the bow shock. Table-1 shows the dates of events, periodicities (in min) of PP electric field (with stable phase relationship) and $|\Phi|$. The absence of any causal relationship is marked by a dash in the table. It can be noted from Table-1 that, 13 out of 22 events have shown causal relationship between IMF Bz and EEJ at different periodicities wherein, $|\Phi| < 6^\circ$. These events are marked in black color. The 6 events that do not show any causal relationship (though they have common periodicities), are marked in red color in Table 1. It is to be noted that for these events, $|\Phi| > 6^\circ$. Among all these periodicities, ~ 60 and ~ 30 min periodic components have occurred 5 and 4 times, respectively. In fact, in most of the cases these two periodic components in IMF Bz (IEFy) are found to affect EEJ over the Jicamarca sector. Therefore, out of all 22 events, this criterion of solar wind flow angle determining geoeffectiveness was found to be valid for 19 events (86.4% of the total cases considered). These events are marked in blue fonts in Table 1.

5.5 Discussion

The superposed epoch analysis in Figure 5.2 brings out the characteristic features of stream interface during CIR events. These signatures in solar wind parameters are well established and explained by *Forsyth and Marsch (1999)*.

Event No.	Date	Periodicities (in min) of PP Electric field coherent with EEJ	Average $ \Phi $ (in degree)
1	9 Apr. 2006	27	5.1
2	15 Jun. 2006	25	2.1
3	4 Jul. 2006	60	1.0
4	7 Aug. 2006	60	5.3
5	7 May 2007	46	3.8
6	20 Nov. 2007	48	2.3
7	31 Jan. 2008	37	1.3
8	1 Feb. 2008	70	5.4
9	22 Jul. 2008	30	5.7
10	23 Jul. 2008	32	4.4
11	7 Nov. 2008	60	3.1
12	13 Mar. 2009	60	3.7
13	11 Nov. 2010	60	1.7
14	20 Feb. 2006	-	9.6
15	18 May 2006	-	6.4
16	17 Dec. 2007	-	6.3
17	5 Jan. 2008	-	6.6
18	10 Feb. 2008	-	6.3
19	23 Dec. 2008	-	6.2
20	16 Nov. 2006	-	5.3
21	6 Aug. 2009	53	6.8
22	26 Jun. 2010	-	2.4

Table 5.1: A list of events along with the dates of the events that show coherent periodicities of PP electric field in minutes with those of EEJ. The causal relationship is found at these periodicities. The azimuthal flow angle ($|\Phi|$) in degrees is shown. Out of 22 events, 13 show a causal relationship between IMF Bz and EEJ and these are shown in black colors. Events with common periodicities that do not show any causal relationship are shown in red color and events for which the flow angle criterion was ineffective are shown in blue colors. The absence of causal relationship is marked by a dash.

The histogram in Figure 5.3(b) emphasizes the fast fluctuating components present in IMF Bz during the CIR events. The periodicities in IMF including the most dominant periodicities, in the range of 15-25 min, are associated with the Alfvénic fluctuations in IMF (e.g. *Tsurutani et al., 2006; Korth et al., 2011*) in CIR. It may be noted that the percentage occurrence of 20 min periodicity is very small (in contrast to quiet time feature as reported by *Reddy and Devasia (1976)* for example) in EEJ although the same periodicity is quite dominant in IMF Bz. This may be associated with the EEJ during disturbed conditions. It is known that although the variations in IMF Bz (or IEFy) comprises of a wide range of periodicities, only a few periodic fluctuations affect low/equatorial ionosphere. The periodicity in IMF Bz that affects low latitude depends on the shielding process at the inner edge of the ring current. The typical shielding time constant is ~ 30 minutes (e.g. *Senior and Blanc, 1984*). However, earlier observations reveal that shielding can remain broken for longer duration of time (*Huang et al., 2005; Chakrabarty et al., 2015*). Therefore, although it is clear that the frequency response around the ring current region decides the PP frequency, the nature (e.g. *Ohtani and Uozumi, 2014*) of the processes that decide this response is not comprehensively understood. Nevertheless, the present study (Table-1) shows that on some occasions, DP2 (30 and 60 min periodicities) type (*Nishida, 1968; Sastri et al., 2000; Chakrabarty et al., 2008, 2015*) periodic fluctuations can reach up to dip equatorial ionosphere in daytime during the passage of CIRs.

Table-1 suggests that the presence of PP electric field during CIR depends on the azimuthal solar wind flow angle (Φ) with the events which do not show causal relationship between EEJ and IMF Bz, having $|\Phi|$ more than 6° . This is strikingly valid barring three events studied in this work. In other words, when the solar wind flow becomes non-radial (in the ecliptic plane) beyond a critical angle (6°), the dayside merging of IMF Bz with the geomagnetic field becomes less efficient. The importance of this critical angle can be evaluated

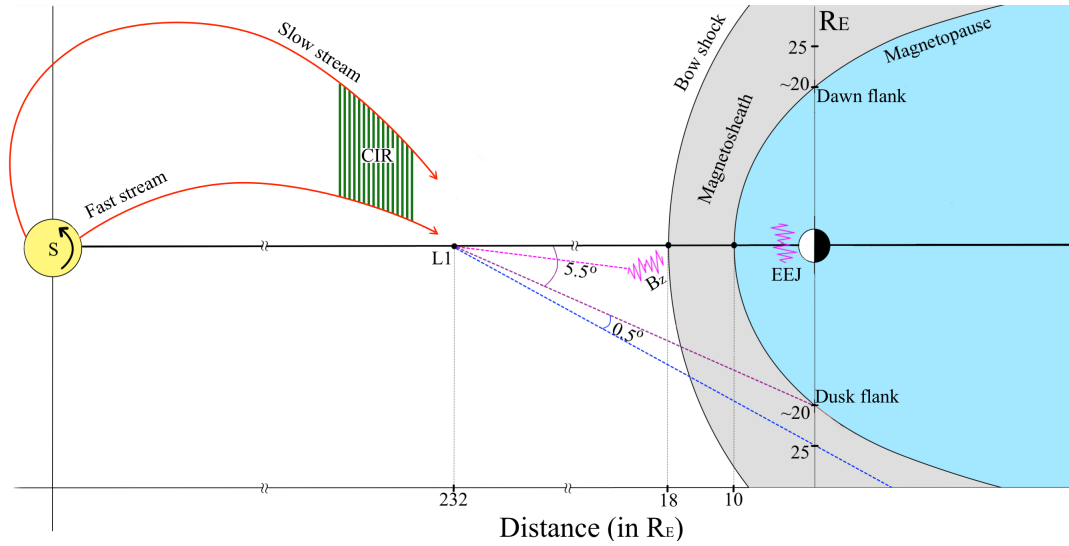


Figure 5.6: A schematic (not to scale) showing the geometry of solar wind flow angle at L1 point and position of bow shock, magnetopause, dawn and dusk flank of magnetopause. For the flow angle below 6° , measured at L1 with respect to the Sun-Earth line, the fluctuations in IMF B_z are causally connected to EEJ strength in the ionosphere. The CIR events are not geoeffective for the flow angle more than 6° . Graphic help: Madhusudan Ingale

geometrically by invoking the typical size of the dayside magnetopause and by using the flow angle at the L1 point from where the CIR observations are made. Figure 5.6 shows a schematic (not to scale) of the solar wind azimuthal flow angle (Φ) and the positions of bow shock and magnetopause at dawn-dusk flanks of the magnetosphere are also marked. For a given azimuthal flow angle Φ measured at L1 point, assuming that there is no interaction as the solar wind proceeds from L1 point to the terrestrial magnetopause, the distance of either sides of dawn or dusk flank can be calculated by using the formula, $D_{flank} = D_{L1} \tan \Phi$, where D_{flank} (in R_E) is the distance of dawn or dusk side flank from the center of the Earth and D_{L1} (in R_E) is the distance of the L1 point from the center of Earth. Considering the azimuthal flow angle, $|\Phi| = 6^\circ$ and the distance of the L1 point to be $\sim 232 R_E$ ($1 R_E = 6371$ km), the dawn/dusk flank of magnetopause turns out to be $\sim 25 R_E$ away. The

location of dayside magnetopause in XY plane is shown in Figure 5.7 (Walsh *et al.*, 2012). It can be easily seen that the typical distance of dawn-dusk flank of the magnetopause is $\sim 20 R_E$ away from the center of the Earth. This essentially means that the CIR will miss the magnetopause if Φ exceeds 6° assuming the CIRs undergo no further interaction between the L1 point and the magnetopause. Under this scenario, the probability of merging of IMF B_z with the terrestrial magnetic field decreases significantly. As a consequence, the geoeffectiveness of the CIR events decreases drastically as the flow angle exceeds 6° which is the highlight of the present investigation. It is, therefore, expected that PP occurs only on those cases when the solar wind flow angle is within 6° .

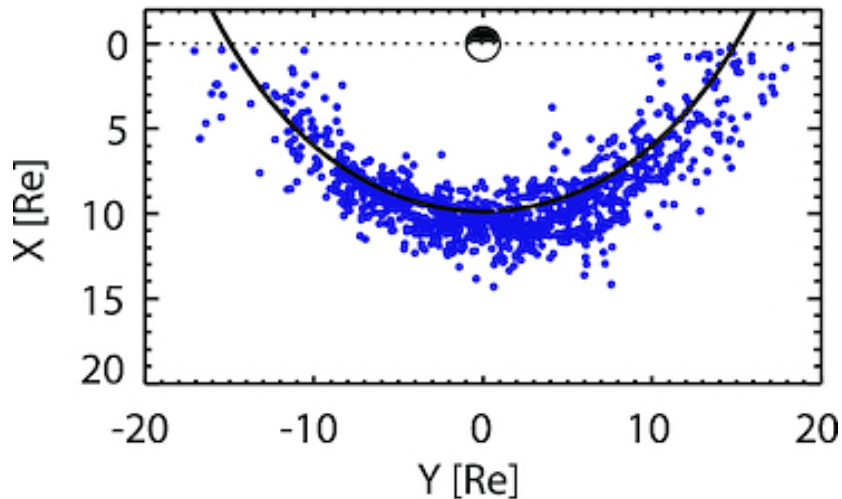


Figure 5.7: Locations (GSE coordinate system) of dayside magnetosheath measurements just outside the magnetopause in the XY plane. The dashed line indicates the dawn-dusk flank of the magnetopause distances. From Walsh *et al.* (2012)

At this juncture, it is important to note that once the solar wind hits the magnetopause at angles less than 6° , two mechanisms can be invoked to explain the dayside merging process. The dayside merging process is mediated through the merging electric field (e.g. Kan and Lee, 1979; Siscoe and Crooker, 1974) which is defined as $E_r = V_{SW} B_T \sin^2 \theta / 2$, where θ is the clock angle,

V_{SW} is the solar wind velocity and B_T is the total magnetic field. The merging electric field is generally believed to operate on a macroscopic scale. This is supported by the works of *Fejer et al. (2007)* and *Wei et al. (2008)* that suggest the critical role of merging electric field in M-I coupling. On the other hand, it was shown (*Borovsky, 2008; Borovsky et al., 2008; Borovsky and Birn, 2014*) that the merging electric field is controlled by the local plasma parameters in the magnetosheath and magnetosphere and that these plasma parameters are controlled by the solar wind conditions. Hence, it was argued by them that the parameters in the solar wind decide the merging electric field. Recently, it has been experimentally observed (*Zhang, 2016*) that the reconnection takes place in an asymmetric medium as the plasma parameters are not the same on the bow shock and magnetopause side of the magnetosheath region. Therefore, depending on the local plasma processes, the merging can be different on some occasions even if the flow angle is well within 6° . Further, the assumption of no modification(s) in the CIR propagation between the L1 point and the magnetosphere may not be valid during these events. These could be a probable reason for the anomalous cases (see Table-1) reported in this work wherein, the flow angle is less than 6° but the associated CIRs do not affect the equatorial ionosphere. This aspect requires further investigations.

The important role of the flow angle gets further support from the results of *Oliveira and Raeder (2015)* who showed that IP shocks with similar upstream conditions (such as magnetic field, speed, density and Mach number) can have different levels of geoeffectiveness, depending on their shock normal orientation (which can change if the flow angle changes). Therefore, it is apparent that the solar wind flow angle at the L1 point plays a key role in determining the geoeffectiveness of CIR events.

5.6 Summary

The present investigation suggests that 30 and 60 min periodicities in IMF Bz are efficient in penetrating into the equatorial ionosphere during CIR events as long as the solar wind azimuthal flow angle is less than $\sim 6^\circ$ at the L1 point. This is attributed to the reduction in the merging electric field in the dayside magnetosphere that occurs when the solar wind flow angle increases beyond a threshold. Therefore, this work provides a quick and easy method to forecast the geoeffectiveness of CIR events based on the observations from the L1 point.

Chapter 6

A new type of prompt electric field disturbance driven solely by solar wind density variation

Abstract: During space weather events, several types of prompt electric field disturbances affect equatorial ionosphere almost instantaneously. As it is shown in Chapter-3, 4 and 5 that the electric field perturbations over low latitude can occur during geomagnetic storms (during the passage of ICME and CIR), magnetospheric substorms and pseudo-breakup events. In addition to these effects, the electric field disturbances over low latitude can be associated with changes in IMF B_y and due to the fast compression of magnetosphere owing to the increase in the solar wind dynamic pressure. In this chapter, it is explicitly shown for the first time that prompt electric field perturbation can occur during enhancements in solar wind dynamic pressure solely due to the increase in solar wind density. It is important to mention here that the electric field during density events is believed to get generated inside the magnetosphere which is different from the dawn-dusk PP electric field imposed by solar wind bulk flow. Therefore, this chapter will address a new type of prompt electric field and its possible generation mechanism.

6.1 Introduction

The transient electric field disturbances during storm sudden commencements (SSC) (*Sastri et al., 1993*) or sudden impulses (SI) (*Akasofu and Chao, 1980*) or main impulse (MI) (*Sastri et al., 1993*) fall in the last category. These events are mostly associated with the enhancement in the dynamic (ram) pressure during the passage of interplanetary shocks. Interplanetary shocks are primarily governed by changes in the solar wind velocity (*Tsurutani et al., 1995*) and these events have been reported earlier. However, it remains to be observed whether equatorial ionospheric electric field gets affected solely due to change in the solar wind density. Till date, to the best of this author's knowledge, the evidence for the changes in the equatorial ionospheric electric field due to changes dominated by the solar wind density alone is not available. One of the reasons for this is the simultaneous changes in the solar wind velocity and density during most of the ram pressure enhancement events (*Sastri, 2002; Huang et al., 2008*). In order to show this, Figures 6.1(a-e) are introduced. This figure depicts the variations in the IMF Bz, solar wind flow velocity (V, in kms^{-1}), proton density (Np, in cm^{-3}), dynamic pressure (P, in nPa), and vertical drift over Jicamarca during 1600-2100 UT (universal time) on 27 August, 2001 (Ap=13). Corresponding local time (LT = UT - 5 h) of Jicamarca is also shown on top of Figure 6.1(a) which is used to infer the ionospheric prompt electric field perturbations over the Jicamarca sector. It is clearly noticed that the solar wind velocity and density show significant changes while the IMF Bz in the northward. So in this case, the simultaneous changes in solar wind density and velocity have brought a change in dynamic pressure from ~ 2 nPa to ~ 10 nPa at 1946 UT. It is to be noted that an eastward electric field perturbation was observed where the vertical plasma drift increased from ~ 6 ms^{-1} to ~ 21 ms^{-1} due to this pressure change. Though this particular event has also been reported by *Huang et al. (2008)*, they did

not try to delineate the effects of solar wind density and velocity separately.

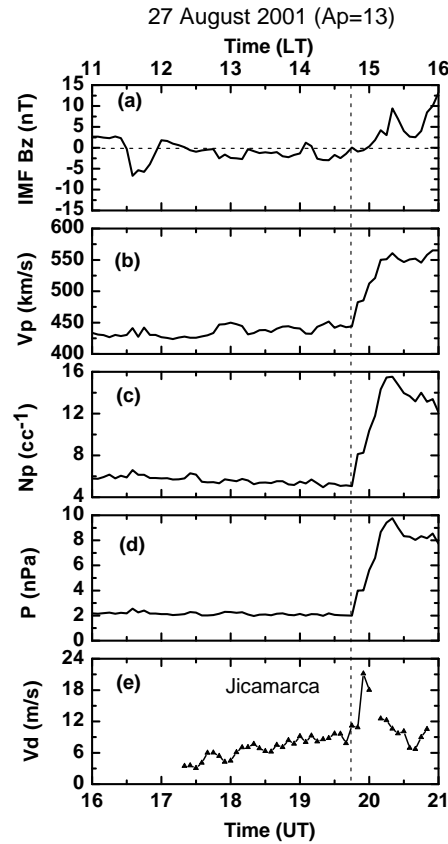


Figure 6.1: Variations in (a) IMF B_z , (b) solar wind velocity, (c) solar wind proton density, (d) solar wind ram pressure and (e) vertical drift, respectively, during 1600–2100 UT on 27 August 2001 ($A_p=13$). Corresponding local time is also shown at the top. The vertical dashed line is marked at 1946 UT (1446 LT) when increase in solar wind ram pressure is observed under change in solar wind density and velocity.

In recent times, a few efforts have been made to capture the changes in the equatorial ionosphere corresponding to changes in the solar wind ram pressure. For example, [Zong *et al.* \(2010\)](#) showed reduction in equatorial TEC corresponding to an interplanetary shock. This shock is associated with changes in the solar wind ram pressure due to simultaneous changes in velocity and density under the northward IMF B_z condition. On the other hand, [Yuan and Deng \(2007\)](#) indicated the role of continuous solar wind pressure variations on the long-lasting penetration of the interplanetary electric field in the equato-

rial ionosphere during southward IMF B_z condition. In addition, [Huang et al. \(2008\)](#) showed that ion velocities over Jicamarca increased following enhancements in the ram pressure regardless of the polarity of IMF B_z . In fact, [Sastri et al. \(1993\)](#) has also investigated the effects of prompt electric field penetration earlier during storm sudden commencement (SSC). It is to be noted that these events are not solely driven by solar wind density change. Therefore, in the present investigation, an attempt has been made to fill this gap by identifying an event where solar wind density changes but not the solar wind velocity under northward IMF B_z condition.

Although such events can throw light on the effects of solar wind ram pressure on the equatorial ionosphere, the role of density is not explicitly evident based on these observations. Recently, [Wei et al. \(2012\)](#) showed significant effect of solar wind density in controlling the prompt electric field disturbance at the equatorial ionosphere during a polar cap saturation event. In their study, the density effects are studied primarily during the main phase of a storm when IMF B_z is southward. In fact, a few global MHD simulations ([Slinker et al., 1999](#); [Lopez et al., 2004](#)) have indicated the role of solar wind density on the magnetosphere and ionosphere. However, it is not still clear that how change in solar wind density will affect the global ionosphere. Further, the observational evidence of prompt electric field disturbance in the equatorial ionosphere driven solely by changes in the solar wind density under northward IMF B_z conditions is still unavailable. The present chapter starts with the identification of a space weather event wherein solar wind density alone seems to have changed before the main phase of a geomagnetic storm. The impact of this density pulse event on global ionosphere in general and equatorial ionosphere in particular are evaluated subsequently.

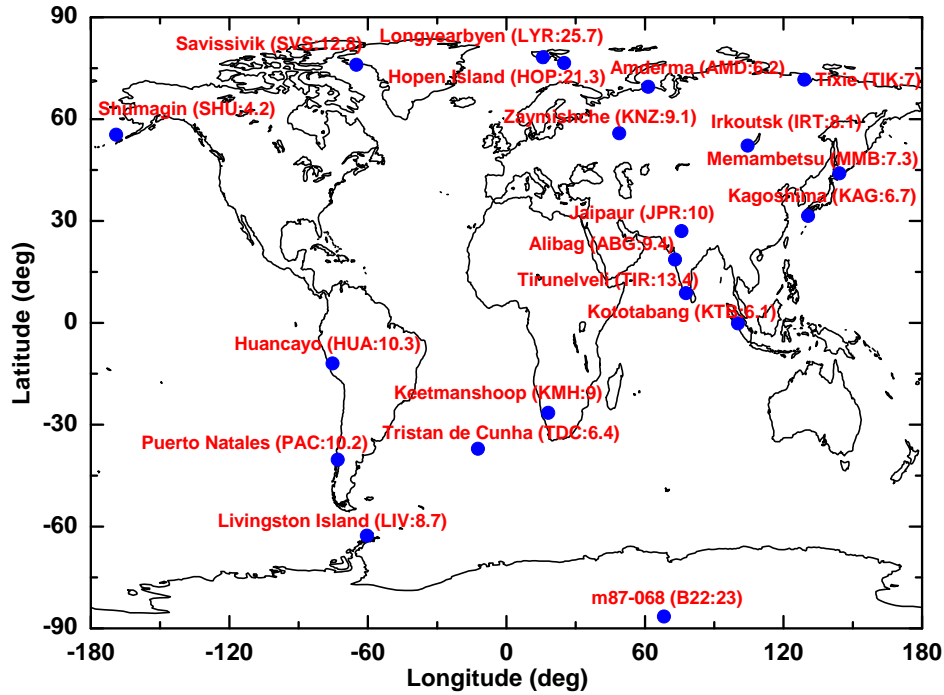


Figure 6.2: A global map with the magnetometer stations marked on it. Magnetic data from these stations are used in the present study.

6.2 Dataset:

In addition to NASA GSFC CDAWeb data (<http://cdaweb.gsfc.nasa.gov/>), the northward component (X) of the geomagnetic field measured at a few longitudinally separated low latitude stations from the Indian, Japanese, African, South American and Pacific sectors are used in the present study. In addition, measurements of X from a few high, middle and low latitude stations in the northern and southern hemispheres are also investigated to capture the latitudinal changes. The ΔX variation for a given station is obtained after subtracting the nighttime base value level. The temporal resolution of the ΔX data is 1 min. Figure 6.2 shows the global map on which the magnetometer stations are marked from where the data sets are used in the present investigation. The ΔX data from these stations are used to construct Figure 6.5 and 6.6 which will be presented in the result section. It is to be mentioned

here that with the exception of three Indian stations (TIR, ABG and JPR) and one Japanese station (KTB), all the other representative magnetic data are taken from SuperMAG network (<http://supermag.jhuapl.edu>).

As already discussed in chapter-2, in absence of direct ionospheric electric field measurements over the Indian dip equatorial sector, magnetometer and ionosonde measurements are used to infer the electric field perturbations during the event under consideration. In order to verify the presence of prompt electric field disturbances over the dip equatorial ionosphere using measurements from another independent technique (other than magnetometer), digisonde measurements over Thumba (Geog.lat: 8.5°N ; Geog.Long: 77°E and dip: 0.5°N) are used. It is known that variation in ionospheric layer heights (e.g. $h'F$, h_mF2) respond to the electric field variations over the dip equator. However, the variations in the virtual base height of the F-layer ($h'F$) contains not only information on the changes due to electric field disturbances but also due to production processes during daytime and loss processes during both day and nighttime. As, the peak height of the F2 layer (h_mF2) is usually above 300 km during daytime, their temporal variation is not affected by loss processes (*Bitencourt and Abdu, 1981*) on most occasions. Further, in the absence of solar flare events, fast changes in h_mF2 during daytime are unlikely to be caused by production processes. Therefore, variation in h_mF2 is used in the present investigation to additionally confirm the electrodynamical perturbations associated with the space weather event under consideration. The h_mF2 values are scaled using the ARTIST software (*Reinisch and Huang, 2001*). The typical uncertainty in the determination of h_mF2 during daytime is ~ 5 km.

6.3 Results

As already stated, in section 6.1, no attempt has been made to separately investigate the effects of density. Therefore, a very unique case has been con-

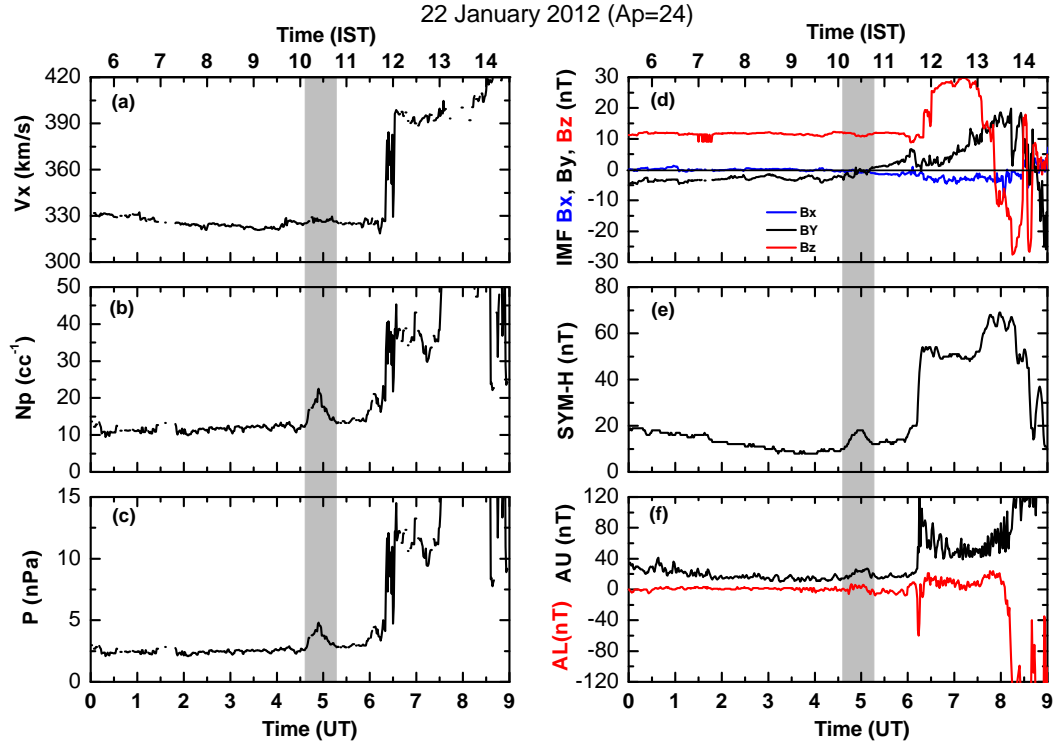


Figure 6.3: Variations in (a) solar wind velocity, (b) solar wind density, (c) solar wind ram pressure, (d) IMF B_x (blue), B_y (black) and B_z (red), (e) SYM-H and (f) AL (red) and AU (black), respectively during 0000-0900 UT on 22 January 2012. Corresponding time in IST is also shown at the top. The gray-shaded rectangular box marks the interval when increase in solar wind density is observed under nearly steady solar wind velocity and northward IMF B_z conditions.

sidered in this present study to investigate PP electric field perturbations over dip equatorial ionosphere where the solar wind pressure is solely driven by solar wind density under steady solar wind velocity and northward IMF B_z conditions. Left panel of Figure 6.3 (a-c) reveals the variation in the solar wind velocity (V_x , in kms^{-1}), proton density (N_p , in cc^{-1}), dynamic pressure (P , in nPa) during 0000-0900 UT (Universal Time) on 22 January 2012. Corresponding Indian Standard Time ($\text{IST} = \text{UT} + 5.5 \text{ hr}$) is also shown on top of Figures 6.3 and 6.4 to facilitate interpretation of Figure 6.7 which is used to infer the ionospheric prompt electric field perturbations over the Indian dip equator. It can be easily seen from Figure 6.3(a-c) that the solar wind density changes

from 10 cc^{-1} to 22 cc^{-1} during 0440-0510 UT and maximizes at ~ 0450 UT. In contrast, velocity (Vx) during this interval changes by only 2 kms^{-1} . The solar wind ram pressure changes from 2.5 nPa to 5 nPa during 0440-0510 UT. Figures 6.3(d) shows the variations in IMF Bx (in blue), IMF By (in black) and IMF Bz (in red) in nT, respectively during the same interval 0440-0510 UT. It is clearly seen that solar wind parameters like Vx and IMF Bz do not show significant changes during this interval (marked by vertical shaded box). IMF By starts changing its polarity during this interval and remains very close to zero at ~ 0450 UT when a peak in the solar wind density is observed. This enhancement (and not the larger enhancement during the onset of SSC at 0612 UT) in the solar wind density is of interest here as this occurs in the absence of any significant change in the solar wind velocity. IMF Bx also remains almost constant during this interval. It is shown in section 6.4 that the density change term contributes significantly for the pressure change. Small but detectable changes are observed in AU (black) and AL (red) (see Figure 6.3f) during this interval. The change in SYM-H (Figure 6.3e) is ~ 10 nT which is significant. It must be noted that, IMF Bz is northward during this time. In addition to the above event, both Vx and N_p register sharp enhancements at 0618 UT under northward IMF Bz condition. In fact, a storm sudden commencement (SSC) occurs at 0612 UT due to the arrival of the associated interplanetary shock at this time. The SSC is followed by an initial phase that continues for ~ 2 hours.

In order to rule out influence of any substorm induced transient electric field at this time, the geosynchronous electron and proton counts s^{-1} measured by the Los Alamos National Laboratory (LANL) satellites are examined. Figure 6.4 shows the temporal variations in electrons (left panel) and proton (right panel) counts s^{-1} as measured by LANL satellites during 0000-0900 UT (0530-1430 IST). LANL-02A and LANL-04A satellites were located around longitudes 70°E and 103°E , respectively during this time (dayside).

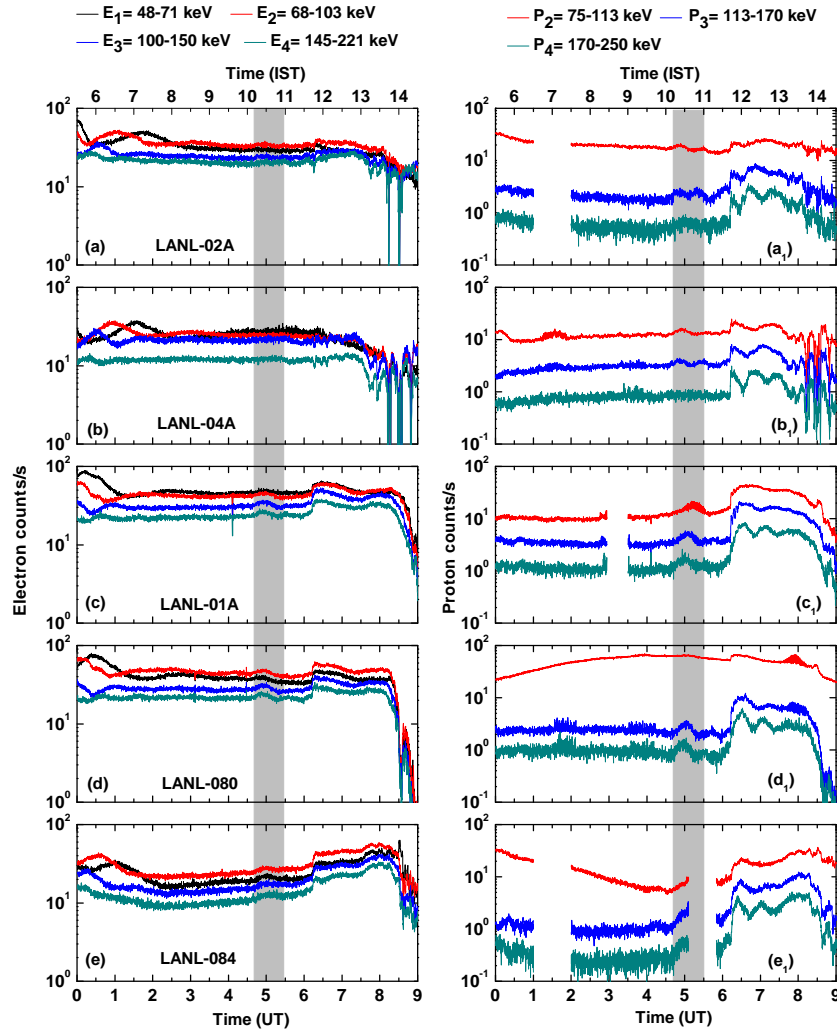


Figure 6.4: Left panel shows the changes in energetic electron counts s^{-1} and the right panel shows the changes in proton counts s^{-1} observed by LANL satellites during 0600-1400 IST on 22 January 2012. The gray-shaded rectangular box highlights the interval (0440-0510 UT) of solar wind density enhancement.

The other three satellites (LANL-01A, LANL-080 and LANL-084) were located around longitudes 165°W , 145°W and 50°W , respectively (nightside). The effect of density associated pressure enhancement during 0440-0510 UT (1010-1050 IST) (marked by vertical box) is noticed conspicuously in the electron counts measured by three nightside satellites. Small but distinct enhancements in electron counts are observed in all the four energy channels of the

nightside satellites. However, dayside electron counts do not seem to respond to this event. In case of proton counts, enhancements are observed by both night and dayside satellites during this time with an exception of the 170-250 keV channel of LANL-04A. In addition, there seems a delay in the proton channels as it goes from higher to lower energy side.

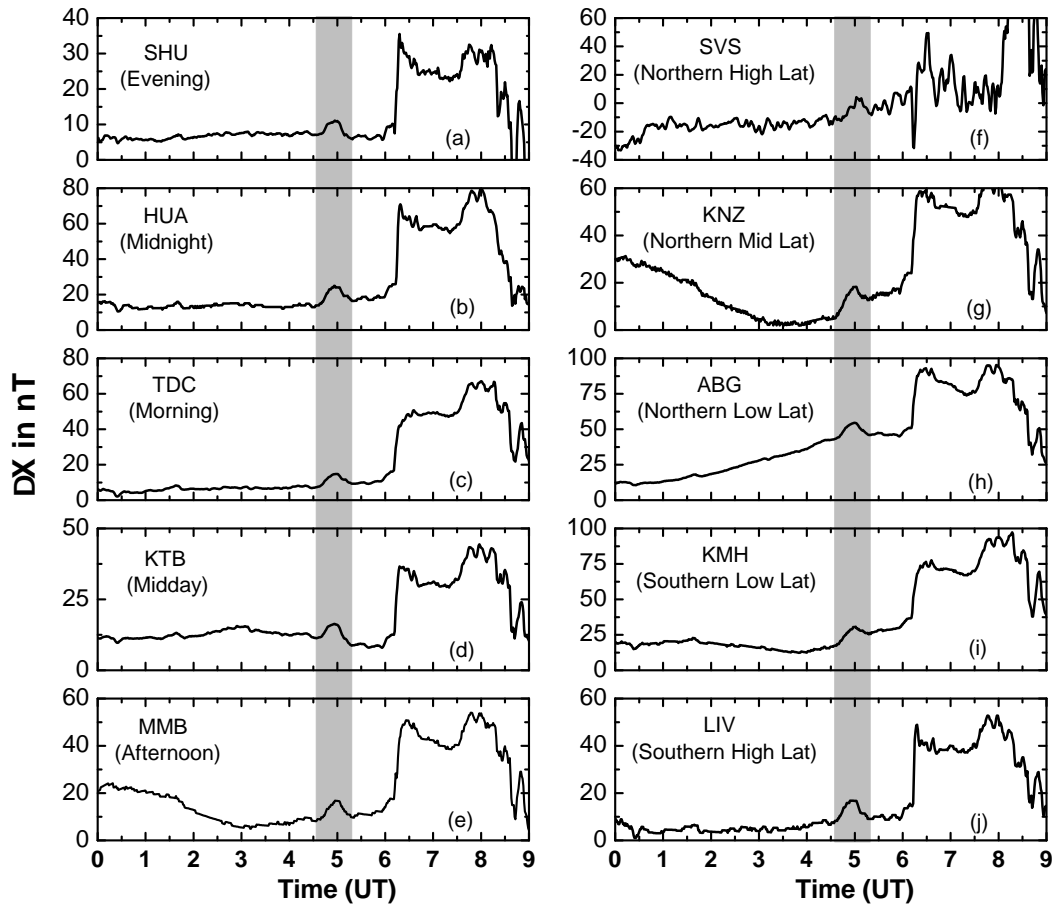


Figure 6.5: The left panel (a-e) and right panel (f-j) show the ΔX variations for a few longitudinally and latitudinally separated stations respectively during 0000-0900 UT. The longitudinally separated stations (SHU, HUA, TDC, KTB and MMB) represent different local times that are mentioned in the figure. The latitudinally separated stations (SVS, KNZ, ABG, KMH and LIV) include northern and southern hemispheric stations. It can be noted that the ΔX variations during 0440-0510 UT (marked by vertical gray-shaded region) show distinct enhancements in all of longitudes and latitudes.

In order to find out the effects of the solar wind density pulse during 0440-0510 UT are global in nature, Figure 6.5 is presented. The left (a-e) and right (f-j) panels of Figure 6.5 show ΔX variations at a few longitudinally and latitudinally separated stations, respectively during 0000-0900 UT. The longitudinally separated stations represent different local time sectors (mentioned in Figure) while the latitudinally separated stations represent high, middle and low latitudes (not along the same meridian) from northern and southern hemispheres. It can be noticed that ΔX variations during 0440-0510 UT (marked by vertical gray shaded region) register distinct enhancements corresponding to the density related pressure enhancement at all longitudes or latitudes. Therefore, Figure 6.5 elicits the global nature of the ΔX enhancement during 0440-0510 UT.

In order to confirm whether the variation in ΔX with latitude follow the characteristic pattern associated with the PP electric field and not the pattern associated with the magnetopause (Chapman-Ferraro) current, Figure 6.6 is presented. This figure shows the latitudinal variation in the amplitude (in nT) of ΔX during 0440-0510 UT when a few dayside stations are considered. The ΔX amplitude maximizes over the auroral region, falls off over mid and low latitudes and enhances again over the dip equator. It is also important to note that the ΔX amplitude over the dip equator is comparable to that over the sub-auroral region and less than that over the polar region. So this variation in ΔX is not associated with magnetopause current. Rather, it is a characteristic feature of PP electric field from high to low latitude. The reason for this inference will be discussed in section 6.4.

Figure 6.7 explores the prompt electric field perturbations, if any, over the equatorial ionosphere during 0440-0510 UT when enhancement in solar wind density (N_p) is observed in absence of any significant change in the solar wind velocity, and IMF components. Figure 6.7 (a-c) depicts variations of the $\Delta H_{TIR} - \Delta H_{ABG}$ and $h_m F2$ during 0200-1100 UT on the event day (22

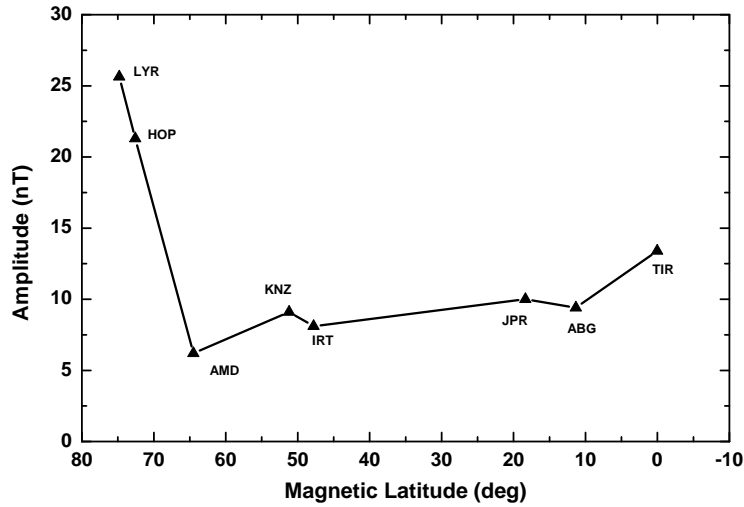


Figure 6.6: Latitudinal variation in the amplitude (in nT) of ΔX during the 0440-0510 UT at the dayside stations spanning from polar region to dip equatorial regions. Dip equatorial enhancement in ΔX can be seen. It can also be noticed that amplitude over the dip equator is comparable to that over the sub-auroral region and less than that over the polar region.

January, 2012) vis-à-vis on 20 and 19 January, 2012 which are magnetically quiet days ($A_p = 4$ and 2, respectively). It is noted that the slow temporal variations in $\Delta H_{TIR} - \Delta H_{ABG}$ and $h_m F2$ grossly agree with each other barring the morning hours. The gray shaded region marked in Figure 6.7a shows the interval of 0440-0510 UT when the fast fluctuations in $\Delta H_{TIR} - \Delta H_{ABG}$ and $h_m F2$ go hand in hand. Interestingly, although fast fluctuations are present in $h_m F2$ and $\Delta H_{TIR} - \Delta H_{ABG}$ on quite days, simultaneous fluctuations in both the parameters (similar to the shaded region on 22 January) are absent on the two quiet days. In order to evaluate the association of the equatorial E and F-region parameters ($\Delta H_{TIR} - \Delta H_{ABG}$ and $h_m F2$, respectively) with the variation in the solar wind density (N_p), the shaded region in Figure 6.7a is blown up and presented along with solar wind density (N_p) in the right column of Figure 6.7. Figure 6.7(d-f) clearly elicits that the enhancements in $h_m F2$ and $\Delta H_{TIR} - \Delta H_{ABG}$ are concomitant with the enhancement in N_p . The implication of this observation will be addressed in the ensuing section.

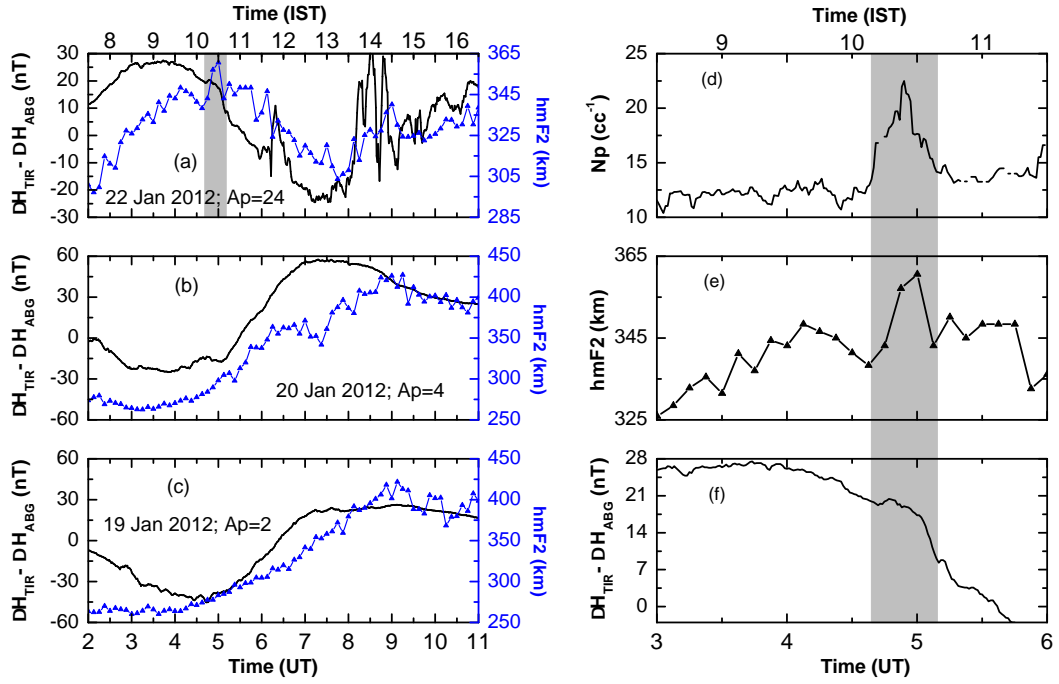


Figure 6.7: Left panel depicts the variations in $\Delta H_{TIR} - \Delta H_{ABG}$ (black) and h_mF2 (blue) during 0200-1100 UT on (a) 22 January vis-à-vis (b) 20 January and (c) 19 January 2012 that are magnetically quiet days. The gray shaded region in (a) shows the interval when simultaneous fluctuations are observed in $\Delta H_{TIR} - \Delta H_{ABG}$ and h_mF2 . The right column shows the zoomed-in variations in (e) $\Delta H_{TIR} - \Delta H_{ABG}$ and (f) h_mF2 vis-à-vis N_p during 0300-0600 UT on 22 January 2012 with the gray-shaded region overlaid. The shaded region clearly shows that the enhancements in $\Delta H_{TIR} - \Delta H_{ABG}$ and h_mF2 are concomitant with the increase in N_p .

6.4 Discussion

Solar wind dynamic (ram) pressure is expressed as follows:

$$P_{dyn} = \rho v^2 \quad (6.1)$$

In the above expression, ρ and v are solar wind density (strictly, mass density) and velocity, respectively. Differential of (6.1) yields the following expression.

$$\Delta P_{dyn} = v^2 \Delta \rho + 2v\rho \Delta v \quad (6.2)$$

Based on equation (6.2), three different conditions can be envisaged through which solar wind dynamic pressure can be changed. These conditions are as follows:

$$\text{Condition - 1 : } v\Delta\rho \approx 2\rho\Delta v$$

$$\text{Condition - 2 : } v\Delta\rho < 2\rho\Delta v$$

$$\text{Condition - 3 : } v\Delta\rho > 2\rho\Delta v$$

During most of the SSC, SI or MI events, conditions 1 or 2 get satisfied and these cases, as mentioned in the introduction section, have been studied in the past. However, evidence for the changes in the ionospheric electric field satisfying condition-3 is not available in the literature particularly when IMF B_z is northward. In the present case, the solar wind velocity is $\sim 330 \text{ kms}^{-1}$ and density is $\sim 10 \text{ cc}^{-1}$ before the arrival of the density pulse centered at 0450 UT. During the density pulse event, the maximum change in solar wind density is 12 cc^{-1} and the change in the solar wind velocity (Δv) is not significant ($\sim 2 \text{ kms}^{-1}$). Slow and nearly constant (in time) solar wind speed coupled with changes in the solar wind density makes the term $v\Delta\rho$ larger than $2\rho\Delta v$. Therefore, temporal changes in ram pressure during this time are primarily driven by the temporal changes in the solar wind density.

The signature of “dispersionless” injection, which is a tell-tale signature of substorm onset ([Reeves, 1998](#)), is absent during 0440-0510 UT. Instead, one can see from Figure 6.4 that the characteristic undulations in the flux patterns in response to the enhancement in the ram pressure enhancement is very similar to the earlier observations by [Lee et al. \(2005\)](#). It has been already shown ([Li et al., 2003](#); [Lee et al., 2004, 2005](#); [Shi et al., 2009](#)) that geosynchronous particle fluxes do respond, on many occasions, to changes in the solar wind dynamic pressure. It is proposed that enhancements in the ram pressure can change the magnetic flux at a given radial distance which, in turn, induces an electric field. This electric field causes charged particles to get energized further and move earthward. Even under northward IMF B_z conditions, enhancements

in the ram pressure (in this case, due to increase in solar wind density) can increase the magnetic flux at the LANL satellite locations. The particle flux at the geosynchronous orbit can have finite or negligible dispersion in energy depending upon the radial profile of the source particle distribution for fixed first and second adiabatic invariants. This scenario is different from substorm “injection” as one does not observe the typical reduction of flux (prior to “dispersionless” injection associated with the substorm onset) to a low/negligible level as seen generally during the substorm growth phase. Further, one can note that the nightside electron counts remain elevated for the same duration as that of the dynamic pressure enhancement caused by increase in the solar wind density. This strongly suggests that the changes in the particle counts at geosynchronous orbit in the present case are not substorm related “injections” and most likely manifestations of the changes in the radial locations of specific drift shells (defined by first and second adiabatic invariants) and consequent arrival of the particles into the detectors. Various observational aspects like the day and nightside differences in the electron fluxes, the absence of such differences for the proton fluxes, time delays between particle channels of different satellites are possibly the manifestations of the spatial variations in the changes in the electron and proton drift shells associated with the dynamic pressure enhancements (*Lee et al., 2004, 2005*). The important point to be noted here that the geosynchronous observations presented here provides an evidence for the presence of an induction electric field (*Shi et al., 2009*) in the magnetosphere during this time that energizes the particles and changes the flux at the geosynchronous altitudes. The delay in energy channels are very clearly seen in proton channels. This is expected as the particle injections in the present case are not associated to any dispersionless (substorm) signatures (*Sarris and Li, 2005*).

Before addressing the electric field perturbations over the Indian dip equatorial station, it is important to verify that the ionospheric plasma convection

got enhanced over high latitudes during this density pulse event as that provides credence to the origin of penetration electric field at the polar region during this time. Figures 6.8, 6.9 and 6.10 in which three high latitude ionospheric convection maps generated by the SuperDARN HF radar network are shown corresponding to the representative intervals of 0440-0442 UT, 0450-0452 UT, and 0510-0512 UT, respectively. An anticlockwise ionospheric flow vortex can be seen to get maximized (see red arrows) during 0450-0452 UT (Figure 6.9). In addition, Figure 6.11 shows the average line of sight velocity (V_{los}) measurement by the HF radar (part of SuperDARN radar network) over Stokkseyri, Iceland (64°N , 22°W) on 22 January 2012 during 0442–0558 UT. The sequence of Figure 6.11 clearly brings out the evolution of the convection velocity along the line of sight before and after the event. It can be conspicuously seen that the convection has increased during 0450-0452 UT (see the enhanced red patches) and then it slowly decreases. This provides a strong evidence for the generation of region-1 field-aligned currents (R1-FAC) (e.g. [Sofko et al., 1995](#)) and presence of convection electric field over high latitudes in the dawn-to-dusk direction during the density pulse event. This electric field can penetrate to lower latitudes nearly simultaneously. Further, the concomitant magnetic variations in the Indian (pre-noon), South American (midnight), Japanese (afternoon), Pacific (afternoon) and African (morning) sectors as well as at the high and mid latitude stations during 0440-0510 UT suggest that the global ionospheric current system responded to the changes in the solar wind density during this time. Moreover, the enhancement (~ 10 nT) in $SYM - H$ corresponding to this solar wind density enhancement is also consistent with the work of [Araki et al. \(1993\)](#) who showed the dynamic pressure dependence of the Dst index is essentially controlled by solar wind density irrespective of northward or southward IMF B_z condition. However, [Araki et al. \(1993\)](#) did not investigate the presence of prompt electric field disturbances over the dip equatorial ionosphere during the intervals when only the solar wind density was changing. As there was no solar flare at this time 0440-0510 UT, the

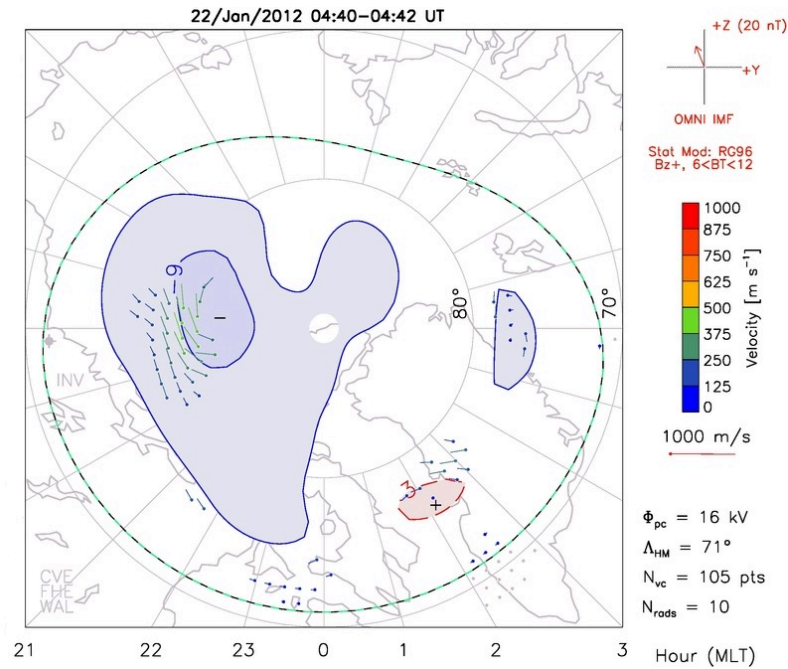


Figure 6.8: The high latitude ionospheric convection maps generated by the SuperDARN HF radar network during 0440-0442 UT. High latitude ionospheric convection is weak at this time.

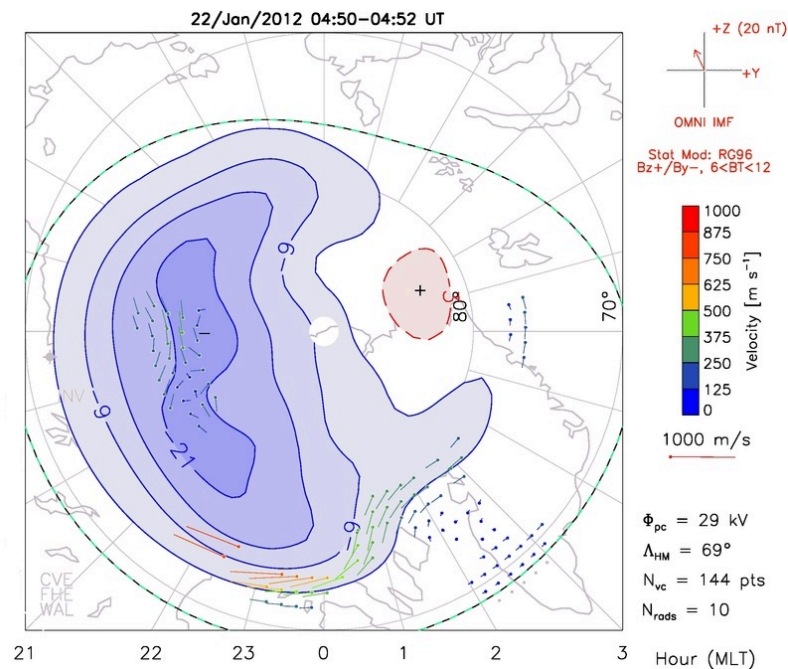


Figure 6.9: Same as Figure 6.8 but for the interval 0510-0512 UT. An anticlockwise and enhanced (see red arrows) ionospheric flow vortex can be seen at this time.

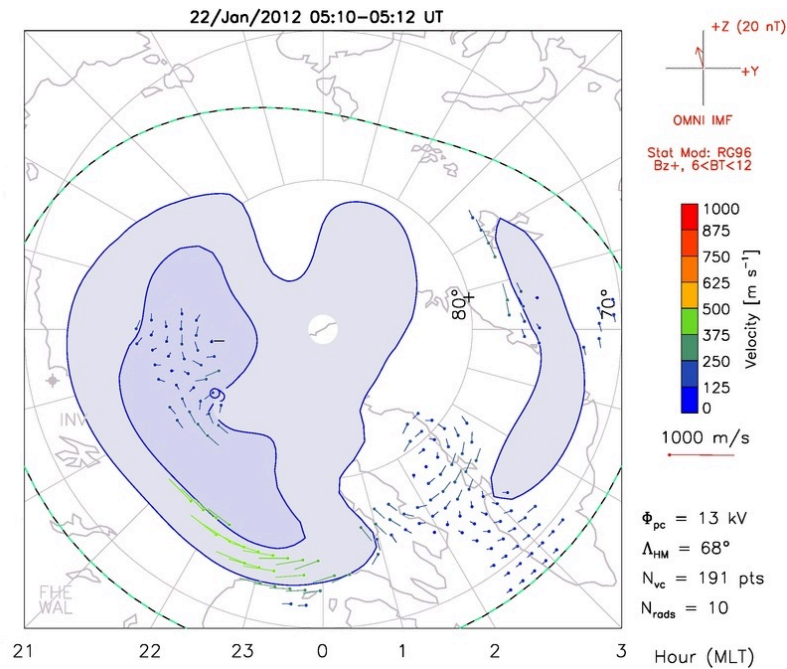


Figure 6.10: Same as Figure 6.8 but for the interval 0510-0512 UT. The anticlockwise ionospheric flow vortex is seen to be weakened substantially at this time.

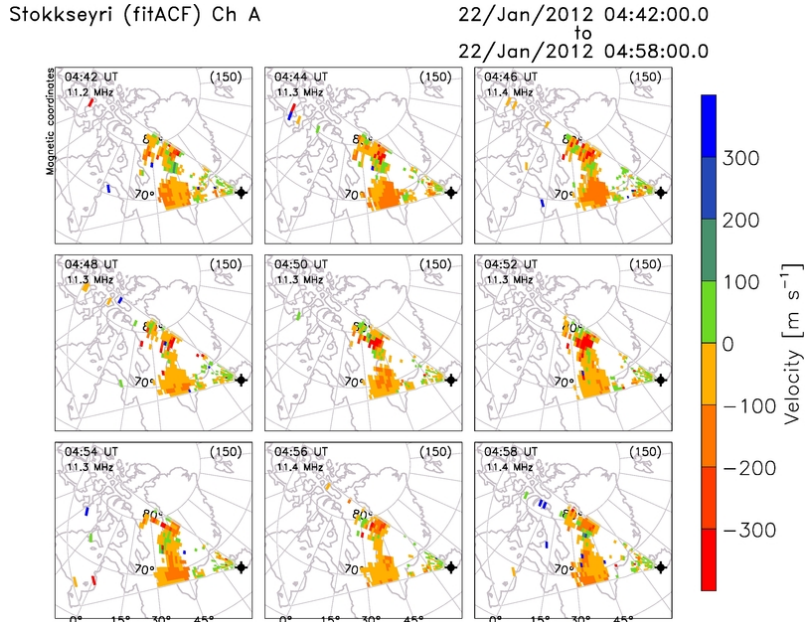


Figure 6.11: The average line of sight velocity (V_{los}) obtained from the HF radars over Stokkseyri, Iceland (64°N , 22°W) on 22 January 2012 during 04:42–05:58 UT. Enhancement of convection (red patches) during 0450-0452 UT can be easily seen. Figure courtesy: M. Ruohoniemi

change in the ionospheric current system over low-equatorial latitudes is not associated with changes in ionization. Thus the magnetic observations with latitudes provide indirect evidence for the change in E-region electric field. Further, as IMF B_y does not change its polarity sharply during 0440-0510 UT when IMF B_z is northward, it is unlikely that the mechanism (unbalanced excess current in one hemisphere under northward IMF B_z and positive IMF B_y conditions partially flowing across the nighttime equatorial zone) offered by *Kelley and Makela (2002)* is operational here.

It is clear from Figure 6.6 that the amplitude of ΔX during 0440-0510 UT at the dayside stations maximizes over the auroral region, falls off over mid and low latitudes and enhances again over the dip equator. As the ΔX amplitude over the polar region is more than those over the sub-auroral and dip equatorial regions, the latitudinal variation depicted in Figure 6.6 points towards the presence of PP electric field during this interval (*Araki, 1977; Koba et al., 2000; Kikuchi et al., 2000*). It is to be noted here that in case of significant enhancement of magnetopause (Chapman-Ferraro) current, one would have expected ΔX amplitude over the dip equator exceeding that over the polar region (*Namikawa et al., 1964*). On the other hand, in the PP scenario, the ionospheric Hall current driven by the high latitude electric field closes through the Pedersen current over the dip equator and hence can generate polarization electric field when its flow is obstructed at the terminator. The ionospheric Pedersen current over the dip equator also gets amplified (*Sastri et al., 2003*) due to Cowling conductivity. Therefore, Figure 6.5 is consistent with the latitudinal characteristics of PP electric field and the generation of this electric field in the present case is associated with the enhancement in solar wind density.

Figure 6.7 brings out the dip equatorial ionospheric signatures of the PP electric field associated with the solar wind density pulse event. Unambiguous enhancement in $\Delta H_{TIR} - \Delta H_{ABG}$ (as shown in Figure 6.7f) when the background

variation is decreasing suggests the enhancement in the eastward electric field perturbation in the E-region during 0440-0510 UT (the shaded interval). Further, the significant rise (by about 23 km) of h_mF2 over Thumba (Figure 6.7e) during the same interval confirms the presence of eastward electric field perturbation in the F-region. The efficacy of daytime h_mF2 in promptly capturing the variations (not magnitude) in the storm time electric field disturbance over the dip equatorial region on occasions, is shown by a few researchers (e.g. [Szuszczewicz et al., 1998](#); [Yue et al., 2008](#)). In the present case, considering a 5 km uncertainty in the determination of h_mF2 , the increase in the F-layer vertical drift during 0438-0506 UT turns out to be $\sim 16.81 \pm 5.2 \text{ ms}^{-1}$. Therefore, simultaneous increases in both h_mF2 and $\Delta H_{TIR} - \Delta H_{ABG}$ during 0440-0510 UT on 22 January, 2012 point towards the prompt electric field disturbance (e.g. [Tsurutani et al., 2004](#); [Sekar et al., 2012](#); [Abdu et al., 2013](#)). Figures 6.7b and 6.7c suggest that this does not happen all the time. Although one can observe small temporal scale fluctuations in h_mF2 and $\Delta H_{TIR} - \Delta H_{ABG}$ probably due to local origin on 20 January as well as on 19 January, 2012, those are not simultaneous fluctuations. Therefore, small temporal scale fluctuations that occurred simultaneously in the dip equatorial E and F-regions during 0440-0510 UT when solar wind density got enhanced strongly point toward the imposition of PP electric field on the equatorial ionosphere. Measurements by a number of independent techniques spread over the globe, provide credence to this proposition. The possible mechanisms through which the equatorial ionosphere can get affected due to the enhancement of solar wind density is addressed in the ensuing paragraph.

The electric field disturbances for about 30-40 min over the dip equatorial ionosphere during enhancements in the solar wind ram pressure were shown by [Huang et al. \(2008\)](#) using Jicamarca drift data. The distinctive point where this investigation is different from the work of [Huang et al. \(2008\)](#) is primarily the isolation of the role of solar wind density in causing the prompt electric

field disturbance. As discussed in [Huang et al. \(2008\)](#), there are two possible mechanisms through which enhancement in solar wind ram pressure can cause prompt electric field disturbance over the equatorial ionosphere. The first mechanism is through the over-compression of the magnetosphere when the solar wind ram pressure enhances. In fact, the compression or decompression of magnetospheric plasma can reach ionosphere by the Alfvén and magnetosonic waves (e.g. [Tamao, 1964](#); [Lysak and Lee, 1992](#); [Lyatsky et al., 2010](#)). [Keller et al. \(2002\)](#) suggests that as the solar wind density pulse propagates along the flank of the magnetopause, a two-step response in field-aligned current (FAC) is expected. In the first step, FACs increase near the polar cap and in the second step the FACs increase near the low latitude. The increase in FAC is also found to be in the same direction as that of region-1 currents. This implies that the azimuthal electric field which is generated inside the magnetosphere due to the earthward motion of the compressed magnetospheric plasma, can penetrate into the low latitude ionosphere ([Shi et al., 2009](#); [Lyatsky et al., 2010](#)). Therefore, this situation is different from the conventional PP scenario in terms of place of origin of the electric field. In the conventional PP scenario, the electric field exists in the solar wind with respect to Earth whereas in this case the electric field is generated inside the magnetosphere. This situation is probably similar to the over compression mechanism discussed by [Huang et al. \(2008\)](#). The distinctive feature associated with this mechanism is the enhancement of the geomagnetic field at all local times. This is what is observed in the present case. The other mechanism is similar to what was proposed by [Araki \(1994\)](#) to explain the main impulse in the low-latitude geomagnetic field in response to solar wind pressure enhancement. The model of [Araki \(1994\)](#) suggests that the low latitude geomagnetic response to the enhancement in the solar wind ram pressure comprises of a preliminary impulse (~ 1 min), a main impulse (~ 10 min) and a step-like increase that continues for some time. While the preliminary impulse and the main impulse are believed to be due to R1-FAC and ionospheric currents, the step-like increase is caused

by the magnetopause current. The characteristic feature in this scenario is the local time differences in the geomagnetic field response. In fact, according to the work of *Araki* (1994) and *Araki et al.* (2006), the effect of main impulse is expected to be highest in the nightside and nominal in the dayside. It can be noted that the present set of observations are not consistent with both the step-like and local time variations in the geomagnetic field features expected from the Araki mechanism. Therefore, the prompt electric field disturbance reported in the present case arose most likely due to the associated effects of over-compression of the magnetosphere due to the density-related changes in the solar wind ram pressure.

Last but not the least, it is important to note that the prompt electric field disturbances presented in this investigation occurs essentially through the increase in the ram pressure. However, based on a case study, it is rather difficult to comment on the differences in the ionospheric effects corresponding to change in solar wind density or velocity. More investigations are needed to address this issue. Further, the mechanism through which magnetosphere is coupled with low latitude ionosphere during the density pulse events is not comprehensively understood. In addition, as the ionospheric electric fields are curl-free, it is expected that the electric field disturbances will have opposite polarity at conjugate longitudes. However, it is not clear how the ionospheric electric field will adjust globally if magnetosphere is compressed asymmetrically by solar wind ram pressure. Global measurements are needed to address this aspect comprehensively.

6.5 Summary:

This case study, based on a unique set of measurements, reveals that a transient change in solar wind density from 10 cc^{-1} to 22 cc^{-1} during 0440-0510 UT under northward IMF B_z condition has not only enhanced the high

latitude convection but also enhanced the global magnetic field as well as equatorial E and F-region electric field simultaneously. The enhanced high latitude ionospheric convection, latitudinal characteristics of the increase in the geomagnetic field strength, enhancement of the geomagnetic field at all local times and the concomitant changes in the equatorial E and F-region parameters elicit the role of solar wind density in generating transient electric field disturbances over the dip equatorial ionosphere possibly through the associated effects of over-compression of the magnetosphere.

Chapter 7

Scope of the Thesis

In the present thesis work, a few scientific issues pertaining to the effects of space weather processes on equatorial ionosphere are addressed. During the course of this work, new scientific problems have emerged and these problems need critical attention in future. These are discussed below.

It is observed from chapter 3 and 5 that the penetration of interplanetary electric field can continue for hours over low latitudes. Neither the existing models nor the observations (*Senior and Blanc, 1984; Somayajulu et al., 1987; Kikuchi et al., 2000*) can explain the mechanism that governs these long duration penetration events. Systematic space based measurements along with modeling studies are required to understand this issue.

Chapter 6 brings out that a small change in solar wind density can drive electric field perturbation in ionosphere on a global scale. However, the mechanism through which this electric field gets generated inside the magnetosphere is an issue that needs further attention. Further, the polarity of PP electric field during the solar wind pressure change is shown to be eastward both in day (*Huang et al., 2008*) as well as in the night (*Sastri, 2002*) sectors over low latitude ionosphere. It is not clear whether changes in ram pressure will generate eastward electric field perturbation all the time or on some occasions. These

issues can be addressed by analyzing large data bases with special emphasis on the rare density pulse events described in this thesis work.

During geomagnetic storms, the DP2 type electric field perturbations are observed over low latitude ionosphere. The periodicities of electric field fluctuations during these events range from a few minutes to a few hours (*Kikuchi et al., 1996; Sastri et al., 2000; Yizengaw et al., 2016*). It is well known that substorms can cause both east and westward PP electric field (*Hui et al., 2017*) perturbations over equatorial ionosphere. So the role of substorms cannot be ignored during the DP2 events. It will be a challenge to understand how substorm modulates the electric field perturbations during DP2 type events. These will help in the understanding of the effects of interactions between storm and substorm.

In Chapter 5, it is shown that the solar wind azimuthal flow angle at L1 point can be an important proxy in deciding the geoeffectiveness of CIR events. It is to be noted that the solar wind flow angle is found to exceed $\pm 20^\circ$ on a few occasions. It is not clear what kind of solar and/or interplanetary processes give rise to the large solar wind flow angle variations. This issue need further attention. Further, on some occasions, the EEJ strengths during the CIR events show causal relationships with IMF Bz although the solar wind azimuthal flow angle is greater than 6° and vice versa. These anomalous cases need explanations in terms of the physical processes. Attempts in this direction will be made.

During the course of this work, it has been noted that the main phase of ring current continues even after the IMF Bz turns northward. This issue can be addressed by using global space weather models like WINDMI and BATS-R-US. These investigations can throw light on the contributions of other current systems (like tail current) in Dst.

References

- Abdu, M. A., J. H. Sastri, H. Luhr, H. Tachihara, T. Kitamura, N. B. Trivedi, and J. H. A. Sobral, DP 2 electric field fluctuations in the dusk-time dip equatorial ionosphere, *Geophysical Research Letters*, *25*(9), 1511–1514, 1998. [77](#)
- Abdu, M. A., J. R. Souza, I. S. Batista, B. G. Fejer, and J. H. A. Sobral, Sporadic E layer development and disruption at low latitudes by prompt penetration electric fields during magnetic storms, *Journal of Geophysical Research: Space Physics*, *118*(5), 2639–2647, 2013. [144](#)
- Akasofu, and J. Chao, Interplanetary shock waves and magnetospheric substorms, *Planetary and Space Science*, *28*(4), 381 – 385, 1980. [101](#), [126](#)
- Akasofu, S., and S. Chapman, The ring current, geomagnetic disturbance, and the van allen radiation belts, *Journal of Geophysical Research*, *66*(5), 1321–1350, 1961. [21](#)
- Alfvén, H., On the effect of a vertical magnetic field in a conducting atmosphere, *Arkiv for Astronomi*, *29*, 1–6, 1943. [5](#)
- Alken, P., and S. Maus, Relationship between the ionospheric eastward electric field and the equatorial electrojet, *Geophysical Research Letters*, *37*(4), L04104, 2010. [48](#), [114](#)
- Alves, M. V., E. Echer, and W. D. Gonzalez, Geoeffectiveness of corotating

- interaction regions as measured by Dst index, *Journal of Geophysical Research: Space Physics*, 111(A7), A07S05, 2006. [8](#)
- Anandarao, B. G., Effects of gravity wave winds and wind shears on equatorial electrojet, *Geophysical Research Letters*, 3(9), 545–548, 1976. [16](#)
- Anderson, D., and D. Rusch, Composition of the nighttime ionospheric F1 region near the magnetic equator, *Journal of Geophysical Research: Space Physics*, 85(A2), 569–574, 1980. [44](#)
- Anderson, D., A. Anghel, K. Yumoto, M. Ishitsuka, and E. Kudeki, Estimating daytime vertical ExB drift velocities in the equatorial F-region using ground-based magnetometer observations, *Geophysical Research Letters*, 29(12), 37–1–37–4, 2002. [48](#)
- Anderson, D., A. Anghel, J. L. Chau, and K. Yumoto, Global, low-latitude, vertical ExB drift velocities inferred from daytime magnetometer observations, *Space Weather*, 4(8), S08003, 2006. [48](#)
- Andriyas, T., and S. Andriyas, Relevance vector machines as a tool for forecasting geomagnetic storms during years 1996–2007, *Journal of Atmospheric and Solar-Terrestrial Physics*, 125126, 10 – 20, 2015. [20](#)
- Araki, T., Global structure of geomagnetic sudden commencements, *Planetary and Space Science*, 25(4), 373 – 384, 1977. [143](#)
- Araki, T., A physical model of the geomagnetic sudden commencement, *Solar Wind Sources of Magnetospheric Ultra-Low-Frequency Waves*, pp. 183–200, 1994. [145](#), [146](#)
- Araki, T., K. Funato, T. Iguchi, and T. Kamei, Direct detection of solar wind dynamic pressure effect on ground geomagnetic field, *Geophysical Research Letters*, 20(9), 775–778, 1993. [140](#)

- Araki, T., K. Keika, T. Kamei, H. Yang, and S. Alex, Nighttime enhancement of the amplitude of geomagnetic sudden commencements and its dependence on IMF Bz, *Earth planets space*, 58(1), 45–50, 2006. [146](#)
- Baker, D., et al., A long-lived relativistic electron storage ring embedded in Earth's outer Van Allen belt, *Science*, 340(6129), 186–190, 2013. [13](#)
- Barbier, D., Les variations d'intensité de la raie 6300 *Astron. & Astrophys. Lett. de la luminescence nocturne*, in *Annales de Geophysique*, vol. 17, p. 3. 1961. [39](#)
- Bartels, J., N. H. Heck, and H. F. Johnston, The three-hour-range index measuring geomagnetic activity, *Terrestrial Magnetism and Atmospheric Electricity*, 44(4), 411–454, 1939. [48](#)
- Belehaki, A., I. Tsagouri, and H. Mavromichalaki, Study of the longitudinal expansion velocity of the substorm current wedge, *Annales Geophysicae*, 16(11), 1423–1433, 1998. [56](#)
- Birn, J., M. F. Thomsen, J. E. Borovsky, G. D. Reeves, D. J. McComas, R. D. Belian, and M. Hesse, Substorm electron injections: Geosynchronous observations and test particle simulations, *Journal of Geophysical Research: Space Physics*, 103(A5), 9235–9248, 1998. [76](#)
- Bittencourt, J. A., and M. A. Abdu, A theoretical comparison between apparent and real vertical ionization drift velocities in the equatorial F region, *Journal of Geophysical Research: Space Physics*, 86(A4), 2451–2454, 1981. [43](#), [57](#), [130](#)
- Blanc, M., and A. Richmond, The ionospheric disturbance dynamo, *Journal of Geophysical Research: Space Physics*, 85(A4), 1669–1686, 1980. [33](#), [57](#)
- Borovsky, J. E., The rudiments of a theory of solar wind/magnetosphere coupling derived from first principles, *Journal of Geophysical Research: Space Physics*, 113(A8), A08228, 2008. [123](#)

- Borovsky, J. E., and J. Birn, The solar wind electric field does not control the dayside reconnection rate, *Journal of Geophysical Research: Space Physics*, 119(2), 751–760, 2014. [123](#)
- Borovsky, J. E., M. Hesse, J. Birn, and M. M. Kuznetsova, What determines the reconnection rate at the dayside magnetosphere?, *Journal of Geophysical Research: Space Physics*, 113(A7), A07210, 2008. [123](#)
- Bothmer, V., and I. A. Daglis, *Space weather: physics and effects*. Springer Science & Business Media, 2007. [1](#)
- Buonsanto, M., S. Gonzalez, X. Pi, J. Ruohoniemi, M. Sulzer, W. Swartz, J. Thayer, and D. Yuan, Radar chain study of the May, 1995 storm, *Journal of Atmospheric and Solar-Terrestrial Physics*, 61(34), 233 – 248, 1999. [101](#)
- Burlaga, L. F., K. W. Behannon, and L. W. Klein, Compound streams, magnetic clouds, and major geomagnetic storms, *Journal of Geophysical Research: Space Physics*, 92(A6), 5725–5734, 1987.
- Burns, A., S. Solomon, L. Qian, W. Wang, B. Emery, M. Wiltberger, and D. Weimer, The effects of corotating interaction region/high speed stream storms on the thermosphere and ionosphere during the last solar minimum, *Journal of Atmospheric and Solar-Terrestrial Physics*, 83, 79 – 87, 2012. [109](#)
- Burnside, R. G., F. A. Herrero, J. W. Meriwether, and J. C. G. Walker, Optical observations of thermospheric dynamics at Arecibo, *Journal of Geophysical Research: Space Physics*, 86(A7), 5532–5540, 1981. [50](#)
- Cayton, T., and M. Tuszewski, Improved electron fluxes from the synchronous orbit particle analyzer, *Space Weather*, 3(11), 2005. [46](#)
- Chakrabarty, D., Investigations on the F region of the ionosphere over low latitudes using optical, radio and simulation techniques, 2007. [39](#)

- Chakrabarty, D., R. Sekar, R. Narayanan, C. V. Devasia, and B. M. Pathan, Evidence for the interplanetary electric field effect on the OI 630.0 nm air-glow over low latitude, *Journal of Geophysical Research: Space Physics*, 110(A11), 2005. [32](#), [39](#), [57](#), [58](#), [100](#)
- Chakrabarty, D., R. Sekar, R. Narayanan, A. K. Patra, and C. V. Devasia, Effects of interplanetary electric field on the development of an equatorial spread F event, *Journal of Geophysical Research: Space Physics*, 111(A12), A12316, 2006. [56](#), [77](#)
- Chakrabarty, D., R. Sekar, J. H. Sastri, and S. Ravindran, Distinctive effects of interplanetary electric field and substorm on nighttime equatorial F layer: A case study, *Geophysical Research Letters*, 35(19), 2008. [32](#), [100](#), [120](#)
- Chakrabarty, D., R. Sekar, J. H. Sastri, B. M. Pathan, G. D. Reeves, K. Yumoto, and T. Kikuchi, Evidence for OI 630.0 nm dayglow variations over low latitudes during onset of a substorm, *Journal of Geophysical Research: Space Physics*, 115(A10), 2010. [58](#)
- Chakrabarty, D., B. G. Fejer, S. Gurubaran, T. K. Pant, M. A. Abdu, and R. Sekar, On the pre-midnight ascent of F-layer in the june solstice during the deep solar minimum in 2008 over the indian sector, *Journal of Atmospheric and Solar-Terrestrial Physics*, 2014. [56](#), [61](#), [62](#)
- Chakrabarty, D., D. Rout, R. Sekar, R. Narayanan, G. D. Reeves, T. K. Pant, B. Veenadhari, and K. Shiokawa, Three different types of electric field disturbances affecting equatorial ionosphere during a long duration prompt penetration event, *Journal of Geophysical Research: Space Physics*, 2014JA020759, 2015. [92](#), [100](#), [104](#), [120](#)
- Chakrabarty, D., D. Hui, D. Rout, R. Sekar, A. Bhattacharyya, G. D. Reeves, and J. M. Ruohoniemi, Role of IMF By in the prompt electric field disturbances over equatorial ionosphere during a space weather event, *Journal*

- of Geophysical Research: Space Physics*, 122(2), 2574–2588, 2016JA022781, 2017. [26](#), [83](#), [84](#)
- Chi, E. C., S. B. Mende, M.-C. Fok, and G. D. Reeves, Proton auroral intensifications and injections at synchronous altitude, *Geophysical Research Letters*, 33(6), 2006. [76](#)
- Chisham, G., et al., A decade of the super dual auroral radar network (superdarn): scientific achievements, new techniques and future directions, *Surveys in Geophysics*, 28(1), 33–109, 2007. [45](#)
- Crowley, G., A. Reynolds, J. P. Thayer, J. Lei, L. J. Paxton, A. B. Christensen, Y. Zhang, R. R. Meier, and D. J. Strickland, Periodic modulations in thermospheric composition by solar wind high speed streams, *Geophysical Research Letters*, 35(21), L21106, 2008. [109](#)
- Davis, T. N., and M. Sugiura, Auroral electrojet activity index ae and its universal time variations, *Journal of Geophysical Research*, 71(3), 785–801, 1966. [49](#)
- Deng, Y., Y. Huang, J. Lei, A. J. Ridley, R. Lopez, and J. Thayer, Energy input into the upper atmosphere associated with high-speed solar wind streams in 2005, *Journal of Geophysical Research: Space Physics*, 116(A5), A05303, 2011. [109](#)
- Denton, M. H., J. E. Borovsky, R. M. Skoug, M. F. Thomsen, B. Lavraud, M. G. Henderson, R. L. McPherron, J. C. Zhang, and M. W. Liemohn, Geomagnetic storms driven by ICME- and CIR-dominated solar wind, *Journal of Geophysical Research: Space Physics*, 111(A7), A07S07, 2006. [108](#)
- Despirak, I., A. Lubchich, A. Yahnin, B. Kozelov, and H. Biernat, Development of substorm bulges during different solar wind structures, *Ann. Geophys*, 27(5), 1951–1960, 2009. [88](#)

- Despirak, I., A. Lubchich, and V. Guineva, Development of substorm bulges during storms of different interplanetary origins, *Journal of Atmospheric and Solar-Terrestrial Physics*, 73(1112), 1460 – 1464, 2011. [88](#)
- Dungey, J. W., Interplanetary magnetic field and the auroral zones, *Physical Review Letters*, 6, 47–48, 1961. [19](#), [27](#), [99](#)
- Erickson, P., L. Goncharenko, M. Nicolls, M. Ruohoniemi, and M. Kelley, Dynamics of north american sector ionospheric and thermospheric response during the november 2004 superstorm, *Journal of Atmospheric and Solar-Terrestrial Physics*, 72(4), 292 – 301, 2010. [101](#)
- Fejer, B., Low latitude electrodynamic plasma drifts: a review, *Journal of Atmospheric and Terrestrial Physics*, 53(8), 677 – 693, 1991. [16](#)
- Fejer, B. G., F region plasma drifts over Arecibo: Solar cycle, seasonal, and magnetic activity effects, *Journal of Geophysical Research: Space Physics*, 98(A8), 13645–13652, 1993. [92](#), [93](#)
- Fejer, B. G., and L. Scherliess, Empirical models of storm time equatorial zonal electric fields, *Journal of Geophysical Research: Space Physics*, 102(A11), 24047–24056, 1997. [16](#), [30](#), [31](#), [56](#)
- Fejer, B. G., E. R. de Paula, S. A. Gonzalez, and R. F. Woodman, Average vertical and zonal F region plasma drifts over Jicamarca, *Journal of Geophysical Research: Space Physics*, 96(A8), 13901–13906, 1991. [16](#)
- Fejer, B. G., J. R. Souza, A. S. Santos, and A. E. Costa Pereira, Climatology of F region zonal plasma drifts over Jicamarca, *Journal of Geophysical Research: Space Physics*, 110(A12), A12310, 2005. [16](#)
- Fejer, B. G., J. W. Jensen, T. Kikuchi, M. A. Abdu, and J. L. Chau, Equatorial Ionospheric Electric Fields During the November 2004 Magnetic Storm, *Journal of Geophysical Research: Space Physics*, 112(A10), A10304, 2007. [26](#), [56](#), [123](#)

- Fejer, B. G., J. W. Jensen, and S.-Y. Su, Seasonal and longitudinal dependence of equatorial disturbance vertical plasma drifts, *Geophysical Research Letters*, 35(20), 2008. [17](#), [56](#), [63](#), [101](#), [105](#)
- Forbes, T. G., A review on the genesis of coronal mass ejections, *Journal of Geophysical Research: Space Physics*, 105(A10), 23153–23165, 2000. [6](#)
- Forsyth, R., and E. Marsch, Solar origin and interplanetary evolution of stream interfaces, *Space Science Review*, 89(1), 7–20, 1999. [8](#), [108](#), [110](#), [118](#)
- Fukushima, N., and Y. Kamide, Partial ring current models for worldwide geomagnetic disturbances, *Reviews of Geophysics*, 11(4), 795–853, 1973. [30](#)
- Gjerloev, J. W., The supermag data processing technique, *Journal of Geophysical Research: Space Physics*, 117(A9), A09213, 2012. [47](#)
- Gonzalez, W. D., J. A. Joselyn, Y. Kamide, H. W. Kroehl, G. Rostoker, B. T. Tsurutani, and V. M. Vasylunas, What is a geomagnetic storm?, *Journal of Geophysical Research: Space Physics*, 99(A4), 5771–5792, 1994. [21](#)
- Gosling, J. T., Coronal mass ejections and magnetic flux ropes in interplanetary space, *Physics of Magnetic Flux Ropes*, pp. 343–364, 1990. [6](#)
- Gosling, J. T., and D. J. McComas, Field line draping about fast coronal mass ejecta: A source of strong out-of-the-ecliptic interplanetary magnetic fields, *Geophysical Research Letters*, 14(4), 355–358, 1987. [7](#)
- Guo, J., X. Feng, P. Zuo, J. Zhang, Y. Wei, and Q. Zong, Interplanetary drivers of ionospheric prompt penetration electric fields, *Journal of Atmospheric and Solar-Terrestrial Physics*, 73(1), 130 – 136, 2011. [89](#)
- Hargreaves, J. K., *The solar-terrestrial environment: an introduction to geospace-the science of the terrestrial upper atmosphere, ionosphere, and magnetosphere*. Cambridge University Press, 1992. [50](#)

- Hashimoto, K. K., T. Kikuchi, S. Watari, and M. A. Abdu, Polar-equatorial ionospheric currents driven by the region 2 field-aligned currents at the onset of substorms, *Journal of Geophysical Research: Space Physics*, 116(A9), 2011. [76](#), [104](#)
- Hedin, A. E., Extension of the MSIS Thermosphere Model into the middle and lower atmosphere, *Journal of Geophysical Research: Space Physics*, 96(A2), 1159–1172, 1991. [44](#)
- Heelis, R., J. K. Lowell, and R. W. Spiro, A model of the high-latitude ionospheric convection pattern, *Journal of Geophysical Research: Space Physics*, 87(A8), 6339–6345, 1982. [29](#)
- Henderson, M. G., G. D. Reeves, R. D. Belian, and J. S. Murphree, Observations of magnetospheric substorms occurring with no apparent solar wind/IMF trigger, *Journal of Geophysical Research: Space Physics*, 101(A5), 10773–10791, 1996. [22](#)
- Huang, C. M., Disturbance dynamo electric fields in response to geomagnetic storms occurring at different universal times, *Journal of Geophysical Research: Space Physics*, 118(1), 496–501, 2013. [25](#), [33](#)
- Huang, C.-S., Eastward electric field enhancement and geomagnetic positive bay in the dayside low-latitude ionosphere caused by magnetospheric substorms during sawtooth events, *Geophysical Research Letters*, 36(18), 2009. [25](#)
- Huang, C.-S., Statistical analysis of dayside equatorial ionospheric electric fields and electrojet currents produced by magnetospheric substorms during sawtooth events, *Journal of Geophysical Research: Space Physics*, 117(A2), A02316, 2012. [25](#), [56](#)
- Huang, C.-S., J. C. Foster, L. P. Goncharenko, G. D. Reeves, J. L. Chau, K. Yumoto, and K. Kitamura, Variations of low-latitude geomagnetic fields

- and Dst index caused by magnetospheric substorms, *Journal of Geophysical Research: Space Physics*, 109(A5), 2004. [25](#), [77](#)
- Huang, C.-S., J. C. Foster, and M. C. Kelley, Long-duration penetration of the interplanetary electric field to the low-latitude ionosphere during the main phase of magnetic storms, *Journal of Geophysical Research: Space Physics*, 110(A11), 2005. [26](#), [32](#), [58](#), [104](#), [120](#)
- Huang, C.-S., S. Sazykin, J. L. Chau, N. Maruyama, and M. C. Kelley, Penetration electric fields: Efficiency and characteristic time scale, *Journal of Atmospheric and Solar-Terrestrial Physics*, 69(10), 1135–1146, 2007. [32](#)
- Huang, C.-S., K. Yumoto, S. Abe, and G. Sofko, Low-latitude ionospheric electric and magnetic field disturbances in response to solar wind pressure enhancements, *Journal of Geophysical Research: Space Physics*, 113(A8), A08314, 2008. [126](#), [128](#), [144](#), [145](#), [149](#)
- Hui, D., D. Chakrabarty, R. Sekar, G. D. Reeves, A. Yoshikawa, and K. Shiokawa, Contribution of storm time substorms to the prompt electric field disturbances in the equatorial ionosphere, *Journal of Geophysical Research: Space Physics*, 2016JA023754, 2017. [25](#), [103](#), [150](#)
- Huttunen, K. E. J., and H. E. J. Koskinen, Importance of post-shock streams and sheath region as drivers of intense magnetospheric storms and high-latitude activity, *Annales Geophysicae*, 22(5), 1729–1738, 2004. [88](#), [99](#)
- Huttunen, K. E. J., H. E. J. Koskinen, and R. Schwenn, Variability of magnetospheric storms driven by different solar wind perturbations, *Journal of Geophysical Research: Space Physics*, 107(A7), SMP 20–1–SMP 20–8, 2002. [88](#)
- Huttunen, K. E. J., H. E. J. Koskinen, A. Karinen, and K. Mursula, Asymmetric development of magnetospheric storms during magnetic clouds and sheath regions, *Geophysical Research Letters*, 33(6), L06107, 2006. [88](#)

- Iijima, T., and T. A. Potemra, The amplitude distribution of field-aligned currents at northern high latitudes observed by Triad, *Journal of Geophysical Research*, *81*(13), 2165–2174, 1976. [30](#)
- Jaggi, R. K., and R. A. Wolf, Self-consistent calculation of the motion of a sheet of ions in the magnetosphere, *Journal of Geophysical Research*, *78*(16), 2852–2866, 1973. [30](#)
- Janardhan, P., K. Fujiki, M. Kojima, M. Tokumaru, and K. Hakamada, Resolving the enigmatic solar wind disappearance event of 11 May 1999, *Journal of Geophysical Research: Space Physics*, *110*(A8), A08101, 2005. [108](#)
- Janardhan, P., D. Tripathi, and H. Mason, The solar wind disappearance event of 11 May 1999: source region evolution, *Astronomy & Astrophysics*, *488*(1), L1–L4, 2008. [108](#)
- Janzhura, A., O. Troshichev, and P. Stauning, Unified PC indices: Relation to isolated magnetic substorms, *Journal of Geophysical Research: Space Physics*, *112*(A9), 2007. [75](#), [103](#)
- Jian, L., C. T. Russell, J. G. Luhmann, and R. M. Skoug, Properties of stream interactions at one AU during 1995-2004, *Solar Physics*, *239*(1), 337–392, 2006. [8](#)
- Johnson, J. R., and S. Wing, External versus internal triggering of substorms: An information-theoretical approach, *Geophysical Research Letters*, *41*(16), 5748–5754, 2014. [22](#)
- Kamide, Y., A. Richmond, and S. Matsushita, Estimation of ionospheric electric fields, ionospheric currents, and field-aligned currents from ground magnetic records, *Journal of Geophysical Research: Space Physics*, *86*(A2), 801–813, 1981. [29](#)

- Kamide, Y., et al., Current understanding of magnetic storms: Storm-substorm relationships, *Journal of Geophysical Research: Space Physics*, 103(A8), 17705–17728, 1998. [8](#)
- Kan, J. R., and L. C. Lee, Energy coupling function and solar wind-magnetosphere dynamo, *Geophysical Research Letters*, 6(7), 577–580, 1979. [122](#)
- Kataoka, R., and Y. Miyoshi, Flux enhancement of radiation belt electrons during geomagnetic storms driven by coronal mass ejections and corotating interaction regions, *Space Weather*, 4(9), S09004, 2006. [9](#)
- Kataoka, R., S. Watari, N. Shimada, H. Shimazu, and K. Marubashi, Downstream structures of interplanetary fast shocks associated with coronal mass ejections, *Geophysical Research Letters*, 32(12), L12103, 2005. [98](#)
- Keller, K. A., M. Hesse, M. Kuznetsova, L. Rasttter, T. Moretto, T. I. Gombosi, and D. L. DeZeeuw, Global mhd modeling of the impact of a solar wind pressure change, *Journal of Geophysical Research: Space Physics*, 107(A7), 2002. [145](#)
- Kelley, M., M. Nicolls, D. Anderson, A. Anghel, J. Chau, R. Sekar, K. Subbarao, and A. Bhattacharyya, Multi-longitude case studies comparing the interplanetary and equatorial ionospheric electric fields using an empirical model, *Journal of Atmospheric and Solar-Terrestrial Physics*, 69(1011), 1174 – 1181, 2007. [83](#), [101](#)
- Kelley, M. C., The Earths ionosphere, *International Geophysics Series*, 43, 71, 1989. [15](#)
- Kelley, M. C., and J. J. Makela, By dependent prompt penetrating electric fields at the magnetic equator, *Geophysical Research Letters*, 29(7), 571–573, 2002. [26](#), [143](#)

- Kelley, M. C., J. J. Makela, J. L. Chau, and M. J. Nicolls, Penetration of the solar wind electric field into the magnetosphere/ionosphere system, *Geophysical Research Letters*, *30*(4), 1158, 2003. [26](#), [31](#), [32](#), [57](#), [109](#)
- Kepko, L., et al., Substorm Current Wedge Revisited, *Space Science Reviews*, *190*(1), 1–46, 2015. [25](#)
- Kikuchi, T., H. Lhr, T. Kitamura, O. Saka, and K. Schlegel, Direct penetration of the polar electric field to the equator during a DP 2 event as detected by the auroral and equatorial magnetometer chains and the eiscat radar, *Journal of Geophysical Research: Space Physics*, *101*(A8), 17161–17173, 1996. [100](#), [150](#)
- Kikuchi, T., H. Lhr, K. Schlegel, H. Tachihara, M. Shinohara, and T.-I. Kitamura, Penetration of auroral electric fields to the equator during a substorm, *Journal of Geophysical Research: Space Physics*, *105*(A10), 23251–23261, 2000. [32](#), [100](#), [143](#), [149](#)
- Kikuchi, T., K. K. Hashimoto, T.-I. Kitamura, H. Tachihara, and B. Fejer, Equatorial counterjets during substorms, *Journal of Geophysical Research: Space Physics*, *108*(A11), 1406, 2003. [25](#), [56](#), [98](#), [104](#)
- Kivelson, M., and C. Russell, Introduction to space physics, cambridge, univ, 1995. [3](#), [4](#), [12](#), [13](#), [14](#), [23](#), [27](#), [49](#)
- Klimenko, M., and V. Klimenko, Disturbance dynamo, prompt penetration electric field and overshielding in the Earths ionosphere during geomagnetic storm, *Journal of Atmospheric and Solar-Terrestrial Physics*, *90*, 146 – 155, 2012. [33](#)
- Kobea, A. T., A. D. Richmond, B. A. Emery, C. Peymirat, H. Lhr, T. Moretto, M. Hairston, and C. Amory-Mazaudier, Electrodynamical coupling of high and low latitudes: Observations on May 27, 1993, *Journal of Geophysical Research: Space Physics*, *105*(A10), 22979–22989, 2000. [143](#)

- Korth, A., E. Echer, Q.-G. Zong, F. Guarnieri, M. Fraenz, and C. Mouikis, The response of the polar cusp to a high-speed solar wind stream studied by a multispacecraft wavelet analysis, *Journal of Atmospheric and Solar-Terrestrial Physics*, 73(1), 52 – 60, 2011. [115](#), [120](#)
- Koskinen, H. E. J., R. E. Lopez, R. J. Pellinen, T. I. Pulkkinen, D. N. Baker, and T. Bösinger, Pseudobreakup and substorm growth phase in the ionosphere and magnetosphere, *Journal of Geophysical Research: Space Physics*, 98(A4), 5801–5813, 1993. [75](#)
- Le, G., J. A. Slavin, and R. J. Strangeway, Space technology 5 observations of the imbalance of regions 1 and 2 field-aligned currents and its implication to the cross-polar cap Pedersen currents, *Journal of Geophysical Research: Space Physics*, 115(A7), A07202, 2010. [29](#)
- Le Huy, M., and C. Amory-Mazaudier, Magnetic signature of the ionospheric disturbance dynamo at equatorial latitudes: Ddyn, *Journal of Geophysical Research: Space Physics*, 110(A10), A10301, 2005. [33](#)
- Lee, D.-Y., L. R. Lyons, and K. Yumoto, Sawtooth oscillations directly driven by solar wind dynamic pressure enhancements, *Journal of Geophysical Research: Space Physics*, 109(A4), A04202, 2004. [138](#), [139](#)
- Lee, D.-Y., L. R. Lyons, and G. D. Reeves, Comparison of geosynchronous energetic particle flux responses to solar wind dynamic pressure enhancements and substorms, *Journal of Geophysical Research: Space Physics*, 110(A9), A09213, 2005. [138](#), [139](#)
- Lee, D.-Y., L. R. Lyons, J. M. Weygand, and C.-P. Wang, Reasons why some solar wind changes do not trigger substorms, *Journal of Geophysical Research: Space Physics*, 112(A6), 2007. [76](#)
- Lei, J., J. P. Thayer, J. M. Forbes, Q. Wu, C. She, W. Wan, and W. Wang,

- Ionosphere response to solar wind high-speed streams, *Geophysical Research Letters*, *35*(19), L19105, 2008. [109](#)
- Li, H., C. Wang, and J. R. Kan, Contribution of the partial ring current to the SYM-H index during magnetic storms, *Journal of Geophysical Research: Space Physics*, *116*(A11), A11222, 2011. [30](#)
- Li, X., D. N. Baker, M. Temerin, G. D. Reeves, and R. D. Belian, Simulation of dispersionless injections and drift echoes of energetic electrons associated with substorms, *Geophysical Research Letters*, *25*(20), 3763–3766, 1998. [25](#)
- Li, X., et al., Energetic particle injections in the inner magnetosphere as a response to an interplanetary shock, *Journal of Atmospheric and Solar-Terrestrial Physics*, *65*(2), 233 – 244, 2003. [138](#)
- Liu, J., L. Liu, B. Zhao, W. Wan, and R. A. Heelis, Response of the top-side ionosphere to recurrent geomagnetic activity, *Journal of Geophysical Research: Space Physics*, *115*(A12), A12327, 2010. [109](#)
- Liu, J.-M., B.-C. Zhang, Y. Kamide, Z.-S. Wu, Z.-J. Hu, and H.-G. Yang, Spontaneous and trigger-associated substorms compared: Electrodynamical parameters in the polar ionosphere, *Journal of Geophysical Research: Space Physics*, *116*(A1), A01207, 2011. [22](#)
- Lomb, N. R., Least-squares frequency analysis of unequally spaced data, *Astrophysics and space science*, *39*(2), 447–462, 1976. [52](#)
- Lopez, R. E., M. Wiltberger, S. Hernandez, and J. G. Lyon, Solar wind density control of energy transfer to the magnetosphere, *Geophysical Research Letters*, *31*(8), L08804, 2004. [128](#)
- Lyatsky, W., G. V. Khazanov, and J. A. Slavin, Alfvén wave reflection model of field-aligned currents at Mercury, *Icarus*, *209*(1), 40 – 45, 2010. [145](#)

- Lyons, L. R., Substorms: Fundamental observational features, distinction from other disturbances, and external triggering, *Journal of Geophysical Research: Space Physics*, 101(A6), 13011–13025, 1996. [58](#), [76](#)
- Lyons, L. R., D.-Y. Lee, S. Zou, C.-P. Wang, J. U. Kozyra, J. M. Weygand, and S. B. Mende, Dynamic pressure enhancements as a cause of large-scale stormtime substorms, *Journal of Geophysical Research: Space Physics*, 113(A8), 2008. [58](#), [76](#)
- Lysak, R. L., and D.-h. Lee, Response of the dipole magnetosphere to pressure pulses, *Geophysical Research Letters*, 19(9), 937–940, 1992. [145](#)
- Manchester, W., T. I. Gombosi, D. L. D. Zeeuw, I. V. Sokolov, I. I. Roussev, K. G. Powell, J. Kta, G. Tth, and T. H. Zurbuchen, Coronal mass ejection shock and sheath structures relevant to particle acceleration, *The Astrophysical Journal*, 622(2), 1225, 2005. [88](#)
- Martinis, C. R., M. J. Mendillo, and J. Aarons, Toward a synthesis of equatorial spread F onset and suppression during geomagnetic storms, *Journal of Geophysical Research: Space Physics*, 110(A7), A07306, 2005. [18](#)
- Maruyama, N., A. D. Richmond, T. J. Fuller-Rowell, M. V. Codrescu, S. Sazykin, F. R. Toffoletto, R. W. Spiro, and G. H. Millward, Interaction between direct penetration and disturbance dynamo electric fields in the storm-time equatorial ionosphere, *Geophysical Research Letters*, 32(17), L17105, 2005. [33](#)
- McComas, D. J., et al., Solar wind observations over Ulysses' first full polar orbit, *Journal of Geophysical Research: Space Physics*, 105(A5), 10419–10433, 2000. [108](#)
- McPherron, R., Physical processes producing magnetospheric substorms and magnetic storms., in *Geomagnetism*, vol. 1, pp. 593–739. 1991. [73](#)

- McPherron, R. L., C. Russell, and M. Aubry, Satellite studies of magnetospheric substorms on August 15, 1968: 9. Phenomenological model for substorms, *Journal of Geophysical Research: Space Physics*, 78(16), 3131–3149, 1973. [73](#)
- Murthy, B. K., and S. Hari, Electric fields in the low latitude F-region, *Advances in Space Research*, 18(6), 93–98, 1996. [63](#)
- Nagatsuma, T., T. Obara, and H. Ishibashi, Relationship between solar wind parameters and magnetic activity in the near-pole region: Application to space weather forecasting, *Advances in Space Research*, 26(1), 103 – 106, 2000. [101](#)
- Nakamura, R., D. N. Baker, T. Yamamoto, R. D. Belian, E. A. Bering, J. R. Benbrook, and J. R. Theall, Particle and field signatures during pseudo-breakup and major expansion onset, *Journal of Geophysical Research: Space Physics*, 99(A1), 207–221, 1994. [75](#), [103](#)
- Namikawa, T., T. Kitamura, T. Okuzawa, and T. Araki, Propagation of weak hydromagnetic discontinuity in the magnetosphere and the sudden commencement of geomagnetic storm, *Rept. Ionosphere Space Res. Japan*, 18, 1964. [143](#)
- Neugebauer, M., and C. W. Snyder, Solar plasma experiment, *Science*, 138(3545), 1095–1097, 1962. [3](#)
- Nishida, A., Geomagnetic DP 2 fluctuations and associated magnetospheric phenomena, *Journal of Geophysical Research: Space Physics*, 73(5), 1795–1803, 1968. [26](#), [56](#), [100](#), [120](#)
- Nopper, R. W., and R. L. Carovillano, Polar-equatorial coupling during magnetically active periods, *Geophysical Research Letters*, 5(8), 699–702, 1978. [31](#), [77](#), [86](#), [101](#), [105](#)

- Obayashi, T., and A. Nishida, Large-scale electric field in the magnetosphere, *Space Science Reviews*, 8(1), 3–31, 1968. [25](#)
- Ohtani, S., and T. Uozumi, Nightside magnetospheric current circuit: Time constants of the solar wind-magnetosphere coupling, *Journal of Geophysical Research: Space Physics*, 119(5), 3558–3572, 2013JA019680, 2014. [120](#)
- Oliveira, D. M., and J. Raeder, Impact angle control of interplanetary shock geoeffectiveness: A statistical study, *Journal of Geophysical Research: Space Physics*, 120(6), 4313–4323, 2015JA021147, 2015. [98](#), [123](#)
- Owens, M. J., and P. Cargill, Non-radial solar wind flows induced by the motion of interplanetary coronal mass ejections, in *Annales Geophysicae*, vol. 22, pp. 4397–4406. European Geosciences Union, 2004. [108](#)
- Pallamraju, D., U. Das, and S. Chakrabarti, Short- and long-timescale thermospheric variability as observed from OI 630.0 nm dayglow emissions from low latitudes, *Journal of Geophysical Research: Space Physics*, 115(A6), A06312, 2010. [56](#), [109](#)
- Pandey, K., R. Sekar, B. G. Anandarao, S. P. Gupta, and D. Chakrabarty, Estimation of nighttime dip-equatorial E-region current density using measurements and models, *Journal of Atmospheric and Solar-Terrestrial Physics*, 146, 160–170, 2016. [16](#)
- Pandey, K., R. Sekar, S. P. Gupta, D. Chakrabarty, and B. G. Anandarao, Comparison of quiet time vertical plasma drifts with global empirical models over the indian sector: Some insights, *Journal of Atmospheric and Solar-Terrestrial Physics*, 157158, 42 – 54, 2017. [47](#)
- Parker, E., Dynamical theory of the solar wind, *Space Science Reviews*, 4(5-6), 666–708, 1965. [5](#)

- Pedatella, N. M., J. Lei, J. P. Thayer, and J. M. Forbes, Ionosphere response to recurrent geomagnetic activity: Local time dependency, *Journal of Geophysical Research: Space Physics*, 115(A2), A02301, 2010. [109](#)
- Peymirat, C., A. Richmond, and A. Koba, Electrodynamical coupling of high and low latitudes: Simulations of shielding/overshielding effects, *Journal of Geophysical Research: Space Physics*, 105(A10), 22991–23003, 2000. [32](#)
- Pizzo, V., A three-dimensional model of corotating streams in the solar wind, 1. Theoretical foundations, *Journal of Geophysical Research: Space Physics*, 83(A12), 5563–5572, 1978. [8](#), [9](#)
- Pizzo, V. J., The evolution of corotating stream fronts near the ecliptic plane in the inner solar system, 1. Two dimensional fronts, *Journal of Geophysical Research: Space Physics*, 94(A7), 8673–8684, 1989. [108](#)
- Pulkkinen, T., Space Weather: Terrestrial Perspective, *Living Reviews in Solar Physics*, 4(1), 2007. [25](#)
- Pulkkinen, T. I., Pseudobreakup or substorm?, in *International Conference on Substorms*, vol. 389, p. 285. 1996. [22](#)
- Pulkkinen, T. I., et al., Two substorm intensifications compared: Onset, expansion, and global consequences, *Journal of Geophysical Research: Space Physics*, 103(A1), 15–27, 1998. [22](#), [74](#), [75](#), [103](#)
- Pulkkinen, T. I., et al., Magnetospheric current systems during stormtime sawtooth events, *Journal of Geophysical Research: Space Physics*, 111(A11), A11S17, 2006. [99](#)
- Pulkkinen, T. I., N. Partamies, K. E. J. Huttunen, G. D. Reeves, and H. E. J. Koskinen, Differences in geomagnetic storms driven by magnetic clouds and ICME sheath regions, *Geophysical Research Letters*, 34(2), L02105, 2007. [88](#), [99](#), [101](#)

- Qian, L., S. C. Solomon, and M. G. Mlynczak, Model simulation of thermospheric response to recurrent geomagnetic forcing, *Journal of Geophysical Research: Space Physics*, 115(A10), A10301, 2010. [109](#)
- Rastogi, R., and A. Patil, Complex structure of equatorial electrojet current, *Current Sciences*, 55(9), 434, 1986. [47](#)
- Reddy, C., and C. Devasia, Short period fluctuations of the equatorial electrojet, *Nature*, 261(5559), 396–397, 1976. [120](#)
- Reeves, G., et al., IMAGE, POLAR, and geosynchronous observations of substorm and ring current ion injection, *Disturbances in Geospace: The Storm-Substorm Relationship*, pp. 91–101, 2003. [23](#), [103](#)
- Reeves, G. D., New perspectives on substorm injections, Tech. rep., Los Alamos National Lab., NM (United States), 1998. [22](#), [24](#), [138](#)
- Reeves, G. D., R. D. Belian, and T. A. Fritz, Numerical tracing of energetic particle drifts in a model magnetosphere, *Journal of Geophysical Research: Space Physics*, 96(A8), 13997–14008, 1991. [46](#), [75](#)
- Reinisch, B., and X. Huang, Deducing topside profiles and total electron content from bottomside ionograms, *Advances in Space Research*, 27(1), 23 – 30, 2001. [130](#)
- Ridley, A. J., and M. W. Liemohn, A model-derived storm time asymmetric ring current driven electric field description, *Journal of Geophysical Research: Space Physics*, 107(A8), SMP 2–1–SMP 2–12, 2002. [29](#), [30](#)
- Rishbeth, H., The F-region dynamo, *Journal of Atmospheric and Terrestrial Physics*, 43(5-6), 387–392, 1981. [16](#)
- Rostoker, G., On the place of the pseudo-breakup in a magnetospheric substorm, *Geophysical Research Letters*, 25(2), 217–220, 1998. [74](#), [75](#)

- Rouillard, A., Relating white light and in situ observations of coronal mass ejections: A review, *Journal of Atmospheric and Solar-Terrestrial Physics*, *73*(10), 1201–1213, 2011. [6](#), [7](#)
- Rout, D., D. Chakrabarty, P. Janardhan, R. Sekar, V. Maniya, and K. Pandey, Solar wind flow angle and geoeffectiveness of corotating interaction regions: First results, *Geophysical Research Letters*, 2017GL073038, 2017. [100](#)
- Russell, C., The solar wind interaction with the Earth's magnetosphere: a tutorial, *IEEE transactions on plasma science*, *28*(6), 1818–1830, 2000. [19](#)
- Sakai, J., K. Hosokawa, S. Taguchi, and Y. Ogawa, Storm time enhancements of 630.0 nm airglow associated with polar cap patches, *Journal of Geophysical Research: Space Physics*, *119*(3), 2214–2228, 2014. [80](#), [81](#)
- Sarris, T., and X. Li, Evolution of the dispersionless injection boundary associated with substorms, *Annales Geophysicae*, *23*(3), 877–884, 2005. [139](#)
- Sarris, T. E., X. Li, N. Tsaggas, and N. Paschalidis, Modeling energetic particle injections in dynamic pulse fields with varying propagation speeds, *Journal of Geophysical Research: Space Physics*, *107*(A3), SMP 1–1–SMP 1–10, 2002. [25](#)
- Sastri, J. H., Penetration electric fields at the nightside dip equator associated with the main impulse of the storm sudden commencement of 8 July 1991, *Journal of Geophysical Research: Space Physics*, *107*(A12), SIA 9–1–SIA 9–8, 2002. [57](#), [126](#), [149](#)
- Sastri, J. H., J. V. S. V. Rao, and K. B. Ramesh, Penetration of polar electric fields to the nightside dip equator at times of geomagnetic sudden commencements, *Journal of Geophysical Research: Space Physics*, *98*(A10), 17517–17523, 1993. [126](#), [128](#)

- Sastri, J. H., H. Luhr, H. Tachihara, T. I. Kitamura, and J. V. S. V. Rao, Electric field fluctuations (25-35 min) in the midnight dip equatorial ionosphere, *Annales Geophysicae*, 18(2), 252–256, 2000. [26](#), [80](#), [100](#), [120](#), [150](#)
- Sastri, J. H., K. Niranjana, and K. S. V. Subbarao, Response of the equatorial ionosphere in the Indian (midnight) sector to the severe magnetic storm of July 15, 2000, *Geophysical Research Letters*, 29(13), 29–1–29–4, 2002. [16](#)
- Sastri, J. H., Y. Kamide, and K. Yumoto, Signatures for magnetospheric substorms in the geomagnetic field of dayside equatorial region: Origin of the ionospheric component, *Journal of Geophysical Research: Space Physics*, 108(A10), 1375, 2003. [25](#), [73](#), [74](#), [143](#)
- Savitzky, A., and M. J. E. Golay, Smoothing and Differentiation of Data by Simplified Least Squares Procedures., *Anal. Chem.*, 36(8), 1627–1639, 1964. [51](#), [67](#), [114](#)
- Scargle, J. D., Studies in astronomical time series analysis. ii-statistical aspects of spectral analysis of unevenly spaced data, *The Astrophysical Journal*, 263, 835–853, 1982. [52](#)
- Scargle, J. D., Studies in astronomical time series analysis. Fourier transforms, autocorrelation functions, and cross-correlation functions of unevenly spaced data, *The Astrophysical Journal*, 343, 874–887, 1989. [52](#)
- Scherliess, L., and B. G. Fejer, Satellite studies of mid- and low-latitude ionospheric disturbance zonal plasma drifts, *Geophysical Research Letters*, 25(9), 1503–1506, 1998. [16](#)
- Scherliess, L., and B. G. Fejer, Radar and satellite global equatorial F region vertical drift model, *Journal of Geophysical Research: Space Physics*, 104(A4), 6829–6842, 1999. [16](#), [66](#), [77](#), [92](#), [93](#)

- Schulz, M., and K. Stattegger, SPECTRUM: spectral analysis of unevenly spaced paleoclimatic time series, *Computers & Geosciences*, 23(9), 929–945, 1997. [53](#), [54](#), [67](#), [95](#), [114](#), [115](#)
- Schunk, R., and A. Nagy, *Ionospheres: physics, plasma physics, and chemistry*. Cambridge university press, 2009. [27](#)
- Sekar, R., Plasma instabilities and their simulations in the equatorial F region—recent results, *Space science reviews*, 107(1), 251–262, 2003. [18](#)
- Sekar, R., and D. Chakrabarty, Role of overshielding electric field on the development of pre-midnight plume event: Simulation results, *Journal of Atmospheric and Solar-Terrestrial Physics*, 70(17), 2212 – 2221, 2008. [18](#), [56](#)
- Sekar, R., and M. C. Kelley, On the combined effects of vertical shear and zonal electric field patterns on nonlinear equatorial spread F evolution, *Journal of Geophysical Research: Space Physics*, 103(A9), 20735–20747, 1998. [18](#), [79](#)
- Sekar, R., and R. Raghavarao, Role of vertical winds on the Rayleigh-Taylor mode instabilities of the night-time equatorial ionosphere, *Journal of atmospheric and terrestrial physics*, 49(10), 981–985, 1987. [18](#)
- Sekar, R., R. Suhasini, and R. Raghavarao, Effects of vertical winds and electric fields in the nonlinear evolution of equatorial spread F, *Journal of Geophysical Research: Space Physics*, 99(A2), 2205–2213, 1994. [18](#)
- Sekar, R., R. Suhasini, and R. Raghavarao, Evolution of plasma bubbles in the equatorial F region with different seeding conditions, *Geophysical Research Letters*, 22(8), 885–888, 1995. [18](#)
- Sekar, R., D. Chakrabarty, R. Narayanan, S. Sripathi, A. K. Patra, and K. S. V. Subbarao, Characterization of VHF radar observations associated with equatorial spread F by narrow-band optical measurements, *Annales Geophysicae*, 22(9), 3129–3136, 2004. [63](#)

- Sekar, R., D. Chakrabarty, and D. Pallamraju, Optical signature of shear in the zonal plasma flow along with a tilted structure associated with equatorial spread F during a space weather event, *Journal of Atmospheric and Solar-Terrestrial Physics*, 75, 57–63, 2012. [144](#)
- Senior, C., and M. Blanc, On the control of magnetospheric convection by the spatial distribution of ionospheric conductivities, *Journal of Geophysical Research: Space Physics*, 89(A1), 261–284, 1984. [26](#), [30](#), [32](#), [77](#), [81](#), [86](#), [109](#), [120](#), [149](#)
- Shi, Y., E. Zesta, and L. R. Lyons, Features of energetic particle radial profiles inferred from geosynchronous responses to solar wind dynamic pressure enhancements, *Annales Geophysicae*, 27(2), 851–859, 2009. [138](#), [139](#), [145](#)
- Siegel, A. F., Testing for periodicity in a time series, *Journal of the American Statistical Association*, 75(370), 345–348, 1980. [53](#)
- Siscoe, G., and N. Crooker, A theoretical relation between dst and the solar wind merging electric field, *Geophysical Research Letters*, 1(1), 17–19, 1974. [122](#)
- Slinker, S. P., J. A. Fedder, W. J. Hughes, and J. G. Lyon, Response of the ionosphere to a density pulse in the solar wind: Simulation of traveling convection vortices, *Geophysical Research Letters*, 26(23), 3549–3552, 1999. [128](#)
- Sofko, G. J., R. Greenwald, and W. Bristow, Direct determination of large-scale magnetospheric field-aligned currents with SuperDARN, *Geophysical Research Letters*, 22(15), 2041–2044, 1995. [140](#)
- Somayajulu, V., C. Reddy, and K. Viswanathan, Penetration of magnetospheric convective electric field to the equatorial ionosphere during the substorm of March 22, 1979, *Geophysical research letters*, 14(8), 876–879, 1987. [32](#), [149](#)

- Southwood, D. J., The role of hot plasma in magnetospheric convection, *Journal of Geophysical Research*, 82(35), 5512–5520, 1977. 30
- Spiro, R., R. Wolf, and B. G. Fejer, Penetrating of high-latitude-electric-field effects to low latitudes during SUNDIAL 1984, in *Annales Geophysicae*, vol. 6, pp. 39–49. 1988. 30, 32
- Subbarao, K. S. V., and B. V. KrishnaMurthy, Seasonal variations of equatorial spread-F, *Annales Geophysicae*, 12(1), 33–39, 1994. 44
- Sulzer, M. P., N. Aponte, and S. A. Gonzalez, Application of linear regularization methods to Arecibo vector velocities, *Journal of Geophysical Research: Space Physics*, 110(A10), A10305, 2005. 89
- Szuszczewicz, E. P., M. Lester, P. Wilkinson, P. Blanchard, M. Abdu, R. Hانبابا, K. Igarashi, S. Pulinets, and B. M. Reddy, A comparative study of global ionospheric responses to intense magnetic storm conditions, *Journal of Geophysical Research: Space Physics*, 103(A6), 11665–11684, 1998. 144
- Tamao, T., A hydromagnetic interpretation of geomagnetic ssc*, *Rept. Ionosphere Space Res. Japan*, 18, 1964. 145
- Temmer, M., A. Veronig, E. Kontar, S. Krucker, and B. Vršnak, Combined STEREO/RHESSI study of coronal mass ejection acceleration and particle acceleration in solar flares, *The Astrophysical Journal*, 712(2), 1410, 2010. 6
- Toffoletto, F., S. Sazykin, R. Spiro, and R. Wolf, Inner magnetospheric modeling with the rice convection model, *Space science reviews*, 107(1), 175–196, 2003. 30
- Troshichev, O., and V. Andrezen, The relationship between interplanetary quantities and magnetic activity in the southern polar cap, *Planetary and Space Science*, 33(4), 415 – 419, 1985. 100

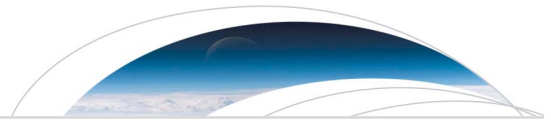
- Troshichev, O., and D. Sormakov, PC index as a proxy of the solar wind energy that entered into the magnetosphere: 2. Relation to the interplanetary electric field E_{kl} before substorm onset, *Earth, Planets and Space*, *67*(1), 170, 2015. [104](#)
- Troshichev, O., V. Andrezen, S. Vennerström, and E. Friis-Christensen, Magnetic activity in the polar cap-A new index, *Planetary and Space Science*, *36*(11), 1095 – 1102, 1988. [49](#)
- Troshichev, O. A., R. Y. Lukianova, V. O. Papitashvili, F. J. Rich, and O. Rasmussen, Polar cap index (PC) as a proxy for ionospheric electric field in the near-pole region, *Geophysical Research Letters*, *27*(23), 3809–3812, 2000. [92](#), [101](#)
- Tsunomura, and Araki, Numerical analysis of equatorial enhancement of geomagnetic sudden commencement, *Planetary and Space Science*, *32*(5), 599 – 604, 1984. [77](#), [86](#)
- Tsunomura, S., Numerical analysis of global ionospheric current system including the effect of equatorial enhancement, *Annales Geophysicae*, *17*(5), 692–706, 1999. [80](#)
- Tsurutani, B., et al., Global dayside ionospheric uplift and enhancement associated with interplanetary electric fields, *Journal of Geophysical Research: Space Physics*, *109*(A8), A08302, 2004. [144](#)
- Tsurutani, B. T., and W. D. Gonzalez, The cause of high-intensity long-duration continuous ae activity (HILDCAAs): Interplanetary alfvén wave trains, *Planetary and Space Science*, *35*(4), 405 – 412, 1987. [99](#)
- Tsurutani, B. T., W. D. Gonzalez, A. L. C. Gonzalez, F. Tang, J. K. Arballo, and M. Okada, Interplanetary origin of geomagnetic activity in the declining phase of the solar cycle, *Journal of Geophysical Research: Space Physics*, *100*(A11), 21717–21733, 1995. [8](#), [108](#), [126](#)

- Tsurutani, B. T., et al., Corotating solar wind streams and recurrent geomagnetic activity: A review, *Journal of Geophysical Research: Space Physics*, 111(A7), A07S01, 2006. [8](#), [108](#), [120](#)
- Tulasi Ram, S., J. Lei, S.-Y. Su, C. H. Liu, C. H. Lin, and W. S. Chen, Dayside ionospheric response to recurrent geomagnetic activity during the extreme solar minimum of 2008, *Geophysical Research Letters*, 37(2), L02101, 2010. [109](#)
- Tulasi Ram, S., M. Yamamoto, B. Veenadhari, S. Kumar, and S. Gurubaran, Corotating interaction regions (CIRs) at sub-harmonic solar rotational periods and their impact on ionosphere-thermosphere system during the extreme low solar activity year 2008, *Indian Journal of Radio and Space Physics*, 41, 294–245, 2012. [109](#)
- Usmanov, A. V., M. L. Goldstein, K. W. Ogilvie, W. M. Farrell, and G. R. Lawrence, Low-density anomalies and sub-Alfvnic solar wind, *Journal of Geophysical Research: Space Physics*, 110(A1), A01106, 2005. [108](#)
- Vasyliunas, V. M., Mathematical models of magnetospheric convection and its coupling to the ionosphere, in *Particles and Fields in the Magnetosphere*, pp. 60–71. Springer, 1970. [26](#), [30](#)
- Vemareddy, P., and W. Mishra, A full study on the sun–earth connection of an earth-directed CME magnetic flux rope, *The Astrophysical Journal*, 814(1), 59, 2015. [98](#)
- Volland, H., A semiempirical model of large-scale magnetospheric electric fields, *Journal of Geophysical Research*, 78(1), 171–180, 1973. [26](#)
- Volland, H., A model of the magnetospheric electric convection field, *Journal of Geophysical Research: Space Physics*, 83(A6), 2695–2699, 1978. [29](#), [30](#)

- Walsh, B. M., D. G. Sibeck, Y. Wang, and D. H. Fairfield, Dawn-dusk asymmetries in the earth's magnetosheath, *Journal of Geophysical Research: Space Physics*, 117(A12), A12211, 2012. [122](#)
- Webb, D. F., and R. A. Howard, The solar cycle variation of coronal mass ejections and the solar wind mass flux, *Journal of Geophysical Research: Space Physics*, 99(A3), 4201–4220, 1994. [6](#)
- Wei, Y., M. Hong, W. Wan, A. Du, J. Lei, B. Zhao, W. Wang, Z. Ren, and X. Yue, Unusually long lasting multiple penetration of interplanetary electric field to equatorial ionosphere under oscillating IMF Bz, *Geophysical Research Letters*, 35(2), L02102, 2008. [123](#)
- Wei, Y., et al., Responses of the ionospheric electric field to the sheath region of ICME: A case study, *Journal of Atmospheric and Solar-Terrestrial Physics*, 73(1), 123 – 129, 2011. [89](#)
- Wei, Y., W. Wan, B. Zhao, M. Hong, A. Ridley, Z. Ren, M. Fraenz, E. Dubinin, and M. He, Solar wind density controlling penetration electric field at the equatorial ionosphere during a saturation of cross polar cap potential, *Journal of Geophysical Research: Space Physics*, 117(A9), A09308, 2012. [128](#)
- Weimer, D. R., D. M. Ober, N. C. Maynard, M. R. Collier, D. J. McComas, N. F. Ness, C. W. Smith, and J. Watermann, Predicting interplanetary magnetic field (imf) propagation delay times using the minimum variance technique, *Journal of Geophysical Research: Space Physics*, 108(A1), 1026, 2003. [48](#)
- Weygand, J. M., R. McPherron, K. Kauristie, H. Frey, and T.-S. Hsu, Relation of auroral substorm onset to local AL index and dispersionless particle injections, *Journal of Atmospheric and Solar-Terrestrial Physics*, 70(18), 2336–2345, 2008. [76](#)

- Wolf, R., R. Spiro, S. Sazykin, and F. Toffoletto, How the Earth's inner magnetosphere works: An evolving picture, *Journal of Atmospheric and Solar-Terrestrial Physics*, 69(3), 288–302, 2007. [26](#), [31](#)
- Wolf, R. A., Effects of ionospheric conductivity on convective flow of plasma in the magnetosphere, *Journal of Geophysical Research*, 75(25), 4677–4698, 1970. [26](#)
- Wu, C.-C., and R. P. Lepping, Effects of magnetic clouds on the occurrence of geomagnetic storms: The first 4 years of wind, *Journal of Geophysical Research: Space Physics*, 107(A10), SMP 19–1–SMP 19–8, 1314, 2002. [98](#)
- Yamazaki, Y., and M. J. Kosch, The equatorial electrojet during geomagnetic storms and substorms, *Journal of Geophysical Research: Space Physics*, 120(3), 2276–2287, 2014JA020773, 2015. [33](#)
- Yamazaki, Y., and A. Maute, Sq and EEJ-A Review on the Daily Variation of the Geomagnetic Field Caused by Ionospheric Dynamo Currents, *Space Science Reviews*, 206(1), 299–405, 2017. [33](#)
- Yeeram, T., Interplanetary drivers of daytime penetration electric field into equatorial ionosphere during CIR-induced geomagnetic storms, *Journal of Atmospheric and Solar-Terrestrial Physics*, 157158, 6 – 15, 2017. [109](#)
- Yizengaw, E., et al., Response of the equatorial ionosphere to the geomagnetic DP 2 current system, *Geophysical Research Letters*, 43(14), 7364–7372, 2016GL070090, 2016. [100](#), [150](#)
- Yuan, Z., and X. Deng, Effects of continuous solar wind pressure variations on the long-lasting penetration of the interplanetary electric field during southward interplanetary magnetic field, *Advances in Space Research*, 39(8), 1342 – 1346, 2007. [127](#)

- Yue, C., and Q. Zong, Solar wind parameters and geomagnetic indices for four different interplanetary shock/ICME structures, *Journal of Geophysical Research: Space Physics*, 116(A12), A12201, 2011. [98](#), [99](#)
- Yue, X., W. Wan, J. Lei, and L. Liu, Modeling the relationship between EX B vertical drift and the time rate of change of hmF2 (hmF2/t) over the magnetic equator, *Geophysical Research Letters*, 35(5), L05104, 2008. [144](#)
- Zhang, Y., Distinct characteristics of asymmetric magnetic reconnections: Observational results from the exhaust region at the dayside magnetopause, *Scientific reports*, 6, 2016. [123](#)
- Zong, Q.-G., B. W. Reinisch, P. Song, Y. Wei, and I. A. Galkin, Dayside ionospheric response to the intense interplanetary shocks-solar wind discontinuities: Observations from the digisonde global ionospheric radio observatory, *Journal of Geophysical Research: Space Physics*, 115(A6), A06304, 2010. [127](#)
- Zuo, P. B., F. S. Wei, X. S. Feng, and F. Yang, The relationship between the magnetic cloud boundary layer and the substorm expansion phase, *Solar Physics*, 242(1), 167–185, 2007. [88](#)
- Zurbuchen, T. H., and I. G. Richardson, *In-Situ Solar Wind and Magnetic Field Signatures of Interplanetary Coronal Mass Ejections*, pp. 31–43. Springer New York, New York, NY, 2006. [7](#)



RESEARCH LETTER

10.1002/2017GL073038

Solar wind flow angle and geoeffectiveness of corotating interaction regions: First results

Diptiranjan Rout¹, D. Chakrabarty¹, P. Janardhan¹, R. Sekar¹, Vrunda Maniya¹, and Kuldeep Pandey¹

¹Physical Research Laboratory, Ahmedabad, India

Key Points:

- A few periodicities (~30 and 60 min) in IMF B_z predominantly affect EEJ during CIR events on occasions
- The geoeffectiveness of CIR events are evaluated in terms of these prompt penetration periodicities in the equatorial ionosphere
- The CIRs are found to be geoeffective when the average solar wind flow is radial to within 6degrees

Correspondence to:

D. Rout,
diptir@prl.res.in

Citation:

Rout, D., D. Chakrabarty, P. Janardhan, R. Sekar, V. Maniya, and K. Pandey (2017), Solar wind flow angle and geoeffectiveness of corotating interaction regions: First results, *Geophys. Res. Lett.*, 44, doi:10.1002/2017GL073038.

Received 10 FEB 2017

Accepted 1 MAY 2017

Accepted article online 4 MAY 2017

Abstract A total of 43 Corotating Interaction Region (CIR)-induced geomagnetic storms during the unusually deep solar minimum of solar cycle 23 (2006–2010) were identified using a superposed epoch analysis technique. Of these 43 events, detailed cross-spectrum analyses, between the variations in the Z component of the interplanetary magnetic field (IMF B_z) and the equatorial electrojet (EEJ) strength, were performed for 22 events when the daytime EEJ strengths from Jicamarca were available. The analyses revealed that the ~30 and ~60 min periodic components in IMF B_z were causally related to the EEJ strength subject to the average solar wind flow being radial to within 6° at L1 during the interval for which EEJ strengths were considered. This investigation elicits the important role of average solar wind azimuthal flow angle in determining the geoeffectiveness of CIR events.

Plain Language Summary Corotating Interaction Regions (CIRs) can disturb the near-Earth geospace significantly as the charged particles are accelerated in the shocked region in the interplanetary medium due to the passage of CIR and these energetic particles can reach Earth's orbit. Satellites are vulnerable to these high-energy particles during CIRs. In a technologically developed/developing society, the health of its satellites in the near-Earth space is crucial. Therefore, determining the geoeffectiveness of CIR is important.

1. Introduction

It is well known that the fast solar wind (600–800 km s⁻¹) originates in high-latitude coronal holes, while the slow speed solar wind (300–400 km s⁻¹) is confined to the low-latitude equatorial belt [Ananthkrishnan et al., 1995]. The fast solar wind interacts with the slow stream solar wind near the ecliptic plane in the interplanetary medium creating an interaction region generally known as a “Corotating Interaction Region” or CIR [Tsurutani et al., 2006; Denton et al., 2006]. In a CIR, the stream interface is conventionally identified by increases in solar wind velocity and proton temperature, a sharp drop in proton density as well as shear in solar wind flow that can make the flow angle nonradial [Forsyth and Marsch, 1999; Tsurutani et al., 1995]. The interaction regions are long-lived, have intense magnetic field, and corotate with the Sun and are bounded by forward and reverse shock regions. It has been suggested by Pizzo [1989] that for a corotating solar wind structure, the interface acts like a wall or an obstacle thereby deflecting the impinging solar wind and making it nonradial. However, the deviation from the radial nature of the solar wind is in general not very significant, with azimuthal velocities being usually between 30 and 50 km s⁻¹ and nonradial flow angles rarely exceeding 10°. Some extreme cases of long-lasting nonradial solar wind outflows have, however, been reported when azimuthal flow velocities exceeded 100 km s⁻¹ [Janardhan et al., 2005, 2008]. Such events are small in number and may not be a conventional CIR in terms of their generation mechanism. In present work, no attempt is made to address this aspect, and only characteristic changes in solar wind parameters, as discussed above, are only used to identify the CIR or CIR-like events.

It is also known that the Alfvénic waves associated with the high-speed streams [Burns et al., 2012] cause fast fluctuations in the interplanetary magnetic field (IMF). In a CIR, such Alfvénic fluctuations are expected to affect the equatorial ionosphere nearly instantaneously, if the rate of change of the IMF B_z fluctuations (or in other words, fluctuations in the dawn-dusk component of interplanetary electric field or IEFy) is faster than the shielding time constant [e.g., Senior and Blanc, 1984] at the inner edge of the ring current region. The electric

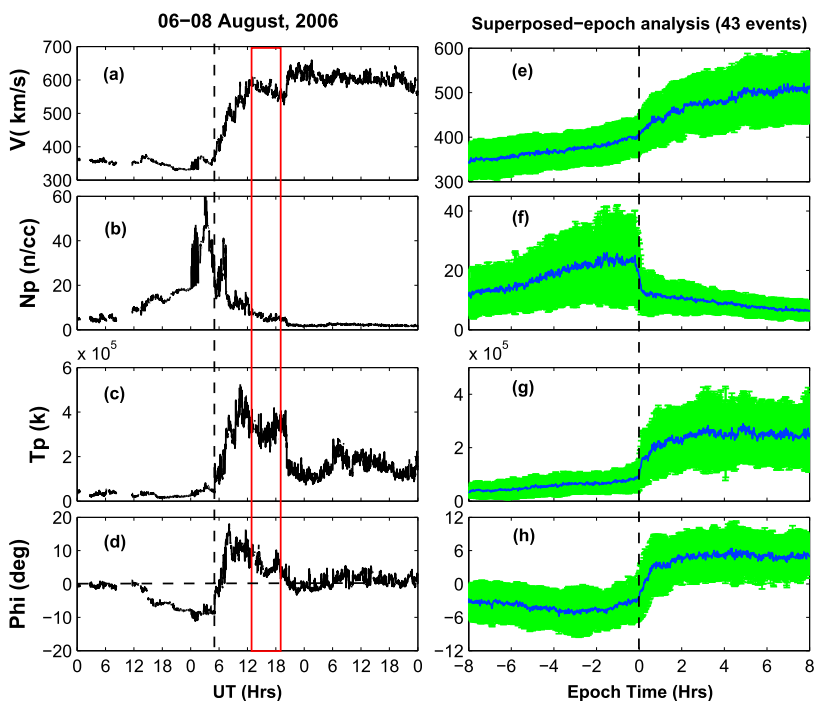


Figure 1. Variations in (a) solar wind flow velocity (V in km/s), (b) proton density (N_p in cm^{-3}), (c) proton temperature (T_p in K), and (d) flow angle (Φ in degrees) during 6–8 August 2006. The stream interface is marked by the vertical dotted line at ~ 0510 UT. Superposed epoch analyses for (e) V , (f) T_p , (g) N_p , and (h) Φ for all the 43 events are shown. The dashed line represents zero epoch time. The green envelop represents the standard deviations from the mean values.

field perturbations that arise from the fast fluctuations in IEFy are generically known as prompt penetration (PP) electric field [e.g., Kelley et al., 2003]. As the solar wind speed remains relatively steady compared to the fast fluctuations in IMF B_z , the fluctuations in IEFy or convection electric field can be attributed to the fluctuations in IMF B_z .

A comprehensive knowledge about the PP electric field periodicities during CIR events can be used to gauge their geoeffectiveness. Though the impacts of the CIR events on ionosphere and thermosphere, with periodicity of the order of solar rotational period (27 days) and its subharmonics (e.g., 27 days, 13.5 days, and 9 days) have been reported [e.g., Lei et al., 2008; Pedatella et al., 2010], signatures of the same periodic components have not been found in EEJ (driven primarily by the zonal electric field) that flows in the dip equatorial E region [Tulasi Ram et al., 2012]. In fact, as far as the effects of the CIR-related fast fluctuating (period ≤ 2.0 h) components in IMF B_z on the equatorial ionosphere are concerned, which are generically associated with PP events, there has been a real dearth of comprehensive investigation. The geoeffectiveness of CIR events in terms of their impact on the equatorial ionosphere is also poorly understood. Given this context, the present investigation is important on two counts as it shows, for the first time, the key role played by the solar wind flow angle in determining the geoeffectiveness of the CIR events and also brings out the periodic components (≤ 2.0 h) in CIR that affect EEJ.

2. Data Analysis and Result

A total of 43 minor geomagnetic storm events during 2006–2010, the deep solar minimum of solar cycle 23, were selected for the present investigation in which the stream interface was identified following the methodology discussed in Forsyth and Marsch [1999]. The solar wind parameters have been corrected for propagation lag till the bow shock nose. Figures 1a–1d show variations in solar wind flow velocity (V in km s^{-1}), proton density (N_p in cm^{-3}), proton temperature (T_p in K), and flow angle ($\Phi = \tan^{-1} \left(\frac{V_y}{V_x} \right)$ in degrees) for one such event during 6–8 August 2006. The stream interface is marked by the vertical dotted line at ~ 0510 UT. The characteristic increases in V and T_p , drop in N_p , and the change in Φ downstream of the stream interface region

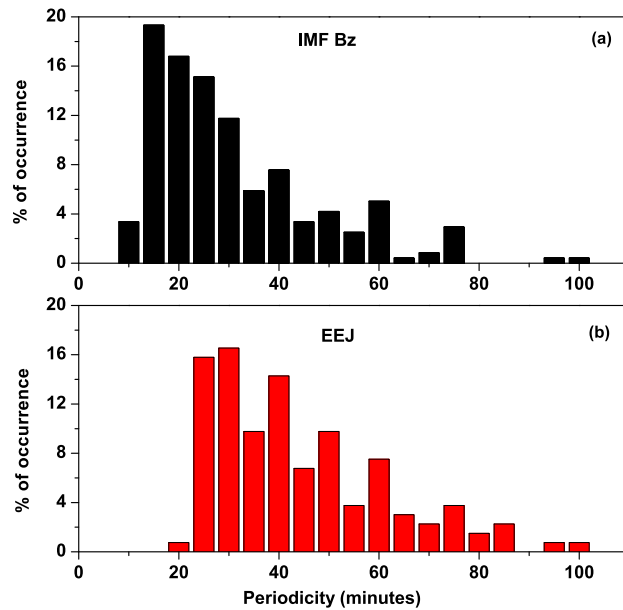


Figure 2. Histograms of (a) IMF B_z and (b) EEJ periodicities.

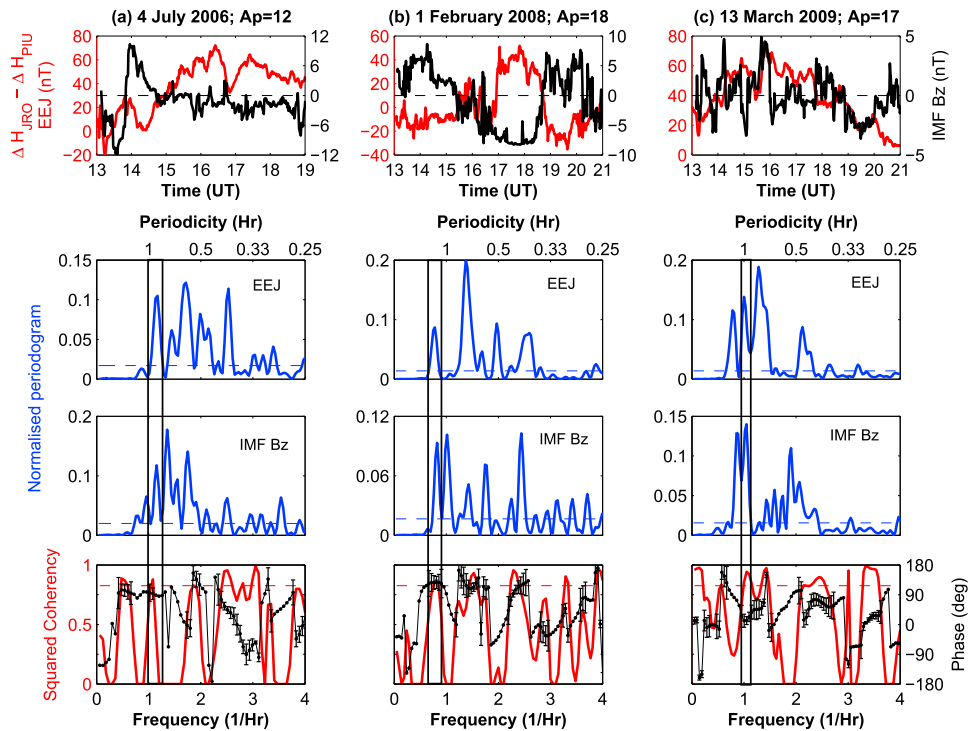


Figure 3. (a) The top panel shows the temporal variations of EEJ (red) and IMF B_z (black) during 1300–1900 UT on 4 July 2006; the middle two panels show the Lomb-Scargle normalized periodograms for EEJ and IMF B_z where the blue horizontal line shows the 95% confidence limit, and the bottom panel represents the squared coherency (red) with the phase spectra (black) for the two time series. The false alarm level is marked at 80% and is shown by a red dashed line. (b and c) Similar results as Figure 3a but for the other two events on 1 February 2008 and 13 March 2009 during 1300–2100 UT. The rectangular box is marked to show the common periodic components where the time series of EEJ and IMF B_z show significant coherency with stable phase relationship (essential to infer causal relationship).

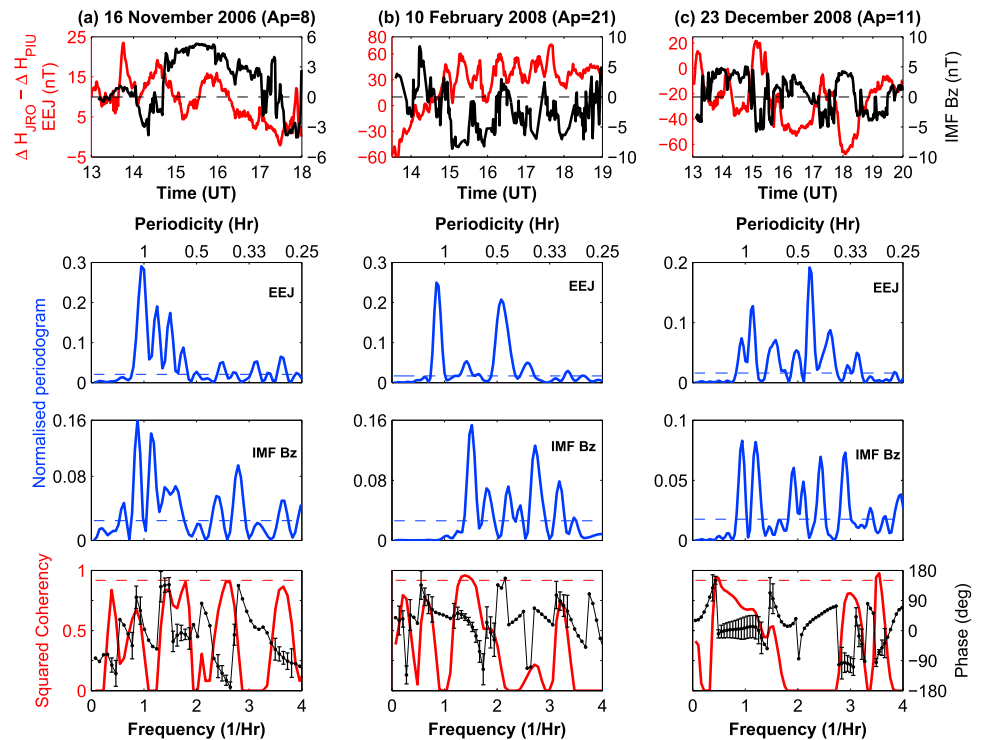


Figure 4. Same as Figure 3 but for (a) 16 November 2006 during 1300–1800 UT, (b) 10 February 2008 during 1330–1900 UT, and (c) 23 December 2008 during 1300–2000 UT, respectively. No causal relationship is noticed in these cases.

can be clearly seen. In order to extract the average trends of the solar wind parameters, a superposed epoch analysis was performed with the zero epoch corresponding to the time when the Earth is hit by the stream interface. Figures 1e–1h shows superposed epoch plots for V , T_p , N_p , and Φ for the 43 events and reveals the important characteristics of the stream interface typically associated with CIR events. The dashed line and the green envelope show, respectively, the zero epoch time and the standard deviation from the mean values.

3. Causal Connection Between IMF B_z and EEJ Strength During CIR Events

The EEJ strength over the Jicamarca sector, given by $\Delta H_{JIC} - \Delta H_{PIU}$, is based on the difference between the horizontal component of geomagnetic field over Jicamarca (JIC: 12°S, 76.8°W, 0.8° dip) and an off-equatorial station Piura (PIU: 5.2°S, 80.6°W, 6.8° dip). For Jicamarca, the local time (LT) = Universal time (UT) – 5 h. The EEJ strength over Jicamarca was shown to be same with the variations deduced by JULIA radar for the ionospheric E region electric field [Alken and Maus, 2010]. EEJ data with 1 min resolution during 1300–2100 UT (0800–1600 LT) were considered. As the EEJ data are available only during daytime, the investigation was restricted to 22 out of 43 events considered.

The fast (≤ 2.0 h) fluctuations (residuals) in EEJ and IMF B_z during these events were extracted (by detrending) using the Savitzky-Golay (SG) smoothing algorithm [Savitzky and Golay, 1964]. In order to know the dominant periodicities present in IMF B_z and EEJ, a detailed spectral analysis was carried out by using the standard Lomb-Scargle method [Schulz and Stattegger, 1997] which can handle unevenly sampled data. Only periodicities exceeding the 95% confidence limit were considered. Histograms with 5 min bin size based on the periodicities obtained from IMF B_z and EEJ residual time series data for 22 events are shown in Figures 2a and 2b, respectively. It is to be noted here that the lower cutoff periodicity in this case is chosen to be 10 min as the Brunt-Vaisala period at E region height is ~ 5 min. Further, it is known that Alfvénic waves in CIR with periods more than 8 min [e.g., Korth et al., 2011] can efficiently affect ionosphere. As the EEJ data are available mostly for 6–8 h, periodicities ≤ 2.0 h can safely be addressed. It is clear from the histograms that the two most

Table 1. A Numbered (Column 1), Dated (Column 2) List of Events Showing Coherent Periodicities of Prompt Penetration Electric Field in Minutes (Column 3) Having Stable Phase Relationship and the Azimuthal Flow Angle $|\Phi|$ in Degrees (Column 4)^a

Event	Date	Periodicities (min) of Prompt Penetration Electric Field	Average $ \Phi $ (deg)
1	9 Apr 2006	27	5.1
2	15 Jun 2006	25	2.1
3	4 Jul 2006	60	1.0
4	7 Aug 2006	60	5.3
5	7 May 2007	46	3.8
6	20 Nov 2007	48	2.3
7	31 Jan 2008	37	1.3
8	1 Feb 2008	70	5.4
9	22 Jul 2008	30	5.7
10	23 Jul 2008	32	4.4
11	7 Nov 2008	60	3.1
12	13 Mar 2009	60	3.7
13	11 Nov 2010	60	1.7
15	20 Feb 2006	-	9.6
17	18 May 2006	-	6.4
14	17 Dec 2007	-	6.3
16	5 Jan 2008	-	6.6
18	10 Feb 2008	-	6.3
19	23 Dec 2008	-	6.2
21	16 Nov 2006	-	5.3
20	6 Aug 2009	53	6.8
22	26 Jun 2010	-	2.4

^aOut of 22 events, 13 show a causal relationship between IMF B_z and EEJ, and these are shown in black. Events with common periodicities that do not show any causal relationship are shown in red, and events for which the flow angle criterion was ineffective are shown in blue. The absence of causal relationship is marked by a dash.

dominant periodic components in EEJ are 25 and 30 min, whereas in case of IMF B_z , the dominant periodic components are 15 and 20 min during the CIR events. In fact, some other common significant periodicities (30, 40, 50, and 60 min) are also present in both the parameters.

In order to establish the causal relationship between IMF B_z and EEJ, cross-spectrum analyses with coherency and phase spectra calculations were carried out [Schulz and Stattegger, 1997]. In Figure 3a, the top panel shows the temporal variations of EEJ (red) and IMF B_z (black) during 1300–1900 UT on 4 July 2006 ($A_p = 12$). The middle two panels show the normalized periodograms for EEJ and IMF B_z where the blue horizontal line is marked at 95% confidence limit, and the bottom panel represents the squared coherency (red) with the phase spectra (black) for the two time series. The false alarm level is marked at 80% (red dashed line). Figures 3b and 3c show the similar results for the other two events on 1 February 2008 ($A_p = 18$) and 13 March 2009 ($A_p = 17$) during 1300–2100 UT. The rectangular box is marked to show the common periodic components where the time series of EEJ and IMF B_z show significant coherency with stable phase relationship (essential to infer causal relationship). The periodicity of 60 min is found to be causally connected on 4 July 2006. Similarly, the periodicities of 70 min and 60 min in EEJ are found to be causally connected with IMF B_z on 1 February 2008 and 13 March 2009, respectively. Though there are multiple common periodicities present in both the parameters, only a few periodic components in EEJ are found to be responding to the corresponding fluctuations in IMF B_z . It is to be noted that on many occasions (Figure 3), periodicities adjacent to the causally connected ones do not show either high coherency and/or stable phase relationship. This probably indicates

sharp frequency response as far as the magnetosphere-ionosphere (M-I) coupling is concerned. Figure 4 is the same as Figure 3, but for (a) 16 November 2006 ($A_p = 8$) during 1300–1800 UT, (b) 10 February 2008 ($A_p = 21$) during 1330–1900 UT, and (c) 23 December 2008 ($A_p = 11$) during 1300–2000 UT, respectively. In all these cases, both EEJ and IMF B_z show fast fluctuations and they have common periodicities as well. As an example, one can take the case shown in Figure 4a wherein the 60 min periodicity is present in both IMF B_z and EEJ on 16 November 2006, but they are not causally related as neither the coherency is high nor the phase relationship is stable.

4. Causal Connection and Solar Wind Azimuthal Flow Angle

In Figures 1a–1d, the red rectangular box is marked for a typical event where the EEJ data have been analyzed (1300–1900 UT on 7 August 2006). For all the events considered, the modulus of the average value of the solar wind azimuthal flow angle ($|\Phi|$ in degrees) during this interval was calculated. Table 1 provides the date of events, periodicities (in min) of prompt penetration electric field (with stable phase relationship) and $|\Phi|$. The absence of any causal relationship is marked by a dash in the table. It can be noted from Table 1 that 13 out of 22 events have shown causal relationship between IMF B_z and EEJ at different periodicities wherein $|\Phi| < 6^\circ$. These events are marked in black. The six events that do not show any causal relationship (though they have common periodicities) are marked in red in Table 1. For these events, $|\Phi| > 6^\circ$. Among all these periodicities, ~ 60 and ~ 30 min periodic components have occurred five and four times, respectively. In fact, in most of the cases these two periodic components in IMF B_z (IEFy) are found to affect EEJ over the Jicamarca sector. Therefore, out of all 22 events, this criterion of solar wind flow angle determining geoeffectiveness was found to be valid for 19 events (86.4% of the total cases considered). These events are marked in blue in Table 1.

5. Discussion

The histogram in Figure 2b emphasizes the fast fluctuating components present in IMF B_z during the CIR events. The periodicities in IMF including the most dominant periodicities, in the range of 15–25 min, are associated with the Alfvénic fluctuations in IMF [e.g., *Tsurutani et al.*, 2006; *Korth et al.*, 2011] in CIR. It may be noted that the percentage occurrence of 20 min periodicity is very small (in contrast to quite time feature as reported by *Reddy and Devasia* [1976], for example) in EEJ although the same periodicity is quite dominant in IMF B_z . This may be associated with the EEJ during disturbed condition. It is known that although IMF B_z (or IEFy) comprises a wide range of periodicities, only a few periodic fluctuations affect low/equatorial ionosphere. The periodicity in IMF B_z that affects low latitude depends on the shielding process at the inner edge of the ring current. The typical shielding time constant is ~ 30 min [e.g., *Senior and Blanc*, 1984]. However, earlier observations reveal that shielding can remain broken for longer duration of time [*Huang et al.*, 2005; *Chakrabarty et al.*, 2015]. Therefore, although it is clear that the frequency response around the ring current region decides the prompt penetration frequency, the nature [e.g., *Ohtani and Uozumi*, 2014] of the processes that controls this response is not comprehensively understood. Nevertheless, the present study (Table 1) shows that on some occasions, DP2 (30 and 60 min periodicities) type [*Nishida*, 1968; *Sastri et al.*, 2000; *Chakrabarty et al.*, 2008, 2015] periodic fluctuations can reach up to dip equatorial ionosphere in daytime during the passage of CIRs.

Table 1 suggests that the presence of PP electric field during CIR depends on the azimuthal solar wind flow angle (Φ) with the events which do not show causal relationship between EEJ and IMF B_z , having $|\Phi|$ more than 6° . This is strikingly valid barring three events studied in this work. In other words, when the solar wind flow becomes nonradial (in the ecliptic plane) beyond a critical angle (6°), the dayside merging of IMF B_z with the geomagnetic field becomes less efficient. The importance of this critical angle can be evaluated geometrically by invoking the typical size of the dayside magnetopause and by using the flow angle at the L1 point from where the CIR observations are made. Considering the azimuthal flow angle, $|\Phi| = 6^\circ$, and the distance of the L1 point to be $\sim 232 R_E$ ($1 R_E = 6371$ km), the dawn/dusk flank of magnetopause turns out to be $\sim 25 R_E$ away. This extends beyond the magnetopause flank that can be typically taken to be $\sim 20 R_E$ [e.g., *Walsh et al.*, 2012] away from the center of the Earth. This essentially means that the CIR will miss the magnetopause if Φ exceeds 6° assuming the CIRs undergo no further interaction between the L1 point and the magnetopause. Under this scenario, the probability of merging of IMF B_z with the terrestrial magnetic field decreases significantly. As a consequence, the geoeffectiveness of the CIR events decreases drastically as the flow angle exceeds 6° which is the highlight of the present investigation. It is, therefore, expected that prompt penetration occurs only on those cases when the solar wind flow angle is within 6° .

At this juncture, it is important to note that once the solar wind hits the magnetopause at angles less than 6° , two mechanisms can be invoked to explain the dayside merging process. The dayside merging process is mediated through the merging electric field [e.g., Kan and Lee, 1979; Siscoe and Crooker, 1974] which is defined as $E_r = V_{SW} B_T \sin^2 \theta / 2$, where θ is the clock angle, V_{SW} is the solar wind velocity, and B_T is the total magnetic field. The merging electric field is generally believed to operate on a macroscopic scale. This is supported by the works of Fejer et al. [2007] and Wei et al. [2008] that suggest the critical role of merging electric field in M-I coupling. On the other hand, it was shown [Borovsky, 2008; Borovsky et al., 2008; Borovsky and Birn, 2014] that the merging electric field is controlled by the local plasma parameters in the magnetosheath and magnetosphere, and these plasma parameters are controlled by the solar wind conditions. Hence, it was argued by them that the parameters in the solar wind decide the merging electric field. Recently, it has been experimentally observed [Zhang, 2016] that the reconnection takes place in an asymmetric medium as the plasma parameters are not same on the bow shock and magnetopause side of the magnetosheath region. Therefore, depending on the local plasma processes, the merging can be different on some occasions even if the flow angle is well within 6° . This probably explains the anomalous cases (see Table 1) reported in this work wherein the flow angle is less than 6° but the associated CIRs do not affect the equatorial ionosphere. This proposition is consistent with the solar wind-magnetosphere coupling mechanism suggested by Borovsky [2008].

The important role of the flow angle gets further support from the results of Oliveira and Raeder [2015] who showed that IP shocks with similar upstream conditions (such as magnetic field, speed, density, and Mach number) can have different levels of geoeffectiveness, depending on their shock normal orientation (which can change if the flow angle changes). Therefore, it is apparent that the solar wind flow angle at the L1 point plays a key role in determining geoeffectiveness of CIR events.

6. Summary

The present investigation suggests that 30 and 60 min periodicities in IMF B_z are efficient in penetrating into the equatorial ionosphere during CIR events as long as the solar wind azimuthal flow angle is less than $\sim 6^\circ$ at the L1 point. This is attributed to the reduction in the merging electric field in the dayside magnetosphere that occurs when the solar wind flow angle increases beyond a threshold. Therefore, this work provides a quick and easy method to forecast the geoeffectiveness of CIR events based on the observations from the L1 point.

Acknowledgments

The magnetic data over Jicamarca used in this work were taken from Madrigal Database at Jicamarca Radio Observatory (<http://jro1.igpp.gov.pe/madrigal/>). The Jicamarca Radio Observatory is a facility of the Instituto Geofísico del Perú operated with support from the NSFAGS-1433968 through Cornell University. Special thanks are due to Marco Milla for allowing us to use the magnetometer data. The geomagnetic indices and solar wind data were obtained from NASA GSFC CDWeb (http://cdaweb.gsfc.nasa.gov/istp_public/). We thank Madhusudan Ingale for helping us in making schematic diagram. This work is supported by the Department of Space, Government of India.

References

- Alken, P., and S. Maus (2010), Relationship between the ionospheric eastward electric field and the equatorial electrojet, *Geophys. Res. Lett.*, *37*, L04104, doi:10.1029/2009GL041989.
- Ananthkrishnan, S., V. Balasubramanian, and P. Janardhan (1995), Latitudinal variation of solar wind velocity, *Space Sci. Rev.*, *72*(1), 229–232, doi:10.1007/BF00768784.
- Borovsky, J. E. (2008), The rudiments of a theory of solar wind/magnetosphere coupling derived from first principles, *J. Geophys. Res.*, *113*, A08228, doi:10.1029/2007JA012646.
- Borovsky, J. E., and J. Birn (2014), The solar wind electric field does not control the dayside reconnection rate, *J. Geophys. Res. Space Physics*, *119*, 751–760, doi:10.1002/2013JA019193.
- Borovsky, J. E., M. Hesse, J. Birn, and M. M. Kuznetsova (2008), What determines the reconnection rate at the dayside magnetosphere?, *J. Geophys. Res.*, *113*, A07210, doi:10.1029/2007JA012645.
- Burns, A., S. Solomon, L. Qian, W. Wang, B. Emery, M. Wiltberger, and D. Weimer (2012), The effects of corotating interaction region/high speed stream storms on the thermosphere and ionosphere during the last solar minimum, *J. Atmos. Sol. Terr. Phys.*, *83*, 79–87, doi:10.1016/j.jastp.2012.02.006.
- Chakrabarty, D., R. Sekar, J. H. Sastri, and S. Ravindran (2008), Distinctive effects of interplanetary electric field and substorm on nighttime equatorial f layer: A case study, *Geophys. Res. Lett.*, *35*, L19108, doi:10.1029/2008GL035415.
- Chakrabarty, D., D. Rout, R. Sekar, R. Narayanan, G. D. Reeves, T. K. Pant, B. Veendhari, and K. Shiokawa (2015), Three different types of electric field disturbances affecting equatorial ionosphere during a long-duration prompt penetration event, *J. Geophys. Res. Space Physics*, *120*, 4993–5008, doi:10.1002/2014JA020759.
- Denton, M. H., J. E. Borovsky, R. M. Skoug, M. F. Thomsen, B. Lavraud, M. G. Henderson, R. L. McPherron, J. C. Zhang, and M. W. Liemohn (2006), Geomagnetic storms driven by ICME- and CIR-dominated solar wind, *J. Geophys. Res.*, *111*, A07507, doi:10.1029/2005JA011436.
- Fejer, B. G., J. W. Jensen, T. Kikuchi, M. A. Abdu, and J. L. Chau (2007), Equatorial ionospheric electric fields during the November 2004 magnetic storm, *J. Geophys. Res.*, *112*, A10304, doi:10.1029/2007JA012376.
- Forsyth, R., and E. Marsch (1999), Solar origin and interplanetary evolution of stream interfaces, *Space Sci. Rev.*, *89*(1), 7–20, doi:10.1023/A:1005235626013.
- Huang, C.-S., J. C. Foster, and M. C. Kelley (2005), Long-duration penetration of the interplanetary electric field to the low-latitude ionosphere during the main phase of magnetic storms, *J. Geophys. Res.*, *110*, A11309, doi:10.1029/2005JA011202.
- Janardhan, P., K. Fujiki, M. Kojima, M. Tokumaru, and K. Hakamada (2005), Resolving the enigmatic solar wind disappearance event of 11 May 1999, *J. Geophys. Res.*, *110*, A08101, doi:10.1029/2004JA010535.
- Janardhan, P., D. Tripathi, and H. Mason (2008), The solar wind disappearance event of 11 May 1999: Source region evolution, *Astron. Astrophys.*, *488*(1), L1–L4.
- Kan, J. R., and L. C. Lee (1979), Energy coupling function and solar wind-magnetosphere dynamo, *Geophys. Res. Lett.*, *6*(7), 577–580, doi:10.1029/GL0061007p00577.

- Kelley, M. C., J. J. Makela, J. L. Chau, and M. J. Nicolls (2003), Penetration of the solar wind electric field into the magnetosphere/ionosphere system, *Geophys. Res. Lett.*, *30*(4), 1158, doi:10.1029/2002GL016321.
- Korth, A., E. Echer, Q.-G. Zong, F. Guarnieri, M. Fraenz, and C. Mouikis (2011), The response of the polar cusp to a high-speed solar wind stream studied by a multispacecraft wavelet analysis, *J. Atmos. Sol. Terr. Phys.*, *73*(1), 52–60, doi:10.1016/j.jastp.2009.10.004.
- Lei, J., J. P. Thayer, J. M. Forbes, E. K. Sutton, and R. S. Nerem (2008), Rotating solar coronal holes and periodic modulation of the upper atmosphere, *Geophys. Res. Lett.*, *35*, L10109, doi:10.1029/2008GL033875.
- Nishida, A. (1968), Geomagnetic Dp 2 fluctuations and associated magnetospheric phenomena, *J. Geophys. Res.*, *73*(5), 1795–1803, doi:10.1029/JA073i005p01795.
- Ohtani, S., and T. Uozumi (2014), Nightside magnetospheric current circuit: Time constants of the solar wind-magnetosphere coupling, *J. Geophys. Res. Space Physics*, *119*, 3558–3572, doi:10.1002/2013JA019680.
- Oliveira, D. M., and J. Raeder (2015), Impact angle control of interplanetary shock geoeffectiveness: A statistical study, *J. Geophys. Res. Space Physics*, *120*, 4313–4323, doi:10.1002/2015JA021147.
- Pedatella, N. M., J. Lei, J. P. Thayer, and J. M. Forbes (2010), Ionosphere response to recurrent geomagnetic activity: Local time dependency, *J. Geophys. Res.*, *115*, A02301, doi:10.1029/2009JA014712.
- Pizzo, V. J. (1989), The evolution of corotating stream fronts near the ecliptic plane in the inner solar system: 1. Two dimensional fronts, *J. Geophys. Res.*, *94*(A7), 8673–8684, doi:10.1029/JA094iA07p08673.
- Reddy, C., and C. Devasia (1976), Short period fluctuations of the equatorial electrojet, *Nature*, *261*(5559), 396–397.
- Sastri, J., H. Luhr, H. Tachihara, T.-I. Kitamura, and J. V. S. V. Rao (2000), Letter to the editor electric field fluctuations (25–35 min) in the midnight dip equatorial ionosphere, *Ann. Geophys.*, *18*(2), 252–256, doi:10.1007/s00585-000-0252-2.
- Savitzky, A., and M. J. Golay (1964), Smoothing and differentiation of data by simplified least squares procedures, *Anal. Chem.*, *36*(8), 1627–1639.
- Schulz, M., and K. Stattegger (1997), Spectrum: Spectral analysis of unevenly spaced paleoclimatic time series, *Comput. Geosci.*, *23*(9), 929–945.
- Senior, C., and M. Blanc (1984), On the control of magnetospheric convection by the spatial distribution of ionospheric conductivities, *J. Geophys. Res.*, *89*(A1), 261–284, doi:10.1029/JA089iA01p00261.
- Siscoe, G., and N. Crooker (1974), A theoretical relation between Dst and the solar wind merging electric field, *Geophys. Res. Lett.*, *1*(1), 17–19, doi:10.1029/GL001i001p00017.
- Tsurutani, B. T., W. D. Gonzalez, A. L. C. Gonzalez, F. Tang, J. K. Arballo, and M. Okada (1995), Interplanetary origin of geomagnetic activity in the declining phase of the solar cycle, *J. Geophys. Res.*, *100*(A11), 21,717–21,733, doi:10.1029/95JA01476.
- Tsurutani, B. T., et al. (2006), Corotating solar wind streams and recurrent geomagnetic activity: A review, *J. Geophys. Res.*, *111*, A07501, doi:10.1029/2005JA011273.
- Tulasi Ram, S., M. Yamamoto, B. Veenadhari, S. Kumar, and S. Gurubaran (2012), Corotating interaction regions (CIRS) at sub-harmonic solar rotational periods and their impact on ionosphere-thermosphere system during the extreme low solar activity year 2008, *Indian J. Radio Space Phys.*, *41*, 294–245.
- Walsh, B. M., D. G. Sibeck, Y. Wang, and D. H. Fairfield (2012), Dawn-dusk asymmetries in the Earth's magnetosheath, *J. Geophys. Res.*, *117*, A12211, doi:10.1029/2012JA018240.
- Wei, Y., M. Hong, W. Wan, A. Du, J. Lei, B. Zhao, W. Wang, Z. Ren, and X. Yue (2008), Unusually long lasting multiple penetration of interplanetary electric field to equatorial ionosphere under oscillating IMF B_z , *Geophys. Res. Lett.*, *35*, L02102, doi:10.1029/2007GL032305.
- Zhang, Y. (2016), Distinct characteristics of asymmetric magnetic reconnections: Observational results from the exhaust region at the dayside magnetopause, *Sci. Rep.*, *6*, 27592.

RESEARCH ARTICLE

10.1002/2016JA022475

Key Points:

- Prompt penetration electric field driven by solar wind density
- Equatorial electric field disturbance under northward IMF B_z
- Signatures in global magnetic data and geosynchronous count rate

Correspondence to:

D. Rout,
diptir@prl.res.in

Citation:

Rout, D., D. Chakrabarty, R. Sekar, G. D. Reeves, J. M. Ruohoniemi, T. K. Pant, B. Veenadhari, and K. Shiokawa (2016), An evidence for prompt electric field disturbance driven by changes in the solar wind density under northward IMF B_z condition, *J. Geophys. Res. Space Physics*, 121, 4800–4810, doi:10.1002/2016JA022475.

Received 2 FEB 2016

Accepted 28 APR 2016

Accepted article online 2 MAY 2016

Published online 26 MAY 2016

An evidence for prompt electric field disturbance driven by changes in the solar wind density under northward IMF B_z condition

Diptiranjan Rout¹, D. Chakrabarty¹, R. Sekar¹, G. D. Reeves², J. M. Ruohoniemi³, Tarun K. Pant⁴, B. Veenadhari⁵, and K. Shiokawa⁶

¹Physical Research Laboratory, Ahmedabad, India, ²Los Alamos National Laboratory, Los Alamos, New Mexico, USA,

³Bradley Department of Electrical and Computer Engineering, Virginia Polytechnic Institute and State University,

Blacksburg, Virginia, USA, ⁴Space Physics Laboratory, VSSC, Thiruvananthapuram, India, ⁵Indian Institute of

Geomagnetism, Navi Mumbai, India, ⁶ISEE, Nagoya University, Nagoya, Japan

Abstract Before the onset of a geomagnetic storm on 22 January 2012 ($A_p = 24$), an enhancement in solar wind number density from $10/\text{cm}^3$ to $22/\text{cm}^3$ during 0440–0510 UT under northward interplanetary magnetic field (IMF B_z) condition is shown to have enhanced the high-latitude ionospheric convection and also caused variations in the geomagnetic field globally. Conspicuous changes in ΔX are observed not only at longitudinally separated low-latitude stations over Indian (prenoon), South American (midnight), Japanese (afternoon), Pacific (afternoon) and African (morning) sectors but also at latitudinally separated stations located over high and middle latitudes. The latitudinal variation of the amplitude of the ΔX during 0440–0510 UT is shown to be consistent with the characteristics of prompt penetration electric field disturbances. Most importantly, the density pulse event caused enhancements in the equatorial electrojet strength and the peak height of the F layer ($h_m F_2$) over the Indian dip equatorial sector. Further, the concomitant enhancements in electrojet current and F layer movement over the dip equator observed during this space weather event suggest a common driver of prompt electric field disturbance at this time. Such simultaneous variations are found to be absent during magnetically quiet days. In absence of significant change in solar wind velocity and magnetospheric substorm activity, these observations point toward perceptible prompt electric field disturbance over the dip equator driven by the overcompression of the magnetosphere by solar wind density enhancement.

1. Introduction

During space weather events, several types of prompt electric field disturbances affect equatorial ionosphere almost instantaneously. These include electric fields due to the undershielding [Chakrabarty *et al.*, 2005, 2006] and overshielding effects [Fejer *et al.*, 2007; Sekar and Chakrabarty, 2008] associated with IMF B_z (or IEF_y), penetration electric field associated with IMF B_y [Kelley and Makela, 2002], induction electric field due to dipolarization of geomagnetic field at the substorm onset [Kikuchi *et al.*, 2003; Chakrabarty *et al.*, 2015], and induced electric field due to the compression of equatorial magnetic flux owing to the increase in the solar wind dynamic pressure. The transient electric field disturbances during storm sudden commencements (SSCs) [Sastri *et al.*, 1993] or sudden impulses (SIs) [Akasofu and Chao, 1980] or main impulse (MI) [Sastri *et al.*, 1993] fall in the last category. These events are mostly associated with the enhancement in the dynamic (ram) pressure during the passage of interplanetary shocks. Interplanetary shocks are primarily governed by changes in the solar wind velocity, and these events have been reported earlier. However, it remains to be observed whether changes in the solar wind density affect equatorial ionospheric electric fields. Till date, to the best of these authors' knowledge, evidence for the changes in the equatorial ionospheric electric field due to changes dominated by the solar wind density alone is not available. One of the reasons for this is the simultaneous changes in the solar wind velocity and density during most of the ram pressure enhancement events. Further, during southward IMF B_z conditions, other kinds of prompt electric field disturbances (mentioned earlier) can be present to obfuscate the effects due to change in the solar wind density alone.

In recent times, a few efforts have been made to capture the changes in the equatorial ionosphere corresponding to changes in the solar wind ram pressure. For example, Zong *et al.* [2010] showed reduction in equatorial

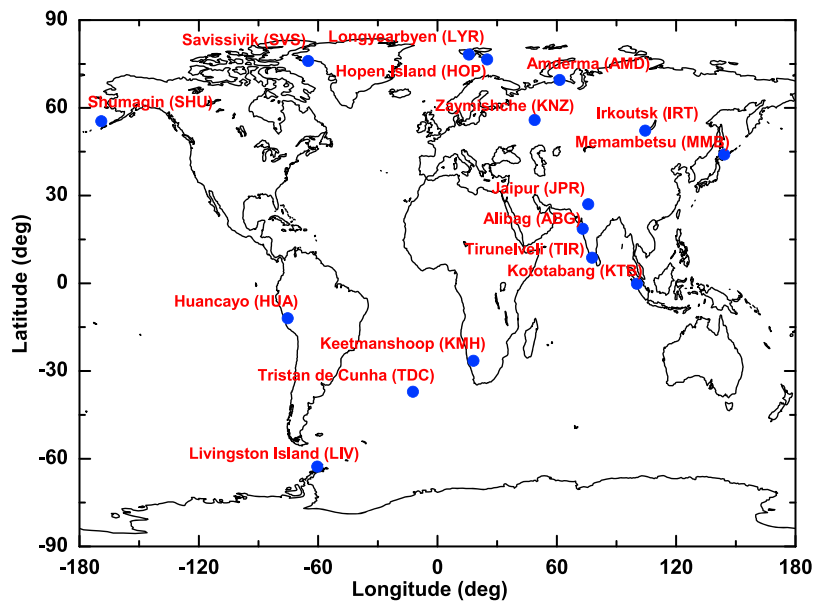


Figure 1. A global map with the magnetometer stations marked on it. Magnetic data from these stations are used in the present study.

total electron content corresponding to an interplanetary shock. This shock is associated with changes in the solar wind ram pressure due to simultaneous changes in velocity and density under the northward IMF B_z condition. On the other hand, *Yuan and Deng* [2007] indicated the role of continuous solar wind pressure variations on the long-lasting penetration of the interplanetary electric field in the equatorial ionosphere during southward IMF B_z condition. In addition, *Huang et al.* [2008] showed that ion velocities over Jicamarca increased following enhancements in the ram pressure regardless of the polarity of IMF B_z . Although such events can throw light on the effects of solar wind ram pressure on the equatorial ionosphere, the role of density is not explicitly evident based on these observations. Recently, *Wei et al.* [2012] showed significant effect of solar wind density in controlling the prompt electric field disturbance at the equatorial ionosphere during a polar cap saturation event. In their study, the density effects are studied primarily during the main phase of a storm when IMF B_z is southward. In fact, a few global MHD simulations [*Slinker et al.*, 1999; *Lopez et al.*, 2004] have indicated the role of solar wind density on the magnetosphere and ionosphere. However, observational evidence for the presence of prompt electric field disturbance in the equatorial ionosphere driven solely by changes in the solar wind density under northward IMF B_z conditions is still unavailable. The present investigation, based on a case study, provides evidence that the equatorial ionospheric electric field changes nearly simultaneously corresponding to a change in the solar wind density under northward IMF B_z condition.

2. Data Set

The solar wind parameters (like solar wind velocity, density, and magnetic field) are taken from the NASA Goddard Space Flight Center (GSFC) Coordinated Data Analysis Web (CDAWeb) (<http://cdaweb.gsfc.nasa.gov/>) wherein solar wind parameters are corrected for propagation lag till the bow shock nose. The temporal resolution of solar wind parameters is 1 min. The indices like *SYM-H* (symmetric component of ring current) and *AL* (westward auroral electrojet) are taken from CDAWeb with 1 min temporal resolution. The northward component (X) of the geomagnetic field measured at a few longitudinally separated low-latitude stations in the Indian, Japanese, African, South American, and Pacific sectors is used in the present study. In addition, measurements of X from a few high, middle and low latitude stations in the Northern and Southern Hemispheres are also investigated to capture the latitudinal changes. The ΔX variation for a given station is obtained after subtracting the nighttime base value level. The temporal resolution of the ΔX data is 1 min. Figure 1 shows the global map on which the magnetometer stations are marked from where the data sets are used in the present investigation. The ΔX data from these stations are used to construct Figures 3 and 4 which will be presented in section 3. It is to be mentioned here that with the exception of three Indian

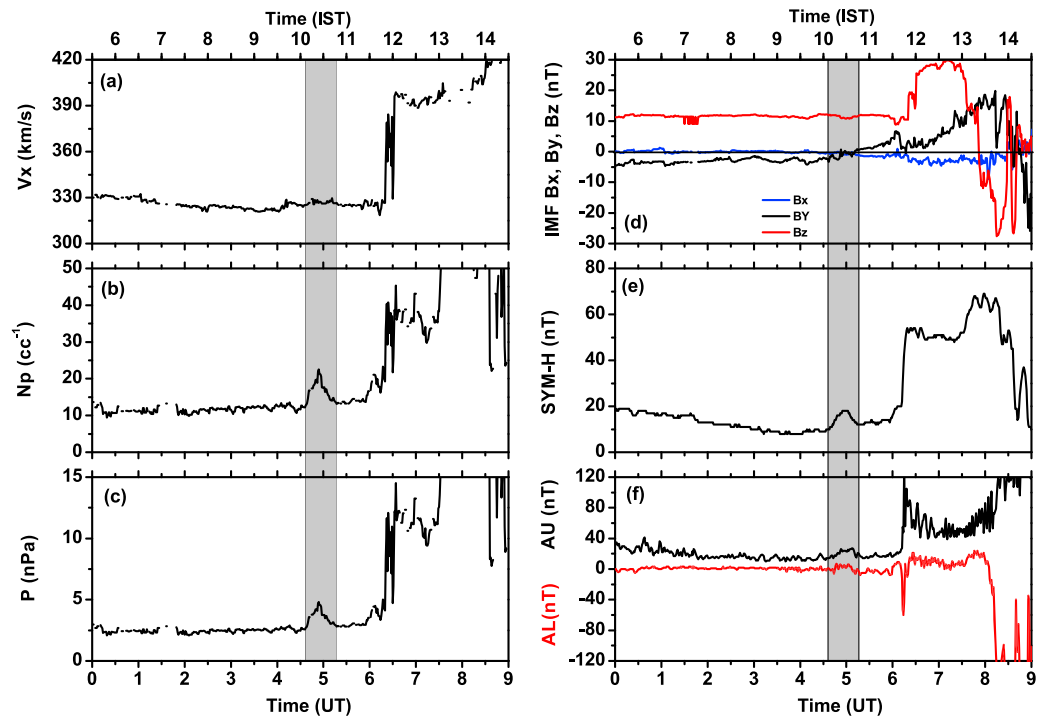


Figure 2. Variations in (a) solar wind velocity; (b) solar wind density; (c) solar wind ram pressure; (d) IMF B_x (blue), B_y (black), and B_z (red); (e) SYM-H; and (f) AL (red) and AU (black), respectively, during 0000–0900 UT on 22 January 2012. Corresponding time in IST is also shown at the top. The gray shaded rectangular box marks the interval when increase in solar wind density is observed under steady solar wind velocity and northward IMF B_z conditions.

stations (TIR, ABG, and JPR) and one Japanese station (KTB), all the other representative magnetic data are taken from SuperMAG network (<http://supermag.jhuapl.edu>).

In absence of direct ionospheric electric field measurements over the Indian dip equatorial sector, magnetometer and ionosonde measurements are used to infer the electric field perturbations during the event under consideration. It is known that $\Delta H_{TIR} - \Delta H_{ABG}$ represents the difference in the variation in the horizontal component of geomagnetic field over an equatorial (TIR) and an off-equatorial station (ABG) in the Indian sector. Therefore, this difference cancels out the magnetospheric contribution (not expected to change significantly between TIR and ABG) and can be taken to represent ionospheric contributions only. This methodology proposed by *Rastogi and Patil [1986]* is shown to represent the E region electric field variations that are responsible for the changes in electrojet current during daytime over the Indian dip equatorial region. As the precision of the magnetic measurements are very high (~ 0.1 nT), small variations in the EEJ strength can be captured by this technique.

In order to verify the presence of prompt electric field disturbances over the dip equatorial ionosphere using measurements from another independent technique (other than magnetometer), digisonde measurement over Thumba (geographic latitude: 8.5°N ; geographic longitude: 77°E and dip: 0.5°N) is used. It is known that ionospheric layer heights (e.g., $h'F$, h_mF_2) respond to the electric field variations over the dip equator. However, the virtual base height of the F layer ($h'F$) cannot be used to infer the electric field disturbances as it is also affected by production (during daytime) and loss (during both day and nighttime) processes. On the other hand, the peak height of the F_2 layer (h_mF_2) is minimally affected by loss processes as it is above 300 km [*Bittencourt and Abdu, 1981*] on most occasions. Further, in the absence of solar flare events, fast changes in h_mF_2 during daytime is unlikely to be caused by production processes. Therefore, variation in h_mF_2 is used in the present investigation to additionally confirm the electrodynamical perturbations associated with the space weather event under consideration. The h_mF_2 values are scaled using the ARTIST software [*Reinisch and Huang, 2001*]. The typical uncertainty in the determination of h_mF_2 during daytime is ~ 5 km.

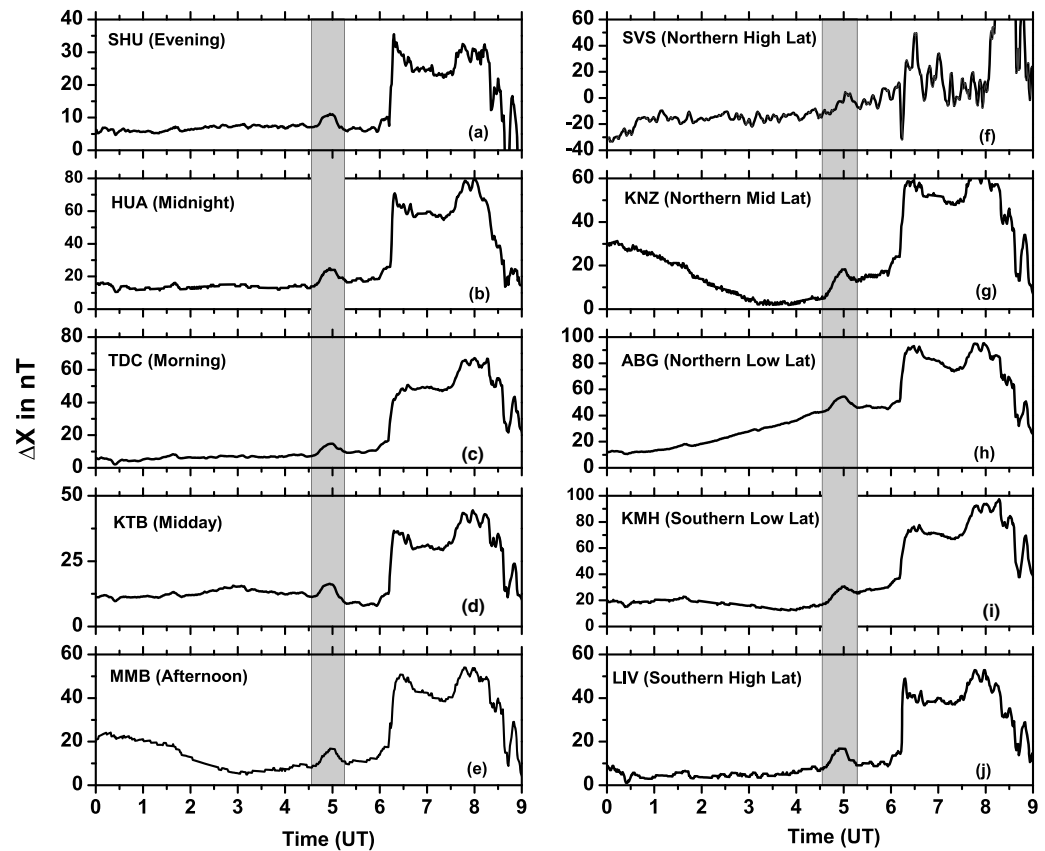


Figure 3. The ΔX variations for a few (a–e) longitudinally and (f–j) latitudinally separated stations during 0000–0900 UT. The longitudinally separated stations (SHU, HUA, TDC, KTB, and MMB) represent different local times that are mentioned in the figure. The latitudinally separated stations (SVS, KNZ, ABG, KMH, and LIV) include Northern and Southern Hemispheric stations. It can be noted that the ΔX variations during 0440–0510 UT (marked by vertical shaded region) show distinct enhancements irrespective of longitude and latitude.

3. Results

Figures 2a–2c reveals the variation in the solar wind velocity (V_x , in km/s), proton density (N_p , in $/\text{cm}^3$), and dynamic pressure (P , in nPa) during 0000–0900 UT (universal time) on 22 January 2012. Corresponding Indian Standard Time (IST = UT + 5.5 h) is also shown on top of Figures 2 and 5 to facilitate interpretation of Figure 5 which is used to infer the ionospheric prompt electric field perturbations over the Indian dip equatorial sector. Figure 2d shows the variations in IMF B_x (in blue), IMF B_y (in black), and IMF B_z (in red) in nanotesla, respectively, during the same interval. It is clearly seen that solar wind parameters like V_x and IMF B_z do not show significant changes during 0440–0510 UT (marked by vertical shaded box). IMF B_y starts changing its polarity during this interval and remains very close to zero at ~ 0450 UT when a peak in the solar wind density is observed. This enhancement (and not the larger enhancement during the onset of SSC at 0612 UT) in the solar wind density is of interest here as this occurs in the absence of any significant change in the solar wind velocity. IMF B_x also remains almost constant during this interval. Solar wind density changes from $10/\text{cm}^3$ to $22/\text{cm}^3$ during 0440–0510 and maximizes at ~ 0450 UT. In contrast, velocity (V_x) during this interval changes by only 2 km/s. The solar wind ram pressure changes from 2.5 nPa to 5 nPa during 0440–0510 UT. Small but detectable changes are observed in AU (black) and AL (red) (see Figure 2f) during this interval. The change in $SYM-H$ (Figure 2e) is ~ 10 nT which is significant. It must be noted that IMF B_z is northward during this time. In addition to the above event, both V_x and N_p register sharp enhancements at 0618 UT under northward IMF B_z condition. In fact, a storm sudden commencement (SSC) occurs at 0612 UT due to the arrival of the associated interplanetary shock at this time. The SSC is followed by an initial phase that continues for ~ 2 h. As the earlier SSC-related prompt electric field penetration effects [Sastri *et al.*, 1993] did not explicitly attempt to delineate

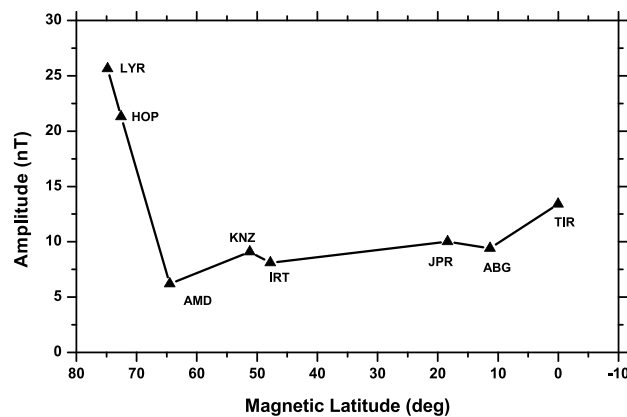


Figure 4. Latitudinal variation in the amplitude (in nT) of ΔX during the 0440–0510 UT at the dayside stations spanning from polar region to dip equatorial regions. Dip equatorial enhancement in ΔX can be seen. It can also be noticed that amplitude over the dip equator is comparable to that over the subauroral region and less than that over the polar region.

Northern and Southern Hemispheres. It can be noticed that ΔX variations during 0440–0510 UT (marked by vertical shaded region) register distinct enhancements at all stations irrespective of longitude or latitude corresponding to the density-related pressure enhancement. Therefore, Figure 3 elicits the global nature of the ΔX enhancement during 0440–0510 UT.

In order to confirm whether the variation in ΔX with latitude follow the characteristic pattern associated with the prompt penetration electric field and not the pattern associated with the magnetopause

the impact of solar wind density alone, the present investigation fills this gap by identifying an event where solar wind density changes but not the solar wind velocity.

In order to find out the effects of the solar wind density pulse during 0440–0510 UT on the global magnetic field, Figure 3 is presented. Figures 3a–3e and Figures 3f–3j show ΔX variations at a few longitudinally and latitudinally separated stations, respectively, during 0000–0900 UT. The longitudinally separated stations represent different local time sectors (mentioned in the figure), while the latitudinally separated stations represent high, middle, and low latitudes (not along the same meridian) from

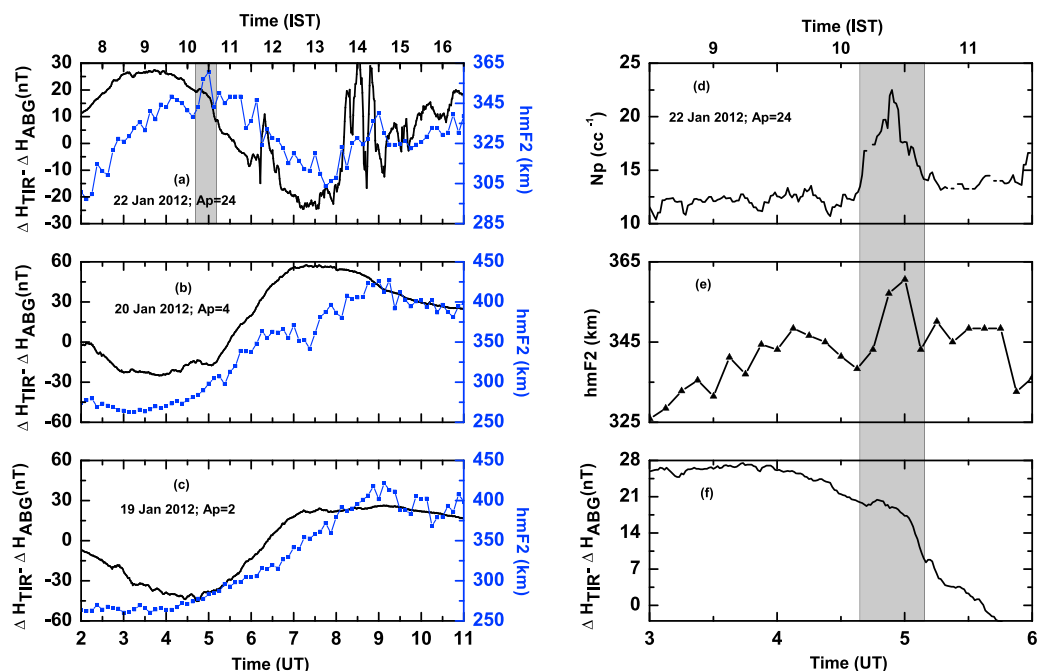


Figure 5. (a–c) The variations in $\Delta H_{TIR} - \Delta H_{ABG}$ (black) and $h_m F_2$ (blue) during 0200–1100 UT on (Figure 5a) 22 January, vis-à-vis (Figure 5b) 20 January, and (Figure 5c) 19 January 2012 that are magnetically quiet days. The gray shaded region in Figure 5a shows the interval when simultaneous fluctuations are observed in $\Delta H_{TIR} - \Delta H_{ABG}$ and $h_m F_2$. (d–f) The zoomed-in variations in (Figure 5e) $\Delta H_{TIR} - \Delta H_{ABG}$ and (Figure 5f) $h_m F_2$ vis-à-vis N_p during 0300–0600 UT on 22 January 2012 with the gray shaded region overlaid. The shaded region clearly shows that the enhancements in $\Delta H_{TIR} - \Delta H_{ABG}$ and $h_m F_2$ are concomitant with the increase in N_p .

(Chapman-Ferraro) current, Figure 4 is presented. This figure shows the latitudinal variation in the amplitude (in nT) of ΔX during 0440–0510 UT by considering a few dayside stations are considered. The ΔX amplitude maximizes over the auroral region, falls off over middle and low latitudes, and enhances again over the dip equator. It is also important to note that the ΔX amplitude over the dip equator is comparable to that over the subauroral region and less than that over the polar region.

Figure 5 explores the prompt electric field perturbations, if any, over the equatorial ionosphere during 0440–0510 UT when enhancement in solar wind density (N_p) is observed in absence of any significant change in the solar wind velocity, and IMF components. Figures 5a–5c depict comparisons of the $\Delta H_{\text{TIR}}-\Delta H_{\text{ABG}}$ and $h_m F_2$ variations during 0200–1100 UT on the event day (22 January 2012) vis-à-vis on 20 and 19 January 2012 which are magnetically quiet days ($A_p = 4$ and 2, respectively). It is noted that the slow temporal variations in $\Delta H_{\text{TIR}}-\Delta H_{\text{ABG}}$ and $h_m F_2$ grossly agree with each other barring morning hours. The gray shaded region marked in Figure 5a shows the interval of 0440–0510 UT when the fast fluctuations in $\Delta H_{\text{TIR}}-\Delta H_{\text{ABG}}$ and $h_m F_2$ go hand in hand. Interestingly, although fast fluctuations are present in $h_m F_2$ and $\Delta H_{\text{TIR}}-\Delta H_{\text{ABG}}$ on quite days, simultaneous fluctuations in both the parameters (similar to the shaded region on 22 January) are absent on the two quiet days. In order to evaluate the association of the equatorial E and F region parameters ($\Delta H_{\text{TIR}}-\Delta H_{\text{ABG}}$ and $h_m F_2$, respectively) with the variation in the solar wind density (N_p), the shaded region in Figure 5a is blown up and presented along with solar wind density (N_p) in Figures 5d–5f. Figures 5d–5f clearly elicit that the enhancements in $h_m F_2$ and $\Delta H_{\text{TIR}}-\Delta H_{\text{ABG}}$ are concomitant with the enhancement in N_p . The implication of this observation will be addressed in the ensuing section.

4. Discussion

Solar wind dynamic (ram) pressure is expressed as follows.

$$P_{\text{dyn}} = \rho v^2 \quad (1)$$

In the above expression, ρ and v are solar wind density (strictly, mass density) and velocity, respectively. Differential of (1) yields the following expression.

$$\Delta P_{\text{dyn}} = v^2 \Delta \rho + 2v\rho \Delta v \quad (2)$$

Based on (2), three different conditions can be envisaged through which solar wind dynamic pressure can be changed. These conditions are as follows.

Condition 1: $v\Delta\rho \approx 2\rho\Delta v$

Condition 2: $v\Delta\rho < 2\rho\Delta v$

Condition 3: $v\Delta\rho > 2\rho\Delta v$

During most of the SSC, SI, or MI events, conditions 1 or 2 get satisfied and these cases, as mentioned in section 1, have been studied in the past. However, evidence for the changes in the ionospheric electric field satisfying condition 3 is not available in the literature particularly when IMF B_z is northward. In the present case, the solar wind velocity is ~ 330 km/s and density is $\sim 10/\text{cm}^3$ before the arrival of the density pulse centered at 0450 UT. During the density pulse event, the maximum change in solar wind density is $12/\text{cm}^3$ and the change in the solar wind velocity (Δv) is not significant (~ 2 km/s). Slow and nearly constant (in time) solar wind speed coupled with changes in the solar wind density makes the term $v\Delta\rho$ larger than $2\rho\Delta v$. Therefore, temporal changes in ram pressure during this time are primarily driven by the temporal changes in the solar wind density.

It must also be noted at this point that IMF B_z and B_y remain nearly steady when changes in $\Delta\rho$ occur during 0440–0510 UT. In order to rule out influence of any substorm-induced transient electric field at this time, the geosynchronous electron and proton counts per second measured by the Los Alamos National Laboratory (LANL) satellites are shown in Figure 6. Although data from all the LANL satellites are investigated, observations from a single nightside satellite (1991-080) are presented here for brevity. Electron counts per second (Figure 6a) in four energy channels (E1: 48.15–69.85 keV; E2: 68.5–102.5 keV; E3: 99.95–149.45 keV; E4: 145.6–220.6 keV) and proton counts per second (Figure 6b) in three energy channels (P2: 75–113 keV; P3: 113–170 keV; P4: 170–250 keV) are shown. The signature of “dispersionless” injection, which is a telltale signature of substorm onset, is absent during 0440–0510 UT. Instead, one can see the characteristic undulations in the flux patterns in response to the enhancement in the ram pressure enhancement similar to what was shown earlier by Lee *et al.* [2005].

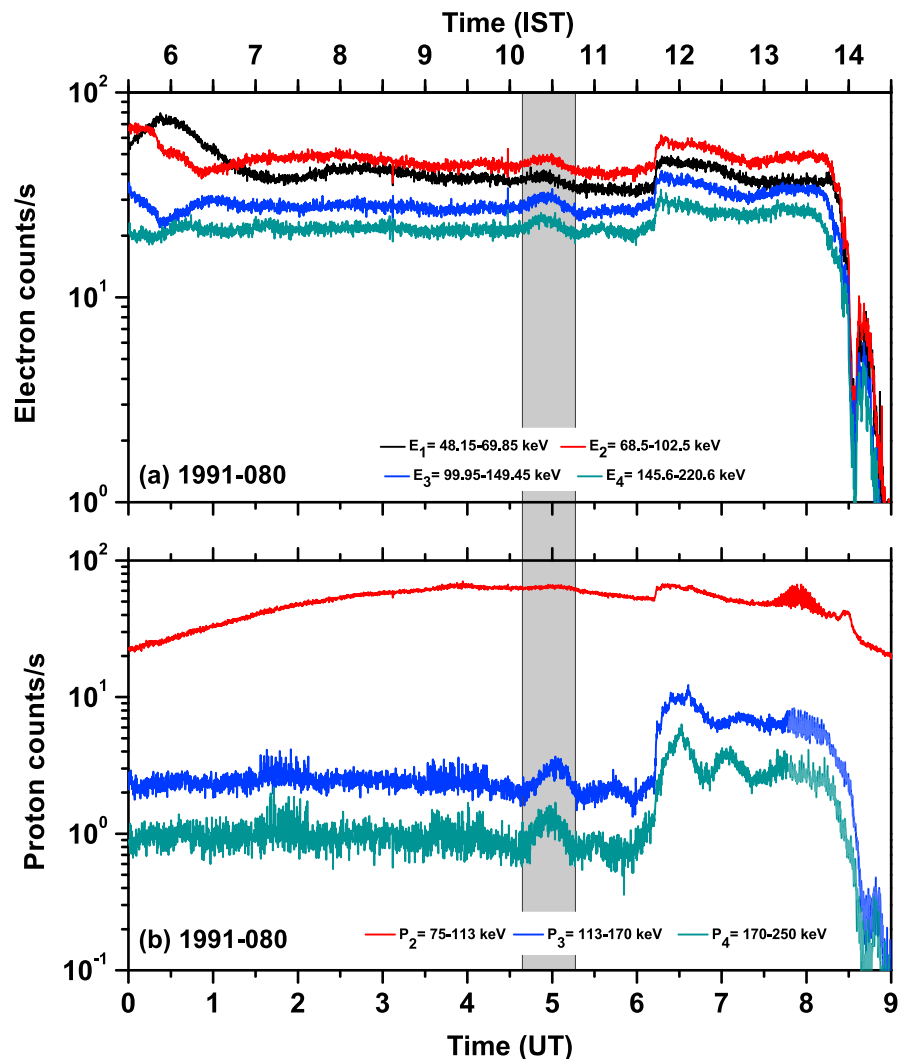


Figure 6. The changes in energetic (a) electron and (b) proton counts per second observed by LANL (1991-080) satellite during 0000–0900 UT on 22 January 2012. The gray shaded rectangular box highlights the interval (0440–0510 UT) of solar wind density enhancement.

Before addressing the electric field perturbations over the Indian dip equatorial sector, it is important to verify that the ionospheric plasma convection got enhanced over high latitudes during this density pulse event. Figures 7–9 in which three high-latitude ionospheric convection maps generated by the Super Dual Auroral Radar Network (SuperDARN) HF radar network are shown corresponding to the representative intervals of 0440–0442 UT, 0450–0452 UT, and 0510–0512 UT, respectively. An anticlockwise ionospheric flow vortex can be seen to get maximized (see red arrows) during 0450–0452 UT (Figure 8). This provides a strong evidence for the generation of region 1 field-aligned currents (R1-FACs) [e.g., Sofko *et al.*, 1995] and presence of convection electric field over high latitudes in the dawn-to-dusk direction during the density pulse event. This electric field can penetrate to lower latitudes nearly simultaneously. Further, the concomitant magnetic variations in the Indian (prenoon), South American (midnight), Japanese (afternoon), Pacific (afternoon), and African (morning) sectors as well as at the high- and middle-latitude stations during 0440–0510 UT suggest that the global ionospheric current system responded to the changes in the solar wind density during this time. Moreover, the enhancement (~ 10 nT) in *SYM-H* corresponding to this solar wind density enhancement is also consistent with the work of Araki *et al.* [1993] who showed that the dynamic pressure dependence of

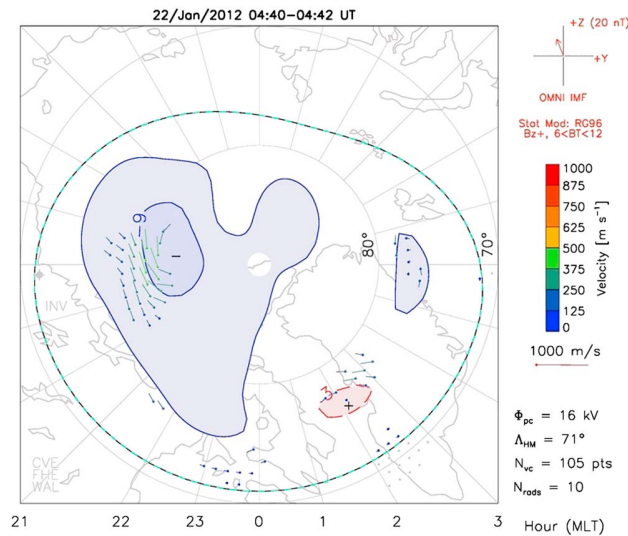


Figure 7. The high-latitude ionospheric convection maps generated by the SuperDARN HF radar network during 0440–0442 UT. High-latitude ionospheric convection is weak at this time.

the dayside stations maximizes over the auroral region, falls off over middle and low latitudes, and enhances again over the dip equator. As the ΔX amplitude over the polar region is more than those over the subauroral and dip equatorial regions, the latitudinal variation depicted in Figure 4 points toward the presence of prompt penetration electric field during this interval [Araki, 1977; Koba et al., 2000; Kikuchi et al., 2000]. It is to be noted here that in the case of significant enhancement of magnetopause (Chapman-Ferraro) current, one would have expected ΔX amplitude over the dip equator exceeding that over the polar region [Namikawa et al., 1964]. On the other hand, in the prompt penetration scenario, the ionospheric Hall current driven by the high-latitude electric field closes through the Pedersen current over the dip equator and hence can generate polarization electric field when its flow is obstructed at the terminator. The ionospheric Pedersen current over the dip equator also gets amplified [Sastri et al., 2003] due to Cowling conductivity. Therefore, Figure 4 is consistent with the latitudinal characteristics of prompt penetration electric field, and the generation of this

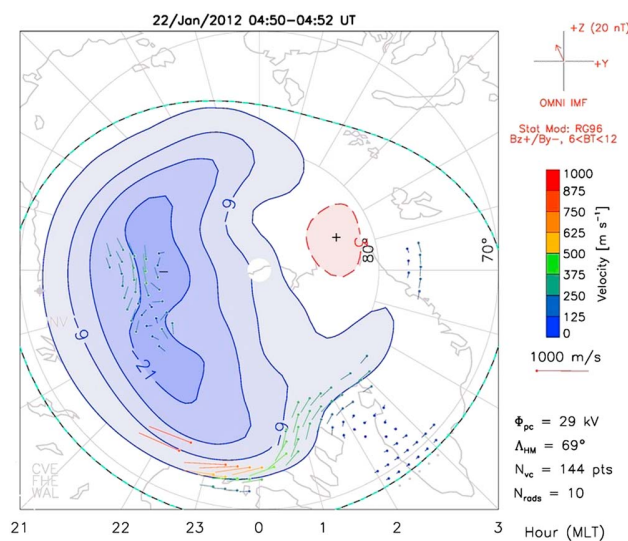


Figure 8. Same as Figure 7 but for the interval 0510–0512 UT. An anticlockwise and enhanced (see red arrows) ionospheric flow vortex can be seen at this time.

electric field in the present case is associated with the enhancement in solar wind density. Figure 5 brings out the dip equatorial ionospheric signatures of the prompt penetration electric field associated with the solar wind density pulse event. Unambiguous enhancement in $\Delta H_{TIR} - \Delta H_{ABG}$ (as shown in Figure 5f) when the background variation is decreasing suggests the enhancement in the eastward electric field perturbation in the *E* region during 0440–0510 UT (the shaded interval). Further, the significant rise (by about 23 km) of $h_m F_2$ over Thumba (Figure 5e) during the same interval suggests the presence of eastward electric field perturbation in the *F* region. The efficacy of $h_m F_2$ in promptly capturing the electric field

It is clear from Figure 4 that the amplitude of ΔX during 0440–0510 UT at

the dip equator is associated with the enhancement in solar wind density.

Figure 5 brings out the dip equatorial ionospheric signatures of the prompt penetration electric field associated with the solar wind density pulse event. Unambiguous enhancement in $\Delta H_{TIR} - \Delta H_{ABG}$ (as shown in Figure 5f) when the background variation is decreasing suggests the enhancement in the eastward electric field perturbation in the *E* region during 0440–0510 UT (the shaded interval). Further, the significant rise (by about 23 km) of $h_m F_2$ over Thumba (Figure 5e) during the same interval suggests the presence of eastward electric field perturbation in the *F* region. The efficacy of $h_m F_2$ in promptly capturing the electric field

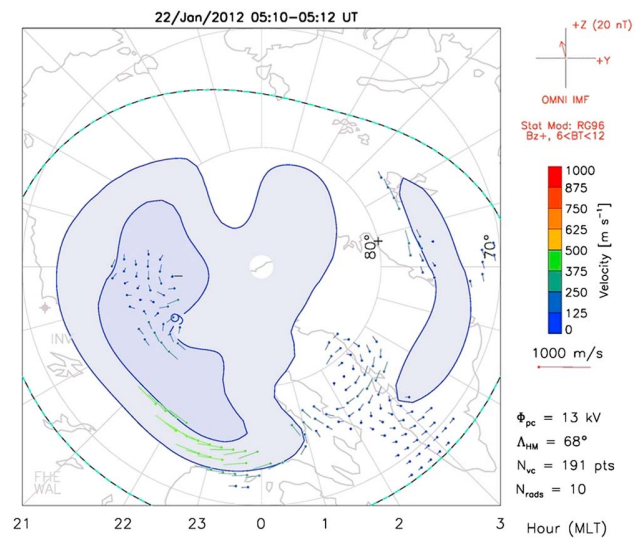


Figure 9. Same as Figure 7 but for the interval 0510–0512 UT. The anticlockwise ionospheric flow vortex is seen to be weakened substantially at this time.

effects of local origin. Therefore, small temporal scale fluctuations that occurred simultaneously in the dip equatorial *E* and *F* regions during 0440–0510 UT when solar wind density got enhanced strongly point toward the imposition of prompt electric field disturbance on the equatorial ionosphere. Measurements by a number of independent techniques spread over the globe provide credence to this proposition. The possible mechanisms through which the equatorial ionosphere can get affected due to the enhancement of solar wind density are addressed in the ensuing paragraph.

The electric field disturbances for about 30–40 min over the dip equatorial ionosphere during enhancements in the solar wind ram pressure was shown by *Huang et al.* [2008] using Jicamarca drift data. The distinctive point where this investigation is different from the work of *Huang et al.* [2008] is primarily the isolation of the role of solar wind density in causing the prompt electric field disturbance. As discussed in *Huang et al.* [2008], there are two possible mechanisms through which enhancement in solar wind ram pressure can cause prompt electric field disturbance over the equatorial ionosphere. The first mechanism is through the overcompression of the magnetosphere when the solar wind ram pressure enhances. In fact, the compression or decompression of magnetospheric plasma can reach ionosphere by the Alfvén and magnetosonic waves [e.g., *Tamao*, 1964; *Lysak and Lee*, 1992; *Lyatsky et al.*, 2010]. *Keller et al.* [2002] suggest that as the solar wind density pulse propagates along the flank of the magnetopause, a two-step response in field-aligned current (FAC) is expected. In the first step, FACs increase near the polar cap, and in the second step, the FACs increase near the low latitude. The increase in FAC is also found to be in the same direction as that of region 1 currents. This implies that the azimuthal electric field, which is generated inside the magnetosphere due to the earthward motion of the compressed magnetospheric plasma, can penetrate into the low-latitude ionosphere [*Shi et al.*, 2009; *Lyatsky et al.*, 2010]. Therefore, this situation is different from the conventional prompt penetration scenario in terms of place of origin of the electric field. In the conventional prompt penetration scenario, the electric field exists in the solar wind with respect to Earth, whereas in this case the electric field is generated inside the magnetosphere. This situation is probably similar to the overcompression mechanism discussed by *Huang et al.* [2008]. The distinctive feature associated with this mechanism is the enhancement of the geomagnetic field at all local times. This is what is observed in the present case. The other mechanism is similar to what was proposed by *Araki* [1994] to explain the main impulse in the low-latitude geomagnetic field in response to solar wind pressure enhancement. The model of *Araki* [1994] suggests that the low-latitude geomagnetic response to the enhancement in the solar wind ram pressure comprises a preliminary impulse (~1 min), a main impulse (~10 min), and a step-like increase that continues for some time. While the preliminary impulse and the main impulse are believed to be due to R1-FAC and ionospheric currents, the step-like increase is caused by the magnetopause current. The characteristic feature in this scenario is the local time differences in the geomagnetic field response. In fact, according to the work of *Araki* [1994] and *Araki et al.* [2006], the effect of main

disturbance over the dip equatorial region during storm time is shown by several researchers [*Szuszczewicz et al.*, 1998; *Yue et al.*, 2008]. In the present case, considering a 5 km uncertainty in the determination of $h_m F_2$, the increase in the *F* layer vertical drift during 0438–0506 UT turns out to be $\sim 16.81 \pm 5.2 \text{ m s}^{-1}$. Therefore, simultaneous increases in both $h_m F_2$ and $\Delta H_{TIR} - \Delta H_{ABG}$ during 0440–0510 UT on 22 January 2012 point toward the prompt electric field disturbance [e.g., *Tsurutani et al.*, 2004; *Sekar et al.*, 2012; *Abdu et al.*, 2013]. Figures 5b and 5c suggest that this does not happen all the time. Although one can observe small temporal scale fluctuations in $h_m F_2$ and $\Delta H_{TIR} - \Delta H_{ABG}$ on 20 January as well as on 19 January 2012, those are not simultaneous fluctuations. This indicates toward the electric field

impulse is expected to be highest in the nightside and nominal in the dayside. It can be noted that the present set of observations are not consistent with both the step-like and local time variations in the geomagnetic field features expected from the Araki mechanism. Therefore, the prompt electric field disturbance reported in the present case arose most likely due to the associated effects of overcompression of the magnetosphere due to the density-related changes in the solar wind ram pressure.

Last but not the least, it is important to note that the prompt electric field disturbances presented in this investigation occurs essentially through the increase in the ram pressure. However, based on a case study, it is rather difficult to comment on the differences in the ionospheric effects corresponding to change in solar wind density or velocity. More investigations are needed to address this issue. Further, the mechanism through which magnetosphere is coupled with low-latitude ionosphere during the density pulse events is not comprehensively understood. In addition, as the ionospheric electric fields are curl free, it is expected that the electric field disturbances will have opposite polarity at conjugate longitudes. However, it is not clear how the ionospheric electric field will adjust globally if magnetosphere is compressed asymmetrically by solar wind ram pressure. Global measurements are needed to address this aspect comprehensively.

5. Summary

This case study, based on a unique set of measurements, reveals that a transient change in solar wind density from $10/\text{cm}^3$ to $22/\text{cm}^3$ during 0440–0510 UT under northward IMF B_z condition has not only enhanced the high-latitude convection but also enhanced the global magnetic field as well as equatorial E and F region electric field simultaneously. The enhanced high-latitude ionospheric convection, latitudinal characteristics of the increase in the geomagnetic field strength, enhancement of the geomagnetic field at all local times and the concomitant changes in the equatorial E and F region parameters elicit the role of solar wind density in generating transient electric field disturbances over the dip equatorial ionosphere through the associated effects of overcompression of the magnetosphere.

Acknowledgments

Magnetic data from the three Indian stations (TIR, ABG, and JPR) are provided by Indian Institute of Geomagnetism, India. Data from the one Japanese station (KTB) is provided by the Solar Terrestrial Environment Laboratory, Japan, and this station is part of 210 MM chain (<http://stdb2.stelab.nagoya-u.ac.jp/mm210/>). This work of K.S. is supported by the JSPS Core-to-Core Program, B. Asia-Africa Science Platforms, and JSPS KAKENHI grants 16H06286 and 15H05815. All the other representative magnetic data used in this work are taken from SuperMAG network (<http://supermag.jhuapl.edu>). The authors are grateful to the PIs of the magnetic observatories and the National institutes that support the observatories based on which the present study is carried out. SuperDARN data are available from the Virginia Tech SuperDARN website (<http://vt.superdarn.org/>). SuperDARN is a collection of radars funded by national scientific funding agencies of Australia, Canada, China, France, Japan, South Africa, United Kingdom and United States of America. The geosynchronous particle injection data are provided by Los Alamos National Laboratory, USA. The geomagnetic indices and solar wind data are obtained from NASA GSFC CDAWeb (<http://cdaweb.gsfc.nasa.gov/>). We thank the reviewers for the insightful comments.

References

- Abdu, M. A., J. R. Souza, I. S. Batista, B. G. Fejer, and J. H. A. Sobral (2013), Sporadic E layer development and disruption at low latitudes by prompt penetration electric fields during magnetic storms, *J. Geophys. Res. Space Physics*, *118*, 2639–2647, doi:10.1002/jgra.50271.
- Akasofu, S.-I., and J. K. Chao (1980), Interplanetary shock waves and magnetospheric substorms, *Planet. Space Sci.*, *28*(4), 381–385, doi:10.1016/0032-0633(80)90042-2.
- Araki, T. (1977), Global structure of geomagnetic sudden commencements, *Planet. Space Sci.*, *25*(4), 373–384, doi:10.1016/0032-0633(77)90053-8.
- Araki, T. (1994), A physical model of the geomagnetic sudden commencement, in *Solar Wind Sources of Magnetospheric Ultra-Low-Frequency Waves*, edited by M. J. Engebretson, K. Takahashi, and M. Scholer, pp. 183–200, AGU, Washington, D. C.
- Araki, T., K. Funato, T. Iguchi, and T. Kamei (1993), Direct detection of solar wind dynamic pressure effect on ground geomagnetic field, *Geophys. Res. Lett.*, *20*(9), 775–778, doi:10.1029/93GL00852.
- Araki, T., K. Keika, T. Kamei, H. Yang, and S. Alex (2006), Nighttime enhancement of the amplitude of geomagnetic sudden commencements and its dependence on IMF B_z , *Earth Planets Space*, *58*(1), 45–50.
- Bittencourt, J. A., and M. A. Abdu (1981), A theoretical comparison between apparent and real vertical ionization drift velocities in the equatorial F region, *J. Geophys. Res.*, *86*(A4), 2451–2454, doi:10.1029/JA086iA04p02451.
- Chakrabarty, D., R. Sekar, R. Narayanan, C. V. Devasia, and B. M. Pathan (2005), Evidence for the interplanetary electric field effect on the OI 630.0 nm airglow over low latitude, *J. Geophys. Res.*, *110*, A11301, doi:10.1029/2005JA011221.
- Chakrabarty, D., R. Sekar, R. Narayanan, A. K. Patra, and C. V. Devasia (2006), Effects of interplanetary electric field on the development of an equatorial spread F event, *J. Geophys. Res.*, *111*, A12316, doi:10.1029/2006JA011884.
- Chakrabarty, D., D. Rout, R. Sekar, R. Narayanan, G. D. Reeves, T. K. Pant, B. Venadhari, and K. Shiokawa (2015), Three different types of electric field disturbances affecting equatorial ionosphere during a long duration prompt penetration event, *J. Geophys. Res. Space Physics*, *120*, 4993–5008, doi:10.1002/2014JA020759.
- Fejer, B. G., J. W. Jensen, T. Kikuchi, M. A. Abdu, and J. L. Chau (2007), Equatorial ionospheric electric fields during the November 2004 magnetic storm, *J. Geophys. Res.*, *112*, A10304, doi:10.1029/2007JA012376.
- Huang, C.-S., K. Yumoto, S. Abe, and G. Sofko (2008), Low-latitude ionospheric electric and magnetic field disturbances in response to solar wind pressure enhancements, *J. Geophys. Res.*, *113*, A08314, doi:10.1029/2007JA012940.
- Keller, K. A., M. Hesse, M. Kuznetsova, L. Rastätter, T. Moretto, T. I. Gombosi, and D. L. DeZeeuw (2002), Global MHD modeling of the impact of a solar wind pressure change, *J. Geophys. Res.*, *107*(A7), 1126, doi:10.1029/2001JA000060.
- Kelley, M. C., and J. J. Makela (2002), B_y -dependent prompt penetrating electric fields at the magnetic equator, *Geophys. Res. Lett.*, *29*(7), 571–573, doi:10.1029/2001GL014468.
- Kikuchi, T., H. Lühr, K. Schlegel, H. Tachihara, M. Shinohara, and T.-I. Kitamura (2000), Penetration of auroral electric fields to the equator during a substorm, *J. Geophys. Res.*, *105*(A10), 23,251–23,261, doi:10.1029/2000JA000016.
- Kikuchi, T., K. K. Hashimoto, T.-I. Kitamura, H. Tachihara, and B. Fejer (2003), Equatorial counter-electrojets during substorms, *J. Geophys. Res.*, *108*(A11), 1406, doi:10.1029/2003JA009915.
- Kobe, A. T., A. D. Richmond, B. A. Emery, C. Peymirat, H. Lühr, T. Moretto, M. Hairston, and C. Amory-Mazaudier (2000), Electrodynamic coupling of high and low latitudes: Observations on May 27, 1993, *J. Geophys. Res.*, *105*(A10), 22,979–22,989, doi:10.1029/2000JA000058.

- Lee, D.-Y., L. R. Lyons, and G. D. Reeves (2005), Comparison of geosynchronous energetic particle flux responses to solar wind dynamic pressure enhancements and substorms, *J. Geophys. Res.*, *110*, A09213, doi:10.1029/2005JA011091.
- Lopez, R. E., M. Wiltberger, S. Hernandez, and J. G. Lyon (2004), Solar wind density control of energy transfer to the magnetosphere, *Geophys. Res. Lett.*, *31*, L08804, doi:10.1029/2003GL018780.
- Lyatsky, W., G. V. Khazanov, and J. A. Slavin (2010), Alfvén wave reflection model of field-aligned currents at mercury, *Icarus*, *209*(1), 40–45, doi:10.1016/j.icarus.2009.11.039.
- Lysak, R. L., and D.-h. Lee (1992), Response of the dipole magnetosphere to pressure pulses, *Geophys. Res. Lett.*, *19*(9), 937–940, doi:10.1029/92GL00625.
- Namikawa, T., T. Kitamura, T. Okuzawa, and T. Araki (1964), Propagation of weak hydromagnetic discontinuity in the magnetosphere and the sudden commencement of geomagnetic storm, *Rept. Ionosphere Space Res. Jpn.*, *18*, 218–227.
- Rastogi, R., and A. Patil (1986), Complex structure of equatorial electrojet current, *Curr. Sci.*, *85*(9), 433–436.
- Reinisch, B., and X. Huang (2001), Deducing topside profiles and total electron content from bottomside ionograms, *Adv. Space Res.*, *27*(1), 23–30, doi:10.1016/S0273-1177(00)00136-8.
- Sastri, J. H., J. V. S. V. Rao, and K. B. Ramesh (1993), Penetration of polar electric fields to the nightside dip equator at times of geomagnetic sudden commencements, *J. Geophys. Res.*, *98*(A10), 17,517–17,523, doi:10.1029/93JA00418.
- Sastri, J. H., Y. Kamide, and K. Yumoto (2003), Signatures for magnetospheric substorms in the geomagnetic field of dayside equatorial region: Origin of the ionospheric component, *J. Geophys. Res.*, *108*(A10), 1375, doi:10.1029/2003JA009962.
- Sekar, R., and D. Chakrabarty (2008), Role of overshielding electric field on the development of pre-midnight plume event: Simulation results, *J. Atmos. Sol. Terr. Phys.*, *70*(17), 2212–2221, doi:10.1016/j.jastp.2008.04.015.
- Sekar, R., D. Chakrabarty, and D. Pallamraju (2012), Optical signature of shear in the zonal plasma flow along with a tilted structure associated with equatorial spread F during a space weather event, *J. Atmos. Terres Phys.*, *75–76*, 57–63, doi:10.1016/j.jastp.2011.05.009.
- Shi, Y., E. Zesta, and L. R. Lyons (2009), Features of energetic particle radial profiles inferred from geosynchronous responses to solar wind dynamic pressure enhancements, *Ann. Geophys.*, *27*(2), 851–859, doi:10.5194/angeo-27-851-2009.
- Slinker, S. P., J. A. Fedder, W. J. Hughes, and J. G. Lyon (1999), Response of the ionosphere to a density pulse in the solar wind: Simulation of traveling convection vortices, *Geophys. Res. Lett.*, *26*(23), 3549–3552, doi:10.1029/1999GL010688.
- Sofko, G. J., R. Greenwald, and W. Bristow (1995), Direct determination of large-scale magnetospheric field-aligned currents with SuperDARN, *Geophys. Res. Lett.*, *22*(15), 2041–2044, doi:10.1029/95GL01317.
- Szuszczewicz, E. P., M. Lester, P. Wilkinson, P. Blanchard, M. Abdu, R. Hanbaba, K. Igarashi, S. Pulinet, and B. M. Reddy (1998), A comparative study of global ionospheric responses to intense magnetic storm conditions, *J. Geophys. Res.*, *103*(A6), 11,665–11,684, doi:10.1029/97JA01660.
- Tamao, T. (1964), A hydromagnetic interpretation of geomagnetic SSC*, *Rep. Ionosphere Space Res. Jpn.*, *18*, 16–31.
- Tsurutani, B., et al. (2004), Global dayside ionospheric uplift and enhancement associated with interplanetary electric fields, *J. Geophys. Res.*, *109*, A08302, doi:10.1029/2003JA010342.
- Wei, Y., W. Wan, B. Zhao, M. Hong, A. Ridley, Z. Ren, M. Fraenz, E. Dubinin, and M. He (2012), Solar wind density controlling penetration electric field at the equatorial ionosphere during a saturation of cross polar cap potential, *J. Geophys. Res.*, *117*, A09308, doi:10.1029/2012JA017597.
- Yuan, Z., and X. Deng (2007), Effects of continuous solar wind pressure variations on the long-lasting penetration of the interplanetary electric field during southward interplanetary magnetic field, *Adv. Space Res.*, *39*(8), 1342–1346, doi:10.1016/j.asr.2007.02.033.
- Yue, X., W. Wan, J. Lei, and L. Liu (2008), Modeling the relationship between $E \times B$ vertical drift and the time rate of change of $h_m F_2$ ($\Delta h_m F_2 / \Delta t$) over the magnetic equator, *Geophys. Res. Lett.*, *35*(5), L05104, doi:10.1029/2007GL033051.
- Zong, Q.-G., B. W. Reinisch, P. Song, Y. Wei, and I. A. Galkin (2010), Dayside ionospheric response to the intense interplanetary shocks-solar wind discontinuities: Observations from the digisonde global ionospheric radio observatory, *J. Geophys. Res.*, *115*, A06304, doi:10.1029/2009JA014796.